The University Of Sheffield.

Application of Microbubbles Generated by Fluidic Oscillation in the Upgrading of Bio Fuels

A Thesis

Submitted to the University of Sheffield for the degree of Doctor of Philosophy in the Faculty of Engineering

By

Nada N. Abdulrazzaq

THE UNIVERSITY OF SHEFFIELD

Department of Chemical and Biological Engineering

September 2016

Dedication

To my husband and sons, my parents and brothers and to the wonderful memory of my husband's father

Nada

Acknowledgments

First of all, I would like to express my sincere thanks and gratitude to my supervisor “Professor Will BJ Zimmerman” for his valuable guidance, encouragement, and motivation during my research study. It was a wonderful experience working with him. I also want to thank my second supervisor “Dr. Julia Rees” for her kindness and great support in reading this thesis and the related published papers which has improved their quality significantly. Without the support of my supervisors, this work could never have completed.

Special acknowledgment to all the technicians at the Department of Chemical and Biological Engineering in the University of Sheffield, especially, Andy Patrick and Keith Penny for their great efforts in constructing the rig for this system and helping in the analysis process.

Thanks and appreciation to all my colleagues in the microfluidic group for their kind assistance and helpful suggestions.

I must thank my husband Baseem for his unwavering love, constantly support, patience and understanding throughout my doctoral study. I owe all my successful to him. I would like to thank my lovely parents, my brothers and my husband’s mother for their unconditional love, support and encouragement during my study. Thanks to my sweet children for their patience as I could not spend enough time with them for such a long time.

I thank my sponsor “the Higher Committee of Education and Development in Iraq” for funding me in this scholarship.

Application of Microbubbles Generated by Fluidic Oscillation in the Upgrading of Bio Fuels

Abstract

With increasing energy demand and environmental concerns associated with the use of fossil based fuels, the use of renewable sources of energy, such as biomass, has attracted considerable attention. Biofuels, such as bioethanol and bio-oil which are derived from the pyrolysis of biomass, are potential candidates to replace conventional fuels. However, the utilization of these fuels poses some challenges. In the case of bioethanol, it must have a composition higher than 98% to be used as an additive to gasoline in automobile engines. Pyrolysis oils, on the other hand, suffer from thermal instability, low heating values due to high water content and high acidity due to high acid content. In both cases conventional distillation is not a feasible method for separation due to the azeotropic barrier, the high operating temperatures and the long residence times associated with its operation.

The current work is a serious attempt to address these concerns by using a novel distillation technique mediated by hot microbubbles. The study suggests injecting a hot carrier gas in the form of microbubbles to remove the volatile components from the liquid phase and thus minimizing the sensible heat transfer to the liquid. Preliminary experiments were carried out with a 50 vol/vol ethanol-water mixture to evaluate the separation ability of microbubble mediated distillation. The experiments were planned based on a central composite rotatable design method, from which an empirical model was developed, giving an inference about the optimum operating conditions of the process. The results from the binary distillation experiments showed that upon decreasing the height of the liquid mixture in the bubble tank and increasing the temperature of air microbubbles, the separation efficiency of ethanol was improved significantly. Furthermore, it was demonstrated that separation can be achieved with

only a small rise in the temperature of the liquid mixture, making this system suitable for treating thermally sensitive mixtures.

Microbubble mediated distillation was successful for breaking the equilibrium barrier in separating liquid mixtures by traditional distillation. The enrichment of ethanol in the vapor phase was found to be higher than that predicted from equilibrium conditions for all liquid ethanol mole fractions considered, including the azeotrope, and within a very short contact time for the microbubbles in the liquid phase (i.e. thin liquid levels). Ethanol with a purity of 98.2% vol. was obtained using a thin liquid level of 3 mm in conjunction with a microbubble air temperature of 90°C.

Microbubble distillation was used to isolate the major problematic components, water and carboxylic acids, from a model bio-oil mixture. The model mixture was chosen to contain water, acetic acid and hydroxypropanone with concentrations close to those in real bio-oil mixtures. It was found that 84% of the water content and 75% of the corrosive acid content were removed from the model mixture after 150 min. These reductions, in turn, will increase the calorific value, reduce the corrosivity and improve the stability of the bio-oil mixture. This upgrading was accomplished with only a slight increase in the liquid temperature of about 5°C under conditions of 3 mm liquid depth and 100°C microbubble air temperature making this technique convenient for separating bio-oil mixtures without affecting their quality.

A computational model of a single gas microbubble was developed using a Galerkin finite element method to complement the binary distillation experiments of ethanol-water mixtures. This model incorporates a novel rate law that evolves on a timescale related to the internal mixing of the microbubbles of 10^{-3} s. The model predictions were shown to be in very good agreement with the experimental data, demonstrating that the ratios of ethanol to water in the microbubble regime are higher than those predicted from equilibrium theory for all initial bubble temperatures and all liquid ethanol mole fractions considered. Furthermore, these ratios were achieved within very short contact times in the liquid mixture. The modelling data demonstrate that at shorter residence times, microbubbles are more efficient than fine bubbles in the separation process, however, as time passes the effect of bubble size diminishes. The modelling also showed improvements in the stripping efficiency of ethanol upon increasing the temperature of the air microbubbles, and an increase in the gas temperature with decreasing the residence time of the microbubbles. All of these results are consistent with experimental findings.

Contents

List of Tables ..... **x**
List of Figures ..... **xi**
Chapter One: General Introduction and Project Goals **1**
1.1 Introduction 2
1.2 Research hypothesis and objectives 4
1.3 General benefits of the research 5
1.5 Thesis organization 6
Chapter Two: Background and Literature Review **8**
2.1 Introduction 9
2.2 Properties of pyrolysis liquid (Bio-oil) 9
2.3 Pyrolysis process 13
2.4 Bio-oil problems 17
2.4.1 Low calorific value (heating value) 17
2.4.2 Chemical/thermal instability 18
2.4.3 Acidity 20
2.5 Applications of bio-oil 21
2.6 Bio-oil upgrading 23
2.6.1 Hydrodeoxygenation 24
2.6.2 Catalytic cracking 25
2.6.3 Extraction by supercritical fluids 25
2.6.4 High pressure thermal treatment (HPTT) 26
2.6.5 Catalytic biomass pyrolysis 27
2.6.6 Distillation 28
2.6.6.1 Molecular distillation 28
2.6.6.2 Reactive distillation 29
2.6.7 Emulsification 30
2.6.8 Solvent addition 30
2.7 Bioethanol 31
2.8 Microbubbles 33
2.8.1 Characteristics of microbubbles 33

2.8.2 Common methods of microbubbles generation....37
2.8.3 Difficulties in small bubbles generation....37
2.8.4 Generation of microbubbles using a fluidic oscillator....39
2.8.5 Energy efficiency of generating microbubbles by fluidic oscillation approach....43
2.8.5.1 Coanda effect....44
2.8.5.2 Boundary layer effect....44
2.8.6 Applications microbubbles....45
2.9 Mass and heat transfer dynamics of bubbles....47
2.10 Summary....52
Chapter Three: Experimental Design, Materials & Methodology....54
3.1 Introduction....55
3.2 Experimental Set-up....55
3.2.1 Design optimization....55
3.2.2 Experimental rig....58
3.2.3 Experimental procedure....60
3.3 Model aqueous solutions....61
3.3.1 Binary mixture....61
3.3.1.1 Materials....61
3.3.1.2 Experimental plan....62
3.3.1.2.1 Central Composite Rotatable Design method....63
3.3.1.3 Operating conditions....64
3.3.2 Azeotropic mixture....66
3.3.2.1 Materials....66
3.3.2.2 Operating conditions....66
3.3.3 Simulated bio-oil mixture....66
3.3.3.1 Materials....66
3.3.3.2 Operating conditions....67
3.4 Analytical methods....67
3.4.1 Gas chromatography (GC)....67
3.4.2 Gas sensors....68
3.4.2.1 Metal Oxide Gas Sensors....69
3.4.2.2 Measurements of the vapor phase concentration in binary mixtures....70
3.4.2.3 Measurements of the liquid phase concentration in ternary mixtures....74
3.4.3 Gas chromatography/mass spectrometry (GC-MS)....77

3.5 Bubble size measurement....78
Chapter Four: Separation of Binary Mixture....81
4.1 Introduction....82
4.2 Results and discussion....82
4.2.1 The effect of the process operating variables and fluidic oscillator on the separation efficiency....83
4.2.1.1 Effect of liquid depth and fluidic oscillator....83
4.2.1.2 Effect of microbubble air temperature and fluidic oscillator....88
4.2.1.3 Effect of evaporation time and fluidic oscillator....90
4.2.2 The effect of the process operating variables and fluidic oscillator on the temperature of the liquid mixture....93
4.2.2.1 Effect of depth of the liquid mixture and fluidic oscillator....93
4.2.2.2 Effect of microbubble air temperature....95
4.2.2.3 Effect of evaporation time....96
4.3 Effect of the humidity of the injected air and the presence of bubbles on the separation efficiency....97
4.4 Effect of air flowrate....98
4.5 Results bubble size analysis....100
4.6 Model development using a central composite rotatable design method (CCRD) 102
4.6.1 Effect of liquid depth and microbubble air temperature on the removal efficiency of ethanol....105
4.6.2 Effect of microbubble air temperature and evaporation time on the removal efficiency of ethanol....107
4.6.3 Effect of liquid depth and evaporation time on the removal efficiency of ethanol....108
4.7 Summary....109
Chapter Five: Separation of Azeotropic Mixtures....111
5.1 Introduction....112
5.2 Azeotropic mixture....112
5.3 Results and discussion....115
5.4 Comparison study between microbubble distillation and traditional distillation....118
5.5 Summary....122
Chapter Six: Separation of Multi Component Mixture....123
6.1 Introduction....124

6.2 Model pyrolysis oil mixture 124
6.3 Results and discussion 125
6.3.1 Effect of depth of the liquid mixture 125
6.3.2 Effect of microbubble air temperature 132
6.4 Summary 134
Chapter Seven: Modelling of Microbubble 136
7.1 Introduction 137
7.2 Model definition 138
7.2.1 Governing equations 139
7.2.2 Initial and Boundary conditions 141
7.3 Numerical method 144
7.3.1 Grid convergence study 144
7.4 Results and Discussion 145
7.4.1 Modelling profiles 146
7.4.2 Model sensitivity analysis 151
7.4.2.1 Variation of bubble size 151
7.4.2.2 Variation of inlet gas temperature 155
7.4.2.3 Variation of liquid mixture concentration 156
7.4.2.4 Variation of K parameter 158
7.5 Comparison between experimental and modelling data 161
7.6 Summary 162
Chapter Eight: Conclusions and Recommendation for Future Work 164
8.1 Introduction 165
8.2 Conclusions 165
8.3 Recommendations for future work 167
References 169
Appendix A: Schematic diagram of the diffuser base 190
Appendix B: Algorithm for electronic nose calculations 191
Appendix C: Physical properties for the evaporation dynamics of a hot bubble rising in an ethanol-water mixture 192

List of Tables

Table 2.1: The representative chemical composition of fast pyrolysis liquids.....10
Table 2.2: Comparison of bio-oil and typical fuels characteristics 12
Table 2.3: Decomposition products of pyrolysis process 15
Table 2.4: List of probable chemical reactions occurring in bio-oil during storage.....19
Table 2.5: Common organic acids in bio-oil mixture 21
Table 3.1: Chemical composition of the binary mixture 62
Table 3.2: Coded and real values of the variables according to CCRD method 63
Table 3.3: Operating conditions for the binary mixture experiments.....65
Table 3.4: Chemical composition of the azeotropic mixture.....66
Table 3.5: Operating conditions for azeotropic mixture experiments 66
Table 3.6: Chemical composition of the simulated bio-oil mixture 67
Table 3.7: Operating conditions for ternary mixture experiments.....67
Table 3.8: Test sample measurements 73
Table 3.9: Calibration concentrations of water.....77
Table 3.10: Summary of the operating conditions and the tools used for the bubble size measurement 78
Table 4.1: Independent variables with their real and coded levels 102
Table 4.2: The estimated regression coefficients for the empirical model 103
Table 4.3: Estimated and observed values of the removal efficiency of ethanol from the liquid mixture.....104
Table 5.1: Comparison between the vapor composition obtained by the microbubble distillation technique and those for isothermal equilibrium 118
Table 7.1: Grid convergence results at t=0.002 s 145
Table 7.2: Domain size convergence results at t=0.002 s.....145
Table 7.3: Ethanol vapor concentrations in the bubble regime as predicted by the numerical study and isothermal equilibrium data for different initial liquid ethanol mole fractions.....157

List of Figures

Figure 2.1: Picture of fast pyrolysis bio-oil 11
Figure 2.2: Fractionation sketch of bio-oil mixture 13
Figure 2.3: Fast pyrolysis unit 17
Figure 2.4: Applications of pyrolysis products 23
Figure 2.5: Bioethanol production 32
Figure 2.6: Division of a single large bubble into a number of smaller, equally sized bubbles which produces additional surface area 34
Figure 2.7: The relationship between bubble rising velocity and bubble diameter for air bubbles as shown theoretically and experimentally 36
Figure 2.8: Surface tension law 36
Figure 2.9: Growth of a single bubble on accordance of others 38
Figure 2.10: The fluidic oscillator 39
Figure 2.11: Geometry of the fluidic oscillator with dimensions 40
Figure 2.12: Jet diversion in fluidic oscillator by Coanda effect 41
Figure 2.13: Graph of frequency of oscillation as a function of the length of the feedback loop at different gas supply flow rate 42
Figure 2.14: Images of microbubble generation using microporous ceramic diffuser under different conditions (a) with fluidic oscillator (b) without fluidic oscillator 43
Figure 2.15: The main bubbling systems in direct contact evaporation (a) homogenous and (b) heterogeneous. 50
Figure 2.16: Variation of the average concentration of the bubble with time for a bubble with an inlet temperature of 423K 51
Figure 3.1: The 3D printed chamber for the bubble tank. 56
Figure 3.2: (a) CAD schematic diagram of the second built aluminum bespoke diffuser for the bubble tank, (b) The final assembly of the chamber with the diffusers. 57

Figure 3.3: The time profile for the liquid temperature using two different purpose built bespoke diffusers 58
Figure 3.4: Image of the experimental set-up 59
Figure 3.5: Schematic diagram of the experimental set-up 59
Figure 3.6: Picture of the fluidic oscillator. 60
Figure 3.7: Different metal oxide gas sensors. 69
Figure 3.8: Gas sensor circuit schematic 70
Figure 3.9: Gas concentration measurement apparatus 71
Figure 3.10: Dynamic response of gas sensors 72
Figure 3.11: Gas sensors calibration curves 72
Figure 3.12: Graph of the real concentrations of acetic acid versus the estimated ones by Eq. 3.10 76
Figure 3.13: Graph of the real concentrations of acetol versus the estimated ones by Eq. 3.10 76
Figure 3.14: Schematic view of the experimental set up for the bubble size measurement 79
Figure 4.1: Graph of the evaporation percentage of the liquid mixture, ethanol and water against liquid mixture depth at a microbubble air temperature of 90°C and evaporation time of 125 min. All experiments were carried out with the use of the fluidic oscillator 84
Figure 4.2: Graph of the evaporation percentage of liquid mixture with and without the use of fluidic oscillator (FO) against liquid mixture depth at a microbubble air temperature of 90°C and evaporation time of 125 min 84
Figure 4.3: Graph of the concentration of ethanol in the liquid phase against liquid mixture depth at a microbubble air temperature of 90°C and evaporation time of 125 min 85
Figure 4.4: Graph of the concentration of ethanol in the vapor phase against liquid mixture depth at a microbubble air temperature of 90°C and evaporation time of 125 min 85
Figure 4.5: Graph of the evaporation percentage of liquid mixture against microbubble air temperature at a liquid depth of 7 mm and an evaporation time of 125 min 88
Figure 4.6: Graph of the concentration of ethanol in the liquid phase against microbubble air temperature at a liquid depth of 7 mm and an evaporation time of 125 min 89
Figure 4.7: Graph of the concentration of ethanol in the vapor phase against microbubble air temperature at a liquid depth of 7 mm and an evaporation time of 125 min 89

Figure 4.8: Graph of the evaporation percentage against evaporation time at a liquid depth of 7 mm and microbubble air temperature of 90°C 91
Figure 4.9: Graph of the concentration of ethanol in the liquid phase against evaporation time at a liquid depth of 7 mm and microbubble air temperature of 90°C 91
Figure 4.10: Graph of the concentration of ethanol in the vapor phase against evaporation time at a liquid depth of 7 mm and microbubble air temperature of 90°C 92
Figure 4.11: Graph of the temperature of the liquid mixture against evaporation time for different liquid depths at a microbubble air temperature of 90 °C and an evaporation time of 125 min.....93
Figure 4.12: Graph of the temperature of the liquid mixture against evaporation time for different air microbubble temperatures at a liquid depth of 7 mm and evaporation time of 125 min. 95
Figure 4.13: Graph of the temperature of the liquid mixture against evaporation time for different evaporation times at a liquid depth of 7 mm and microbubble air temperature of 90C. 96
Figure 4.14: Graph of the evaporation percentage against depth of liquid mixture for different separation modes at a microbubble air temperature of 90°C and an evaporation time of 125 min. 97
Figure 4.15: Graph of the concentration of ethanol against microbubble air temperature at a microbubble air temperature of 90°C and an evaporation time of 125 min.....98
Figure 4.16: Plot of the evaporation percentage of the liquid mixture against air flowrate 99
Figure 4.17: Plot of the final concentration of ethanol in the liquid mixture against air flowrate. 100
Figure 4.18: Time profiles of the liquid mixture for different air flowrates.....100
Figure 4.19: Graph of bubble diameter versus relative frequency for the analysis of images taken for bubbles generated in (a) pure water and (b) 50% vol. ethanol-water solution under oscillatory flow 101
Figure 4.20: Graph of the estimated values versus the observed values of the recovery efficiency of ethanol from the liquid mixture 105
Figure 4.21: Response surface predicting removal efficiency of ethanol from the model equation: effect of liquid level and microbubble air temperature.....106

Figure 4.22: Response surface predicting removal efficiency of ethanol from the model equation: effect of evaporation time and microbubble air temperature 107
Figure 4.23: Response surface predicting the removal efficiency of ethanol from the model equation: effect of liquid level and evaporation time 108
Figure 5.1: Liquid-vapor equilibrium diagram for an ethanol-water mixture 113
Figure 5.2: Variation of the final concentration of ethanol in the liquid mixture with the liquid mixture level 115
Figure 5.3: Variation of the final concentration of ethanol in the vapor phase with the liquid mixture level at a microbubble temperature of 90°C 116
Figure 5.4: Variation of the percentage of evaporation of the liquid mixture versus liquid mixture height at a microbubble temperature of 90°C 116
Figure 5.5: Concentration of ethanol in the vapor phase (Yexp) and their corresponding concentrations at the equilibrium state (Yeq) at different evaporation times. Initial conditions are: 96 %vol. ethanol solution, 3 mm liquid level and 90°C air microbubble temperature 117
Figure 5.6: Comparison between the K-values of ethanol obtained by the microbubble distillation (K microbubble distillation) and the corresponding equilibrium values (K equilibrium) at different liquid ethanol compositions. The error bars represent the standard error of the experiments. The initial conditions are 3 mm liquid level and 90°C microbubble temperature 119
Figure 5.7: Temperature of the outlet air from the bubble tank plotted against evaporation time for the azeotropic mixture at different liquid levels for an air microbubble temperature of 90°C and evaporation time of 90 min 120
Figure 5.8: Temperature of the azeotropic liquid mixture against time for different liquid levels at a microbubble air temperature of 90°C and evaporation time of 90 min 121
Figure 6.1: Variation of the concentration water in the model mixture with time at varying liquid depths 126
Figure 6.2: Variation of the concentration acetic acid in the model mixture with time at varying liquid depths 126
Figure 6.3: Variation of the concentration of acetol in the model mixture with time at varying liquid depths 127
Figure 6.4: Graph of the separation efficiency of each component in the model bio-oil mixture at two liquid levels: 3 mm and 5 mm after 150 min evaporation time 129

Figure 6.5: Time profile for the temperature of the liquid mixture during the experiment after 150 min at two different liquid levels 130
Figure 6.6: GC-MS spectrum at 150 min for (a) 5 mm and (b) 3 mm liquid levels 131
Figure 6.7: Variation of the concentration of water in the model mixture with time at two microbubble air temperatures 132
Figure 6.8: Variation of the concentration of acetic acid in the model mixture with time at two microbubble air temperature 132
Figure 6.9: Variation of the concentration of acetol in the model mixture with time at two microbubble air temperatures 133
Figure 6.10: Time profile for the temperature of the liquid mixture during the experiment after 150 min at two different air microbubbles temperature 134
Figure 7.1: The 2-D axisymmetric model configuration 138
Figure 7.2: k values versus the square errors 143
Figure 7.3: The 2-D axisymmetric, free triangular mesh used for modelling 144
Figure 7.4: Microbubble profile with R=100 microns, T_0=423 K and 50% mole ethanol liquid concentration after $t = 0.0015$ s. 146
Figure 7.5: The steady state velocity field inside and around the bubble 147
Figure 7.6: The variation of the average microbubble temperature with time. The initial conditions are 50% mole ethanol liquid concentration and bone dry air with T_0 =393 K injected in the microbubbles 147
Figure 7.7: The variation of the average concentration of ethanol and water in the microbubble with time. The initial conditions are 50% mole ethanol liquid concentration and bone dry air with T_0=423 K injected in the microbubbles 148
Figure 7.8: The variation of the average mole fractions of ethanol and water in the microbubble with time. The initial conditions are 50% mole ethanol liquid concentration and bone dry air with T_0=423 K injected in the microbubbles 150
Figure 7.9: A log-log plot for the average mass fluxes for ethanol and water at the bubble skin versus time. The initial conditions are 50% mole ethanol liquid concentration and bone dry air with T_0=423 K injected into the microbubbles 151
Figure 7.10: Variation of the average concentration of ethanol with bubble size. The initial bubble temperature is T_0 =393 K and the initial liquid concentration is 50% mole ethanol 152

Figure 7.11: Variation of the average temperature of the bubble with bubble size R=0.0005 m (top), R =0.00025 m, R =0.0001 m, R =0.00005 m, R =0.000025 m (bottom). Initial bubble temperature is T_0 =393 K and initial liquid concentration is 50% mole ethanol 153
Figure 7.12: The temperature and concentration profiles at $t = 0.0003$ s. for (a) fine bubble with R=0.0005 m and (b) microbubble with R=0.0001 m. The initial conditions are 50% mole ethanol liquid concentration and bone dry air with T_0 =393 K injected in the microbubbles 154
Figure 7.13: Variation of the average concentration of ethanol with bubble temperatures T_0 =423 K (top line), 393 K, 373 K, 353 K and 333 K (bottom line). The initial condition is bone dry air injected into the microbubbles 155
Figure 7.14: Semi-log plot of the variation of the average bubble temperature at different initial bubble temperatures T_0 =423 K (top line), 393 K, 373 K, 353 K and 333 K (bottom line). The initial condition is bone dry air injected into the microbubbles 156
Figure 7.15: Average concentration profile data for ethanol at different liquid compositions: 90% mole ethanol (top line), 70% mole, 50% mole, 30% mole, 10% mole (bottom line). The initial condition corresponds to bone dry air at T0 =393 K injected into the microbubbles 157
Figure 7.16: Variation of the average temperature of the bubble with K value. Initial bubble temperature is T_0 =393 K and initial liquid concentration is 50% mole ethanol. 158
Figure 7.17: Variation of the average concentration of ethanol with K value. Initial bubble temperature is T_0 =393 K and initial liquid concentration is 50% mole ethanol 159
Figure 7.18: The average mole fraction profiles of ethanol at different boundary conditions at the gas-liquid interface 160
Figure 7.19: Comparison between experimental and modelling data for different liquid ethanol mole fractions after 0.00015 s and 0.003 s. The initial conditions are bone dry air with T0=363 K injected into the microbubble and 293 K liquid temperature 162
Figure 8.1: Continuous microbubble mediated distillation column concept 168

The University Of Sheffield.

Chapter One

General Introduction and Project Goals

Chapter One

General Introduction and Project Goals

1.1 Introduction

Today, the subject of energy has become the most imperative topic in the globe as a whole. Threats of energy shortage, increasing the cost of the fossil fuels along with their ecological concerns are the most daunting challenges facing the present time. Fossil fuels, including oil and coal, are the major energy sources in the world today while they are responsible for about 98% of carbon emissions (Balat et al. 2009). Such emissions can cause numerous environmental crises represented by air pollution and global warming as well as many hazards to human health.

One possible way to reduce these emissions is by switching to renewable bio-based fuels. One of the most promising alternative sources of energy on earth is biomass (Klass 2004). The term biomass refers to plant or animal derived materials. It is the only sustainable source of renewable carbon which is produced by the natural photosynthesis process of plants. The abundance, renewability and high energy value of biomass make it preferable to many other renewable energy sources. Biomass is also an environmentally friendly resource since its contents of nitrogen, sulfur and ash are negligible, thus its emissions of nitrogen oxides (NOx) and sulfur dioxides (SO_2) are low. Moreover, its carbon emissions are neutrally balanced as CO_2 emitted during biomass burning will be consumed later by the plant growth (Zhang et al. 2007).

The basic concept of using biomass as a renewable source of energy involves converting it into chemicals or fuels such as bioethanol and bio-oil. Bioethanol can be produced from the fermentation of sugars present in plant crops (Baeyens et al. 2015), while bio-oil is produced from the thermal degradation of agricultural feedstocks in a process called pyrolysis (Kim et al. 2012). Although these liquid fuels have the potential to replace fossil based fuels in the near future as they are produced from renewable sources and are associated with low carbon emissions, their direct utilization is limited. Bioethanol needs to have high purity in order to be

utilized as an additive fuel to gasoline in motor vehicles. Pyrolysis oil, on the other hand, is a complex mixture with several unfavorable properties such as high viscosity, high corrosiveness, thermal instability upon heating and low heating value resulting from their high contents of water and reactive oxygenated compounds (Diebold 2000).

In order to improve the quality of bio-fuels, upgrading is necessary. Pyrolysis oil quality can be greatly improved by lowering its water and acid contents which consequently leads to an increase in its heating value and stability and reduce corrosivity (Oasmaa et al. 2005). Over the years, many technologies have been proposed and tested to address pyrolysis oils concerns including hydro-deoxygenation, catalytic cracking of pyrolysis vapors, emulsification, solvent addition and esterification. Most of these processes, however, are associated with high energy requirements and operational difficulties (Xu et al. 2010; Kim et al. 2014). Industrially, distillation is the main technology that is considered for the separation of liquid mixtures. Unfortunately, it cannot be used to improve the quality of bio-oil as it leads to undesirable chemical changes and the formation of a large amount of solid residue upon operating at high temperatures for long distillation times (Balat et al. 2009). In addition, the formation of constant boiling mixtures (i.e. azeotropes) limits the degree of purity for numerous chemicals (Julka et al. 2009; Oliveira et al. 2013).

On the basis of the above considerations, the development of a new technique for upgrading biofuels is essential. Separation of liquid mixtures by bringing the liquid phase into contact with a gas phase is a major technique for separating or concentrating solutions at temperatures significantly lower than their boiling points, thus it can be utilized for treating thermally sensitive liquids. Direct contact evaporation (DCE) has been widely used for many years for separating aqueous solutions through injecting fine (1-3 mm) (Francis & Pashley 2009) or coarse (~1 cm) (Ribeiro & Lage 2004) superheated gas bubbles. Bubbles are normally created by injecting a gas phase through a porous material, perforated plate or a set of perforated pipes located at the bottom of a bubble column or evaporator containing the target solution. Owing to the absence of any separating walls between the processing fluids, this technique has high thermal efficiency, which reaches to around 95% with a temperature difference of only 2-5°C between the bubble and the liquid phases (Ribeiro et al. 2005; Ribeiro et al. 2007; Ribeiro & Lage, 2004; Ribeiro & Lage, 2005; Jacobs, 1988; Kang et al. 2002; Díaz et al. 2008).

If the gas phase is injected as a cloud of uniformly dispersed, non-coalescent microbubbles (Zimmerman et al. 2008; Zimmerman et al. 2009; Zimmerman, et al. 2011), there exists a

potential for increasing the rates of both heat and mass transfers. The high surface area to volume ratio offered by microbubbles will enhance the heat and mass transfers since the rate of these interfacial transport processes are hugely dependent on the contact area between the gas and liquid phases. Additionally, smaller bubbles have high internal pressures due to surface tension which also significantly enhances the driving force for both heat and mass transfers (Bredwell & Worden 1998; Worden & Bredwell 1998).

This research project was attempted in order to address the major problems of biofuels experimentally with the engagement of microbubbles. While the concept of traditional distillation depends on boiling the liquid phase to raise the vapor, the current technique uses hot bubbles to intensify the vaporization in a similar manner to that of direct contact evaporation. Microbubbles used in the current work are generated via a cheap yet energy efficient method using a fluidic oscillator (Zimmerman et al. 2008; Zimmerman et al. 2009; Zimmerman et al. 2011). Unlike conventional methods for the generation of microbubbles which are dependent upon the construction of the porous materials, the characteristics of the fluidic oscillator, by contrast, help to reduce the size of the generated bubbles when connected to a diffuser by ensuring an early break off for the bubbles, offering the smallest possible size. The fluidic oscillator offers several benefits for the generation of microbubbles. It is a cheap device with no moving mechanical parts which make it simple, robust, reliable and long life (Tesař 2014). It is easy to manufacture, it uses no electricity, and requires only an air supply to generate uniformly spaced non-coalescent microbubbles of approximately the same size as the pores of the sparger. Low energy consumption is the main feature that distinguishes this approach from the traditional methods of microbubble generation that require a significant supply of energy (Zimmerman et al. 2011). To the best of our knowledge, there is currently no report in the literature that addresses the use of hot air microbubbles for the separation and the upgrading of biofuels.

1.2 Research hypothesis and objectives

The term “microbubble distillation” refers to the use of hot microbubbles generated by fluidic oscillation for the separation of liquid mixtures. This research program hypothesizes that the technique of microbubble distillation can separate thermally sensitive mixtures without destroying their useful characteristics. The principle involves heating the gas phase instead of the liquid phase to achieve vaporization and use of a thin layer of liquid film through which

hot bubbles can ascend. It is expected that the presence of this thin film layer will lead to evaporation/mass transfer processes dominating over sensible heat transfer and thus providing an appropriate system for upgrading pyrolysis oils.

The research also hypothesizes that non-equilibrium operation between the contact phases can be achieved by tuning the height of the liquid film to control the contact times for the rising bubbles. The concept involves injecting microbubbles into a laminar regime to prevent them from equilibrating very rapidly with the surrounding liquid, thus ensuring that transport is continuous.

The objectives are:

1. Design and develop a unit for microbubble distillation to efficiently upgrade biofuels.
2. Investigate the effects of varying different operating conditions such as the inlet temperature of air microbubbles, the height of the liquid layer in the bubble tank and the time of evaporation to provide information on their influences on the recovery efficiency of the target components and on the final temperature of the product.
3. Investigate the feasibility of applying the microbubble mediated distillation technique in the purification of bioethanol.
4. Investigate the feasibility of applying the microbubble mediated distillation technique in the upgrading of thermally sensitive mixtures, e.g. pyrolysis oils, through the separation of water and unfavorable volatile acids without significantly increasing the temperature of the bio-oil mixture.
5. Establish a numerical model using the technique of computational fluid dynamics (CFD) with COMSOL MULTIPHYSICS Software to describe the evaporation dynamics of the microbubbles for the purpose of improving our understanding of the principles of microbubble distillation along with the effects of operational factors.

1.3 General benefits of the research

The upgrading of biofuels will contribute significantly to reducing the heavy reliance on our limited stock of fossil based fuels, meeting the world's energy demand and decreasing the UK's dependence on the expensive foreign energy sources. Moreover, biofuels are clean fuels with low environmental risks and pollution levels and thus their use will massively diminish

greenhouse gas emissions and other regulated air pollutants that cause global warming and climate change.

The current study provides information about the optimum operating conditions for a new cost effective separation process which will have the potential to be scaled up for use in larger commercial upgrading plants. It is expected that this novel approach can overcome the disadvantages of traditional distillation by minimizing sensible heat transfer to the liquid mixtures, improving the separation efficiency as well as reducing the operational costs.

1.4 Thesis Organization

This project is constructed into eight chapters.

Chapter one consists primarily of a general introduction to the research, research hypothesis, objectives and benefits.

Chapter two provides a detailed literature review about bio-oil properties and production and discusses the past work and investigations on bio-oil upgrading. This is followed by a significant review on microbubbles, their applications and generation methods.

Chapter three describes the materials and methodologies applied to accomplish this study. This includes a description of the experimental design of the microbubble mediated distillation unit, the experimental procedures for the separation experiments and the chemical characterization techniques of liquid and vapor mixtures.

Chapter four presents the first experimental investigation results which explore the performance of the microbubble distillation technique for the separation of an ethanol-water binary mixture. An experimental plan was established to optimize the operating variables for the process efficiency. Microbubbles generated with, and without, the use of the fluidic oscillator device are applied in this study in order to compare the efficiency of the separation process for these two cases.

Chapter five is dedicated to the investigation of bioethanol purification. This chapter displays the results of the separation of azeotropic mixture of ethanol-water under different experimental conditions. A comparison study between microbubbles mediated distillation and atmospheric traditional distillation is also established.

Chapter six presents the results of the application of the proposed technology on the separation of a simulated bio-oil mixture. This explores the simultaneous separation of water and carboxylic acids from a model bio-oil mixture under different operating conditions.

Chapter seven discusses the results of the numerical modelling of microbubble using COMSOL MULTIPHYSICS Software. The effect of bubble size, bubble initial temperature and liquid composition on the evaporation dynamics of microbubbles are studied. A validation study with the experimental data is also included.

Chapter eight summarizes the overall conclusions of the study findings and contains recommendations for the future work.

The University Of Sheffield.

Chapter Two

Background and Literature Review

Chapter Two

Background and Literature Review

2.1 Introduction

This chapter provides a critical overview about the key topics of this thesis. The first part presents a general survey about bio-oil, its characteristics, its production from the process of pyrolysis, its problems and its applications. This is followed by a detailed review about some of the most common bio-oil upgrading technologies and recent development, including discussions on their features and shortcomings. Next, a review about bioethanol properties and production processes is presented. As this research study is motivated by the application of a novel generation technique for microbubbles which is based on oscillatory flow, this literature review includes a section related to microbubbles, their characteristics, applications and methods of generation. The working mechanism of the novel aeration system (fluidic oscillator) for the generation of microbubbles is also discussed. The next part presents a review on the heat and mass transfer dynamics of bubbles in a bubble column, as well as a synopsis of the theory of the current study. A general summary, including the themes of the current thesis, is given in last part of this chapter.

2.2 Properties of pyrolysis liquid (Bio-oil)

Bio-oil is a dusky brown mobile organic liquid with a smoky odor. It is a complex blend of more than 400 compounds with wide range of boiling points and different chemical functional groups (Nolte & Liberatore 2011). These include acids, alcohols, ketones, aldehydes, esters, sugars, furans and phenols. The typical composition of bio-oil is listed in table 2.1.

Pyrolysis oils are most commonly derived from the partial de-polymerization of the three fundamental polymers of biomass (cellulose, hemicellulose and lignin) in a process called pyrolysis in the absence of air and at atmospheric pressure (Zhang et al. 2007). The partial decomposition of biomass causes the chemical composition of bio-oils to be feedstock

dependent. The pyrolysis conditions, such as temperature, heating rate and residence time, also play a significant role in the determination of the composition of bio-oils. Thus, the properties and constituents of bio-oils vary significantly depending on these factors (Bridgwater 2012; Wu et al. 2008). Bio-oils have unique advantages over the biomass from which they are produced. These include higher energy density than that of the biomass, easier handling, storage and transportation (Maggi & Delmon 1994).

Table 2.1: The representative chemical composition of fast pyrolysis liquids (Balat et al. 2009).

Major bio-oil components	***wt. %***
Water	20-30
Lignin fragments	15-30
Aldehydes	10-20
Carboxylic acids	5-15
Carbohydrates	2-5
Phenols	1-4
Furfurals	2-5
Alcohols	2-5
Ketones	1-5

Due to the large number and diversity of components in bio-oils, they have the potential of being a resource of numerous valuable chemicals that can be extracted and used for other purposes (Bridgwater 2003; Liu et al. 2012). However, some of these compounds, such as acids, aldehydes and ketones, are highly reactive and can cause instability issues (Karimi et al. 2010; Drese et al. 2011). Diebold (2000) reported that bio-oils are highly unstable mixtures and their properties change significantly during storage in a process referred to as "aging". These changes can be observed as a boost in the viscosity, decrease in the volatility, formation of carbon dioxide from the decarboxylation of carboxylic acids, an increase in the water content and eventually a phase separation into two distinct layers which are different in their physicochemical properties: aqueous polar phase and sticky organic phase (Diebold 2000; Yu et al. 2007; Xu et al. 2011). Pyrolysis oils have been described as a micro-emulsion in which a discontinuous phase (pyrolytic lignin molecules) is stabilized by a continuous phase (holo-cellulose decomposition products which are soluble in water) by phenomena such as hydrogen

bonding and it is generally supposed that the phenomenon of "aging" is caused by the collapse of this emulsion (Asadullah et al. 2007). A photograph of pyrolysis oil is shown in figure 2.1.

Figure 2.1: Image of fast pyrolysis bio-oil (Cset.iastate.edu).

Bio-oils are highly polar mixtures due to the presence of a significant portion of oxygenated compounds. This high polarity is the major reason of their poor solubility in hydrocarbon fuels as well as for their low energy density when compared to conventional fuels (Balat et al. 2009). Physical and chemical properties of bio-oils are markedly different from those of traditional fuels (Oasmaa & Meier 2005; Sipila et al. 1998). A comparison between the typical properties of bio-oil with those of conventional fuels are outlined in table 2.2.

Bio-oil density is about 1200 kg/m^3, which is significantly higher than that of fossil fuels (around 850 kg/m^3). This high density results from the presence of high molecular weight compounds which make up about 30% by weight of the liquid bio-oil (Gayubo et al. 2004) and it is an indication of high oxygen content rather than high aromatic content (Asadullah et al. 2007). The viscosity of bio-oils ranges from 25 to about 1000 cP, depending mainly on the water content, the proportion of low molecular weight components in the oil mixture and storage conditions (Venderbosch & Prins 2010) and it is an indicator of the bio-oil age and

stability. In addition, bio-oils have low pH values (2.5-3) caused by the presence of organic acids such as acetic acid and formic acid (Karimi et al. 2010).

Table 2.2: Comparison of bio-oil and typical fuels characteristics (Bridgwater et al. 2002).

Properties	***Unit***	***Bio-oil***	***Diesel***	***Heavy oil***
Density	kg/m^3 at 15°C	1220	854	963
Typical composition	%C	48.5	86.3	86.1
	%H	6.4	12.8	11.8
	%O	42.5	-	-
	%S	-	0.9	2.1
Kinematic viscosity	cSt at 50°C	13	2.5	351
Flash point	°C	66	70	100
Pour point	°C	27	20	21
Ash	%wt.	0.13	0.01	0.03
Sulfur	%wt.	0	0.15	2.5
Water	%wt.	20-30	0.1	0.1
LHV	MJ/kg	17.5	42.9	40.7
Acidity	pH	3	-	-

The complex nature of bio-oil mixture makes the analytical process difficult and in most cases it requires a series of analysis techniques to determine its chemical composition (Wang et al. 2012). Characterization of the bio-oil mixture is usually carried out using gas chromatography/mass spectrometry (GC/MS) which is used for the quantitative and qualitative analysis of bio-oil compounds. However, the major limitation in this technique is that it only detects the volatile components which make up about 40% wt. of the total bio-oil mixture (Garcia-Perez et al. 2007; Bayerbach & Meier 2009). The non-volatile fraction could be analyzed using other testing techniques such as high performance liquid chromatography (HPLC), gel permeation chromatography (GPC) or thermogravimetry (TG) (Zhang & Kong 2012; Garcia-Perez et al. 2007). Fourier transform infrared (FT-IR) is another promising analysis method that could be used as a fast technique for identifying the quantity of functional groups present in bio-oil mixtures. In this technique, the bio-oil mixture can be treated as being

composed of a few chemical functional groups instead of hundreds of components (Murtala et al. 2012; Shawal et al. 2012).

One of the suggested strategies to simplify the chemical analysis process is to separate the bio-oil mixture into fractions, or groups of chemicals, using organic solvents of different polarity or acidity. Thereafter, each fraction can be analyzed separately using a suitable technique of any of the above mentioned analytical techniques. This liquid-liquid extraction approach makes the chemical analysis process simple, precise and able to identify more species (Garcia-Perez et al. 2007; Venderbosch et al. 2010). The proposed solvent fractionation scheme for a bio-oil mixture is shown figure 2.2.

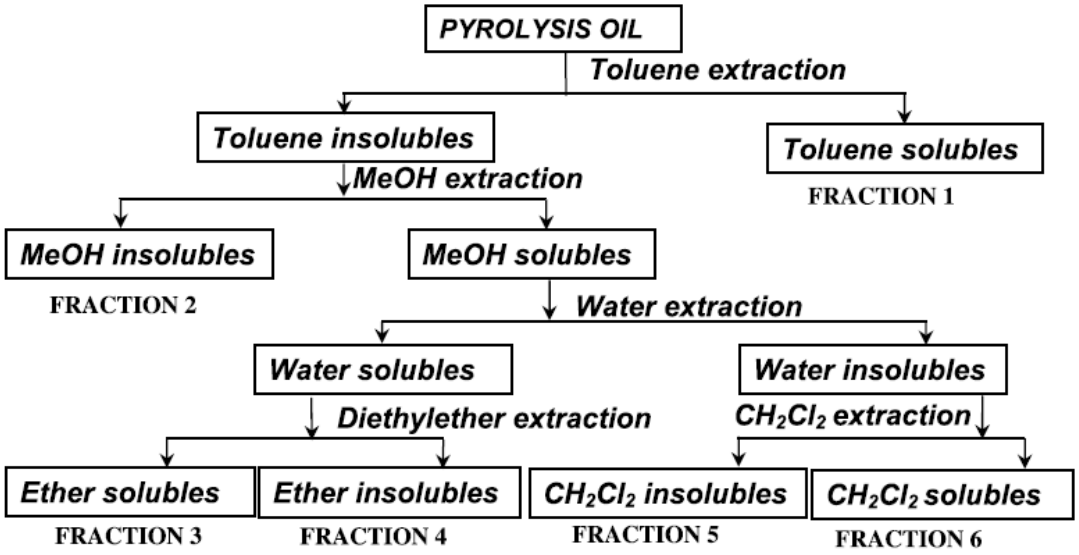

Figure 2.2: Fractionation sketch of bio-oil mixture (Garcia-Perez et al. 2007).

2.3 Pyrolysis Process

Pyrolysis can be defined as the thermochemical decomposition of the organic materials (cellulose, hemicellulose and lignin) present in lignocellulosic biomass without the existence of oxygen (Mohan et al. 2006; Demirbas 2011). During this process, feedstock (or biomass) is converted into three major products: liquid, solid and gas in different proportions (Mullen & Boateng 2008). The liquid product is called "bio-oil" or "pyrolysis oil", the solid product is called "bio-char" and the gaseous product is called "bio-gas". These three products are of great interest since they represent renewable alternative sources of energy.

The distribution of these three pyrolysis products depends mainly on the process conditions (Moens et al. 2009). High temperatures and long hot vapor residence times would be required to maximise the gas yield. Low temperatures and longer vapor residence times are necessary for charcoal production, while the optimum conditions for increasing the liquid proportion are moderate temperatures and short vapor residence times (Balat et al. 2009; Bridgwater 2012). The mode for which the liquid output is at the maximum level is called fast pyrolysis (also defined as thermolysis), while the mode associated with maximum charcoal production is called conventional or slow pyrolysis (Balat et al. 2009).

Pyrolysis is considered to be one of the most auspicious technologies by which biomass is converted into more valuable materials (Czernik et al. 1994; Pattiya et al. 2006; Peng & Wu, 2011). Interestingly, there is limited dissipation of energy during this process. The liquid product (bio-oil) can be used directly as a liquid fuel or upgraded to motor fuels. The char (solid product) has different usages; it can be used as solid fuel, upgraded to activated carbon or used as a soil fertilizer because of its high mineral content (Pattiya et al. 2012). The hot non-condensable gases, which are composed mainly of CO_2, CO, CH_4 and H_2, can be recycled back into the pyrolysis process and used to provide the heat necessary for burning or drying the biomass (Venderbosch & Prins 2010). This technique leads to a significant reduction in the overall cost for the heating of the system (Rout et al. 2009).

In fast pyrolysis, feedstock is decomposed by heating at a moderate temperature (around 500°C) and high heating rate in the absence of oxygen. The vapors produced are quenched rapidly in a short residence time (1-2 s). Under such conditions, char generation is minimized and secondary cracking reactions, which break down the large molecules into gaseous products, are hindered (Bridgwater 2012). Pyrolysis oil is the main product from the fast pyrolysis process and the product distribution is as follows: 70-75 %wt of bio-oil, 15-25 %wt of char and 10-25 %wt of non-condensable gases, depending on the feedstock used (Li et al. 2011; Li et al. 2015). The main decomposition products of the pyrolysis process are listed in table 2.3.

Different types of biomass can be used as a raw material in the fast pyrolysis process and this is the main advantage that characterizes this process from other thermochemical conversion methods (Bridgwater 2012). The most common biomasses used are: energy crops such as sugar and corn, agricultural waste, forest residue and plastic wastes. Among these different types of biomass, those which are not for use in the food industry are the most promising choices.

Feedstock such as forest residues (i.e. wood thinning) and agriculture wastes (i.e. sugarcane bagasse, rice husk, peanut hall and wheat straw) are being considered as favorable sources for bio-oil production (Gayubo et al. 2005; Venderbosch & Prins 2010).

Table 2.3: Decomposition products of pyrolysis process (Fivga 2011).

Lignocellulosic biomass components	***Degradation temperature***	***Pyrolysis decomposition products***
Cellulose	275-350 °C	**Volatiles**: carbon monoxide, carbon dioxide, methanol, acetaldehyde. acetic acid, hydroxyacetaldehyde (glycolaldehyde), I-hydroxy-2-propanone (acetol), and certain < C,-hydrocarbons and/or their derivatives); **Anhydroglucopyranose**: (1,6-anhydro-p-D-glucopyranose (levoglucosan)); **Anhydroglucofuranose:** (1,6-anhydro-p-D-glucofuranose); **Dianhydroglucopyranose**: (1,4;3,6-dianhydro-a-Dgludopyranose); **Furans**: (mainly (2H)-furan-3-one, methyl-(3H)-furan-2-one (orangelicalactone), 2-furaldehyde (furfural), 5-methyl-2-furaldehyde, and 5-hydroxymethyl-3-furaldehyde); **Others**: (5-hydroxy-2-(hydroxymethyl)- 2,3-dihydro-(4H)-pyran-4-one (1,5-anhydro-4-deoxy-DglJ>cerohex-I-en-3-ulose) and 3-hydroxy-5,6-dihydro-(2H)-pyran4-one (1.5anhydro-bdeoxypent-1-en-3-ulose)).
Hemicellulose	150-350 °C	**Volatiles:** carbon dioxide, formic acid. Acetic acid,hydroxyacetaldehyde, 1-hydroxy-2-propanone Anhydroglucopyranose: (1,6-anhydro-p-D-glucopyranose (levoglucosan)); other anhydroglucoses: (1,6-anhydro-_-D-glucofuranose); other anhydrohexoses: (1,6-anhydro-_-D-mannopyranose); levoglucosenone: Furans: (2H)-furan-3-one, 2-furaldehyde, 5-methyl-2-furaldehyde furfural
Lignin	250-500 °C	**Volatiles**: carbon monoxide, carbon dioxide, diethyl ether, acetic acid, **Catechols:** catechol **Vanillins:** vanillin, homovanillin, vanillic acid; **Other guaiacols**: guaiacol **Propyl guaiacols:** coniferyl alcohol **Other phenols**: phenol, 2-methyl phenol, **Aromatic hydrocarbons:** benzene

In order to achieve the specific requirements for heat and mass transfer in the fast pyrolysis process, biomass requires pretreatment processing before entering the pyrolysis plant. Due to the low thermal conductivity of biomass, it should be ground into small particles (below 3mm in diameter) to ensure that they achieve the optimum process temperature quickly. This is the most important parameter in the process. Other key parameters include the reaction temperature and the residence time since exposure of biomass to lower temperatures and longer residence times favors char formation. Another important stage is the drying of the feedstock. Typically, biomass should contain no more than 10% moisture in order to reduce the water content in the final liquid product (Bridgwater 2003; Bridgwater 2012).

In general, pyrolysis systems comprise four fundamental parts: injection system, pyrolysis reactor, collection system and control system (Zhang et al. 2011). The pyrolysis reactor is the core piece of equipment in a pyrolysis plant. Pyrolysis can be carried out using a number of reactor configurations, for example ablative reactors, fluidized bed reactors, vacuum reactors, free fall reactors, circulating fluid bed reactors and entrained flow reactors. However, amongst all of these types, the fluidized bed is the most widespread configuration in both research and industrial fields because of its ease of operation and its ability to efficiently transfer heat to the feedstock (Bridgwater 1999).

The other important part in the pyrolysis plant is the bio-oil collection system. It is responsible for the quality and the quantity of the oil produced. The collection system involves two main sections: the first section contains mechanical cyclones which help to remove the entrained char particles from organic vapors and the second section condenses the pyrolysis vapors. Char has to be removed from bio-oil before storing or further processing as it contains different metals that can act as catalysts for polymerization reactions which affect bio-oil properties through increasing its viscosity. However, cyclones are not efficient in removing fine char particles smaller than 10μm. Another system, called the hot vapor filtration system, is being developed for this purpose and can remove smaller particles from hot pyrolysis vapors more effectively (Bridgwater 2012; Diebold 2000).

The last section in the pyrolysis plant is the condensation train system in which pyrolysis vapors are condensed to obtain the final liquid product (Zhang et al. 2011). Hot pyrolysis vapors should be condensed quickly to avoid any secondary reactions occurring. These secondary reactions lead to the breakdown of heavy molecules into lighter ones and eventually into non-condensable gases. Therefore, this section requires a careful design and control to increase the

yield of the liquid bio-oil product and also to optimize the yield of desired chemical species over others. A schematic diagram of the fast pyrolysis system is presented in figure 2.3.

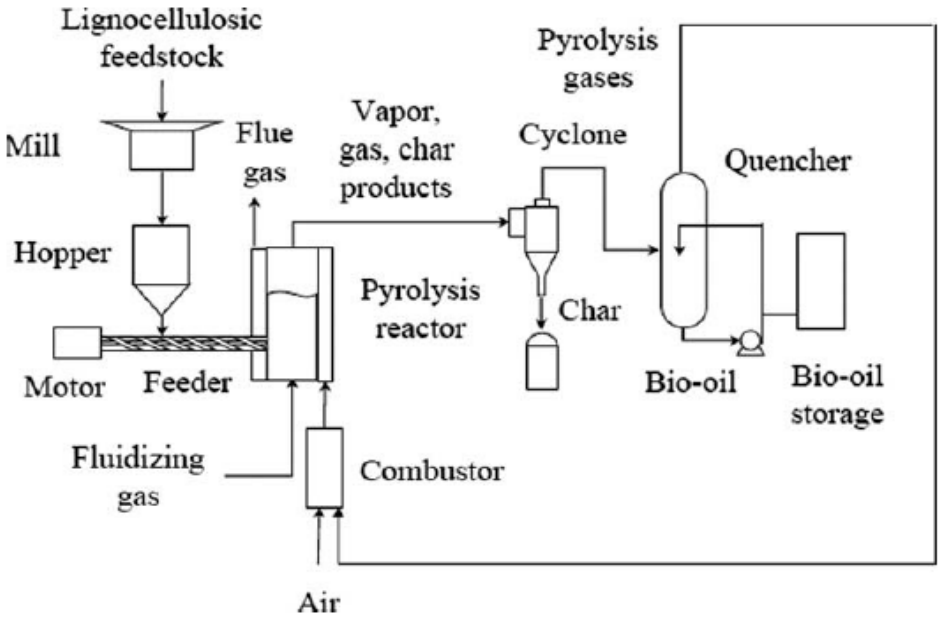

Figure 2.3: Fast pyrolysis unit (Balat et al. 2009).

2.4 Bio-Oil Problems

2.4.1 Low calorific value (heating value)

The heating value, or calorific value, is the amount of heat that is released from a fuel during a combustion process. The heating value of biofuels is typically in the range between 15-22 MJ/kg which is about half that of petroleum fuels (43-46 MJ/kg). This is attributed mainly to the high water content (15-30 % wt.) of biofuels and also to the high oxygen content (30-40 %wt.) associated with the main functional groups of O-H, C=O and C-O (Lohitharn & Shanks 2009; Nolte & Liberatore 2011).

During combustion processes, C=O bonds do not liberate energy and this is the reason why oxygenated compounds are responsible for the lower heating value of pyrolysis oils (Islam et al. 2010). The other reason is the high water content which can be as much as 15-30 %. This fraction cannot be easily removed from bio-oil by conventional separation methods (e.g. distillation) because of the thermal sensitivity of this mixture. The high proportion of water in

pyrolysis oils comes from the moisture present in the original biomass plus the water produced from dehydration reactions that occur during the pyrolysis process (Tsai et al. 2006).

In fact, the existence of water in bio-oil has both advantages and disadvantages. On the one hand, most of the components present in bio-oil are soluble in water. Therefore, it serves as a good solvent for decreasing the oil viscosity and improving its fluidity which makes it suitable for pumping, atomization and combustion in engines. It also lowers the combustion temperature which in turns leads to minimize the NO_x emissions during combustion processes. On the other hand, too much water results in inhomogeneity and phase separation. It is the direct cause of the low heating value and low flame temperature of bio-oil. In addition it can lead to delays in the ignition of biofuel, which consequently reduces its combustion rate (Zhang et al. 2007; Oasmaa & Czernik 1999).

2.4.2 Chemical/thermal instability

Pyrolysis oils are produced by the rapid heating of the feedstock followed by the rapid cooling or quenching of the vapors and aerosols produced in a very short residence time. Under such conditions, the liquid produced is a product that is not in a thermodynamic equilibrium during pyrolysis or upon storage as the pyrolysis vapors condense before further reactions involving the cracking of heavy species are completed (Balat et al. 2009).

Diebold (2000) and Bhattacharya et al. (2010) claimed that bio-oil is a thermally unstable mixture and that this instability is associated with the presence of reactive oxygenated species. These oxygenated functional groups in pyrolysis oil, which include hydroxyl, carbonyl and carboxylic compounds, tend to achieve equilibrium during storage, leading to additional chemical reactions and changes in the bio-oil composition. Most of these physicochemical changes of pyrolysis liquids happen during the first 6 months of the storage duration (Oasmaa & Kuoppala 2003; Mohan et al. 2006; Jiang et al. 2012). Table 2.4 shows a list of some of the probable chemical reactions that contribute to the bio-oil instability.

Broadly, these reactions are divided into two groups: polymerization and poly-condensation reactions (Chaala et al. 2004). Polymerization reactions occur between carbonyl components (aldehydes and ketones) and produce complex and higher molecular weight compounds. Poly-condensation reactions, which involve hydroxyl and carboxyl constituents, include esterification, etherification and acetalization from which water is generated as a byproduct.

An increase in the viscosity of a bio-oil signifies the existence of polymerization reactions, while occurrence of condensation reactions is confirmed by augmentation in water content during storage (Diebold 2000). Increasing water content during storage is expected to decrease bio-oil viscosity. However, occurrence of the opposite scenario has been reported, suggesting that the effect of increasing the molecular weight of bio-oil (i.e. increasing viscosity from polymerization reactions) is more effective than the effect of dilution of water produced from condensation reactions (Oasmaa & Czernik 1999).

Table 2.4: List of probable chemical reactions occurring in bio-oil during storage (Diebold 2000).

No.	***Reaction***
1	Organic acids with alcohols to form esters and water
2	Organic acids with olefins to form esters
3	Aldehydes and water to form hydrates
4	Aldehydes and alcohols to form hemiacetals, or acetals and water
5	Aldehydes to form oligomers and resins
6	Aldehydes and phenolics to form resins and water
7	Aldehydes and proteins to form oligomers
8	Organic sulfur to form oligomers
9	Unsaturated compounds to form polyolefins
10	Air oxidation to form more acids and reactive peroxides that catalyze the polymerization of unsaturated compounds

Diebold (2000) indicated that these reactions take place naturally without the presence of catalysts but could take a long time which available upon storage or occur quickly with the aid of catalysts that already exist in the bio-oil mixture (carboxylic acids, ash and solid particles). He also justified that high temperatures accelerate the emergence of the aging effects. At elevated temperatures, the rate of these reactions increases causing an increase in the viscosity of the bio-oil mixture over time because of the increase in the average molecular weight. It was found that the increase in the viscosity that produced by storing bio-oil for 3 months at 37°C is similar to that obtained when bio-oil stored at 60°C for 4 days or at 90°C for 6 hours (Czernik et al. 1994). In addition, there is a good correlation between viscosity increase and molecular weight increase over this temperature range (37-90°C) (Czernik et al. 1994). These results inspired research involving accelerated aging tests at elevated temperatures. Data obtained

from these tests were analyzed in order to gain insight into what happens during bio-oil storage at lower temperatures but for longer times. The major benefit of accelerated aging trials is that they reduced the time needed to demonstrate the changes occurring in bio-oil properties during storage (Diebold 2000). There is no typical method for checking the stability of pyrolysis oil but the most common way is based on measuring the change of viscosity during aging. This test is recommended for testing bio-oil stability during storage and has been applied in several other studies (Diebold & Czernik 1997; Oasmaa et al. 2005; Oasmaa et al. 2011).

In addition to the temperature influence, Naske et al. (2012) mentioned that exposure of bio-oil into air leads also to changes in its properties resulting from the oxidation of some of its organic compounds (aldehydes and alcohols) to form additional acids and reactive peroxides which can catalyze polymerization reactions. The inorganic content of the bio-oil also plays a big role in its poor stability. It has been demonstrated that aging reactions are catalyzed by alkali metals contained in char particles such as Ca, Mg, Na and Zn (Balat et al. 2009; Diebold 2000). Chemical changes that occur during bio-oil storage can lead to changes in the mutual solubility between its different components, ending finally in phase separation (Diebold 2000). Removal of the compounds that are responsible for these changes is an important issue that needs to be addressed in order to produce bio-oils that maintain their favorable properties during storage or transportation.

2.4.3 Acidity

Acidity is the main factor that restricts the use of pyrolysis oil as a transportation fuel. Bio-oil contains a large fraction of organic acids, with components mostly acetic and formic acids. This results in low pH values of about 2-3 which diminish its ability to be stored over a long period of time (Zhang et al. 2007). Oasmaa et al. (2010) mentioned that about 60-70% of bio-oil acidity comes from volatile acids. They suggested that phenolic compounds, fatty acids and resin acids also contribute to the acidity of the oil but to a lesser degree. High acidity causes serious problems with storage and processing and makes bio-oils corrosive to the most prevalent construction materials such as aluminum and carbon steel. Furthermore, the intensity of corrosiveness increases when the water content is high and when pyrolysis oils are used at high temperatures (Czernik & Bridgwater 2004). This means that additional costs are required in terms of construction materials for the storage tanks, boilers or gas turbines. Therefore, an upgrading process is an essential step to take in order to solve the corrosiveness problem and

to utilize biofuels in large scales (Zhang et al. 2007; Oasmaa & Czernik 1999). Table 2.5 presents the common organic acids identified in bio-oil mixtures.

Table 2.5: Common organic acids in bio-oil mixture (Diebold 2000).

Compound	***%wt.***
Acetic acid	0.5-12
Formic acid	0.3-9.1
Propionic acid	0.1-1.8
Hydroxyacetic acid	0.1-0.9
Pentanoic acid	0.1-0.8
Butanoic acid	0.1-0.5
4-oxypentanoic acid	0.1-0.4
Heptanoic acid	0.3
Benzoic acid	0.2-0.3
Hexanoic acid	0.1-0.3

2.5 Applications of bio-oil

Despite the fact that pyrolysis oil is associated with several significant problems which restrict the range of its applications, biomass derived fuels have gained a wide interest, especially over the last two decades. They are now used in a wide range of applications including: heat and power generation, production of chemicals and transport fuels (Czernik & Bridgwater 2004).

A series of combustion tests have been carried out to evaluate the performance and emission properties of bio-oil (Venderbosch & Prins 2010). Even though pyrolysis oil has a low heating value and high water content, the results showed that it has favorable burning characteristics reflected by its lower emissions, especially NO_x emissions, than those were generated from burning conventional oils. This makes it a good substitute for light fuel oil in industrial boilers, furnaces, turbines and engines for heat and power production. The use of pyrolysis oils for heat generation has been applied commercially at the Red Arrow pyrolysis plant in Wisconsin over 10 years (Venderbosch & Prins 2010; Czernik & Bridgwater 2004) and tests in this area showed that high viscosity is a major problem. Therefore, there are some requirements to be achieved to make bio-oils appropriate for this application: *i)* bio-oil should either be preheated to 70-80

°C before combustion or mixed with some additives such as alcohols to reduce its viscosity, *ii)* conventional fuels should be used during the start-up and in the shutdown to avoid clogging the nozzle systems with the coke depositions and *iii)* the solid content should be reduced to < 0.1 %wt. (Oasmaa et al. 2005). In terms of utilization in boilers, experiments showed that bio-oils can be used, but some modifications to the existing instruments are required to improve combustion efficiency (Czernik & Bridgwater 2004).

Pyrolysis oil has also been utilized in diesel engines for electricity generation, but this application is accompanied by some drawbacks such as high viscosity and corrosiveness of bio-oils. High acidity can cause deterioration in the engine whilst high viscosity can destroy nozzles and injection systems (Venderbosch & Prins 2010).

Another remarkable application is the co-firing of bio-oil with petroleum fuels. This approach is widely useful in terms of reducing emissions from burning pure fossil fuels alone. Virtual tests have already been done in this field at the Manitowac power station in the USA for electricity generation. The results showed that combustion was efficient with an acceptable level of emission and without any changes in the operation of the boiler unit (Czernik & Bridgwater 2004).

Recently, there is a strong move towards the utilization of biofuels in the biorefinery system as an alternative source for fuels and the manufacture of high value chemicals. The main benefit of using biofuels rather than petroleum to produce chemicals or fuels is the chance to reduce the dependence on nonrenewable sources and to mitigate greenhouse emissions (Fernando et al. 2006).

Hundreds of commodity chemical components have been identified through the analysis of bio-oil. The majority of these components are present in small concentrations in the bio-oil mixture but their high value makes the recovery process commercially valuable. Examples of chemicals that have been reported as being produced from bio-oil are fertilizers, resins, levoglucosan, fatty acids, carboxylic acids, phenols, adhesives and food flavors such as liquid smoke. These chemicals can be extracted either as individual components or as families of chemicals (Bridgwater 2003).

Hydrogen, a clean source of energy and an important product for bio-oil upgrading processes, can be produced from bio-oil itself by steam reforming of the aqueous phase of bio-oil. Bio-oil can be readily separated into two phases by adding water (Kim et al. 2012). The top water-rich

phase, which consists mostly of water and low molecular weight species, such as acids, ketones and aldehydes, can be steam reformed to generate hydrogen that is required for the upgrading of the bottom waterless phase of bio-oil (Pan et al. 2012; Ortiz-Toral et al. 2011). The major challenge in the production of hydrogen from bio-oil is catalyst deactivation. This effect becomes much more severe in the reforming of the whole bio-oil mixture (Ortiz-Toral et al. 2011).

In fact, the use of pyrolysis oils as transport fuels is not technically and economically feasible at the present time because of some undesirable characteristics of bio-oil, particularly its low calorific value and high acidity. A number of upgrading methods for bio-oil have been suggested to improve its quality and expand its implementations. Examples of these are hydrotreating, catalytic cracking and emulsification. However, none of these technologies is economically attractive and they are still associated with technical problems (Czernik & Bridgwater 2004).

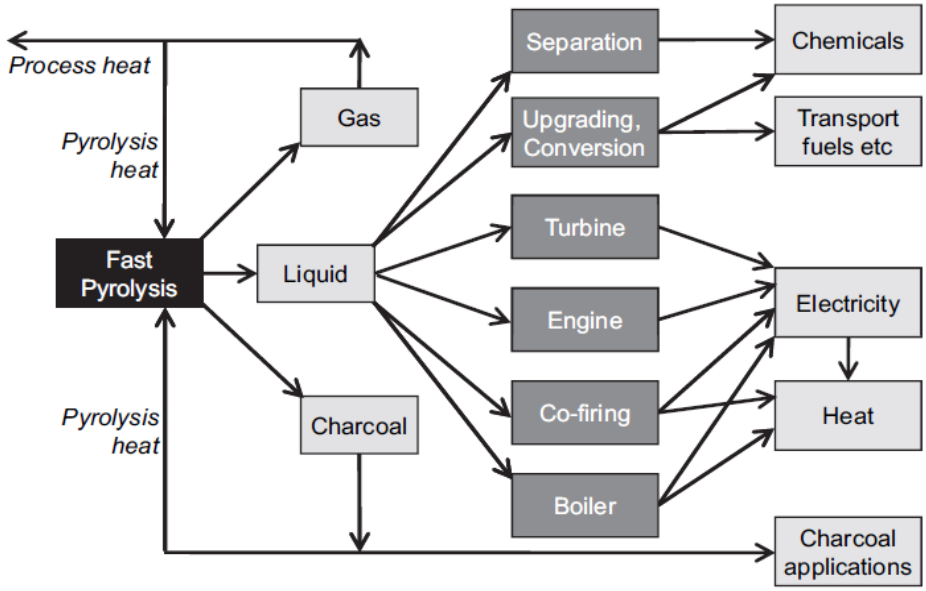

Figure 2.4: Applications of pyrolysis products (Bridgwater 2012).

2.6 Bio-oil upgrading

The aforementioned unfavorable properties of bio-oil (high water content, high viscosity, high density, immiscibility with fossil fuels, corrosiveness, low calorific value, chemical instability

and tendency to polymerize when exposed to air or high temperatures) render this product inappropriate for direct applications and make its long term storage problematic. In order to be utilized as transportation fuel or chemical feedstock, bio-oil quality needs to be improved through upgrading. Upgrading can be achieved through removing water and oxygenated compounds either partially or totally (Fisk et al. 2009). A broad range of upgrading processes have recently been available, some of which are reviewed below.

2.6.1 Hydrodeoxygenation

During this process, oxygen in bio-oil is converted into H_2O and hydrocarbon via catalytic reaction with hydrogen. This process requires high pressure (20 MPa), moderate temperatures (around 400°C) and heterogeneous catalysts. The most common catalysts used in this process are either sulfided CoMo or NiMo loaded on Al_2O_3 (Bridgwater 2012).

Normally, this method consists of two main steps. In the first one, bio-oil is stabilized by treating it at a moderate temperature of around 250°C to avoid polymerization reactions and coke formation while the second step involves treating bio-oil at a higher temperature to complete the hydrotreating process (Ahmed et al. 2010).

Zhang et al. (2005) used this method to improve the stability of the bio-oil obtained from the pyrolysis of sawdust. It was found that the high amount of water existing in bio-oil results in further pressure during the hydrotreating process. Therefore, bio-oil was separated into two phases: watery and oily phases via the addition of water. The oil fraction was then upgraded through hydro-treatment in the presence of sulfided Co-Mo-P/Al_2O_3 as a catalyst. The results showed that the oxygen content of bio-oil was decreased significantly from 41.8 %wt. to 3 %wt. resulting in an increase in the calorific value from 21.3 to 41.4 MJ/kg. In addition, the original bio-oil was highly soluble in methanol while the treated one was highly miscible in toluene due to the de-hydroxylation of the hydroxyl functional group compounds.

Although the hydro-treating process proved to be an effective method for treating pyrolysis oils, it involves many drawbacks. Catalyst fast deactivation and reactor clogging are serious challenges (Chen et al. 2014; Şenol et al. 2005). Char content in bio-oil shorten the catalyst life which means that regeneration of catalysts is required periodically. Many investigations have been carried out in this field in order to explore different or modified catalysts for continuous process operation but the problem of coke deposition still exists (Centeno et al. 1995).

Moreover, this process consumes large volumes of hydrogen which makes it economically unviable (Zhang et al. 2007).

2.6.2 Catalytic cracking

In catalytic cracking, oxygen in bio-oils is discarded as H_2O, CO_2 or CO with the aid of a Ni-based catalyst. This process is carried out at a temperature of 450°C and a pressure of 1 atm. Under these conditions simultaneous dehydration and decarboxylation reactions occur which result in the elimination of oxygen. A variety of catalysts have been used in this process but zeolite is the most commonly used one (Moens et al. 2009; Wang et al. 2013).

The main feature of this upgrading mode is the low operating cost since processing takes place under atmospheric pressure and also because no hydrogen is required. This approach of upgrading has been investigated by many researchers and recently been reviewed extensively by Liao et al. (2013).

Despite the favorable economics of this route for converting oxygenated compounds into lighter fractions, the inferior quality of the fuels obtained together with catalyst deactivation still pose barriers. Continuous regeneration of the catalyst is essential because of the high yield of the coke formed (8-25%) (Zhang et al. 2007).

2.6.3 Extraction by supercritical fluids

Extraction of bio-oil into fractions by use of fluids under critical conditions has been investigated recently as a technique for bio-oil upgrading through separating water and undesired species. Supercritical CO_2 is one of the important solvents that are used in chemical extraction. Its use is preferable to organic solvents such as ethanol and methanol because of its low toxicity, cheap availability, high purity and noncorrosiveness. The relatively low critical temperature (31.1°C) and moderate critical pressure (73.8 atm) of this process make it beneficial in the separation of thermally sensitive mixtures such as pyrolysis oils (Rout et al. 2009; Wang et al. 2010). In this process, different components can be separated or extracted selectively by changing the pressure of CO_2. Low molecular weight species can be easily extracted at low pressure, while heavy compounds can be separated at high CO_2 pressures. Additionally, water is very soluble in SC- CO_2 and this makes it an attractive option for the separation of water from bio-oil mixtures (Naik et al. 2010).

This method was used by Rout et al. (2009) to fractionate bio-oil produced from a mixed biomass of wheat and wood sawdust and to extract valuable components from it. Their results showed that water was effectively separated from the bio-oil. The fractions obtained had a high calorific value (30 - 44.5 KJ/kg) compared with that of the original biomass (19 KJ/kg) and the moisture content was only 3%. Their results also demonstrated that valuable compounds including furanoids, pyraniods and benzeniods can be enriched in the extracted fractions. Naik et al. (2010) reported that after separating these fine components, the remaining mixture of bio-oil has properties that make it suitable to be used for fuel applications as it is enriched with fatty acids and alcohols.

More recently, Wang et al. (2010) applied this technique to bio-oils pyrolyzed from corn stalk powder. They studied the effect of different adsorbents on the efficiency of the upgrading process and found that best results were achieved in the presence of silica gel. Their results demonstrated that after supercritical extraction by CO_2, a significant decrease in the water and acid contents was found. The total proportion of acids in the bio-oil reduced from 28.15% to 6.92%, while the water content was considerably decreased from 35.90% to 4.91% causing the heating value to rise from 13.95 to 25.41 KJ/kg. The stability of bio-oil extracts was checked by storing them for 6 months under room temperature. Neither noticeable change in the viscosity nor phase separation was observed confirming the fact that this technology is effective in improving bio-oil properties. They also confirmed that valuable chemicals can be isolated from pyrolysis oil by adjusting the operating conditions of temperature and pressure and selecting the suitable adsorbent which has the ability to affect the intermolecular forces between components.

This approach appears to be cost effective in the laboratory scale but it is not economical for large scale applications because of the high pressure required for its operation (Zhang et al. 2013).

2.6.4 High pressure thermal treatment (HPTT)

HPTT is a new deoxygenation upgrading technique developed by the biomass technology group (BTG) in the Netherlands for the purpose of reducing the water and oxygen contents of pyrolysis oils (Mercader et al. 2010). In this process. Bio-oil mixture is treated thermally for few minutes at temperatures in the range of 300-350 °C and at a high pressure of about 200

bar. Under these conditions, bio-oil mixture splits into three phases: gas, liquid and oil phases. High operating pressure is an important condition that is necessary to maintain the water in the bio-oil mixture in its liquid state as water evaporation can lead to extensive char formation.

According to Mercader et al. (2010), who applied this method using a tubular reactor, the oxygen content of the HPTT processed bio-oil was lowered significantly from 40 %wt. to 23 %wt. as a result of two reasons: *i)* oil phase splitting and decarboxylation and *ii)* dehydration reactions occurring during this process. They found that char generation and oil polymerization could be significantly reduced by diluting the bio-oil mixture with water before HPPT treatment. Despite the considerable increase in the energy content of the HPTT pyrolysis oil from 14.1 to 28.4 MJ/kg, this technique is associated with the formation of high molecular weight components and the oil generated has zero miscibility with the conventional fuels (Mercader et al. 2010).

2.6.5 Catalytic biomass pyrolysis

Catalytic pyrolysis is another promising technique for bio-oil upgrading in which a catalyst is used in the pyrolysis process itself. In this case, the catalytic cracking of pyrolysis vapors occurs simultaneously with the thermal pyrolysis of biomass in a single step operation (Thegarid et al. 2014). This is done by placing any appropriate catalyst as a bed material in the pyrolysis fluidized bed reactor instead of the silica sand. Addition of a catalyst to the pyrolysis process can improve bio-oil quality by converting its oxygenated compounds into H_2O and CO_2. The presence of a catalyst is expected to have a dual effect. Firstly, it improves the cracking reactions within the pyrolysis vapors that convert heavy molecules into lighter ones and secondly, it prompts de-oxygenation reactions to lower the oxygen content (Ahmad et al. 2013). The most important parameters that affect the yield and the quality of the oil product in this process are: *i)* type of the catalyst used and *ii)* biomass to catalyst ratio (Thegarid et al. 2014). Different kinds of catalyst have been utilized, comprising fluid catalytic cracking (FCC) catalysts and metal oxides such as ZnO, CuO and Fe_2O_3 (Thegarid et al. 2014). However; most of the catalytic pyrolysis trials have been conducted using zeolite as the catalyst.

Bio-oil produced from the process of catalytic pyrolysis has a marked reduction in its oxygen content in comparison to that produced from conventional non-catalytic pyrolysis. This process however, has a lower liquid bio-oil yield and leads to the formation of additional water, gases and coke (Lappas et al. 2002; Ahmad et al. 2013).

2.6.6 Distillation

Since bio-oils consist of wide range of components with different boiling ranges, separation of components by distillation has been employed in order to improve their quality. The complete vaporization of pyrolysis oil, however, is an impossible task. Traditional distillation procedures require high operation temperatures and long residence times and these conditions are not appropriate for the thermo-sensitive properties of bio-oil (Elkasabi et al. 2014; Resasco & Crossley 2015; Guo et al. 2011). It was found by Boucher et al. (2000) that the atmospheric distillation of bio-oil stops at 140°C due to the severe polymerization and cracking of the high molecular weight components in the bio-oil mixture during distillation test.

2.6.6.1 Molecular distillation

Molecular distillation is a specialized liquid-liquid separation technology that has been adapted for the purification, concentration and separation of heat sensitive, viscous or easily oxidized materials such as bio-oils. The high degree of purity of the chemicals produced has resulted in this technology having applications in various important sectors including chemical, food and pharmaceutical industries (Guo et al. 2010).

During this process, the liquid mixture flows as a thin film on a hot surface at a moderate temperature and the vapors are transported to a second cold surface placed at a specific distance on the opposite side. While traditional distillation depends on the principle of the difference in the boiling points between the components and requires long distillation periods and high temperatures, molecular distillation is based on the difference in the mean free paths of the compounds with only short time and low temperatures needed to complete the process of separation (Wang et al. 2015). The mean free path is the distance that a molecule can travel without colliding with another molecule. The distance between the hot and cold surfaces should be selected so that it is equal to or less than the mean free path of the target components (Wang et al. 2009).

Bio-oil separation tests using molecular distillation technology have shown that water and low molecular weight organics (e.g. acids, aldehydes and ketones) are easier to distill than heavier organics (sugars or phenolic derivatives). After the separation process, the majority of water and light organics were deposited on the condensation board while the heavier organics were collected on the evaporation surface (Guo et al. 2010; Wang et al. 2015).

A molecular distillation was applied by Guo et al. (2011) to separate pyrolysis oil in to fractions. Bio-oil (from pine sawdust) was first vaporized under conditions of 80°C and 1600 Pa to produce a first fraction of bio-oil. A second fraction was obtained by subjecting the remaining heavy fraction into another run of molecular distillation under 80°C and 340 Pa. These two fractions, which are rich in carboxylic acids and ketones, are then mixed together and upgraded by reacting with propanol in the presence of a solid acid catalyst. The results obtained showed both a decline in the acidity of the bio-oil and an improvement in its storage stability. This was achieved by converting carboxylic acids into esters and unsaturated ketones into saturated ones. The acid content reduced from 18.39% to 2.70%, while the proportion of esters increased from 0.72% to 31.17%.

2.6.6.2 Reactive distillation

This upgrading method is done by reacting bio-oil with alcohol under mild conditions using sulfuric acid as a catalyst (Hiwale et al. 2004). The technique of reactive distillation has been examined by several previous studies for upgrading purposes. Junming et al. (2008) applied this method in their study and found that separating volatile organic acids from bio oil, which is an effective way to improve the quality of pyrolysis oil, cannot be achieved by conventional distillation methods because the water present in the bio-oil forms an azoetrope system with the organic acids. Therefore, they investigated converting acids into their corresponding esters through reaction with ethanol over the solid acidic catalyst SO_2^{2-}/ZrO_2. After the reaction, phase separation occurred resulting in two layers: water soluble (light) and water insoluble (heavy) fractions. The results showed that there was an improvement in the properties of the treated bio-oils. Dynamic viscosity decreased from 10.5 mm^2/s for the raw bio-oil to 0.46 and 3.65 mm^2/s for light and heavy fractions respectively and the heating value rose from 14.3 to 21.5 and 24.5 MJ/kg for light and heavy fractions respectively. Furthermore, the stability of the fractions obtained was examined by storing them in atmospheric conditions for 12 weeks. No marked changes were observed. Mahfud et al. (2007) also applied this technique in the presence of H_2SO_4 as a catalyst but the results were disappointing as the pH of the bio-oil dropped from 3 to 0.5 after upgrading.

It should be noted that the above distillation technologies are complicated and require expensive equipment and high energy. In the case of molecular distillation, commercial scale is very costly due to the requirement of high vacuum conditions. In the case of the reactive

distillation mode, application of acid catalysts leads to a decrease in the pH value of the bio-oil meaning that direct application is not possible without the implementation of a prior neutralization stage.

2.6.7 Emulsification

One possible way of stabilizing bio-oil and employing it as a motor fuel is by mixing it with hydrocarbon fuels. As mentioned before, bio-oils are immiscible with petroleum fuels because of the high oxygen content. However, this can be attained through use of a surfactant (Zhang et al. 2007).

Emulsification with bio-diesel brings valuable influences including reduction in the viscosity and increases in the cetane number and the heating value of biofuels (Jiang & Ellis 2010). Blends of diesel fuel and bio-oil in ratios of 25%, 50% and 75% were prepared by Chiaramonti et al. (2003) to study the impact of this technique on the characteristics of bio-oils. They noted that the stability of emulsions was much higher than that of the pure oil. They found also from their experiments that the optimum proportion of surfactant that should be added to gain a reasonable level of viscosity fell within the range of 0.5-2%. Similar results, in terms of emulsion stability, were also reported by Jiang & Ellis (2010) who studied the impact of different parameters such as primary bio-oil/diesel ratio, mixing time, mixing intensity, temperature and surfactant concentration on the stability of the mixtures prepared, while Ikura et al. (2003) also obtained emulsions with lower viscosity and higher pH than that of the native bio-oil.

Emulsification seems an easy approach for improving some of the fuel properties such as ignition characteristics. However, other properties, such as heating value and acidity, are not improved satisfactorily (Junming et al. 2008; Zhang et al. 2013). In addition, the weak stability of emulsions and the high cost of surfactants also limit its application.

2.6.8 Solvent addition

It was reported in the literature that polar solvents have the ability to improve the homogeneity, reduce the viscosity, increase the heating value and decelerate the aging reactions of pyrolysis oils. Diebold & Czernik (1997) proposed that polymerization reactions of bio-oil during storage could be prohibited upon the addition of mono-functional alcohols. These solvents, such as methanol, ethanol and isopropanol can increase the stability of pyrolysis oils by converting

reactive and heavy oxygenated compounds into lighter and more stable ones through these following mechanisms:

- Reacting with the carboxylic acids present in bio-oil to form polyesters. This not only decreases the corrosiveness of bio-oils but also eliminate acids which represent the most effective catalysts for polymerization reactions.
- Converting heavy esters into those with lower molecular weight ones through transesterification reactions leading to improved bio-oil quality.
- Transforming aldehydes and ketones into their neutral light acetals and ketals through acetalization reactions. This is beneficial in reducing their availability for polymerization reactions.

All these reactions require strong acid catalysts such as sulphuric, hydrochloric and sulfonic acids or solid acid catalysts to proceed (Bhattacharya et al. 2010; Li et al. 2011; Hu et al. 2012). It was found by Oasmaa et al. (2004) that concentrations as low as 5 wt.% of methanol prevent aging reactions for about 6 months, while higher concentration of around 10 wt.% have significant effects in hindering the aging rate for about one year. They also concluded that adding methanol to the freshly produced bio-oil is more effective than adding it to the aged one.

Methanol is the most commonly used solvent for this purpose because of its wide availability and more importantly, its low cost. Other solvents such as ethanol and isopropanol were also tested but they were found to be inferior to methanol in regard to its effectiveness in oil quality improvement (Oasmaa et al. 2004). Addition of solvents is a successful and simple method for enhancing bio-oil quality, however, a decrease in the flash point of the bio-oil mixture was observed after solvent addition (Oasmaa et al. 2004).

2.7 Bioethanol

Bioethanol is by far the most important renewable bio-fuel that can be used as an additive in motor vehicles. Its importance raises from its high heating value as well as the ability to directly mixing with gasoline and using in the existing combustion engines without the necessity to any alteration (Vázquez-Ojeda et al. 2013). Brazil and united states are the major producers for this fuel and their production constitute about 26.72% and 56.72% respectively of the total world

production (Gupta & Verma 2015). The vast majority of bioethanol is produced by the fermentation of agricultural crops such as corn and sugarcane where yeast or bacteria are used to metabolize the sugars in the biomass to produce ethanol and CO_2 (Baeyens et al. 2015). It can also be produced from non-food lignocellulose based feedstocks such as sugarcane bagasse and cassava by fast pyrolysis process (Luque et al. 2014), however its production in industrial scale is still not feasible. The former type is called first generation bioethanol while the second one called second generation bioethanol. There is also a third generation version which is produced from algae and still under investigations (Baeyens et al. 2015).

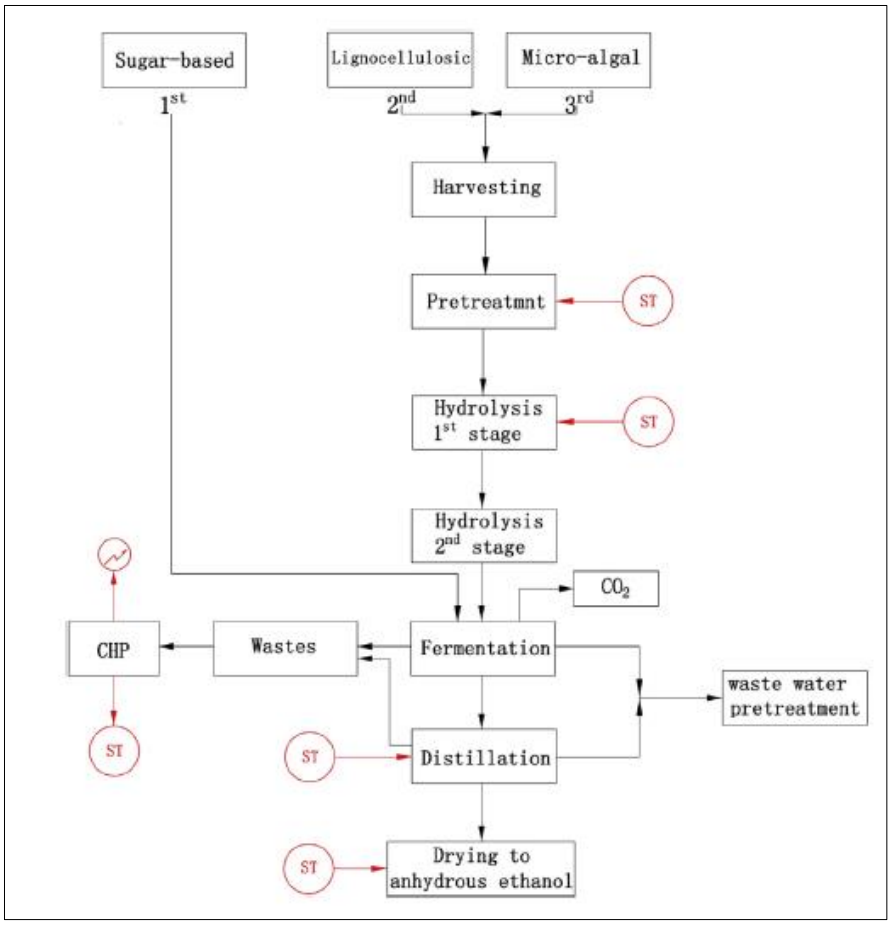

Figure 2.5: Bioethanol production (Baeyens et al. 2015).

Bioethanol must have a purity of about 99% wt. to be utilized as a biofuel in motor engines (Kanchanalai et al. 2013). The typical bioethanol mixtures produced from fermentation processes, however, has as low as 10 %wt. ethanol concentrations (Pacheco-Basulto et al. 2012; Chuntanalerg et al. 2015). The typical procedure to dehydrate this dilute solution is by firstly using conventional distillations to obtain mixtures with concentrations close the azeotropic composition (95% wt.), followed by extractive distillation to obtain purities that reach to

around 99.8% wt. (Vázquez-Ojeda et al. 2013; Pacheco-Basulto et al. 2012), both are associated with high energy consumption. Figure 2.5 summarizes the main steps for the production of the different generations of bioethanol.

2.8 Microbubbles

2.8.1 Characteristics of microbubbles

Microbubbles are tiny bubbles with diameters ranging between 1μm and 1mm. They have numerous applications in many environmental conservation and energy saving technologies because of their superior properties (Muroyama et al. 2012). Microbubbles are mostly used in separation processes such as those for the removal of minerals, biotech materials or oils from water and waste water (Zimmerman et al. 2008). One of the attractive characteristics of microbubbles is the high surface area to volume ratio based on their geometry as explained by the following equation:

$$\frac{S}{V} = \frac{4\pi r^2}{\frac{4}{3}\pi r^3} = \frac{3}{r} \tag{2.1}$$

where S is the total surface area of the bubble phase, V is the total volume of bubble phase and r is the bubble radius. If V is maintained constant, then Eq. 2.1 is transferred into the following form:

$$S = \frac{3}{r} V_o \tag{2.2}$$

where V_o is the total constant volume of the bubble phase.

Equation 2.1 shows that the surface area to volume ratio of a bubble is inversely proportional to the radius of the bubble and equation 2.2 indicates that the surface area of a cloud of bubbles exceeds that of a single larger bubble of the same gas volume. Figure 2.6 demonstrates the key factor in the transport enhancement. It shows how the surface area of a single large bubble is significantly increased after division into a cloud of smaller bubbles with the same overall volume.

This enlargement of the surface area enhances the transfer properties of the microbubbles since the rate of all interfacial transfer processes (mass, heat and momentum transfers) are strongly

dependent on the interfacial surface area between the gas and liquid phases as shown in the following correlations:

$$J = K_L A(c_g - c_l) \tag{2.3}$$

$$Q = HA(T_g - T_l) \tag{2.4}$$

and

$$F = -\mu A \frac{\partial w}{\partial x} \tag{2.5}$$

where

J is the mass transfer rate

Q is the heat transfer rate

F is the viscous drag force,

A is the interfacial area,

c_g and c_l are the molar concentrations in the gas and liquid phases respectively,

T_g and T_l are the temperatures of the gas and liquid phases respectively,

K_L is the mass transfer coefficient,

H is the heat transfer coefficient and

$\frac{\partial w}{\partial x}$ is the velocity gradient.

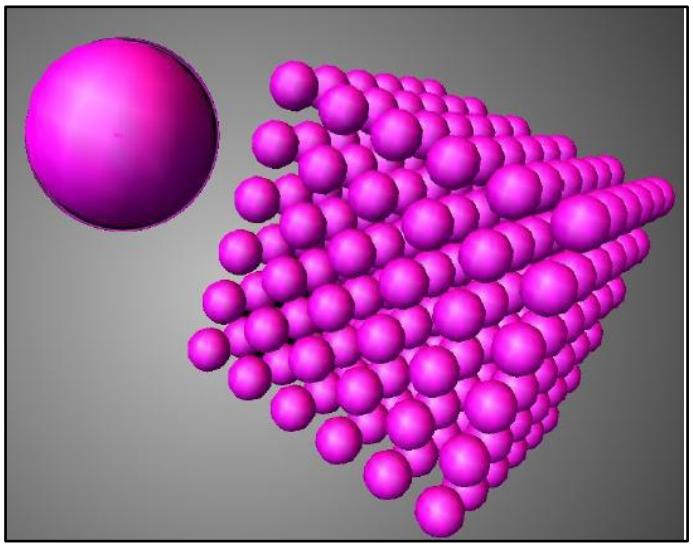

Figure 2.6: Division of a single large bubble into a number of smaller, equally sized bubbles which produces additional surface area (Zimmerman et al. 2008).

The other attractive advantage of miniature bubbles is that they have a considerably lower rising velocity in liquids compared to larger bubbles and this fact can be demonstrated by Stokes' law for the rising velocity of a single rising bubble in a viscous liquid:

$$U_{stokes} = \frac{2g(\rho_l - \rho_g)r^2}{9\mu_l} \tag{2.6}$$

where

U_{stokes} is the terminal velocity of the spherical bubble (m s^{-1})

g is the gravitational acceleration (m s^{-2}),

r is the bubble radius (m),

μ_l is the liquid dynamic viscosity (kg $m^{-1}s^{-1}$)

ρ_l is the mass density of the liquid phase (kg m^{-3}) and

ρ_g is the mass density of the gas phase (kg m^{-3}).

Stokes' law indicates that the rising velocity of a bubble is directly proportional to the square of its radius. Thus tiny bubbles ascend less quickly than larger bubbles through the same height of liquid which means that they have higher residence times in the liquid. Therefore, the mass flux J and heat flux Q are expected to increase with the presence of microbubbles. The effect of microbubbles on the momentum transfer is the same. Despite the fact that individual smaller bubbles have less momentum to transfer to the surrounding liquid, they have a much longer time to do so due to their slow velocity. For this reason, the momentum transfer by a cloud of tiny bubbles is markedly higher (Zimmerman et al. 2008). Due to the slow ascend velocity of microbubbles, it can be concluded that they can provide a higher gas hold up at lower gas flow rates (Zimmerman et al. 2009; Ribeiro & Lage 2004). Figure 2.7 shows the relationship between the rising velocity and the bubble size.

Microbubbles also have higher internal pressure than the surrounding phase due to surface tension effects. For example, the internal pressure of a 1 μm diameter microbubble at 298 K is 3.87 atm which is about four times larger than atmospheric pressure (Tsuge 2014). This effect is confirmed by the Young-Laplace law for surface tension which states that the pressure difference across the bubble skin is inversely proportional to the radius of the curvature (r):

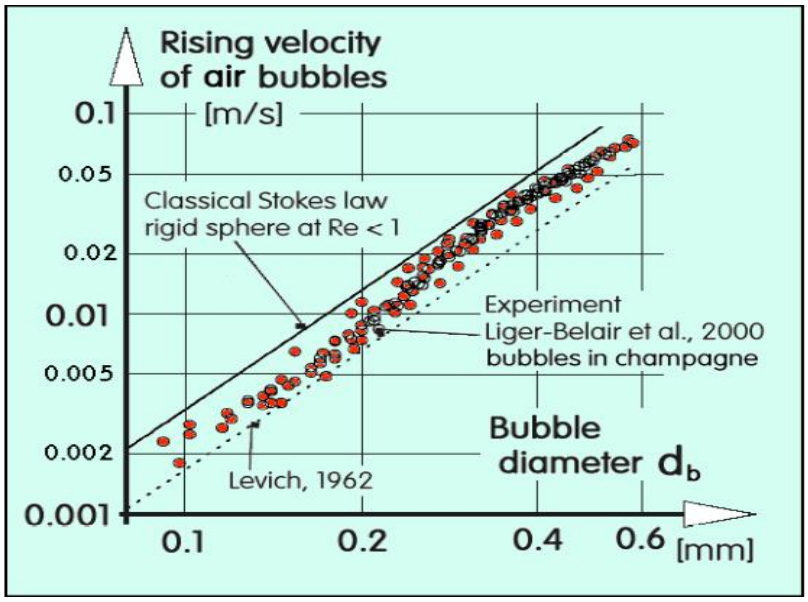

Figure 2.7: Bubble rising velocity against bubble diameter for air bubbles (Zimmerman et al. 2008).

$$P_2 - P_1 = \frac{2\sigma}{r} \tag{2.7}$$

where

P_2 is the pressure inside the bubble (Pa),

P_1 is the surrounding liquid pressure (Pa) and

σ is the surface tension (N/m).

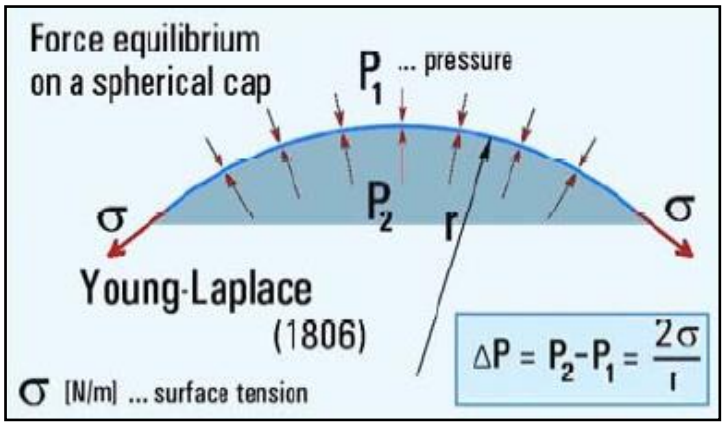

Figure 2.8: Surface tension law (Zimmerman et al. 2008).

With decreasing the bubble size, the inner pressure increases resulting in an increase in the partial pressure of the gas component inside the bubble, thereby raising their dissolving rate to the surrounding according to Henry's law (Agarwal et al. 2011).

2.8.2 Common methods of microbubbles generation

Generally, there are three ways for gas microbubbles generation (Zimmerman et al. 2008). The first one is based on the fundamentals of cavitation and involves dissolving a pressurized air stream at (~ 6 bar) into a liquid at atmospheric pressure through a particular nozzle system, so the liquid become supersaturation and tiny bubbles (mostly nanobubbles) are nucleated as a result of the pressure reduction. In the second technique, microbubbles are produced using ultrasound power to create local cavitation in the ultrasonic waves. The third procedure involves blowing an air stream through a conventional aeration systems (diffusers) under low pressure which then breaks up to form bubbles from the application of an additional action which can be either mechanical vibration, flow focusing or oscillation of the air flow. Although the generation of bubbles from conventional air aerators relies on the construction of the porous materials, the characteristics of the fluidic oscillation technique ensures that the generated bubble breaks off when it has the smallest possible curvature radius for a bubble formed from an aperture (hemispherical shape) (Zimmerman et al. 2008).

In the first two approaches, it seems that both compression and ultrasonic treatment require high energy densities, while the third method with its minimum power requirement has effectively overcome these difficulties, as will be discussed in the following sections.

2.8.3 Difficulties in small bubbles generation

Generation of small bubbles cannot be obtained simply by minimizing the size of the aperture from which they are formed due to the unstable mechanism of bubble growth (Tesař 2012). During the formation stage, the growing bubble attaches to the solid wall of the aperture due to the effects of the wetting forces and continues to grow under the continuous gas flow until it reaches to a point where its buoyant force, which is responsible for bubble rising and directly proportional to the bubble volume, becomes large enough to overcome the wetting forces (Zimmerman et al. 2008). Under these circumstances, bubble detachment occurs at a size

substantially larger than the diameter of the aerator exit and for this reason, the wetting characteristics of the solid surfaces are of great influence on the size of generated bubbles.

In general, there are two types of gas distribution material: hydrophobic and hydrophilic. In hydrophobic surfaces, the bubble spreads over a larger region beyond the aperture perimeter, forming an extra anchor force to bubble detachment. This results in an increased force being required for breaking off the bubble and thereby much larger bubbles are produced. In contrast, in the case of hydrophilic surfaces, a thin liquid film exists between the forming bubble and the gas passage which tends to inhibit the gas from adhering on it (Zimmerman et al. 2011).

The other difficulty in the generation of small bubbles is the channeling problem (Zimmerman et al. 2008). Certainly, not all passages of the diffuser body are perfectly identical in size and this leads to a polydispersity in the sizes created. According to the Young-Laplace surface tension law, the largest bubble generating from one larger aperture tends to grow more quickly at the expense of the other smaller bubbles on the diffuser surface because the pressure inside that bubble decreases as the bubble size increases, providing less resistance to the incoming flow of additional air. Figure 2.9 show how a single bubble can grow in preference to the other bubbles.

Unfortunately, the polydispersity in the sizes of generated bubbles creates another challenge resulting from the difference in the rising velocities of the bubbles and the irregular spaces between them which leads, in turn, to an unavoidable coalescence of bubbles with their neighbors to form larger ones (Zimmerman et al. 2008).

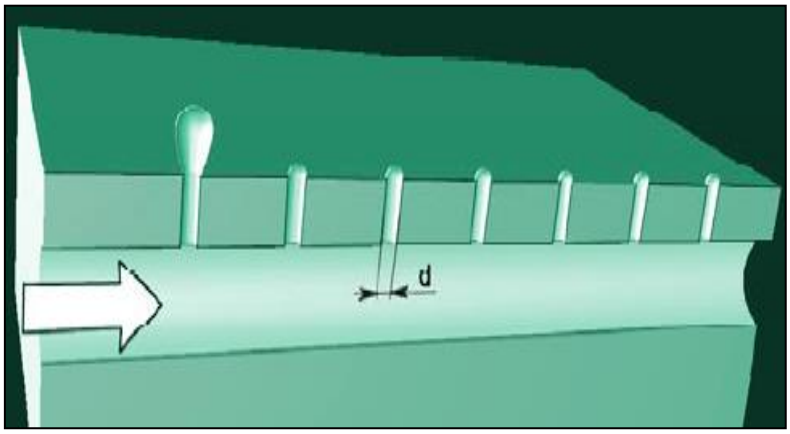

Figure 2.9: Growth of a single bubble on account of others (Zimmerman et al. 2008).

2.8.4 Generation of microbubbles using a fluidic oscillator

As we have seen in the previous section, the formation of tiny bubbles is not an easy task and until recently there has been no desirable way of generating them that is energy efficient (Zimmerman et al. 2009). A novel method of creating microbubbles, of diameters approximately equal to the diameter of the pores in the aerator body, has been described by Zimmerman et al. (2008) using the technique of fluidic oscillation. The fluidic oscillator, as shown in figure 2.10, is a bistable valve that receives a steady gas flow, switching it into an oscillatory flow at a regular frequency ranging between 1-100 Hz. (Tesař 2007; Zimmerman et al. 2008; Tesař & Bandalusena 2010). It is a no-moving part device that works on the Coanda effect (Tesař et al. 2006). The main part of the fluidic oscillator is the amplifier which comprises one inlet terminal, two mid-control terminals and two discharge terminals which are connected to the sparger. This fluidic amplifier is CNC machined from 1.2 mm thick polymethylmetacrylate (PMMA) plates. However, it could also be made of other construction materials to suit various operating conditions. It is provided with a feedback loop which consists simply of a tube connecting its two control ports, X_1 and X_2, as shown in figure 2.10b.

When connected to a diffuser, the characteristics of the fluidic oscillator help to reduce the size of the generated bubbles by ensuring an early break off when the bubble formed at the aperture is hemispherical in shape, offering the smallest possible size. This, in turn, will maximize the surface area to volume ratio of the bubbles, leading to higher mass, heat or momentum transfer rates

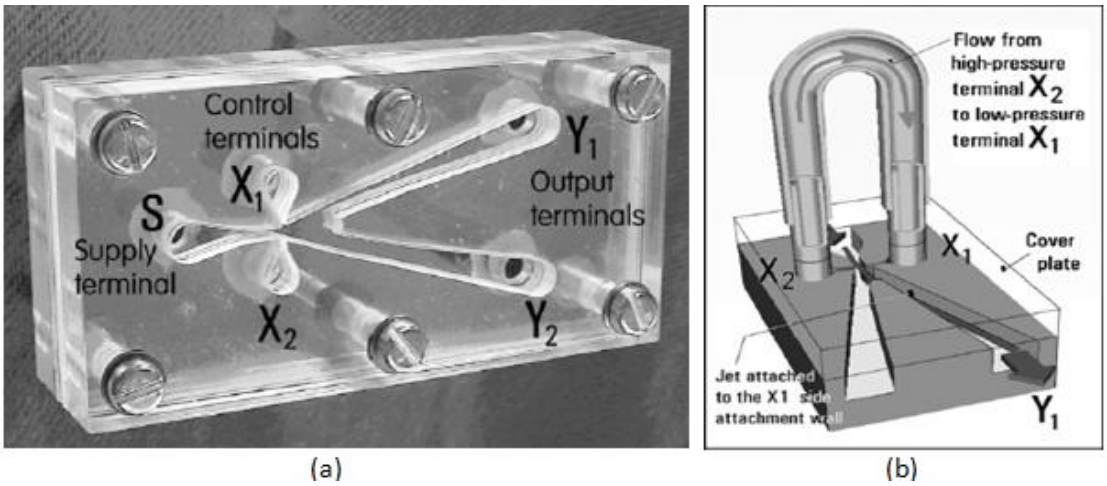

Figure 2.10: The fluidic oscillator (Zimmerman et al. 2009).

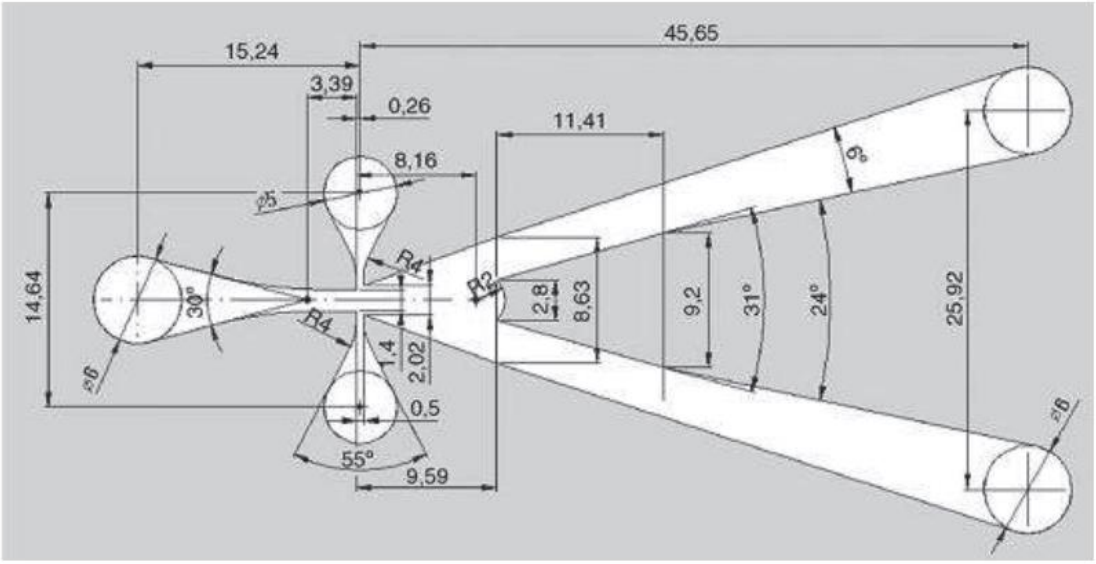

Figure 2.11: Geometry of the fluidic oscillator with dimensions. All dimensions are in millimeters (Tesař et al. 2006).

For microbubble generation with a fluidic oscillator, the basic requirements are: an air supply, bubble diffuser and the fluidic oscillator. As soon as a steady gas flow enters the fluidic diverter valve from its supply port S, it attaches by Coanda effect to either one of the attachment walls between the control ports (X_1 and X_2) and the outlet ports (Y_1 and Y_2) and then exits from Y_1 or Y_2. The Coanda effect can be defined as the ability of a fluid jet to attach itself onto an adjacent wall and remain attached to it even when the wall changes its initial direction. This results in a pressure decrease in the mid port control located at the side of the attachment. The pressure difference between the two control terminals X_1 and X_2 creates a gas flow from the opposite high pressure control terminal to the low pressure terminal through the feedback loop (figure 2.10b).

The main issuing gas flow now becomes attached to the opposite side as low pressure is now created on the opposite side. Because the fluidic oscillator is symmetric, this process is repeated periodically with a regular frequency based on the length of the feedback loop. The periodic switching of the gas flow generates pulses which helps to limit the time available for bubble growth. These pulses can provide a significant inertia force causing the bubbles to break down any anchoring wetting forces. Furthermore, there is a back flow for the liquid during the period between the pulses which helps to break off the bubble earlier. Interestingly, the frequency of

oscillation, which controls the size of the generated bubbles, can be simply tuned by regulating the length of the feedback loop and the flow rate of the inlet gas stream (Tesař 2007; Zimmerman et al. 2009). The oscillation frequency varies inversely with the length of the feedback loop as shown in figure 2.13. Flow deflection by the Coanda effect is shown in figure 2.12.

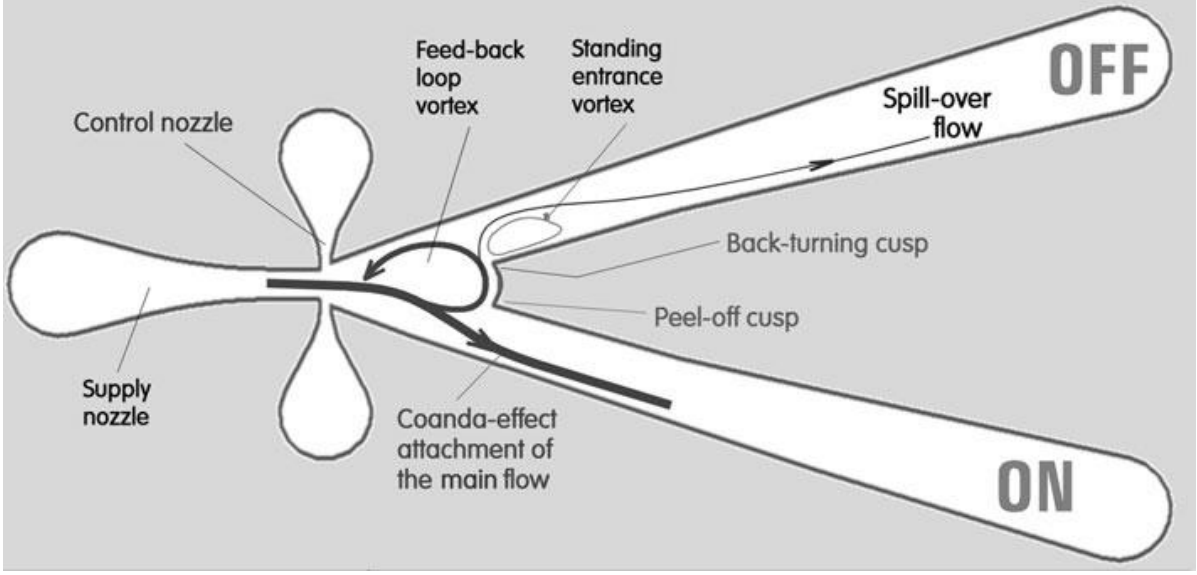

Figure 2.12: Jet diversion in fluidic oscillator by Coanda effect (Tesař & Bandalusena 2011)**.**

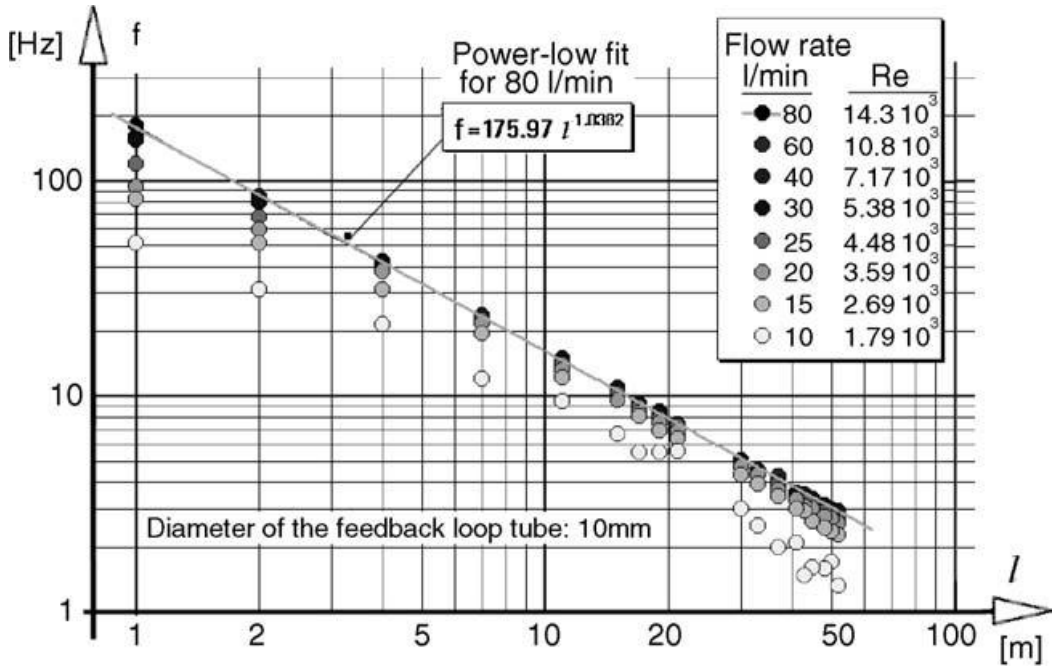

Figure 2.13: Graph of frequency of oscillation as a function of the length of the feedback loop at different gas supply flow rate. The frequency of oscillation (f) is proportional inversely with the length of the feedback channel (*l*) (Tesar et al. 2006).

Tests have been conducted by the microfluidics team in the Department of Chemical and Biological Engineering at the University of Sheffield to demonstrate the effect of fluidic oscillation valve on the task of bubble generation. Figure 2.14 presents the striking difference between bubbles generated with and without use of the fluidic oscillator with the same micro porous diffuser (20 μm pore size ceramic Hp diffuser) being used in the two cases.

It can be clearly seen that the bubbles generated with the use of the fluidic oscillator are uniformly dispersed, non-coalescent and with sizes almost equal to the size of the diffuser pores, while the ones generated without the fluidic oscillator are coalescent and several folds larger. The fluidic oscillation approach ensures that the bubble breaks off as soon as it attains the critical hemispherical cap shape which is the smallest expected radius of curvature for a bubble growing from a gas inlet pore (Zimmerman et al. 2008).

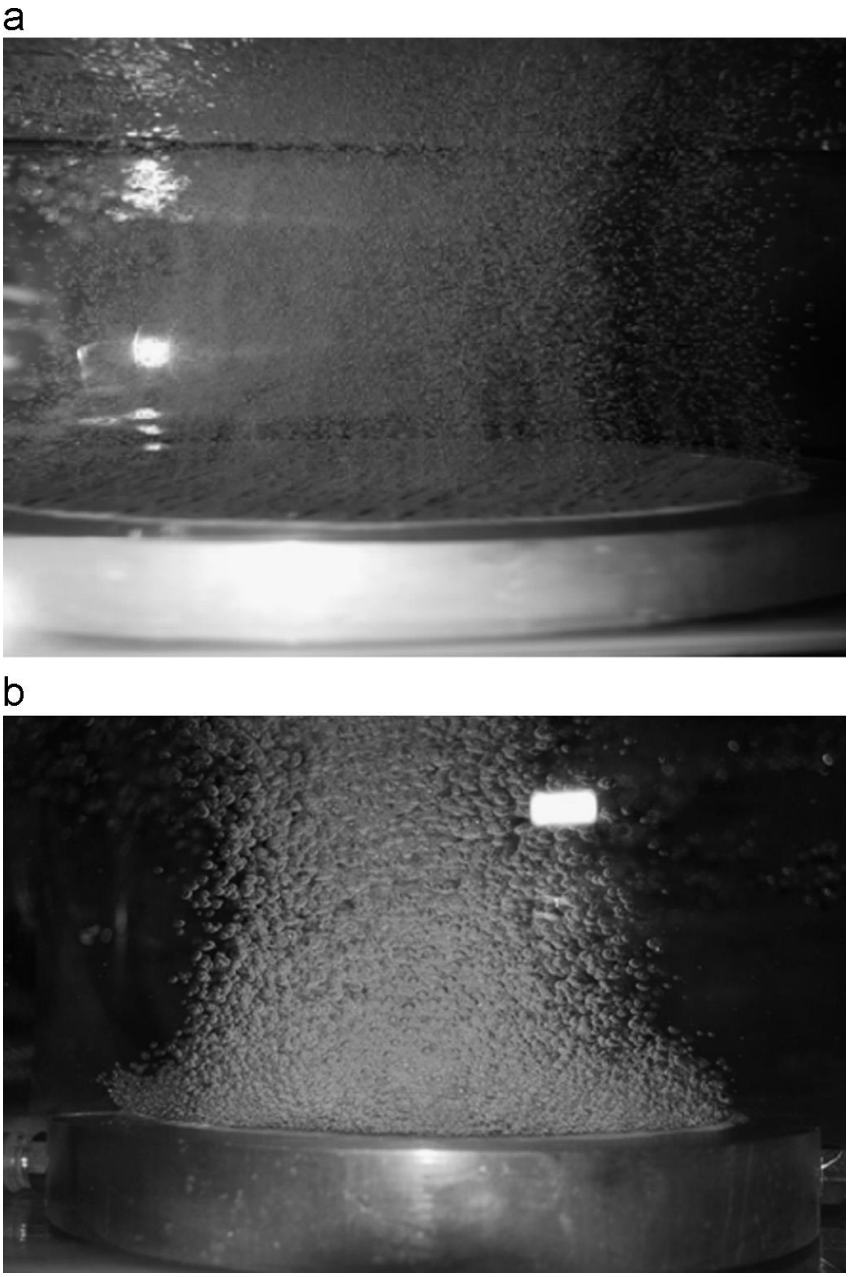

Figure 2.14: Images of microbubble generation using a microporous ceramic diffuser under different conditions (a) with fluidic oscillator (b) without fluidic oscillator (Zimmerman et al. 2013).

2.8.5 Energy efficiency of generating microbubbles by fluidic oscillation approach

It is anticipated that if the fluidic oscillator (figure 2.10) is inserted to any system for a purpose of generating microbubbles, it will significantly increase the energy consumption since fluidic oscillator serves as a splitter valve to the incoming gas jet. Such a splitter valve will increase the power consumption by adding an additional hydraulic resistance to the incoming fluid jet. However, there is unexpected energy saving with use of the fluidic oscillation approach.

Hanotu et al. (2012) reported that microbubble generation by fluidic oscillator consumes 2-3 orders of magnitude less energy than that consumed by the conventional saturation- nucleation generation methods. Two components have been reported to be contributed to this effect: the Coanda effect and the boundary layer disruption effect (Zimmerman et al. 2009).

2.8.5.1 Coanda effect

When a continuous fluid jet enters a T-splitter, there is a stagnation point for the flow at the jet splitting point before distributing between the two discharge channels of the splitter. This stagnation causes a considerable increase in the friction losses (Zimmerman et al. 2009). This is the case with the fluidic oscillator if the feedback loop is removed. However, as soon as the feedback loop is inserted, the incoming gas flow to the fluidic oscillation device will be attached to one of the curved side walls that connected between the control and the outlet terminals via the effect of the Coanda phenomenon and then directed to either of the two discharging terminals (Zimmerman et al. 2008). In this status, the fluid jet becomes free from the stagnation point, thereby avoiding the friction losses at the deflection point.

2.8.5.2 Boundary layer effect

It was demonstrated by Tesař & Bandalusena (2011) that the use of a fluidic oscillation valve becomes advantageous under turbulent flow conditions. As the Reynolds number decreases, the influence of the Coanda effect, which is responsible for directing the fluid jet between the two fluidic valve outlets, becomes less efficient. Therefore, turbulence is considered an important prerequisite for the work of the fluidic oscillator.

It is well known that turbulent flow in pipes has a viscous sub-layer close to the wall where the turbulence is highly dissipated by friction and consequently the flow becomes laminar in this layer. However, for the highly pulsating flow generated by the fluidic oscillator, this laminar boundary layer does not existent as it is disrupted by the fast switching of the flow between the two oscillator outlets (Zimmerman et al. 2009).

It is worth mentioning that this novel device has been applied recently as a cost effective method for microbubble generation with successful outcomes in various fields related to separation and mass transfer. These include: recovery of oil emulsion (Hanotu et al. 2013), separation of algae from culture media (Hanotu et al. 2012), promotion of microalgae growth

for biofuel production (Zimmerman et al. 2011; Al-mashhadani et al. 2012), yeast harvesting from a growth medium (Hanotu et al. 2014) and purification of potable water by ozone microbubbles as a sterilization agent (Lozano-parada & Zimmerman 2010).

2.8.6 Applications of microbubbles

The aforementioned properties of microbubbles have attracted their application in a wide spectrum of industrial and environmental separation processes. Utilization of microbubbles in the water and waste water treatment fields has been given a great interest because of their capability to produce highly reactive free radicals during the process of their collapse. Microbubbles tend to shrink over time and eventually collapse. Along with this shrinkage in size, the pressure inside the bubble increases, causing a rapid dissolution rate of their content to the surrounding fluid (Takahashi 2005; Agarwal et al. 2011). In addition, microbubbles in distilled water are found to have a negative surface charge with an average zeta potential value ranging between -30 to -40 mV irrespective to their size (Tsuge 2014). This surface charge can be exploited for the separation of particulate materials (solid wastes or oil droplets) from potable water and wastewater by processes such as flotation. The basic principle of flotation is that suspended and dissolved matters in water can become positively charged via the effect of coagulants. When negatively charged microbubbles ascend in the water column being treated, they act as collectors for the positive contaminant, resulting in less dense aggregates than the surrounding solution which then rise to the surface by the effect of the buoyancy forces (Burns et al. 1997).

Based on the method used to generate microbubbles in a system, three types of flotation process are possible: dissolved air flotation, electroflotation and dispersed air flotation. Each of these processes is associated with different applications.

Dissolved air flotation is usually used in potable water and waste water treatments. In this approach, microbubbles are generated by dissolving air at a very high pressure (approximately 483 kPa) into a solution at ambient pressure through a needle valve. As soon as the pressure is reduced at the nozzle tip, the air transfers out of this supersaturated solution in the form of bubbles. The average size of bubbles generated by this method ranges between 10-120μm (Burns et al. 1997). Despite this system being very efficient in the separation process, the major

hindrance is the high power consumption because of the high pressures required for air dissolution in water (Zimmerman, et al. 2011).

Microbubbles by electroflotation have been proven to be effective for separating valuable minerals from aqueous phases (Burns et al. 1997) and for treating oil-water emulsions (Hosny 1996). In electroflotation, bubbles of hydrogen and oxygen are generated electronically by splitting water molecules through applying a current into the processed solution. Oxygen microbubbles are formed at the anode while hydrogen microbubbles are formed at the cathode. The diameter of microbubbles generated from this method is between 22-50 μm. Compared with dissolved air flotation, electroflotation has higher flotation efficiency, easier operation and less maintenance.

In dispersed air flotation, bubbles are generated by discharging pressurized continuous air stream through a gas sparger. Microbubbles from this procedure have been used for the removal of particulates, such as quartz with sizes less than 50 μm (Burns et al. 1997).

Very small microbubbles have also been shown to possess useful properties for the application in the biomedical field. Their unique ability to respond to ultrasound makes them useful in medical ultrasound imaging. Additionally, the resonance of microbubbles can be used to generate localized forces to create ruptures in the membranes of cells and blood vessels for drug and gene delivery (Sirsi & Borden 2012; Wheatley & Cochran 2013).

For biological water treatment, microbubbles can be utilized to deliver the oxygen necessary for the growth and activity of micro-organisms in the wastewater. Micro-organisms, mainly bacteria, are responsible for the decomposition of various contaminants including nitrates, phosphates and organic matters. The high surface area of microbubbles and their long stagnation in solution can significantly increase the oxygen transfer efficiency, thereby increasing the rate of removal of pollutants (Zimmerman et al. 2009). It was demonstrated by Rehman et al. (2015) that the mass transfer coefficient (K_{La}) of oxygen improved by about 55% by the use of microbubbles. Microbubbles have also been used for water detoxification processes. It was found that the utilization of air and nitrogen microbubbles can catalyze the chemical reactions that are accountable for enhancing the detoxification efficiency (Agarwal et al. 2011). In addition, microbubbles, containing oxidizing gases such as ozone, are found to have a significant influence on enhancing water disinfection processes because of their high solubility in the solution (Agarwal et al. 2011).

Recently, the use of microbubbles generated by fluidic oscillation approach has been tested in anaerobic digesters in the waste water treatment plants to remove CO_2 which is normally produced from the digestion of organic materials. CO_2 can cause major problems associated with environmental pollution and in the corrosion of pipeline systems in the digestion plants. Results obtained from experiments have shown that the removal efficiency of CO_2 from the gas lift bioreactor is 29% greater in the presence of microbubble sparging system than that with the fine bubbles sparging (Al-mashhadani et al. 2012).

Microbubble aeration systems incorporating fluidic oscillator have also been applied to enhance the production of algal biomass, the important feedstock for biofuel production. Injecting a collection of slow rising CO_2 microbubbles into an airlift bioreactor (ALB) cannot only be employed for dissolving the required nutrients for algal culture growth (i.e. CO_2) much faster, but also for extracting the major inhibitor O_2 produced by algae from the liquid phase. This results in higher growth rates and higher density of biomass. A trial of two weeks with bubbling for one hour per day showed that 30% higher yield in the algal growth was obtained compared to those seen in the conventional growth cultures (Zimmerman, et al. 2011).

2.9 Mass and heat transfer dynamics of bubbles

Utilization of microbubbles in heating and evaporation systems has the potential to increase the rate of both heat and mass transfers for two reasons. The first one is the high surface area to volume ratio offered by microbubbles which increases the contact area between gas and liquid phases, thereby increasing the rate of both these interfacial rates. The second reason is the high internal pressure of microbubbles due to the surface tension which enhances the driving force for both heat and mass transfers (Bredwell & Worden 1998).

Fine (1-3 mm) and coarse (~1 cm) bubbles have been applied in many industrial heating and evaporation processes. One of these processes is the process of direct contact evaporation (DCE). DCE has been applied for many years for concentrating and separating aqueous solutions through injecting superheated gas in the form of bubbles (dispersed phase) into the liquid mixture to be heated or evaporated (continuous phase) so that part of the solvent is removed from the solution by evaporation at a temperature much lower than the boiling point of the solution (Ribeiro & Lage 2004). Gas bubbles are normally created by injecting a gas phase through a porous material, perforated plate or a set of perforated pipes located at the

bottom of the bubble column or the evaporator which contains the target solution. The gas stream is either heated in an external heater before entering the evaporator or generated from a combustion chamber submerged in the bubble tank itself (Ribeiro & Lage 2005).

As the superheated gas bubbles move vertically in the continuous phase, they can transfer their energy to the outside bath in two ways: either as sensible heat, causing an increase in the solution temperature or as latent heat, leading to vaporization of the solution present on the surface of the bubble which carried as a mass flux to the interior of the bubble (Ribeiro & Lage 2004). As time passes, the temperature of the liquid bath increases gradually until a quasi-steady state is achieved, after which the temperature and evaporation rates of the bath are almost constant. At this stage, most of the heat transferred from the bubbles is used for evaporation and the remaining small part is used for compensating heat losses from the system. It is known that the amount of the species evaporated from the liquid phase to the gas bubble varies directly with their saturation vapor pressure at the gas-liquid interface. Therefore, as the liquid temperature increases the fraction of the bubble energy used for vaporization increases (Ribeiro & Lage 2004; Inaba et al. 2002).

This technique has numerous applications in the industrial field for separating various solutions owing to the absence of any separating walls between the processing fluids (Ribeiro & Lage 2005). High thermal efficiency due to large heat transfer contact area, low operating and maintenance costs, simple construction, and the ability to process corrosive mixtures and thermally sensitive mixtures economically are the main features that characterize this process and make it superior to the traditional shell and tube heat exchangers (Ribeiro et al. 2005; Ribeiro et al. 2007; Ribeiro & Lage 2004; Ribeiro & Lage 2005; Jacobs 1988; Kang et al. 2002).

Ribeiro & Lage (2004) studied the use of DCE on an air-water system, focusing mainly on the bubble size characterization and gas hold up calculations, in addition to studying the effects of different gas superficial velocities and different sparger types on the temperature and the evaporation rate of the solution. They found that the evaporation rate of water and its quasi-steady state temperature increase as the gas superficial velocity increases. They found also that higher values of gas hold up and smaller mean bubble diameters can be obtained using a sparger with a smaller aperture size. However, as gas superficial gas velocity goes up, the sparger effect becomes trivial as a result of coalescence (Riberiro & Lage 2004). This technique has also been applied in the concentration of fruit juices, not only because it enables liquid evaporation at

temperatures lower than the normal boiling point, but it also prevents overheating at localized points (Ribeiro et al. 2007).

Inaba et al. (2002) also studied the mass and heat transfer characteristics of fine cold air bubbles ascending in a hot water layer. They investigated the effect of different parameters, including: inlet air flow rate, water temperature and water layer depth. It was found that the size of the generated air bubbles increased with increases in the air superficial velocity due to increases in the coalescence frequency. It was also observed that changing the liquid layer height from 10 to 90 mm has no effect on the mass and heat transfer characteristics of the bubbles, indicating that mass and heat transfer from the hot water to the cold bubbles occurred rapidly in a very short contact time after bubble injection.

More recently, liquid concentration by microbubbles has been investigated by Iwayama et al. (2007) with an aim of solving the problems associated with conventional liquid concentration systems. These include: poor heating efficiency, large equipment size and long residence time. The new system designed by Iwayama et al. (2007) can effectively separate liquid solutions in a short operating time with a small equipment size by using gas microbubbles. This approach comprises two steps: in the first one, air microbubbles are injected into a liquid flowing in a microfluidic chip and in the second, the whole system is heated under vacuum. When the system is heated, volatile components present in the liquid phase are evaporated and transferred to the bubble phase. Volatiles can thereafter be separated from the remaining liquid in gas-liquid separation units.

The approach applied in the current study is similar to the one applied by Iwayama et al. (2007), the main variation, however, is that in the current work microbubbles are heated before they are injected into the liquid phase. The current approach is also similar to the DCE approach, however, the main difference is in the bubble size and the bubble flow regime. In general, bubble columns have two main bubble regimes based on the gas flow rate and the liquid properties. These, as shown in figure 2.15, are: homogenous and heterogeneous bubbles regimes (Ribeiro & Lage 2005; Chaumat et al. 2007). The homogenous regime is recognized by the low gas flow rates, small bubble sizes, narrow bubble size distributions, uniformly spaced and non-interacted bubbles. On the other hand, heterogeneous systems are observed at high gas velocities and larger bubble volumes, which in turn induce bubble break up and coalescence phenomena (Chaumat et al. 2007).

The system recognized in direct contact evaporation processes or even in conventional microbubble generation methods such as dissolved air flotation (Edzwald 1995) is heterogeneous with bubbles injected into turbulent flows (case b). The system used in the current study, however, is homogenous with small bubbles of micro sizes rising slowly at their terminal velocity in the liquid medium (case a). The key difference is that owing to the turbulence in case b, bubbles can reach to thermal equilibrium with the surrounding liquid shortly after their injection while in case a, non-equilibrium conditions can be maintained much longer.

Recently, Zimmerman et al. (2013) have developed a computational model using COMSOL Multiphysics Software to investigate the mass and heat transfer dynamics of a single circulating superheated air microbubble rising in water at room temperature. Their modelling has not modeled the outlet dynamics in the continuous phase and has assumed that the heat transfer coefficient for a bubble with a diameter of 200 µm is 0.1 W/m^2K. This value was estimated based on a value of the heat transfer coefficient of 1080 W/m^2K measured by Kumar et al. (1992) for a rising bubble of about 1cm radius.

The results of their numerical modelling showed that bubble dynamics are transient and that vaporization evolves more quickly than heat transfer as shown in figure 2.16 which presents the time profile for the bubble concentration during the evaporation process.

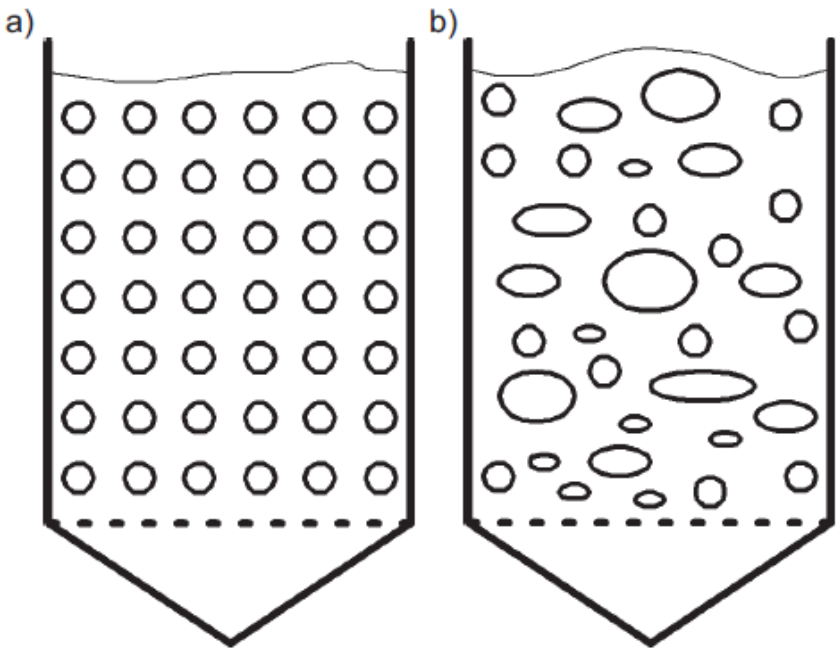

Figure 2.15: The main bubbling systems in direct contact evaporators (a) homogenous and (b) heterogeneous (Ribeiro & Lage 2005).

Figure 2.16 illustrates how the maximum absolute humidity inside a bubble of 200 µm diameter is rapidly achieved within a very short residence time on the order of 0.0001 s, followed by a gradual decay at a very short residence time. This decay occurs because of the re-condensation of the vapors inside the bubble as it cools during the longer contacting times. Results from the modelling study also showed that the temperature profile inside the bubble is almost isothermal, while the concentration profile has a small variance with its lowest concentration occurring close to the bubble skin because of the bubble circulation effect.

Zimmerman et al. (2013) also considered the effect of bubble size in their model by making a comparison between a fine bubble with a diameter of 0.001 m and a coarse bubble with a diameter of 0.01 m. They found that there is a thin layer surrounding the coarse bubble interface which is nearly unheated and with a temperature near to the liquid temperature, while the interior of the bubble remained hot and at a temperature close to the injection temperature. In the case of the fine bubble, bubble content was much more homogenous with only slight difference between the skin and the core of the bubble. From these results, it can be concluded that coarse bubbles cannot reach the maximum evaporation state during short residence times because of their slower mass transport. In contrast, microbubbles have faster mass transport which help them to achieve the condition of maximum humidity within a short residence time in the liquid.

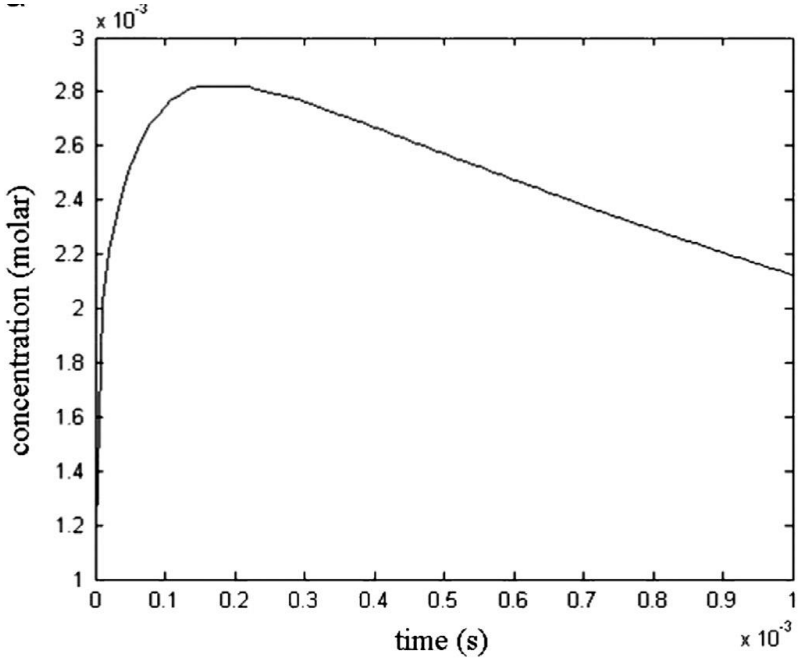

Figure 2.16: Variation of the average concentration of water vapor within the bubble with time for a bubble with an inlet temperature of 423K (Zimmerman et al. 2013).

2.10 Summary

In this chapter, many aspects related to the problems of biofuels and their applications are presented. Although, the technologies applied to treat some of these problems has shown reasonable results, cost challenges and operational obstacles are still the major concerns. The current research proposed a new distillation technology for the upgrading and separation of biofuels: bio-oil and bioethanol using microbubbles generated by the cost effective fluidic oscillation method. The study involves injecting hot gas in the form of microbubbles into the liquid to separate components through evaporation. While ensuring minimum heat transfer to the liquid during separation by heating the gas phase instead of the liquid, microbubble distillation technique also maintains non-equilibrium thermal and chemical conditions through injecting hot dry microbubbles.

In comparison with traditional distillation technique, microbubble distillation can separate thermally unstable solutions. It can also separate azeotropic solutions whose separation is challenged by equilibrium. Microbubble distillation can also reduce the cost required by the existent biofuels upgrading processes. The current technology does not require high pressures or high temperatures during operation. No catalysts or additional chemicals are needed. Low operating and maintenance costs are obtained. On this basis, the fundamentals of this new technique will be investigated in the separation of liquid mixtures and the upgrading of biofuels both experimentally and numerically and the results will be presented in the subsequent chapters in the following manner:

Since microbubble distillation is a novel approach, the first part of this study was dedicated to testing the performance and feasibility of this technology for separating species from liquid mixtures and providing information about the optimum operating conditions for this new separation process. A binary liquid mixture of ethanol-water was chosen for this purpose.

The second part of this study was devoted to the upgrading of bioethanol into a biofuel grade quality. An azeotropic mixture of ethanol-water was used to answer this question. It has also been noted by many researchers that the high amount of water in pyrolysis oils forms an azeotrope with the light organic compounds (Oasmaa et al. 2005; Rout et al. 2009; Naik et al. 2010; Pan et al. 2012) and this poses a difficulty in extracting water from a bio-oil mixture. Since improving bio-oil quality through removing water is also a main intent of this study, it is

significant to investigate the feasibility of the proposed technology for separating azeotropic systems.

The third part of the experimental work was focused on the investigation of upgrading a model bio-oil mixture through simultaneously reducing water and acid contents without significantly increasing their temperatures. Maintaining the temperature rise of the liquid mixture at its minimal value during the separation process is a crucial requirement for ensuring that this approach is suitable for separating thermally sensitive liquids such as pyrolysis oils.

The last part of this study was dedicated to developing a computational study using COMSOL MULTIPHYSICS as a modelling tool. The main aims were to understand the evaporation dynamics for this system and to study the effectiveness of microbubbles generated by fluidic oscillation in the separation/purification of multicomponent liquid mixtures.

The University Of Sheffield.

Chapter 3

Experimental Design, Materials & Methodology

Chapter 3

Experimental Design, Materials & Methodology

3.1 Introduction

This chapter is divided into two main parts. The first part focuses mainly on the experimental set up. This includes the optimization of the experimental design for the microbubble mediated batch separation unit with details about the equipment used in the experimental rig as well as the experimental procedure for the separation experiments. In the second part, materials and methods used for the preparation of the liquid mixtures applied in this study are given. The operating conditions for each system are presented. The chemical analyses applied for the measurements of both liquid and vapor phases for each mixture, along with the procedure for the bubble imaging process, are discussed.

3.2 Experimental set up

3.2.1 Design optimization

The first necessary step in the design of the microbubble mediated distillation unit is to build a suitable system for the generation of hot microbubbles. A hot microbubble generation system consists mainly of: gas source, process heater, chamber and gas distribution system (i.e. porous material or diffuser). In this work, two different types of bespoke diffusers were built and the optimum configuration was selected upon testing with respect to the effectiveness and suitability to conduct the experiments.

To take advantage of the most attractive recent manufacturing technology available today, 3D printing (or additive manufacturing) technology was selected to build our first chamber model or prototype. 3D printing offers customization, sustainability, tool-less, which saves time, effort, and money as well (Winnan 2013). The 3D printed chamber, as shown in figure 3.1, was made from acrylonitrile butadiene styrene (or ABS) thermoplastic material with the aid of a 3D printer model RepRapPro Ormerod-1 which uses the technique of fused filament

fabrication (FFF) to build 3D objects within 0.05 mm overall accuracy. The 3D model of the design was drawn using DesignSpark Mechanical free CAD modular software and the generated STL file was sliced to g-code file format (a file format in which the 3D printer firmware can 'see') using Slic3r open source software. The chamber had dimensions of 174 mm× 85 mm× 26 mm in length, width and depth respectively with 6 mm ID centered inlet hole. With 50% infill density, 3 mm shell thickness, and 30 mm/s linear motion speed, the printer takes approximately 10 hours to complete the printing process. A ceramic micro-porous diffuser (Point Four^{TM} diffuser) was fitted later over this chamber, fixed and kept in place by filling the gaps between the diffuser and the chamber walls with the aid of epoxy adhesive.

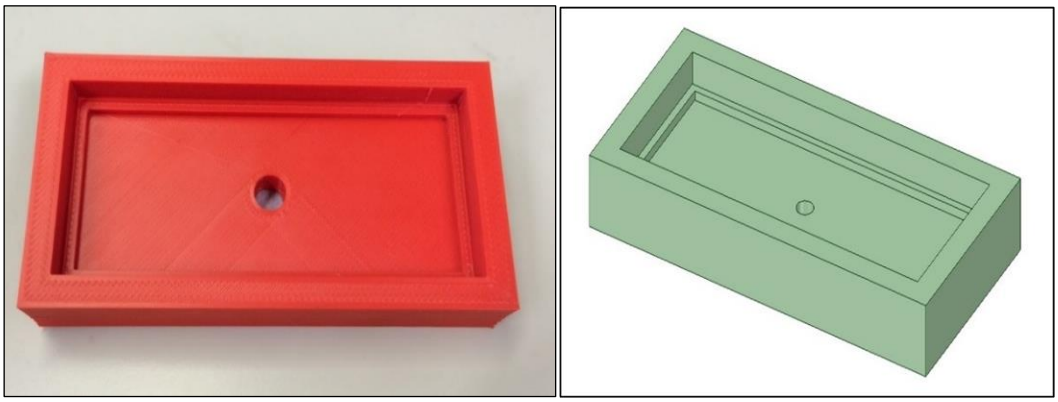

Figure 3.1: The 3D printed chamber for the bubble tank.

Since the glass transition temperature for the ABS is around ~105°C, the chamber was immersed for 60 min in boiling water so that we could check for any deformations due to the exposure to a relatively high temperature. The printed chamber passed the first test successfully. The next step is to test the 3D printed chamber under conditions that simulates a real experiment. Hot air at 100°C was passed inside the chamber through the inlet hole in order to generate hot microbubbles via the diffuser. The diffuser was covered by a layer of deionized water in which the microbubbles will swarm in during the test. This test unfortunately indicated some signs of failure, particularly in the area close to the air inlet since the ABS in this region became slightly softer than the rest of the chamber's body. This may have been due to the combined effect of high temperature and pressure build-up inside the chamber. In fact, this also adds concerns about the area surrounding the diffuser, and the question is if it can perform as expected under the working environment without failure in the future or not, even if there is

nothing noticed during the inspection of this area. In view of the safety concerns related to the durability of the 3D printed chamber, we decided to choose aluminium as the material of construction to build the chamber at the end of this stage.

Based on our experience in the design of the first chamber, the second model was built which consists of an aluminum with dimensions of 158 mm× 130 mm× 27 mm in length, width and depth respectively. Two Point Four microporous ceramic diffusers with dimensions of 150 mm× 60 mm× 5mm in length width and depth respectively were mounted over the chamber. The aluminum chamber was CNC machined at the workshop of the Chemical and Biological Engineering Department. A photo for the aluminum chamber is shown in figure 3.2.

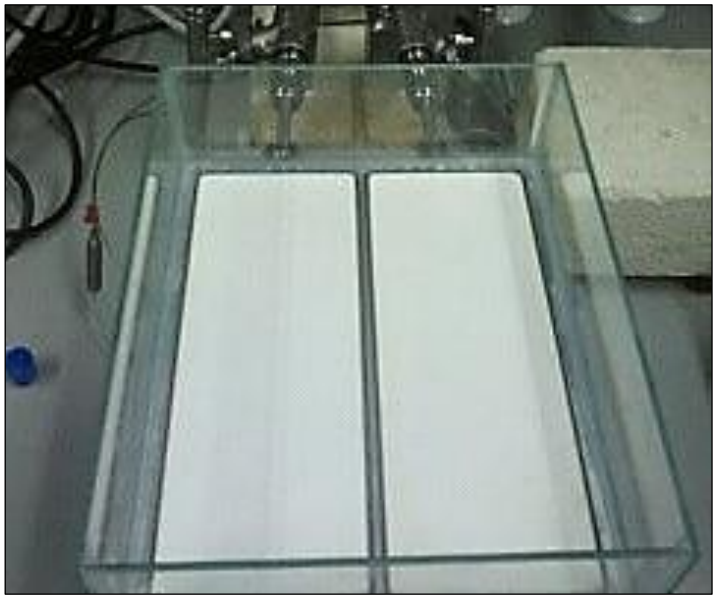

Figure 3.2: A photograph for the final assembly of the aluminum chamber with the diffusers.

For purposes of comparison between the ABS and aluminum chambers, figure 3.3 presents the temperature profiles of the water for both chambers after the injection of hot air microbubbles at 90°C for 100 min evaporation time. It was found that the first configuration (i.e. ABS) helps to significantly reduce the heat-leakage that comes from the diffuser body to the solution in the bubble tank during the evaporation process and this is due to its low thermal conductivity, compared to that of aluminum. However, it is assumed that the slight temperature rise of the liquid with the aluminum chamber has no significant effect on the properties of the thermally sensitive materials.

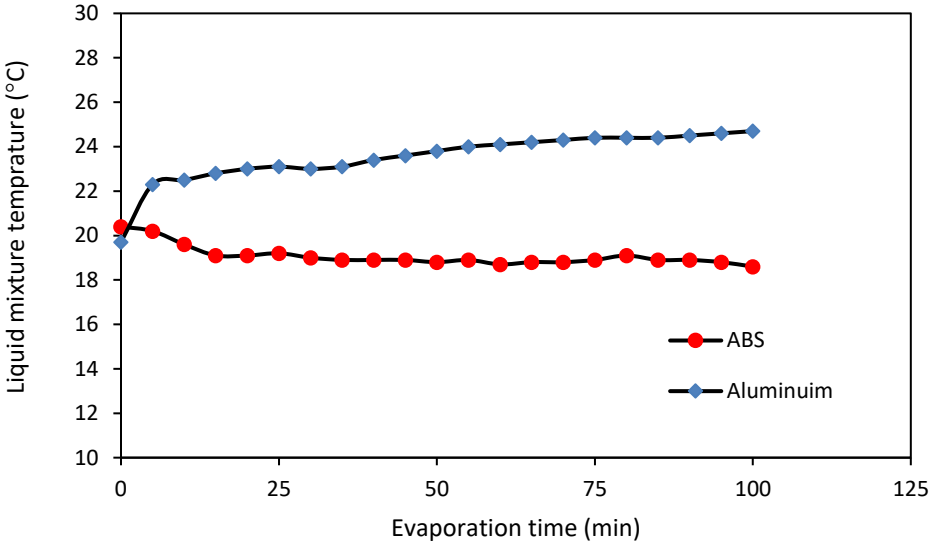

Figure 3.3: The time profiles for the liquid temperature using two different purpose built bespoke diffusers.

3.2.2 Experimental rig

The photograph and the schematic diagram for the bench scale microbubble mediated batch distillation unit is shown in figures 3.4 and 3.5 respectively. It comprises an air process heater, controller, fluidic oscillator and bubble tank. As illustrated in figure 3.5, dry pressurized air, supplied via a laboratory air pipe, was fed through a flow meter in order to measure its flow rate. The air was then passed through the process heater (RS Components Ltd. UK), with a total power of 750 W to increase its temperature to the required value. The temperature of the heater was registered by a thermocouple (type K) and was controlled using a controller with overheating protection which was constructed by the technicians in the electrical workshop of the Chemical and Biological Engineering Department at the University of Sheffield.

The hot air stream then entered the fluidic oscillator. This was constructed from aluminum in order to withstand the high temperatures applied in the experiment. The dimensions of the fluidic oscillator used are: 10 cm x 5 cm x 5 cm in length, height and width respectively. A picture of the fluidic oscillator is given in figure 3.6. The length of the feedback loop connecting the two control terminals was 25 cm. In this device, the air stream is distributed between the two bleed valves and the two outlet streams of the oscillator. The function of the bleed valves is to expel the excess air that is not required to enter the diffuser. The two outlet air streams

from the fluidic oscillator then entered the diffusers in the bubble tank where the microbubbles were generated.

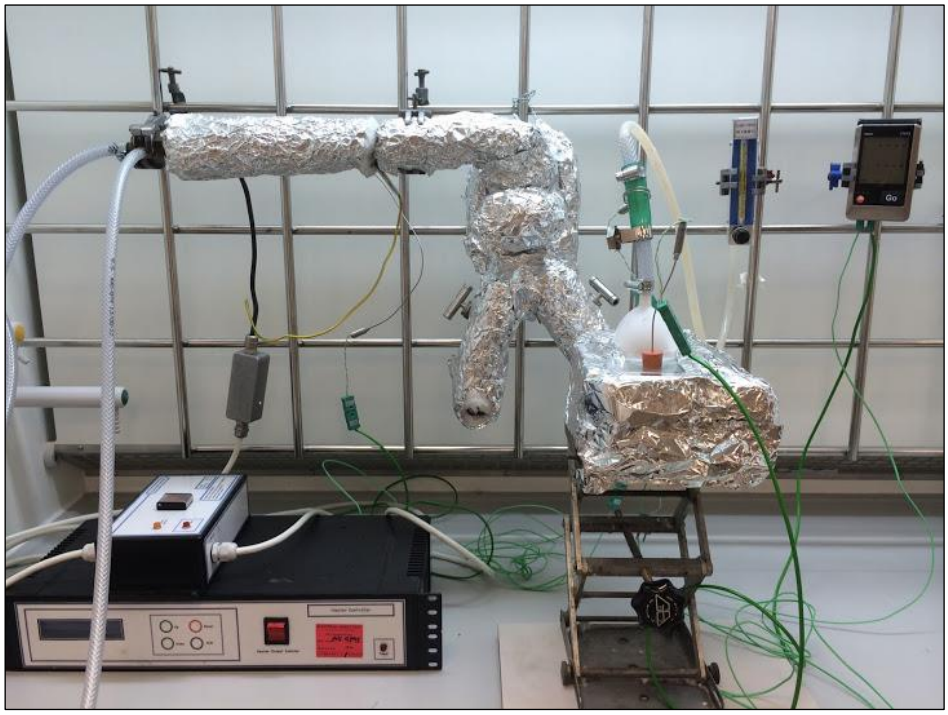

Figure 3.4: Image of the experimental set-up.

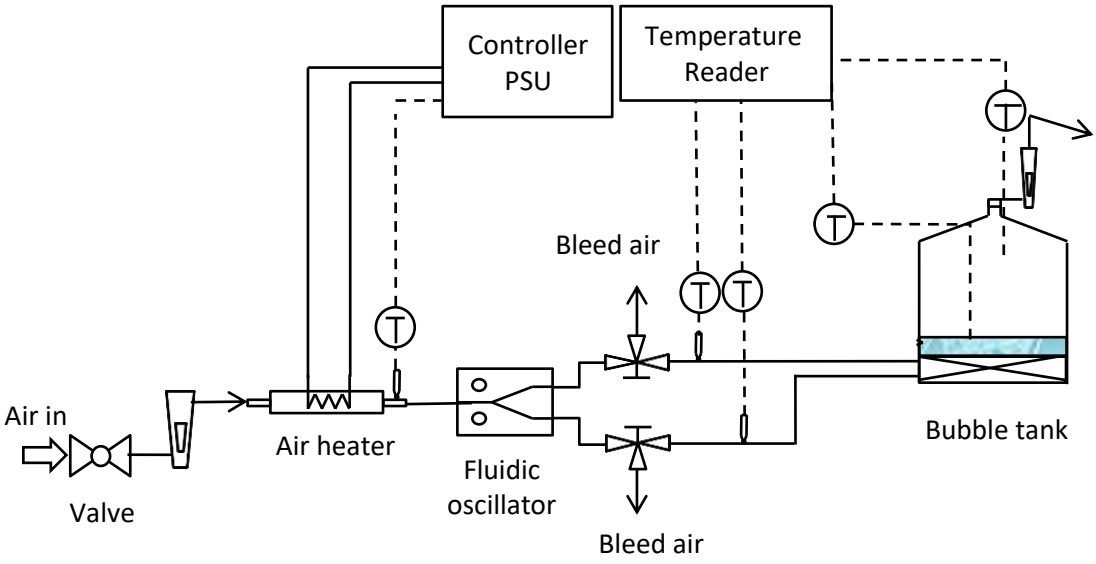

Figure 3.5: Schematic diagram of the experimental set-up.

Figure 3.6: Picture of the fluidic oscillator.

The rectangular bubble tank with glass sidewalls had dimensions of 15.8 cm in length, 13 cm in width and 4 cm in height. Its top was covered with a glass lid on to which a small funnel was inserted to direct the rising vapors to the outlet gas tube in order to minimize their condensation. The gas distribution system located at the bottom of the bubble tank consisted of two rectangular diffusers made from Point Four microporous ceramic plates.

All of the connecting pipelines, the fluidic oscillator, the heater and the bubble column were thoroughly insulated with glass wool, as shown on figure 3.4 to minimize heat losses. Four thermocouples of type K (Ni Cr+/Ni Al-) at different locations within the unit were used to obtain temperature measurements. The two thermocouples positioned in the connecting pipes between the fluidic oscillator and the bubble column were used for measuring the inlet air temperature to the diffuser. The thermocouple near the base of the bubble column was used to measure the temperature of the liquid mixture while the other in the header space measured the temperature of the outlet vapors. The sensors of all these thermocouples were located on the centerline of the pipes and connected to a four channel microprocessor thermometer (Testo Model 176T4) which displayed the temperature readings.

3.2.3 Experimental procedure

At the beginning of each experimental run, the valve of the air supply was opened and the gauge pressure in the air line was kept at 2 bars. The temperature controller was then turned on. Following this, the bleed valves of the fluidic oscillator were closed gradually and adjusted

until an oscillatory air flow was achieved. The oscillation was recognized through a continuous vibrating sound from the fluidic oscillator. When the air in the two inlet streams to the bubble tank had reached the required temperature, a previously measured volume of the target liquid mixture at a temperature of 20°C ± 0.5 was poured into the bubble tank. Immediately after pouring the liquid mixture into the bubble tank, the stopwatch was started and periodic readings of the air temperature at the two inlet streams to the tank, the temperature of the liquid mixture, as well as the temperature of the outlet vapors were recorded at 5 min intervals. At the end of each experiment, a syringe was used to extract the remaining liquid mixture from the tank through a vent in the lid. The volume of this liquid was measured to calculate the rate of evaporation of the liquid mixture. Samples were taken from the remaining solution for analysis. The equation for calculating the percentage of evaporation of the liquid mixture can be expressed by:

$$percentage\ evaporation\ (\%) = \frac{volume\ evaporated}{intial\ volume} = \frac{V_0 - V_f}{V_0} \times 100\% \qquad (3.1)$$

where V_0 is the initial volume of liquid mixture (ml) and V_f is the final volume of liquid mixture after evaporation (ml). V_0 was calculated by:

$$V_0 = Area\ of\ the\ tank\ base \times Height\ of\ liquid\ mixture \qquad (3.2)$$

For all experimental runs, the inlet air flow rate to the fluidic oscillator was maintained at 80 L/min to ensure that the fluidic oscillator was working properly (Tesař et al. 2006), while the flow rate to the diffusers was fixed at 1 L/min which means that about 79 L/min was lost through the bleeding valves of the fluidic oscillator. This flowrate (i.e. 1 L/min) was selected on the basis of an experimental test to allow the generation of small bubbles rising slowly through the liquid. The initial liquid mixture temperature of the prepared solutions was kept around 20°C for all experiments. The inlet air temperature to the bubble tank was controlled to be within the required value for each experiment.

3.3 Model aqueous solutions

3.3.1 Binary mixture

3.3.1.1 Materials

For experimental runs, binary mixtures of ethanol and de-ionized water were freshly prepared before each experiment using high purity ethanol (purity> 99.8%) purchased from Sigma

Aldrich Company, UK. Table 3.1 presents the initial composition of the liquid mixture applied in this work. This mixture was chosen so that there is a significant difference in the boiling points between its constituents (78.3°C for ethanol and 100°C for water). This difference is expected to permit good separation and to provide the opportunity to study the efficiency of this technique for stripping components based on injecting super-heated air microbubbles at a temperature equal to or higher than their boiling points.

Table 3.1: Chemical composition of the binary mixture

Component	***Composition (% vol.)***	***Boiling point (°C)***	***Class***
Ethanol	50	78.3	Alcohol
Water	50	100	Water

3.3.1.2 Experimental plan

The parameters investigated for the separation of the binary liquid mixture are:

- Depth of liquid mixture in the bubble tank. This is the height of liquid above the diffuser through which the bubbles can rise.
- Temperature of inlet air microbubbles.
- Total time of evaporation.

These parameters are important and can affect the separation efficiency of the target species as well as the temperature of the solution during evaporation. These factors were optimized using an experimental design method in accordance with the Central Composite Rotatable Design method (Cochran & Cox, 1992) whose principle is discussed in the next section. The results obtained from these experiments were then used to develop a multiple regression mathematical model which shows the relationship between the response of the system as a function of the three operating variables: liquid mixture level, inlet air microbubble temperature and evaporation time. The response of interest for the current study is the recovery efficiency of ethanol (R) from liquid mixture which can be determined using the following formula:

$$R = \frac{V_0 - V_f}{V_0} \times 100\% \tag{3.3}$$

where V_0 and V_f are the initial and final volumes (ml) of ethanol in the liquid mixture before and after experiment respectively. The final volume of ethanol (V_f) was calculated depending on the total final volume of the binary liquid mixture and the concentration of ethanol in this solution which was measured using GC analysis (section 3.4.1)

3.3.1.2.1 Central Composite Rotatable Design Method

Experimental design and data modeling techniques are widely applied with successful outcomes in the research and industrial fields for optimizing process variables. The most commonly used methods for process analysis and modeling are: full factorial design, partial factorial design and the central composite rotatable design (Aslan 2008).

By far, the central composite rotatable design method (CCRD) is the most economic and effective as it requires significantly fewer numbers of experiments and provide maximum information about the optimal process conditions when compared to the factorial method which is time-consuming (Obeng et al. 2005; Fakheri et al. 2012). Each variable in the CCRD method is coded to lie at ±1 for the factorial points, 0 for the central point and α for the axial points, where $\alpha = \pm 2^{k/4}$ and k is the number of process variables. Table 3.2 presents the relationship between the coded and actual values depending on the minimum ($Xmin$) and maximum ($Xmax$) levels for each variable (Aslan 2008).

The total number of tests required for the CCRD method can be calculated as follows: the standard 2^k factorial points, extra axial $2k+1$ points as well as the number of the replicate points which are important for estimating the experimental error of the model.

Table 3.2: Coded and real values of the variables according to CCRD method (Aslan 2008)

Coded value	***Actual value***
-α	$Xmin$
-1	$[(Xmax + Xmin)/2]$- $[(Xmax - Xmin)/2\alpha]$
0	$(Xmax + Xmin)/2$
+1	$[(Xmax + Xmin)/2]$+$[(Xmax - Xmin)/2\alpha]$
+α	$Xmax$

In the current work, the CCRD method was used to design the experiments and establish a relationship between the recovery efficiency of ethanol (R) from the liquid mixture (response) and three controllable independent variables, namely: the initial temperature of air microbubbles x_1, height of liquid layer in the bubble tank x_2 and time of evaporation x_3 (factors). For 3 x-variables, the response function takes the following form:

$$y = \beta_0 x_0 + \beta_1 x_1 + \beta_2 x_2 + \beta_3 x_3 + \beta_{11} x_1^2 + \beta_{22} x_2^2 + \beta_{33} x_3^2 + \beta_{12} x_1 x_2 + \beta_{13} x_1 x_3 + \beta_{23} x_2 x_3 \quad (3.4)$$

where y is the response, x_0 is a dummy variable which has the value of +1 for every observation in the set (table 3.3), x_1, x_2, x_3 are the dimensionless coded variables, β_0 is the intercept regression coefficient, $\beta_1, \beta_2, \beta_3$ are the linear regression coefficients, $\beta_{12}, \beta_{13}, \beta_{23}$ are the interaction regression coefficients and $\beta_{11}, \beta_{22}, \beta_{33}$ are the quadratic regression coefficients.

This polynomial multi variable model includes the single effect of each variable in addition to the interaction effects between variables. It can also be used to determine the values of the variables at which the responses reach their optimum value which is either maximum or minimum (Fakheri et al. 2012).

The values of the empirical model coefficients can be estimated using the following algorithms for three variables (Cochran & Cox 1992):

$\beta_0 = 0.166338(0y) - 0.056791 \sum(iiy)$

$\beta_i = 0.073224(iy)$

$\beta_{ii} = 0.0625(iiy) + 0.006889 \sum(iiy) - 0.056791(0y)$

$\beta_{ij} = 0.125(ijy)$

where $0y, iy, iiy \; and \; ijy$ are given by the following equations:

$0y = \sum x_0 y$

$iy = \sum x_i y$

$iiy = \sum x_i{}^2 y$

$ijy = \sum x_i (jy)$

For three operating variables, the required number of replicates is 5. Thus, the total number of experiments required for three independent parameters are:

$$2^3 + (2\times3+1) + 5 = 20.$$

3.3.1.3 Operating conditions

As mentioned above, the CCRD method requires a total number of 20 experiments for 3 operating variables, however, 24 experiments have been conducted for this study. The additional experiments (runs 21, 22, 23 and 24) as shown in table (3.3) were found to be useful in the graphical analysis. The range of factors that were taken is:

- Temperature of inlet air: 80-100 °C.
- Depth of liquid layer: 3-10 mm.
- Time of evaporation: 50-200 min.

Table 3.3: Operating conditions for ethanol-water mixture experiments

Test no.	***Coded levels of variables***				***Actual levels of variables***		
	X_0	***X_1***	***X_2***	***X_3***	***Temperature of Inlet air (°C)***	***Depth of liquid layer (mm)***	***Time of evaporation (min)***
1	1	-1	-1	-1	84.1	4	80.4
2	1	1	-1	-1	95.9	4	80.4
3	1	-1	1	-1	84.1	9	80.4
4	1	1	1	-1	95.9	9	80.4
5	1	-1	-1	1	84.1	4	169.6
6	1	1	-1	1	95.9	4	169.6
7	1	-1	1	1	84.1	9	169.6
8	1	1	1	1	95.9	9	169.6
9	1	-1.682	0	0	80	7	125
10	1	1.682	0	0	100	7	125
11	1	0	-1.682	0	90	3	125
12	1	0	1.682	0	90	10	125
13	1	0	0	-1.682	90	7	50
14	1	0	0	1.682	90	7	200
15	1	0	0	0	90	7	125
16	1	0	0	0	90	7	125
17	1	0	0	0	90	7	125
18	1	0	0	0	90	7	125
19	1	0	0	0	90	7	125
20	1	0	0	0	90	7	125
21	-	-	-	-	60	7	125
22	-	-	-	-	120	7	125
23	-	-	-	-	90	5	125
24	-	-	-	-	90	30	125

These experiments were carried out both with and without the presence of the fluidic oscillator to investigate its effect on the separation efficiency.

3.3.2 Azeotropic mixture

3.3.2.1 Materials

The composition of the azeotropic mixture used in this work is shown in table 3.4.

Table 3.4: Chemical composition of the azeotropic mixture

Component	***Composition (% vol.)***	***Boiling point (°C)***	***Class***
Ethanol	96	78.3	Alcohol
Water	4	100	Water

An azeotropic solution of 96% vol. ethanol-water was purchased from Sigma Aldrich Company UK and used directly for the experimental runs.

3.3.2.2 Operating conditions

Effects of liquid mixture level and inlet air microbubble temperature on the efficiency of breaking the azeotrope of ethanol-water mixture were investigated. The key operating conditions for the azeotropic mixture experiments are listed in table 3.5.

Table 3.5: Operating conditions for azeotropic mixture experiments

Parameter	***Value***
Temperature of air microbubble	80 and 90 °C
Depth of liquid mixture in the bubble tank	3, 5 and 10 mm
Initial liquid temperature	20±0.5 °C
Evaporation time	90 min
Air flow rate	1L/min

3.3.3 Simulated bio-oil mixture

3.3.3.1 Materials

Three components were chosen to represent the model bio-oil mixture for this work. The simulated bio-oil feed, as shown in table 3.6, contained acetic acid as a representative for the

carboxylic acids, acetol as a representative for the higher molecular weight ketones and aldehydes in the bio-oil mixture and water.

Table 3.6: Chemical composition of the simulated ternary mixture

Component	*Composition (% vol.)*	*Boiling point (°C)*	*Class*
Water	30	100	Water
Acetic acid	15	118	Alcohol
Acetol	55	147	Ketone

Acetic acid with analytical purity grade (>99.98%) and acetol (1-hydoxy-2-propanone) with purity of 90% wt. in water were purchased from Sigma Aldrich Company UK and used for making up the feed mixtures for this study.

3.3.3.2 Operating conditions

In this set of experiments, the effect of the initial air temperature, depth of liquid layer in the bubble tank and time of evaporation (factors) on the rate of separation of water and acetic acid from the liquid mixture were studied. The operating conditions for the ternary model mixture experiments are presented in table 3.7.

Table 3.7: Operating conditions for ternary mixture experiments

Parameter	*Value*
Inlet air microbubble temperature	80 and 100 °C
Depth of liquid mixture in the bubble tank	3 mm and 5 mm
Initial liquid temperature	20±0.5 °C
Evaporation time	30, 60, 90, 120 and 150 min
Air flow rate	1.2 L/min

3.4 Analytical methods

3.4.1 Gas chromatography (GC)

The chemical compositions of ethanol-water liquid solutions were determined using gas chromatography (GC). GC has a good sensibility to volatile organics, therefore it was selected as the analysis method for this work. A Varian 3900 gas chromatograph (GC) equipped with a

thermal conductivity detector (TCD) was used. The column was a HAYESEP P which had an internal diameter of 4 mm and total length of 2 m. The GC oven temperature was set at 150°C. The injection was splitless at a temperature of 180°C. The carrier gas was nitrogen at a flow rate of 400 ml/min and a pressure of 30 psi. Retention times of ethanol and water were 2 min and 0.8 min, respectively.

3.4.2 Gas sensors

Gas sensors were used to determine the chemical composition of the ethanol-water vapor mixtures as well as the composition of the water-acetic acid-acetol ternary liquid mixtures. Gas sensors are a type of sensor that can detect the presence of gas contaminants in the environment of interest. The detection principle relies on measuring the changes that occur on the sensor's state when one or more gas species acts to alter the physical or chemical properties of the sensor's sensing element. The ultimate aim of gas sensor experimenter is to analyze the information provided by the stimulated sensors in order to qualify and/or quantify the targeted substances in the medium under study (Khalaf 2009) . However, the analysis techniques and the degree of the accuracy required depend mainly on the proposed application of the gas sensors. As a result, the answer might be a straight forward mathematical treatment or could be extended up to an advanced level of analysis complexity (Jeffrey & Kimberly 2012).

Gas sensors offer an attractive solution for a wide range of applications in which gas sensing is an integral part of the system. Gas leakage detectors/alarms, air/food quality control, breath analyzers, pollutants monitoring, medical diagnostics, and electronic noses are common areas in which gas sensors have been applied (Gardener & Bartlett 1999; Pace et al. 2012; Pace et al. 2016; Ryabtsev et al. 1999).

Different technologies were adapted in the manufacturing process of the gas sensors in order to improve their characteristics and performance (Liu et al. 2012). Among these, the method based on measuring the changes in the electrical properties of a sensing element built from a metal oxide semiconductor (MOX) offers many valuable advantages such as: high sensitivity, fast response and recovery times, low power consumption, long life, miniature size, availability, and low cost (Gardener & Bartlett 1999).

The MOX gas sensors were used in the current work for all of the above mentioned benefits. Brief principles for the measurements will be introduced first before going into the details of the experimental rig and the method of analysis.

3.4.2.1 Metal Oxide Gas Sensors

The sensing element of the metal oxide gas sensors was made from semiconductor materials. Typically, tin-dioxide (SnO_2) doped with a tiny quantity of catalytic material such as platinum or palladium was used. When the sensing material is heated up through a heater provided in the gas sensor, it will start to lose electrons to adsorb oxygen from the surrounding air, causing an increase in the electrical resistance according to the reaction (Gardener & Bartlett 1999):

$$\frac{1}{2}mO_2 + e^- \overset{k_1}{\rightarrow} \{O_m^-\}_{ads.} \tag{3.5}$$

Now, in the case of the presence of a reducing gas species X (e.g. organic vapor), it will act to reduce the negative charge density by reacting with the adsorbed oxygen, returning back the previously donated electrons to the semiconductor crystal according to the reaction:

$$X + \{O_m^-\}_{ads.} \overset{k_2}{\rightarrow} XO_m + e^- \tag{3.6}$$

As a result of this, the resistance of the sensing element will be decreased. The rate of the second reaction is affected by the concentration of the reducing gas, temperature, and working conditions. Figure 3.7 shows a photograph of different metal oxide gas sensors.

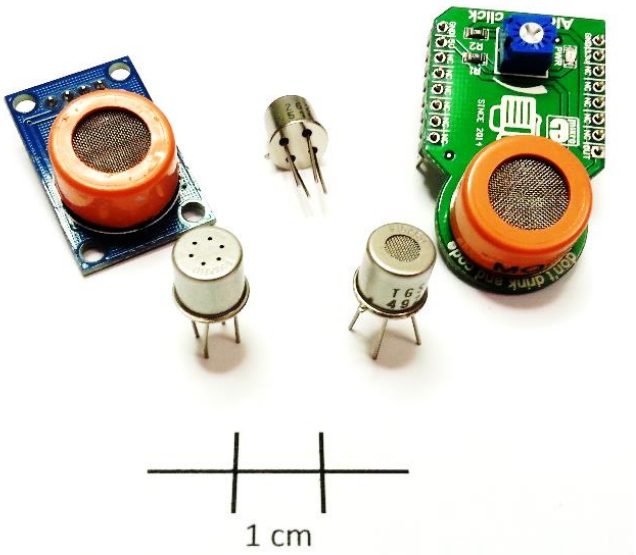

Figure 3.7: Different metal oxide gas sensors.

Figure 3.8 shows a simple circuit diagram used to drive a MQ-3 type gas sensor. This sensor has 6 pins: 2As and 2Bs which acting as sensing element terminals and 2Hs terminals for the heater to raise the temperature of the sensing element up to its working temperature. The change in conductivity can be detected by monitoring the voltage drop over the load resistor R_L.

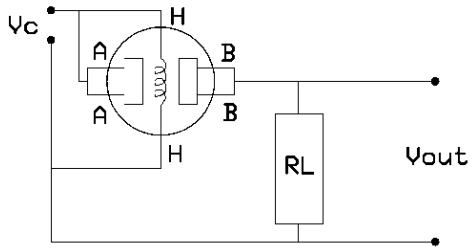

Figure 3.8: Gas sensor circuit schematic.

3.4.2.2 Measurements of the vapor phase concentration in binary mixtures

Traditional condensation methods of vapors would not reflect the actual concentration at a given time during the experiment. Instead, they would provide an accumulated concentration of the condensed vapor over a period of time since it is difficult to condense the vapor instantaneously to get a useful liquid sample for GC analysis. To overcome this problem, gas sensors were used to measure the concentration in the gas phase instantaneously for our binary mixture experiments.

The apparatus that used for performing the gas concentration measurements is shown in Figure 3.9. A set of two MQ-3 gas sensor modules were used to simultaneously provide two measurements for the gas concentration. Measurements were made inside the approximately 1300cc clear acrylic chamber. Sensors were attached to the outer wall of the chamber and connections were provided to the gases in the bulk via a circular hole for each sensor. Both sensors were supplied with a voltage of 5 V from a power supply (Model TTi Ex354D). Received signals from sensors were fed into a Pico ADC-20 high resolution data logger and then relayed to a computer for analysis.

A regulated dry air was allowed to flow inside the chamber at a rate of 1800 cc/min adjusted with the aid of electronic flow meter (Cole-Parmer flow gas mass flow controller Model 32907-75). This clean air stream will remove any moisture from inside the test chamber and isolate it from any contaminants that may interfere with the measurements. In addition, the continuous

flow of the air stream will keep the sensors in a stable state providing a virtually constant operating environment for the duration of the experiment. Outflowing gases exit the chamber at the same flow rate through a hole on the opposite side to the inlet.

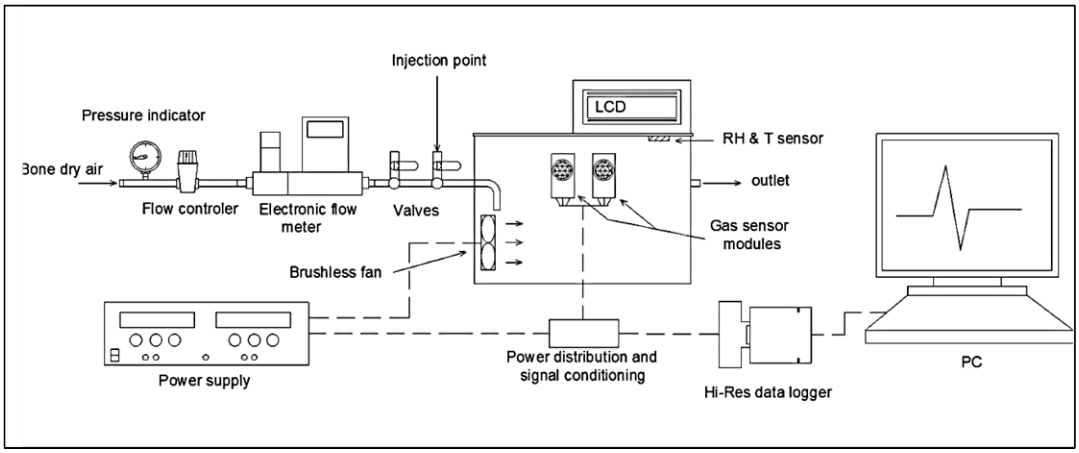

Figure 3.9: Gas concentration measurement apparatus.

The measurement process was implemented by firstly preparing saturated ethanol gas samples from known liquid concentrations, then injecting 3 cc of the saturated gas, taken from calibration samples, into the test chamber by a syringe through the gas mixing valve. Injected vapors will be mixed with the dry air stream, enter the chamber, and become distributed evenly inside the chamber with the aid of the brushless fan. After injection, signals were detected due to the fast change in the sensor's conductivity. Their conductivity will then return back to the initial state when the air inside the chamber became free again from all traces of the injected gas. Calibration curves were made based on the signal peak value of the injected samples.

After calibration, ethanol vapor samples from the bubble tank were injected in the same way as described above. The unknown concentration of the injected gas can be determined from the calibration curves.

It is appropriate to mention here that we experimentally demonstrated that an air flow rate of 1800 cc/min and a sample injection volume of 3 cc are the suitable operating conditions in our system. They provide reasonable residence times for the samples inside the chamber and enable clear peak heights to be detected at different concentrations whilst ensuring that the gas sensors are not saturated.

Figure 3.10 demonstrates the dynamic response of the gas sensors for 10 calibration samples (vapors from 10% vol. up to 100% vol. of liquid ethanol-water mixtures). As can be seen, the two responses are close to each other but this is not a necessary condition, even for the same type of sensors, since identical sensor properties cannot be 100% guaranteed during the manufacturing process. Figure 3.11 shows the calibration curves for each sensor.

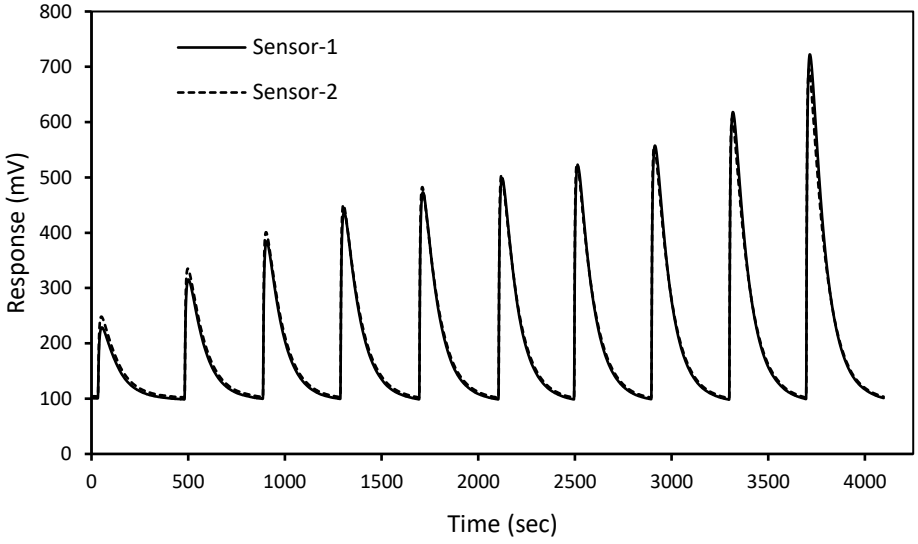

Figure 3.10: Dynamic response of gas sensors.

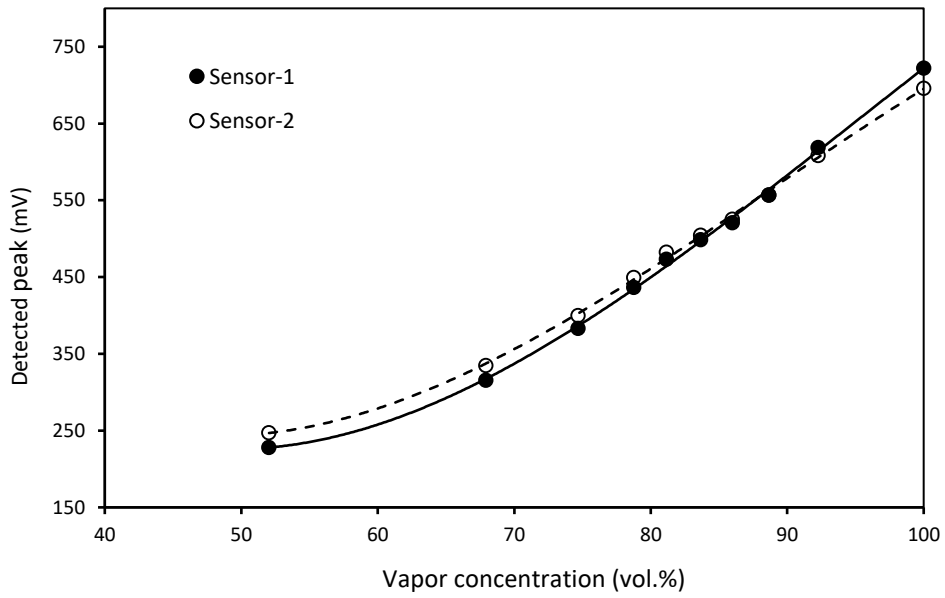

Figure 3.11: Gas sensors calibration curves.

The interesting feature that can be extracted from figure 3.11 is that the range from 70% and above shows a linear relationship between the gas concentration and the sensor's response. The R-squared value was calculated to be of 0.9965 and 0.9977 respectively for sensors 1 and 2.

Table 3.8 shows typical numerical results for 12 different samples measured after the calibration process Ethanol x-y equilibrium data are obtained from Flick (1998). As can be seen, the results are highly accurate and the maximum error reported here is around 1% and the average error is 0.433% confirming the reliability of this method for the measurements. It is not necessary to make the calibration curve for the whole range of concentrations for each experiment, instead, the calibration could be made just for the particular region of interest.

Table 3.8: Test sample measurements

Ethanol x-y equilibrium data (vol.%)		***Measured average vapor concentration (vol.%)***	***Error percentage (%)***
$x_{eq.}$	$y_{eq.}$	$y_{measured}$	
96	96.39	96.35	0.041
98	98.05	98.15	0.102
70	85.99	85.73	0.302
100	100	99.93	0.07
80	88.66	88.70	0.045
90	92.28	92.56	0.303
60	83.67	84.05	0.454
50	81.16	81.40	0.296
15	61.31	61.90	0.962
35	76.75	76.02	0.951
25	71.53	71.00	0.741
65	84.79	85.00	0.248
20	67.93	67.64	0.427
40	78.76	77.88	1.1177

The correlation coefficient was calculated to determine the accuracy of the measurements for the values listed in table 3.8 from the relation:

$$r = \frac{n\left(\sum y_{eq.} y_{measured}\right) - \left(\sum y_{eq.}\right)\left(\sum y_{measured}\right)}{\sqrt{\left[n\sum y_{eq.} - \left(\sum y_{eq.}\right)^2\right]\left[n\sum y_{measured}{}^2 - \left(\sum y_{measured}\right)^2\right]}} \tag{3.7}$$

in which *r* is the correlation coefficient, $y_{eq.}$ denotes the actual values, $y_{measured}$ denotes the measured values, and *n* is the total number of measurements. The calculated value of *r* (0.9817) confirms the strong relationship between the measured values and the actual values. However, values for *r* higher than 0.99 for ethanol were reported by Khalaf et al. (2009).

It should be noted that there is an unavoidable drift of the order of a few millivolts in the base line of each sensor. Consequently, all measurements were adjusted in line with the base line average value following the mapping (Di Carlo & Falasconi 2012):

$$p_f \leftarrow p_i - \left(b_i - \bar{b}\right) \tag{3.8}$$

where p_f is the final value of the signal after correction, p_i represents the highest value of the signal obtained from the injected sample, or simply signal peak value, b_i is the sensor base line of the signal under analysis, and $\bar{b}$ is the average base line of the sensor along the experiment.

3.4.2.3 Measurements of the liquid phase concentration in ternary mixtures

The method adapted to measure the vapor phase in the binary mixtures can be extended to measure liquid concentrations for the ternary mixture (table 3.6) indirectly by vaporizing a known quantity of liquid inside the measuring unit. To achieve this, an electronic nose was developed for this purpose. An electronic nose is a device composed of an array of gas sensors that shows different response patterns when exposed to different gas constituents or concentrations (Gardener & Bartlett 1999). In order to obtain highly accurate results, the gas sensor array should have a number of sensors at least greater than the number of target components in the system (Yang et al. 2013).

Our electronic nose comprised two MickroElectronika MQ-3 gas sensor modules, two Figaro TGS2620, and one Figaro TGS2610 gas sensors connected to different load resistors in order to change their sensitivity. We also introduced the Honeywell HIH-3610 humidity sensor to measure water concentration in the samples. An interesting feature about the humidity sensor is that it is a completely independent sensor and does not respond to any compounds in the mixture except water. This makes a total of 5+1 sensors and all of them were installed in the same unit described in figure 3.9.

The suggested model to correlate the concentration of acetic acid and acetol in the mixture was proposed to follow a complete second order degree polynomial regression of two variables as shown in Eq. (3.9). To calculate the polynomial coefficients, the following minimization equation need to be solved (Khalaf et al. 2008):

$$\min_{A_j,\,B_j,C_j,D_j,E_j,F_j} \sum_{j=1}^{M}\sum_{i=1}^{N}\left(S_{ji} - A_j - B_jC_A - C_jC_B - D_jC_A^2 - E_jC_B^2 - F_jC_AC_B\right)^2 \qquad (3.9)$$

where C_A and C_B are the acetic acid and acetol concentrations measured in volume percentage (%vol.) in the liquid mixture respectively, M is the total number of gas sensors installed (i.e. 5), N is the number of calibration samples, S_{ji} denotes the sensor responses, and a_i are polynomial coefficients.

Once the above equation has been solved and the values of the polynomial coefficients are calculated, we next solve the following minimization equation for the responses of unknown samples:

$$\min_{C_A,C_B} \sum_{j=1}^{M}\left(S_j - A_j - B_jC_A - C_jC_B - D_jC_A^2 - E_jC_B^2 - F_jC_AC_B\right)^2 \qquad (3.10)$$

in which the unknown values in this case are C_A and C_B. Water content was calculated from the constraint $100-C_A-C_B$ and double checked further with the humidity sensor results. MATLAB has been used to solve the minimization for both equations using Nelder-Mead amoeba algorithm.

In the next typical experiment, 20 different interaction samples were prepared. Acetic acid covered concentrations up to 20% vol., while acetol covered concentrations up to 81% vol. All the responses were based on the evaporation of 1 µL of the liquid mixture inside the chamber using a GC micro syringe (Model: Hamilton 7105KH). Figures 3.12 and 3.13 show the actual concentrations and the measured ones from equation 3.10 for acetic acid and acetol respectively. The R-squared values were found to be 0.9865 and 0.9987 for acetic acid and acetol respectively.

Table 3.9 shows the results of water concentrations measured via humidity sensor compared with those calculated from the constraint equation. The R-squared values were found to be 0.9728 and 0.98 for humidity sensor and constraint equation respectively.

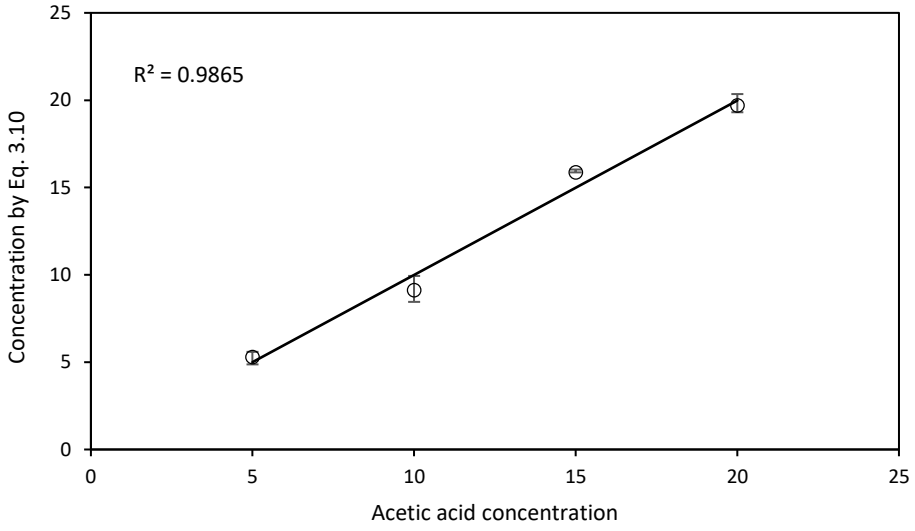

Figure 3.12: Graph of the real concentrations of acetic acid versus the estimated ones by Eq. 3.10.

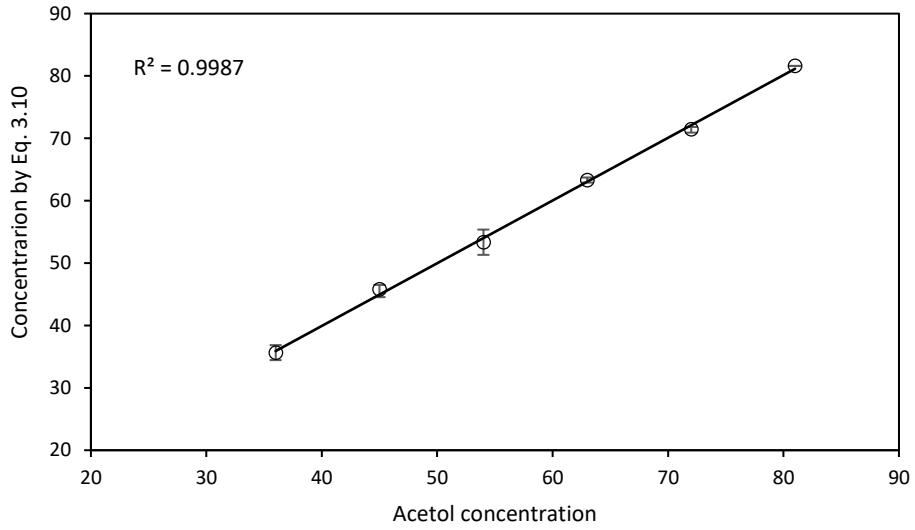

Figure 3.13: Graph of the real concentrations of acetol versus the estimated ones by Eq. 3.10.

Table 3.9: Calibration concentrations of water

Real concentration (%)	***Measured from constraint equation***	***Measured by humidity sensor***
59	59.92	55.36
50	49.32	47.46
41	40.63	38.23
32	30.91	29.99
23	23.75	20.44
14	12.55	12.53
54	52.99	51.41
45	43.61	45.49
36	41.68	36.59
27	27.14	27.36
18	20.53	17.14
49	50.50	49.44
40	37.36	44.17
31	27.465	32.97
22	20.78	22.42
13	13.13	12.70
44	43.98	46.80
35	36.40	38.24
26	26.99	29.01
17	16.57	17.47

3.4.3 Gas chromatography/mass spectrometry (GC-MS)

GC-MS was used to investigate whether there is a reaction between the components of the ternary mixture during the separation process or not. The samples were analyzed using a Perkin Elmer, Turbomass, GC-MS. The column used was a Phenomenex, ZB-WAX which had dimensions of 30 m, 0.25 mm and 0.25 µm in length, internal diameter and film thickness respectively. One µL of sample was injected with a split ratio of 400:1 and a temperature of 250°C. The samples were diluted with methanol before injection. The carrier gas was helium with a constant flow of 1 ml min^{-1}. At first, the column temperature was maintained at 40 °C for 5 min and then increased to 240 °C at a heating rate of 10 °C min^{-1}. The identification of the peaks in the chromatograph was achieved by comparing their mass spectrum with those in the spectral library.

3.5 Bubble size measurement

Various methods are available for the measurements of bubble size and bubble size distribution in a liquid phase. These include: optical, acoustical and laser diffraction techniques. Among these techniques, the optical method is the most widely employed in bubble size characterization. Although the accuracy of visual methods can be affected by factors such as the lighting effect, clarity of the liquid medium as well as the software used for bubble analyses (Vazquez et al. 2005), they are straightforward, cost effective and can provide enough information to be used in both industrial applications and laboratory scale studies (Wesley et al. 2016).

An optical method was employed in the current study to determine the bubble size distribution (Wesley et al. 2016). The experiment was conducted in both deionized water and an ethanol-water binary solution. The operating conditions and the tools used for the bubble size distribution analysis are summarized in table 3.10.

Table 3.10: Summary of the operating conditions and the tools used for the bubble size measurement

Tool or condition	***Value or type***
Diffuser type	Point Four diffuser with 20 μm pore size
Fluidic Oscillator	Yes
Feedback Loop Length	25 cm
Air pressure	2 bar
Main Flow rate to the fluidic oscillator	80 L/min
Flow rate to the diffuser	1 L/min
Tank	Glass rectangular tank (21.5×16 × 30.5) in length, width and height respectively
Solution	• Deionized water • 50% vol. ethanol-water solution
Camera type	High speed camera (Photron SA-3)
Lighting source	Halogen lamp, Model no: HM-682°C; 150W Argos, UK

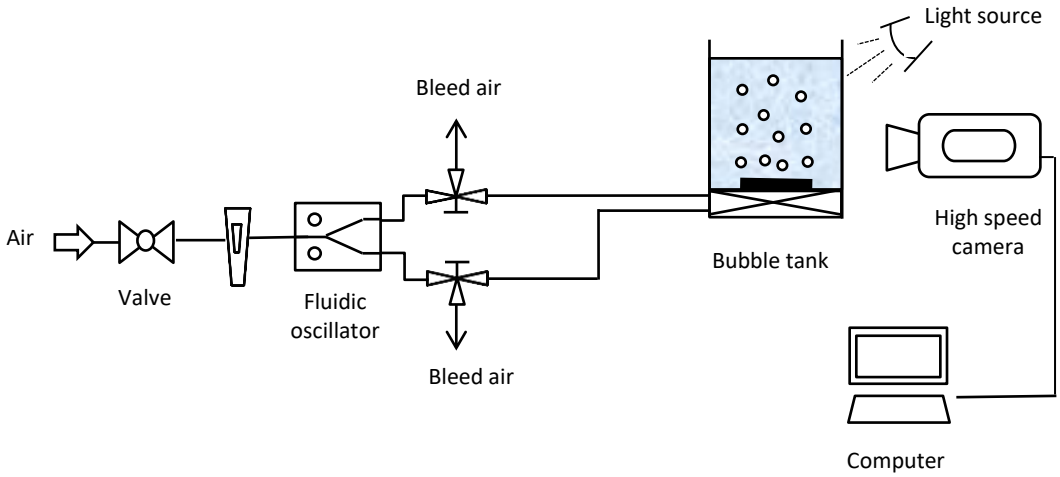

Figure 3.14: Schematic view of the experimental set up for the bubble size measurement.

The photographic bubble imaging system, as presented schematically in figure 3.14, consists of the following elements:

- high speed camera
- lighting source
- rectangular clear glass tank
- air supply
- air flow meter
- computer
- microbubble generation system, including a fluidic oscillator and diffuser

The imaging process was carried out by firstly placing the diffuser in the glass tank, then filling the tank with the required solution. The camera was fixed at a suitable level and distance from the glass tank in which the bubbles were being generated.

To conduct the test, a piece of dark plate was placed beyond the diffuser, with the lighting sources placed beside the camera so as to obtain a sufficient level of clarity in the images. The area of the view was calibrated using a ruler with clear dimensions, allowing the number of pixels equivalent to a certain length to be determined. The high speed camera was set to record at a rate of 2000 frames per second with a 1024×1024 pixel spatial resolution. Snapshots and video images of the bubbling flow were captured and uploaded to the computer for image

analysis. The digital images were then analyzed using digital image processing software (ImageJ) and the results were used to obtain the bubble size distributions for both liquids.

The University Of Sheffield.

Chapter Four

Separation of Binary Mixture

Chapter Four

Separation of Binary Mixture

4.1 Introduction

This chapter is dedicated to the application of microbubble-mediated batch distillation technique for the separation of a binary liquid mixture: ethanol-water (50/50 vol.). The aims were to investigate the efficiency of this new approach in the separation of liquid mixtures and to optimize the factors of the separation process. Experiments under different operating conditions were performed to determine their effect on the separation efficiency of ethanol and on the temperature rise of the binary liquid solution. The experiments were designed in accordance with the central composite rotatable design method (CCRD) in which three parameters were examined: depth of the binary liquid mixture above the microbubble diffuser in the bubble tank, inlet temperature of the air microbubbles entering the bubble tank and time of evaporation. The data obtained were analyzed using multi-variable regression analysis and used to develop an empirical equation representing the recovery efficiency of ethanol as a function of the three operating parameters mentioned above.

This chapter is outlined as follows: in the next section, experimental results of the individual effect of the process variables on the separation efficiency of ethanol and on the temperature rise of the liquid mixture are presented and discussed. A comparison study between bubbles generated under steady flow conditions (without fluidic oscillator) and others generated under oscillatory flow (with fluidic oscillator) conditions are also included. Next, the development of the empirical model, analysis and validation are presented. This is followed by a presentation of the results of the interactive effect of the applied parameters on the objective function. In the last section, a general summary from this study is drawn.

4.2 Results and discussion

The binary ethanol-water system has been tested in accordance with the experimental plan of the CCRD method that was shown in table 3.3. The methodologies employed in this study are

described in section 3.2.3 for the separation procedure and sections 3.4.1 and 3.4.2.2 for the chemical analysis.

4.2.1 The effect of the process operating variables and fluidic oscillator on the separation efficiency

As mentioned earlier, the key variables that impact the efficiency of the separation process are: depth of the solution in the bubble tank, temperature of the air microbubbles and the time required for evaporation. The effect of each of these operating variables, as well as the effect of the fluidic oscillator on the rate of separation of ethanol from the binary ethanol-water liquid solution (50/50 vol.) is discussed below in the following sections.

4.2.1.1 Effect of liquid depth and fluidic oscillator

To investigate the effect of the depth of the liquid mixture in the bubble tank on the separation efficiency of ethanol, the other operating variables (i.e. microbubble air temperature and evaporation time) were kept constant at 90°C and 125 min respectively. Additional experiments were carried out under conditions of continuous flow (i.e. without the use of the fluidic oscillator) to compare their performance. The evaporation percentages were calculated using equation 3.1. The concentration of ethanol in the liquid phase was measured using GC analysis, while the vapor phase was measured using the gas sensor at the end of the experiment for each liquid depth. Experiments were carried out in triplicate and in a random sequence in order to calculate the error bar for each experiment. The results are presented in figures 4.1, 4.2, 4.3 & 4.4 respectively for the evaporation percentage, the concentration of ethanol in the final liquid mixture and concentration of ethanol in the vapor phase at different liquid depths. In these figures the error bars for each experiment represent the standard error.

From the results presented here, it is evident that depth of the liquid mixture has a dramatic effect on both the evaporation rate of the mixture and the removal efficiency of ethanol for conditions both with and without fluidic oscillation.

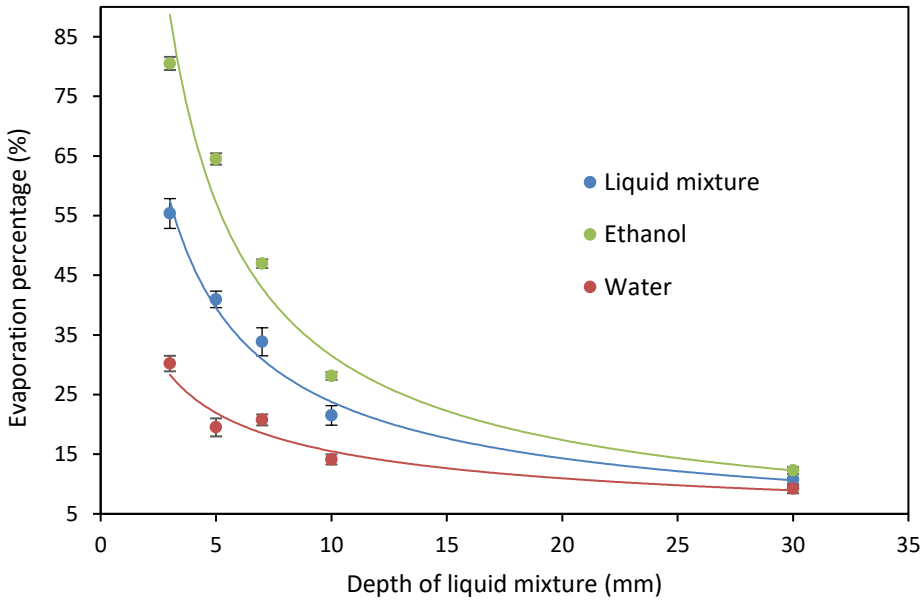

Figure 4.1: Graph of the evaporation percentage of the liquid mixture, the removal efficiency of ethanol and the removal efficiency of water against liquid mixture depth at a microbubble air temperature of 90°C and evaporation time of 125 min. All experiments were carried out with the use of the fluidic oscillator. The error bars represent the standard error.

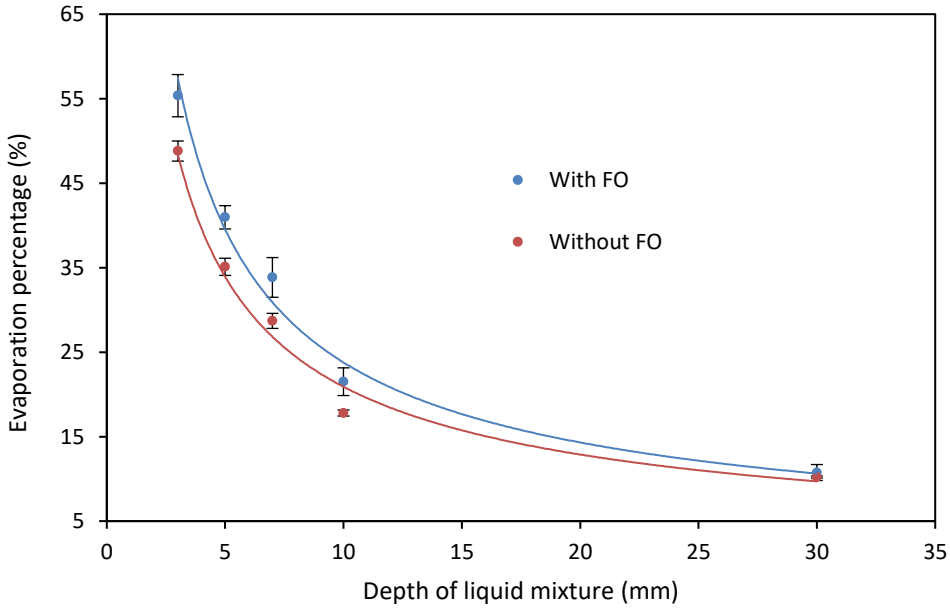

Figure 4.2: Graph of the evaporation percentage of liquid mixture with and without the use of fluidic oscillator (FO) against liquid mixture depth at a microbubble air temperature of 90°C and evaporation time of 125 min. The error bars represent the standard error.

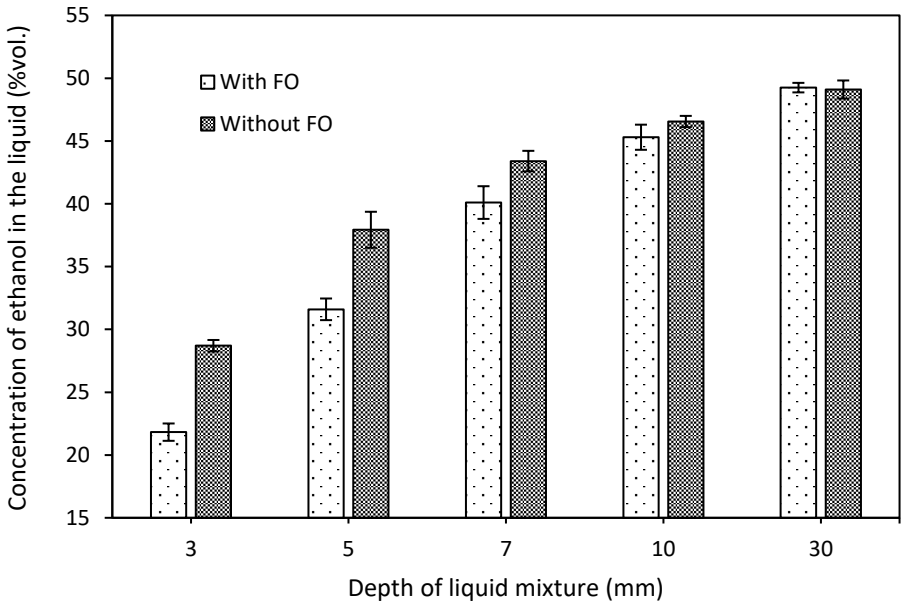

Figure 4.3: Graph of the final concentration of ethanol remained in the liquid phase against liquid mixture depth at a microbubble air temperature of 90°C and evaporation time of 125 min. The error bars represent the standard error.

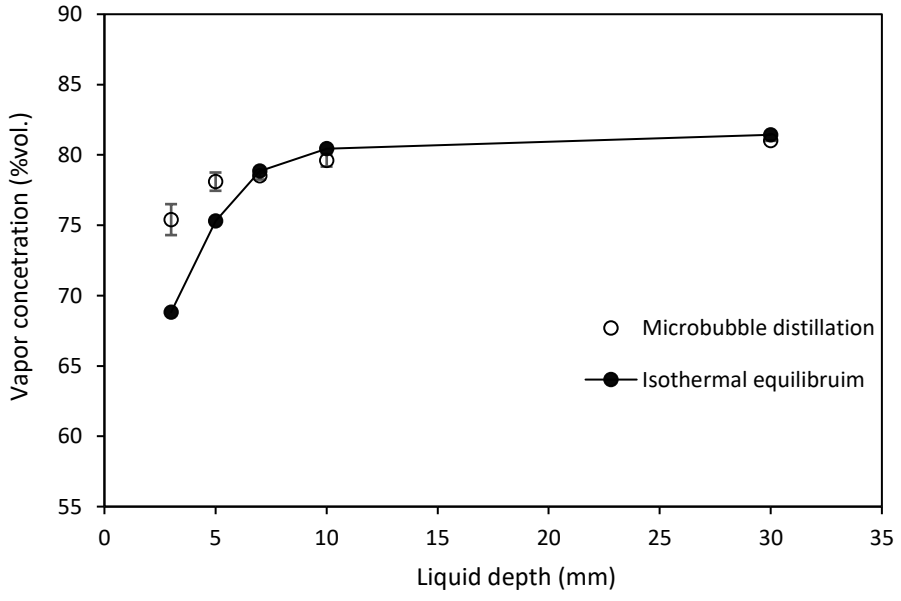

Figure 4.4: Graph of the concentration of ethanol in the vapor phase against liquid mixture depth at a microbubble air temperature of 90°C and evaporation time of 125 min. The error bars represent the standard error.

Figure 4.1 shows clearly that upon decreasing the depth of liquid mixture from 30 mm to 3 mm, the evaporation rate increased dramatically from about 10% to 55% for the liquid mixture, from 12% to 80.5% for ethanol and from 9% to 30% for water, indicating that more liquid is evaporated at lower liquid depths. In figure 4.3, the concentration of ethanol in the liquid was increased with increases in the depth of the liquid mixture layer, indicating that the separation efficiency of ethanol improves at lower liquid levels. The lowest concentration of ethanol in the remaining liquid mixture (21.8% vol.) was achieved at the lowest liquid mixture depth studied in the experiments (i.e. 3 mm), while the highest concentration (about 49% vol.) was obtained at the deepest liquid level (i.e. 30 mm).

The observed increase in the evaporation percentage and decrease in the concentration of ethanol in the liquid phase at low liquid levels can be attributed to the residence time of the microbubbles in the liquid mixture. When hot bubbles are injected into a cold liquid, they transfer their energy to the surrounding mixture in two ways: either as latent heat of evaporation, resulting in an evaporation of the liquid mixture from the surface to the interior of the bubble or as sensible heat transfer, causing a rise in the temperature of the liquid mixture (Riberiro & Lage 2004; Abdulrazzaq et al. 2016). It used to be assumed that the energy transmitted by bubbles is split evenly between heat and mass transfer due to liquid turbulent mixing (Jacobs 1988) and the longer the residence time of the bubbles in the liquid, the greater the vaporization attained as well as the greater the heat transfer (Ribeiro & Lage 2004). However, recent experiments in this field using pure water with microbubbles (Zimmerman et al. 2013) and the present experiments on the ethanol-water binary liquid mixture, have shown that the height of liquid layer in the bubble tank, through which bubbles ascend, or in other words the residence time in the liquid phase, can determine the domination of either of the latent heat or the sensible heat transfer. If the residence time of the bubbles is long in the liquid (i.e. high liquid depths), hot bubbles start to cool as they rise causing a decrease in the vapor pressure of their contents, thereby re-condensing and returning to the outer liquid mixture. However, at shorter bubble residence times, which are associated with thin liquid depths, more separation can be achieved as the re-condensation of vapors can be prevented or minimized (Zimmerman et al. 2013; Abdulrazzaq et al. 2016).

The residence time of bubbles in the liquid mixture can be controlled by altering the depth of the liquid layer through which the bubbles can ascend. Therefore, it seems that there is a critical depth (or critical residence time) through which evaporation increases until it reaches its

maximum value. Beyond this depth, condensation starts causing a loss of the bubble contents. This is most likely the key reason why the evaporation rate of the mixture and the separation efficiency of ethanol is lower at deeper liquid levels compared to their values at shallower liquid levels as the bubble residence time is longer in the case of deeper levels leading to an increase in the likelihood of re-condensation occurring. These results are consistent with the findings of Zimmerman et al. (2013) for the humidification experiments. By injecting hot air microbubbles into pure water, they found that both the evaporation rate of the liquid and the absolute humidity of the outlet air stream increased as the height of the water layer decreased.

Vapor concentration of ethanol was increased from around 75.4% vol. at a liquid level of 3 mm to about 81% vol. at a liquid level of 30 mm as illustrated in figure 4.4. As the final composition of ethanol in the liquid increases with increasing liquid level, the corresponding vapor composition is expected to be increased. The figure also shows a comparison between the vapor concentrations measured by the current experiments and their corresponding concentrations under isothermal equilibrium conditions (Flick 1998). For the liquid depths considered in the experiments, vapor concentrations are almost equal to those attained at equilibrium conditions except those at levels of 3 and 5 mm which show an obvious positive deviation from the equilibrium line. This means that microbubble distillation does not follow the equilibrium principle that dependent by traditional atmospheric distillation for separation. This will be discussing in details in the separation of the azeotropic mixture of ethanol-water whose separation is restricted by the equilibrium hurdle (the next chapter).

Results demonstrate that the use of the fluidic oscillator enhanced the separation efficiency of ethanol from the liquid mixture. The concentrations of ethanol in the liquid phase from the experiments conducted with the fluidic oscillator are lower than those conducted without it as shown in figure 4.3, inferring that more evaporation of ethanol was achieved with the fluidic oscillator. Bubbles generated under oscillatory flow are expected to be smaller in size than those produced under steady flow at the same gas flow rate as discussed before in the literature review (Zimmerman et al. 2011). Compared to fine bubbles, microbubbles have higher surface area to volume ratios, faster mass transport rates and higher residence times in the liquid phase according to Stokes' law (Zimmerman et al. 2013). All these properties render microbubbles more effective than larger bubbles in the separation process.

Although the use of fluidic oscillation provides better separation, the data show that as the liquid depth increased the effect of the fluidic oscillator starts to diminish. At deeper liquid

depths, there would be a greater chance of vapor re-condensation for the microbubbles because of longer contacting times as explained earlier, so the bubble size effect becomes less significant at this stage in the separation process. For this reason, the concentrations of ethanol for both cases become closer and end up equal for the level 30 mm as seen in figure 4.3.

4.2.1.2 Effect of microbubble air temperature and fluidic oscillator

Values of the evaporation rate and ethanol compositions in both liquid and vapor phases were measured while changing the temperature of the injected air to the bubble tank. The liquid level and the evaporation time were kept constant at 7 mm and 125 min respectively according to the experimental plan designed by the CCRD method. Figures 4.5, 4.6 & 4.7 show respectively the results for the evaporation rate and the final concentrations of ethanol in the liquid and vapor phases.

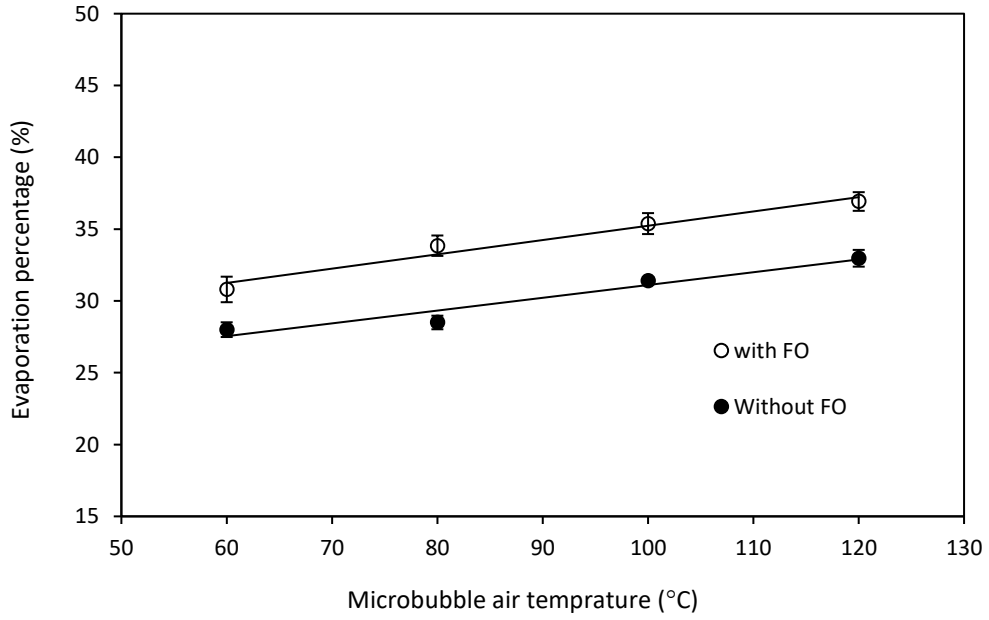

Figure 4.5: Graph of the evaporation percentage of liquid mixture against microbubble air temperature at a liquid depth of 7 mm and an evaporation time of 125 min. The error bars represent the standard error.

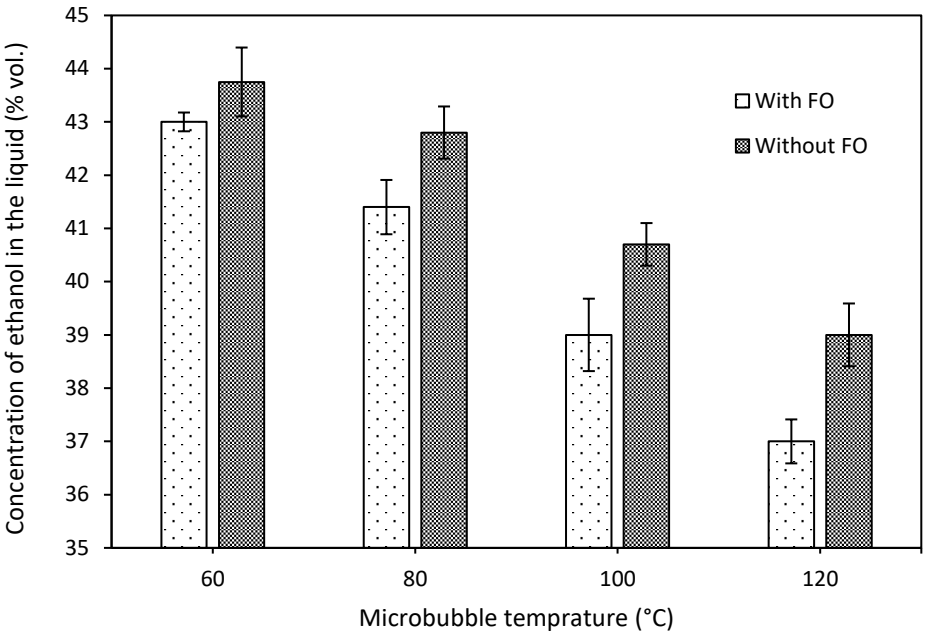

Figure 4.6: Graph of the concentration of ethanol in the liquid phase against microbubble air temperature at a liquid depth of 7 mm and an evaporation time of 125 min. The error bars represent the standard error.

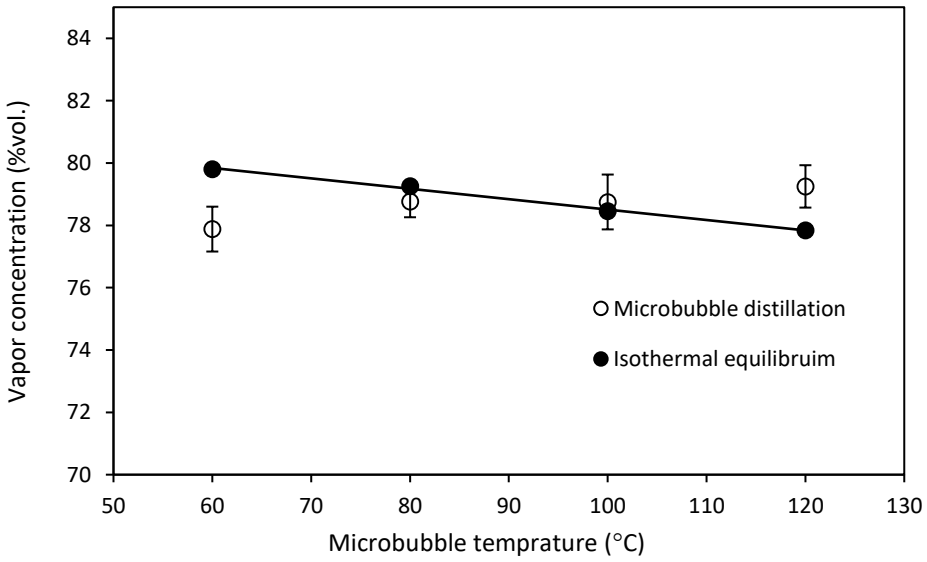

Figure 4.7: Graph of the concentration of ethanol in the vapor phase against microbubble air temperature at a liquid depth of 7 mm and an evaporation time of 125 min. The error bars represent the standard error.

As shown in these figures, increasing the initial temperature of air microbubbles leads to an augmentation of both the evaporation rate and the separation efficiency of ethanol from the liquid mixture. Increasing the microbubble air temperature from 60 to 120 °C causes an increase in the evaporation rate from about 30.8 to 36.9% and a decrease in the final concentration of ethanol in the liquid from 43 to 37% vol. as shown in figures 4.5 and 4.6. These values are respectively changed from 77.8% to around 79.25% vol. for the vapor concentration as shown in figure 4.7. Here also, data with the involvement of the fluidic oscillator show improved efficiency compared to those without it.

This can be understood by considering the amount of available energy for the injected air microbubbles. For molecules of the liquid to evaporate, they need to possess sufficient kinetic energy to escape from the liquid phase to the gaseous phase. Since kinetic energy varies directly with temperature, evaporation is expected to proceed more quickly at higher liquid temperatures and this is what happens at higher microbubble temperatures. Increasing the temperature of the injected microbubbles will increase the energy carried by the gas phase, thus more sensible heat will be transferred to the liquid phase causing an increase in its temperature. Higher liquid temperatures increase the kinetic energy of its molecules which consequently lead to an increase in the fraction of the evaporated liquid solution to the bubble phase (Abdulrazzaq et al. 2016). This is in agreement with the previous results obtained from a direct contact evaporation using an air-water system (Ribeiro & Lage 2004). An augmentation in the rate of evaporation of the liquid phase due to an increase in its temperature during the evaporation process was reported. Likewise, increasing the bubble temperature will increase the saturation vapor pressure at the gas-liquid interface which is the main driving force for evaporation of the components. As a result of this, a greater quantity of ethanol is expected to evaporate at higher bubble temperatures which would lead to a reduction in its concentration in the remaining solution whilst raising its concentration in the vapor phase (figure 4.7).

4.2.1.3 Effect of evaporation time and fluidic oscillator

Data for the evaporation rate and the final concentrations of ethanol in liquid and vapor mixtures under three tested evaporation times: 50 min, 125 min, and 200 min are plotted in figures 4.8, 4.9 & 4.10 respectively.

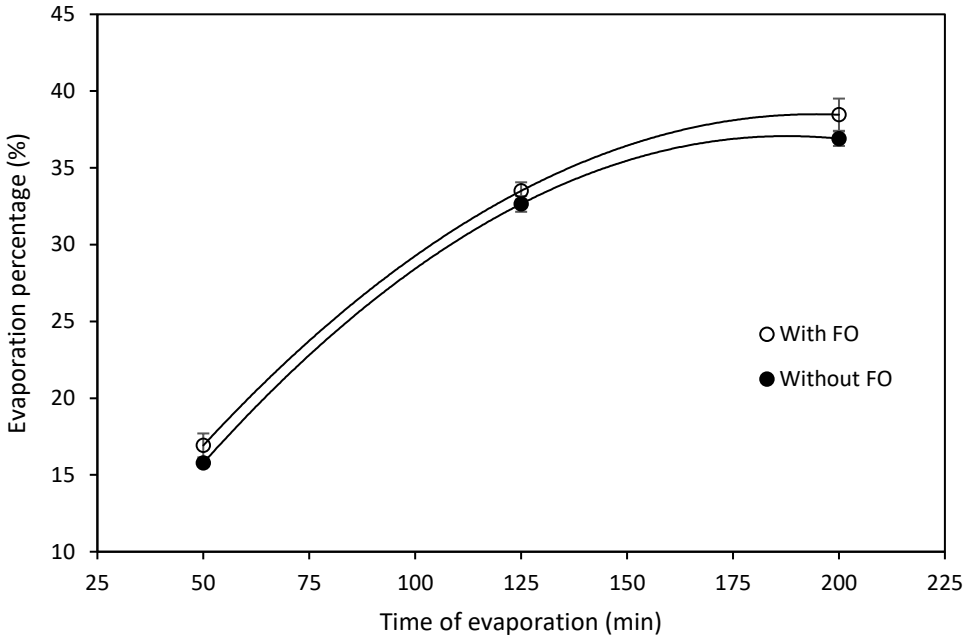

Figure 4.8: Graph of the evaporation percentage against evaporation time at a liquid depth of 7 mm and microbubble air temperature of 90°C. The error bars represent the standard error.

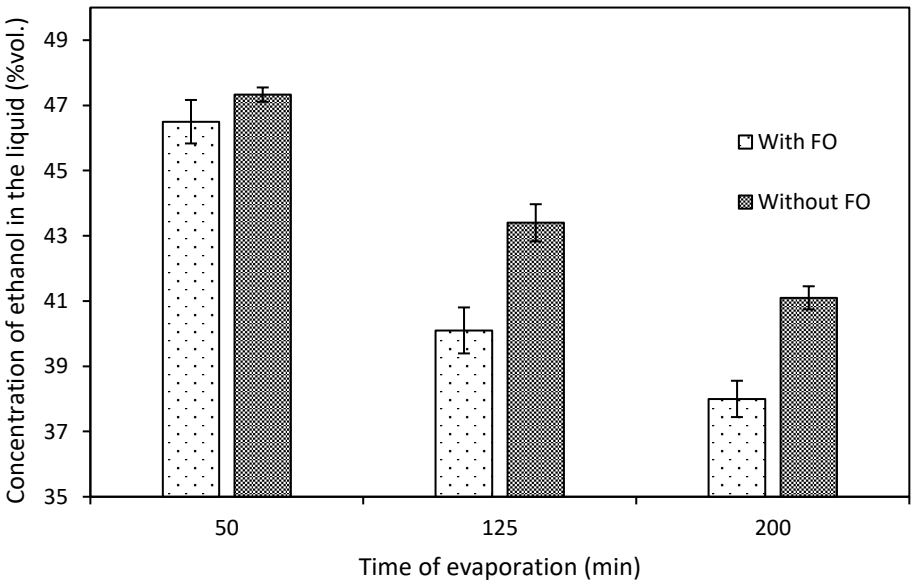

Figure 4.9: Graph of the concentration of ethanol in the liquid phase against evaporation time at a liquid depth of 7 mm and microbubble air temperature of 90°C. The error bars represent the standard error.

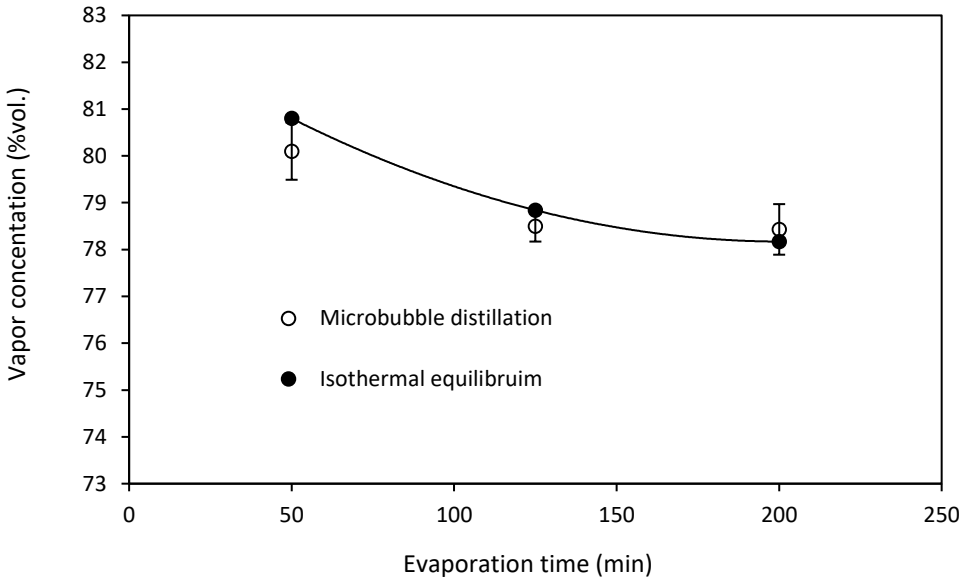

Figure 4.10: Graph of the concentration of ethanol in the vapor phase against evaporation time at a liquid depth of 7 mm and microbubble air temperature of 90°C. The error bars represent the standard error.

The results reveal that both evaporation percentage and ethanol recovery increase as the time available for evaporation increases. As the evaporation time progressed from 50 to 200 min, the evaporation percentage rose from 17% to 38.5% whilst the ethanol liquid composition dropped from 46.5% vol. to 38% vol. Ethanol vapor composition changed from about 80% vol. at an evaporation time of 50 min to nearly 78.4% vol. at a time of 200 min. The vapor data are approximately equal to those observed at isothermal equilibrium conditions.

The amount of liquid evaporated from the skin to the interior of the bubble is directly proportional to the saturation vapor pressure of its components and hence increases with liquid temperature (Ribeiro & Lage 2004). As the time for evaporation progressed, the temperature of the liquid mixture increases due to a transfer of energy from both the hot bubbles and the system itself. Increasing the temperature of the liquid phase causes an increase in the levels of vapor pressure of its components, and hence on the quantities that are evaporated. Additionally, when the liquid was heated, the motion of its molecules increased because of the kinetic energy levels increased. In this state, evaporation rates could rise as the molecules of the liquid have more energy which facilitates their evaporation or escape from the liquid phase to the bubble phase.

4.2.2 The effect of the process operating variables and fluidic oscillator on the temperature of the liquid mixture

The effect of each of the operating variables on the temperature of the binary liquid mixture is discussed in the following sections.

4.2.2.1 Effect of depth of the liquid mixture and fluidic oscillator

The effect of the depth of the liquid mixture, both with (WFO) and without (WOFO) the use of the fluidic oscillator, on the temperature rise of the liquid mixture was investigated and the results are presented in figure 4.11. The microbubble air temperature and evaporation time were kept constant at 90 °C and 125 min respectively in all experiments in accordance with the CCRD experimental design matrix that is shown in table 3.3.

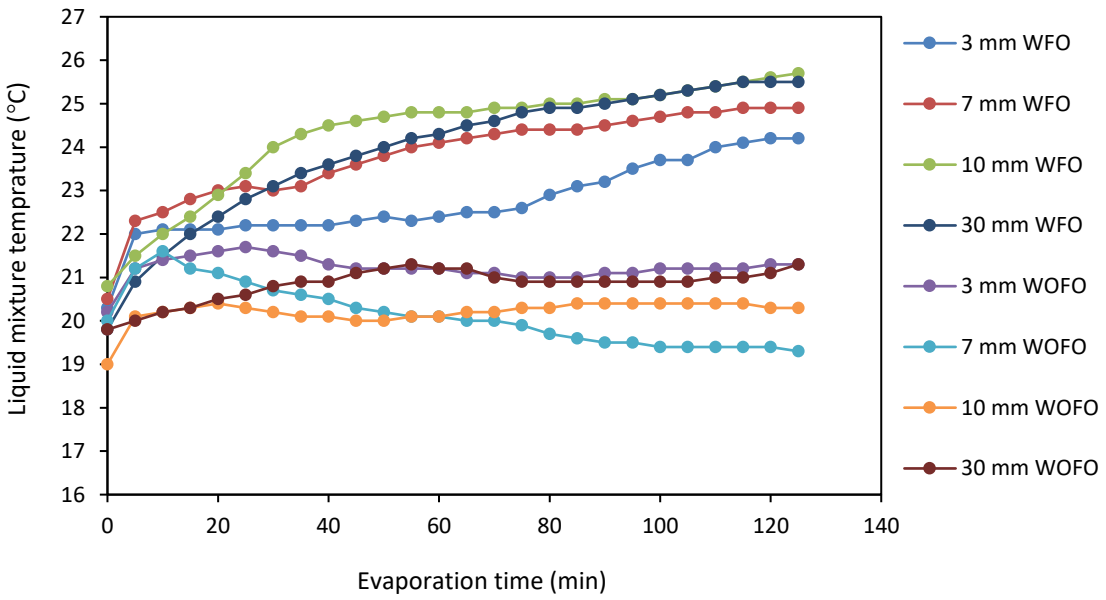

Figure 4.11: Graph of the temperature of the liquid mixture against evaporation time for different liquid depths at a microbubble air temperature of 90 °C and an evaporation time of 125 min. WFO represents the tests performed with the fluidic oscillator while WOFO refers to the tests performed without the fluidic oscillator.

The temperature of the liquid mixture shows an obvious increase with time in all the experiments that incorporated use of the fluidic oscillator whilst a non-monotonic behavior of the liquid temperature was noticed for all experiments without fluidic oscillation. The most likely influence that contributes to this outcome is bubble size. As stated before, fluidic oscillation affects bubble size by facilitating earlier detachment from the orifice of the diffuser prior to the critical stage (i.e. hemispherical shape). In contrast, bubbles continue to grow under conditions of continuous flow (without fluidic oscillator) and the detachment occurs at a comparatively later stage when the bubbles are several orders of magnitude larger than the exit pore (Zimmerman et al. 2008).

As mentioned before, large bubbles have slower mass and heat transfer rates, so in this scenario, they cannot exploit all their supplied energy for either heating or evaporation and they drag the latent heat of vaporization from the ambient solution rather than from their confined internal energy which consequently leads to a decrease in the liquid temperature (evaporative cooling) (Zimmerman et al. 2013).

Another possible reason for this behavior is that in the case of microbubbles, there is a greater chance for the liquid to contact the diffuser and absorb some of its heat from the spaces between the small generating bubbles. However, with larger bubbles generated without fluidic oscillation, the attachment between the liquid and the diffuser would be weaker as bubbles spread on larger areas (Zimmerman et al. 2008) and thus serve as an insulator between the liquid and the diffuser causing less heat to be transferred to the liquid.

For the tests with the fluidic oscillator, the temperature profiles for the liquid levels considered here show some level of heating with minimum rise in the liquid mixture temperature observed at the lowest liquid depth (i.e. 3 mm). This indicates that maximum separation for ethanol could be obtained with the minimum increase in liquid temperature. The reason behind this outcome is related to the residence times of microbubbles in the liquid mixture. According to the theory of the current study, if the residence time of microbubbles in the liquid is high, re-condensation of bubble vapors will occur leading to a rise in the liquid temperature due to the release of sensible heat accompanying the condensation process. In contrast, for shorter residence times, evaporation occurs first and condensation can be minimized since the bubble leaves the liquid before getting cooler.

A more pronounced difference in the temperature rise of the liquid between the different liquid depths might have been expected. However, it seems that heat leakage from the base of the bubble tank (the aluminum base plus the ceramic diffuser) tends to reduce the clarity of this effect. Certainly, the hot air flow through the tank is responsible for increasing the temperature of the aluminum base and consequently that of the liquid above it. This effect was demonstrated by using the same diffuser but with a 3-D printing holder. A marked decrease in the liquid temperature during evaporation was recorded (see figure 3.3).

4.2.2.2 Effect of microbubble air temperature

The effects of four microbubble air temperatures on the temperature of liquid mixture during the experiment are shown in figure 4.12. The results indicate that the higher the temperature of the air microbubbles, the higher the temperature rise of liquid mixture from its initial value.

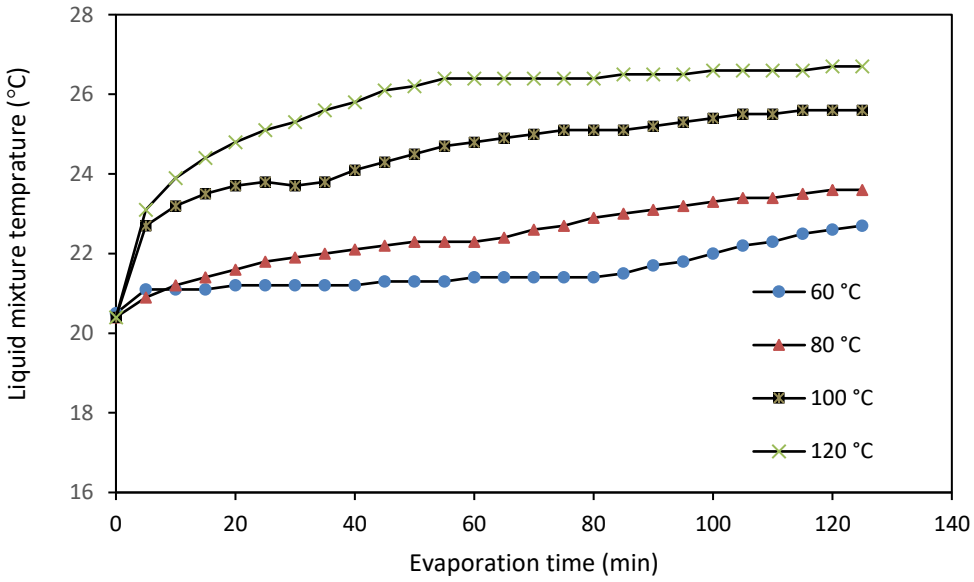

Figure 4.12: Graph of the temperature of the liquid mixture against evaporation time for different air microbubble temperatures at a liquid depth of 7 mm and evaporation time of 125 min.

This trend can be explained by considering the energy of the injected bubbles. As mentioned before, increasing the temperature of the microbubbles will increase the energy of the bubble

as well as increasing the temperature of the tank itself. Thus more sensible heat will be transferred to the liquid causing an increase in its temperature.

4.2.2.3 Effect of evaporation time

Figure 4.13 presents the liquid temperature time profiles at different evaporation times (50, 125 and 200 min). It can be observed that the temperature of liquid increased with time during each experiment until it reached a steady state value of around 25°C.

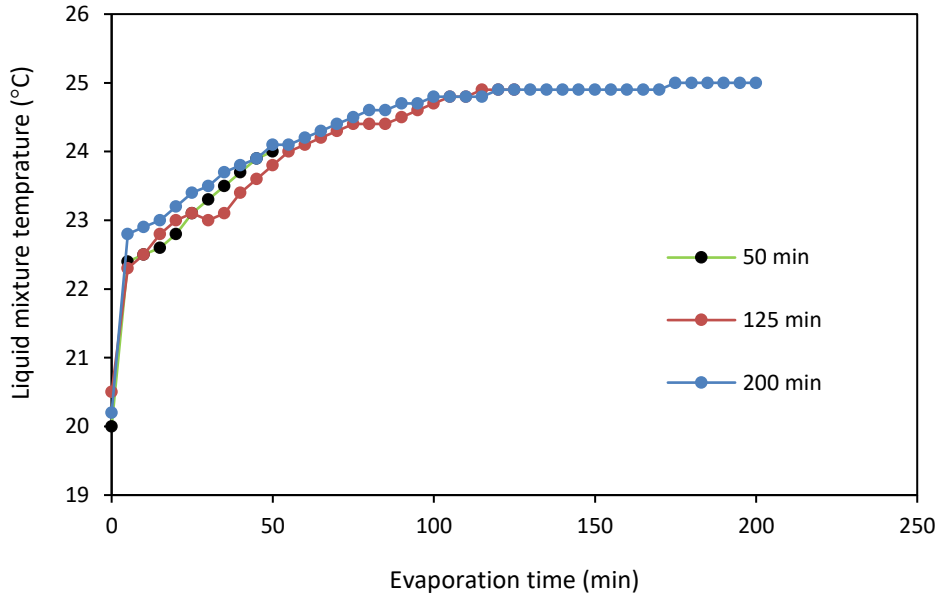

Figure 4.13: Graph of the temperature of the liquid mixture against evaporation time at a liquid depth of 7 mm and microbubble air temperature of 90 °C.

As has been reported in the literature earlier, when hot bubbles are injected into a liquid, the temperature of the liquid starts to rise until it reaches a quai-steady state at which the temperature and the rate of evaporation of the liquid stay approximately constant (Ribeiro & Lage 2004). The results in figure 4.13 indicate that this quasi-steady state regime was attained after about 120 min of evaporation after which the temperature of the liquid mixture is almost constant and most of the energy associated with the bubbles is expected to be used for evaporation, with a small portion of the sensible heat being used to compensate the heat wastage from the system.

4.3 Effect of the humidity of the injected air and the presence of bubbles on the separation efficiency

To better understand the performance of applying "bone dry" air microbubbles on the efficiency of stripping ethanol from the liquid mixture, additional experiments were performed with no bubbles (natural evaporation), and also with humid air microbubbles with relative humidity of around 30% at different liquid levels to compare their effects. Experimental conditions such as microbubble air temperature and evaporation time were kept constant at 90 °C and 125 min respectively for these experiments. The humidity of the air supply was measured by RS Pro Thermo-hygrometer (RS 725-9678) handheld meter. Figures 4.14 and 4.15 compare the results to each separation mode for the evaporation rate and final concentration of ethanol in the liquid mixture respectively.

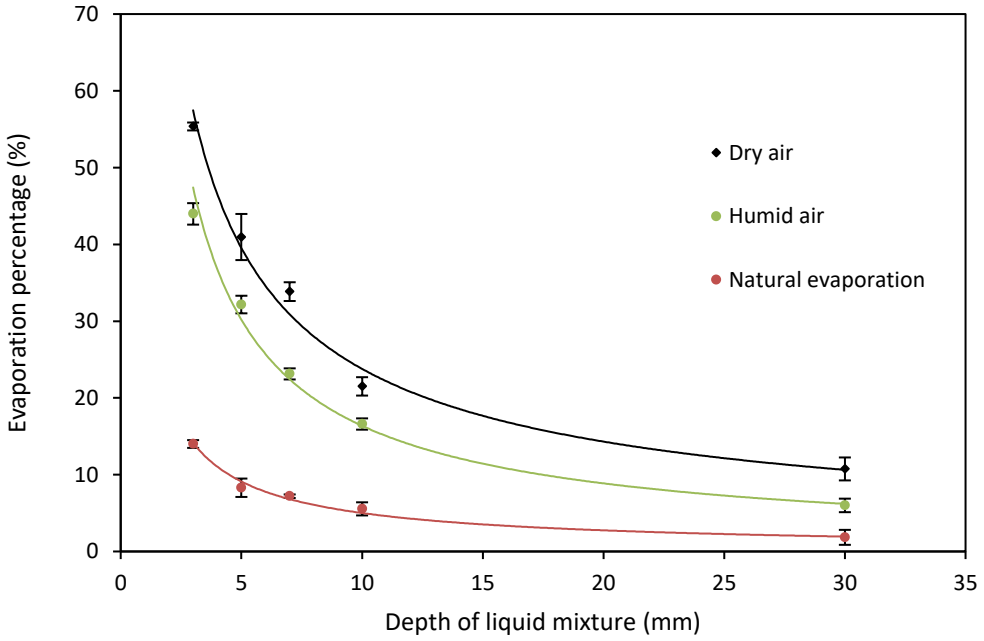

Figure 4.14: Graph of the evaporation percentage against depth of liquid mixture for different separation modes at a microbubble air temperature of 90°C and an evaporation time of 125 min. The error bars represent the standard error.

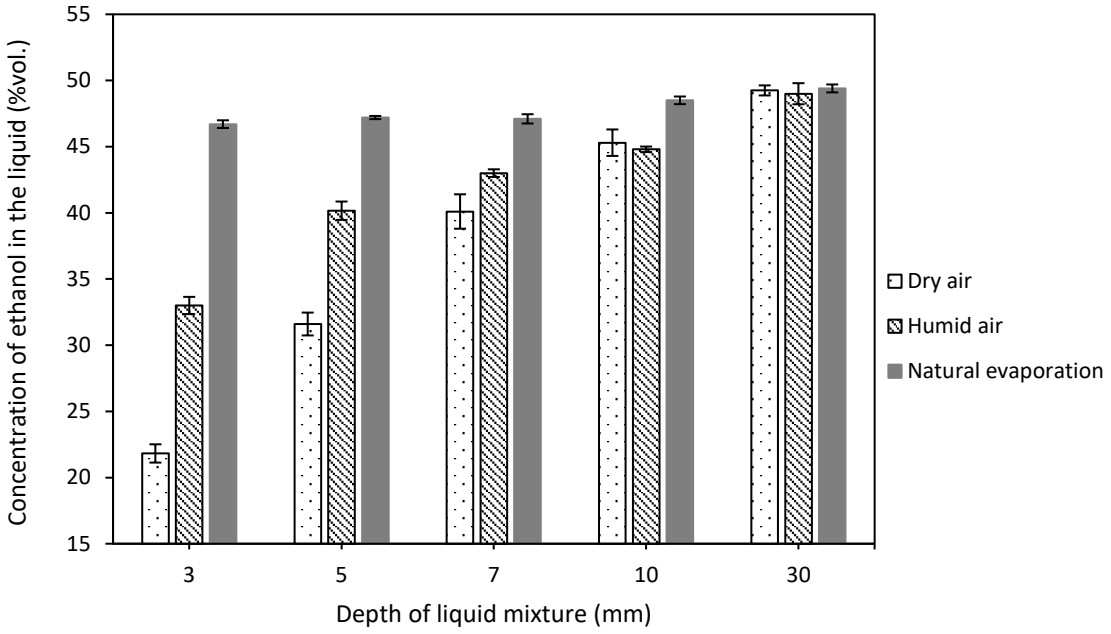

Figure 4.15: Graph of the concentration of ethanol against microbubble air temperature at a microbubble air temperature of 90°C and an evaporation time of 125 min. The error bars represent the standard error.

From the results presented it seems that the application of dry hot bubbles is more effective than the other modes considered for all liquid heights investigated in this test. This effect becomes more pronounced at lower liquid depths. The slight moisture content of air microbubbles causes them to evaporate less ethanol than those with initially dry conditions. With dry hot air microbubbles, an evaporation rate of 55% and an ethanol concentration of 21.8% vol. were recorded at 3 mm liquid depth. Humid air microbubbles showed a lower evaporation rate of about 43.8% and higher ethanol concentration of 33% vol. compared to only 14% and 46.7% vol. respectively obtained with no bubbles at the same liquid level.

4.4 Effect of air flowrate

Additional experiments were carried out at two air flowrates 0.5 & 2 L/min in order to clarify their effects on the separation efficiency of ethanol. The depth of liquid mixture and the initial temperature of the microbubbles were fixed at 7 mm and 90° C respectively. The initial concentration was 50% vol. ethanol for all these tests.

As the gas flow rate increases, the evaporation percentage of the liquid mixture increases accordingly. The evaporation percentage increased from 21.2% to 53.8% as air flow rate increased from 0.5 to 2 l/min as shown in figure 4.16.

Figure 4.17 shows that the concentration of ethanol in the liquid mixture was lower at higher supply flow rates. While it was dropped to 46% at 0.5 l/min, its concentration was only 29.1% at 2 l/min.

The time profiles of liquid temperature related to each flow rate is given at figure 4.18. As evident from the results, the rise in the temperature is higher at lower air flow rates. Liquid temperature was increased by around 4.5°C and 5°C at 2 l/min and 1 l/min respectively. The temperature rise, however, was by about 7°C when the air flow rate was 0.5 l/min. This effect could be related to the difference in the bubble size distribution between these cases. Bubble sizes raise proportionally with gas flow rate at constant pressure (Hanotu et al. 2013) because of growing the coalescence frequencies (Ribeiro & Lage 2004). Since larger bubbles have poor internal mixing as discussed before, latent heat of vaporization is dragged from the liquid side causing the cooling effect. Bearing in mind is that increasing gas flow rates also increases the bubble flux which leads in turn to enhance the evaporation efficiency as proved in figures 4.16 and 4.17.

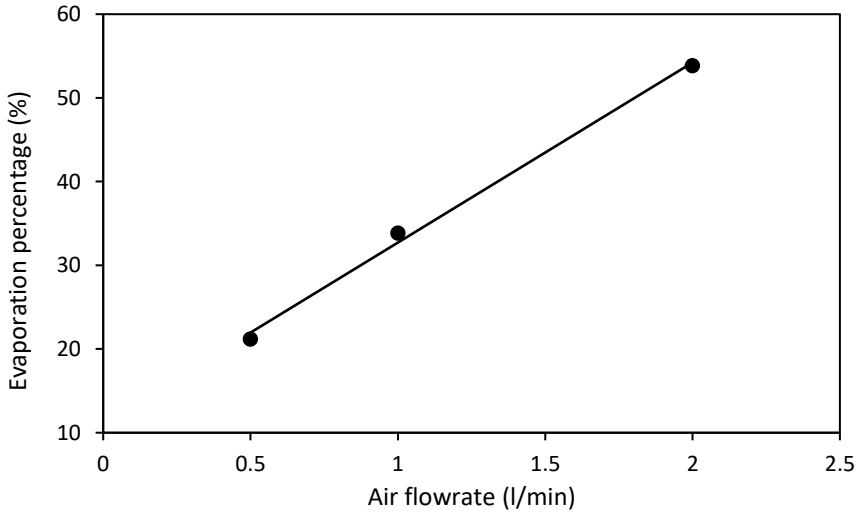

Figure 4.16: Plot of the evaporation percentage of the liquid mixture against air flowrate.

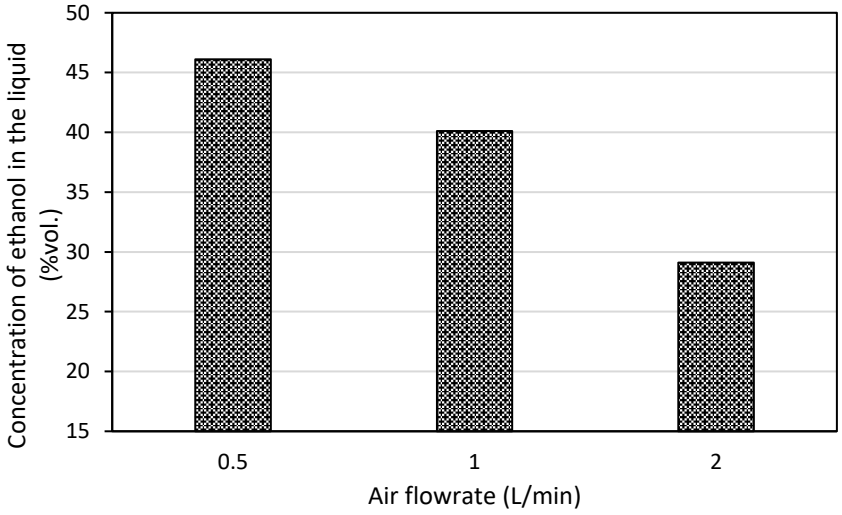

Figure 4.17: Plot of the final concentration of ethanol in the liquid mixture against air flowrate.

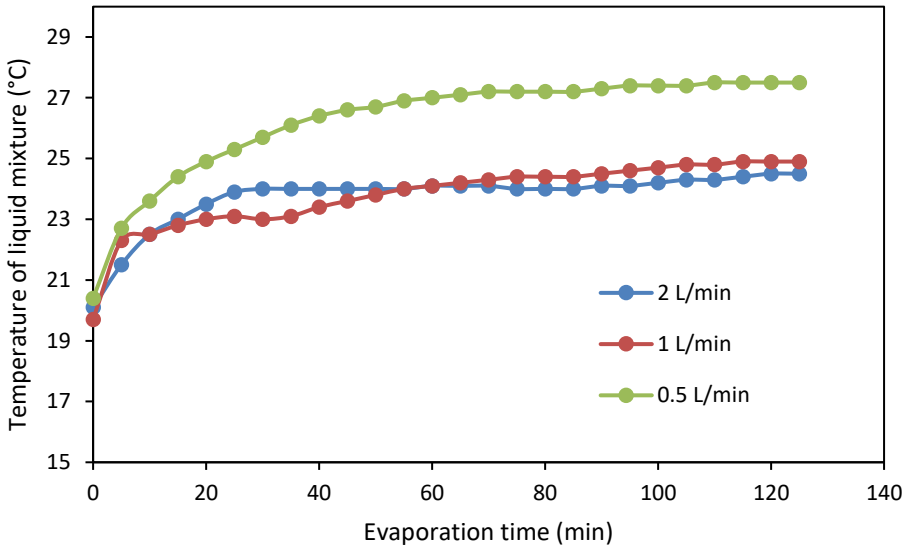

Figure 4.18: Time profiles of the liquid mixture for different air flowrates.

4.5 Results of bubble size analysis

The results in the current study were obtained in accordance with the materials and methods that were described in section 3.5. Bubble size was measured in water as well as in the 50% vol. ethanol-water mixture using a Point Four ceramic diffuser with a pore size of 20 µm. The resulting bubble size distributions are shown in figure 4.19.

Generally, bubbles produced in water are larger than those produced in the ethanol-water solution under the same operating conditions. This can be attributed to the difference in the

interfacial surface tension between the two liquids (73 & 22 mN/m for water and ethanol respectively at 20°C). The bubble size distribution of ethanol-water solution has almost a single dominant peak, indicating the presence of nearly mono size, non-coalescent bubbles in the liquid medium. The results show that more than 60% of the bubbles are below 200 μm in the ethanol-water solution.

(a)

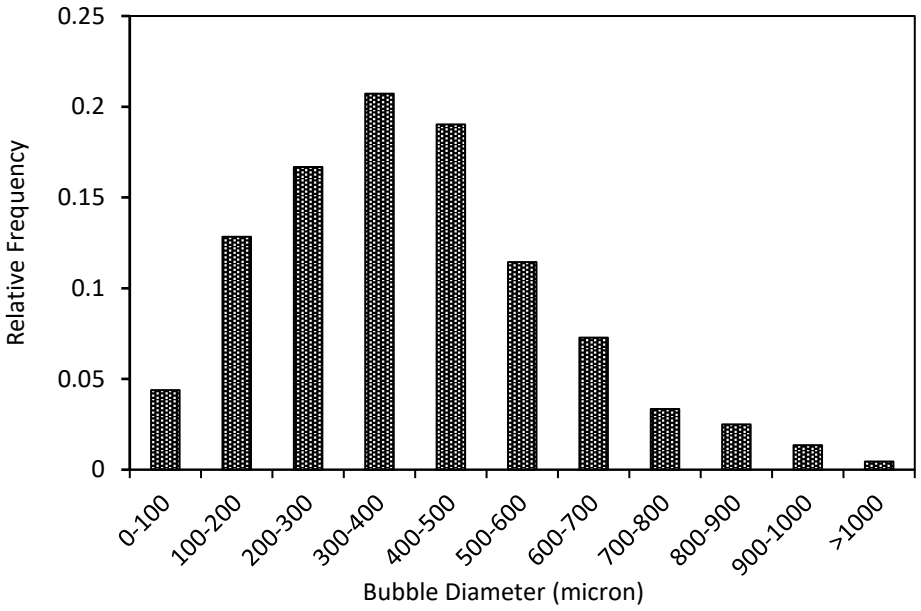

(b)

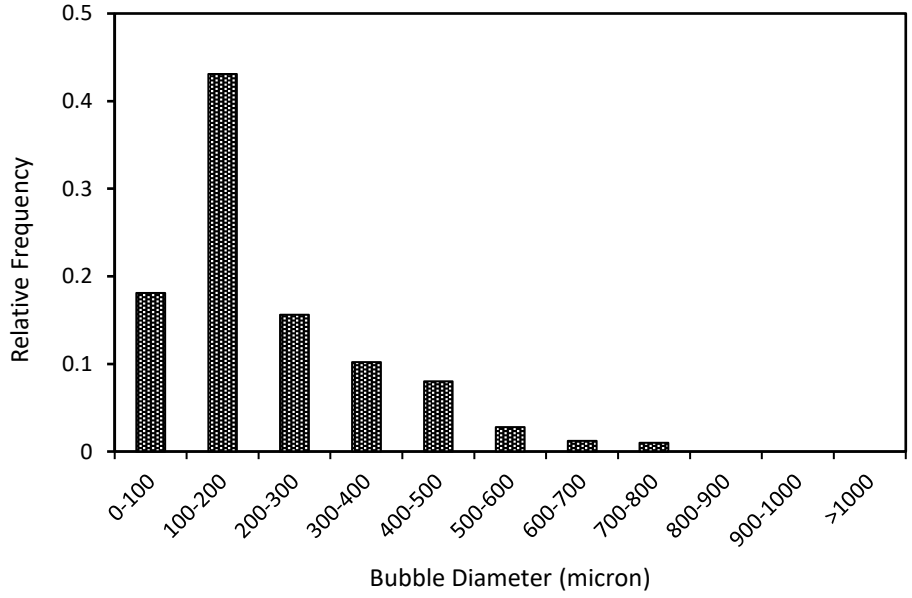

Figure 4.19: Graph of bubble diameter versus relative frequency for the analysis of images taken for bubbles generated in (a) pure water and (b) 50% vol. ethanol-water solution under oscillatory flow.

4.6 Model development using a central composite rotatable design method (CCRD)

The data obtained from the separation of the ethanol-water binary mixture has been used to generate a second order response model which expresses the recovery efficiency of ethanol from the liquid mixture as a function of the three operating variables of the system, namely: temperature of air microbubbles (x_1), depth of liquid mixture layer in the bubble tank (x_2), and time of evaporation (x_3). Five levels for each variable (x_1, x_2, and x_3) were selected for conducting the experiments. The selected levels for each variable together with their coded values are given in table 4.1.

Table 4.1: Independent variables with their real and coded levels

Temperature of air microbubbles (℃)	*Depth of liquid mixture (mm)*	*Time of evaporation (min)*	*Code value*
80	3	50	-1.682
84	4	80	-1
90	7	125	0
96	9	170	+1
100	10	200	+1.682

A multiple stepwise regression analysis was performed using a standard statistical package program, MINITAB 17 to estimate the polynomial coefficients of the quadratic multivariable model whose values are displayed in table 4.2.

Equation 4.1 shows the fitted regression model that describes the system, considering the single and interactive effects of the main factors:

$$Y = 46.7694 + 1.2029x_1 - 16.49374x_2 + 11.8223x_3 - 0.2036x_1x_2 + 0.2464 x_1x_3 - 1.3591x_2x_3 + 0.1691{x_1}^2 + 2.6319{x_2}^2 - 3.5596{x_3}^2 \quad (4.1)$$

where Y is the percentage recovery efficiency of ethanol, x_1, x_2 and x_3 represent the coded ranges (between -1.682 and 1.682) of the microbubble air temperature (°C), liquid mixture depth (mm) and evaporation time (min) respectively.

Table 4.2: The estimated regression coefficients for the empirical model

Regression coefficients	***Estimated values***
β_0	46.7694
β_1	1.2029
β_2	-16.4937
β_3	11.8223
β_{11}	0.1691
β_{22}	2.6319
β_{33}	-3.5596
β_{12}	-0.2036
β_{13}	0.2464
β_{23}	-1.3591

A positive sign for the regression coeffients β_1 & β_3 in the quadratic model (Eq. 4.1) indicate that the removal efficiency of ethanol from the liquid mixture increases as the levels of the factors x_1 (temperature of air microbubbles) and x_3 (time of evaporation) increase. On the other hand, a negative sign for the regression coefficient β_2, signals that there is an increase in the separation effeciency of ethanol as the level of factor x_2 (depth of liquid mixture) decreases. Since the parameter x_2 has the the greatest coeffient (β_2= 16.4937) compared to the other parameters (x_2 and x_3) in the fitted model, it is reasonable to conclude that the height of liquid phase is the major repressive variable that affects the response. This means that the removal efficiency of ethanol from the liquid mixture can be controlled more effectively by changing the height of the liquid mixture in the bubble tank, instead of by changing the other parameters (i.e. temperature of the air microbubbles and the evaporation time).

In order to validate the model developed, it is necessary to compare the observed values from the experiments with those estimated from the equation. The model developed (Eq. 4.1) was used to calculate the estimated values for the recovery of ethanol from the liquid mixture while the observed values were obtained from the experimental data. The results are presented in table 4.3 which shows a comparison between the observed values with those estimated from the empirically developed model. The observed and estimated data are plotted in figure 4.20

which demonstrates that the fitted values from the central composite design model are close to the experimental values.

Table 4.3: Estimated and observed values of the removal efficiency of ethanol from the liquid mixture

Run no.	***Actual levels of variables***			***Removal efficiency of ethanol (%)***	
	Inlet air temperature (°C)	***Height of liquid layer (mm)***	***Time of evaporation (min)***	***Observed***	***Estimated***
1	84.1	4	80.4	46.5	48.2
2	95.9	4	80.4	48.7	50.5
3	84.1	9	80.4	15.4	18.3
4	95.9	9	80.4	16.7	19.8
5	84.1	4	169.6	77.0	74.0
6	95.9	4	169.6	80.1	77.3
7	84.1	9	169.6	40.4	38.7
8	95.9	9	169.6	42.7	41.2
9	80	7	125	45.1	45.2
10	100	7	125	49.6	49.3
11	90	3	125	80.5	81.9
12	90	1	125	28.1	26.5
13	90	7	50	22.4	16.8
14	90	7	200	51.2	56.6
15	90	7	125	46.4	46.8
16	90	7	125	47.0	46.8
17	90	7	125	46.8	46.8
18	90	7	125	47.0	46.8
19	90	7	125	46.5	46.8
20	90	7	125	47.0	46.8

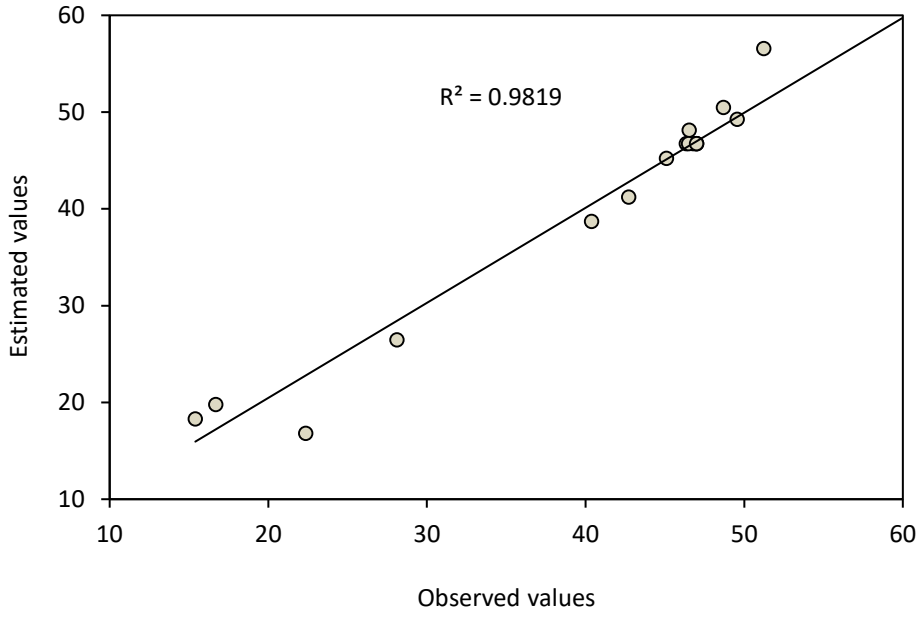

Figure 4.20: Graph of the estimated values versus the observed values of the recovery efficiency of ethanol from the liquid mixture.

4.6.1 Effect of liquid depth and microbubble air temperature on the removal efficiency of ethanol

In order to gain a better understanding of the results obtained, the relative effect of the interaction of the variables on the objective function was studied. Interaction means that the effect created by changing the level of one independent variable depends on the level of the other variable. The combined effect of the process variables is presented using three-dimensional response surface figures which have been plotted using MATLAB software.

In this section, the effect of liquid depth and microbubble air temperature on the removal efficiency of ethanol from the liquid mixture has been studied. The response is shown in figure 4.21. The evaporation time was kept constant at its central level (i.e. 125 min).

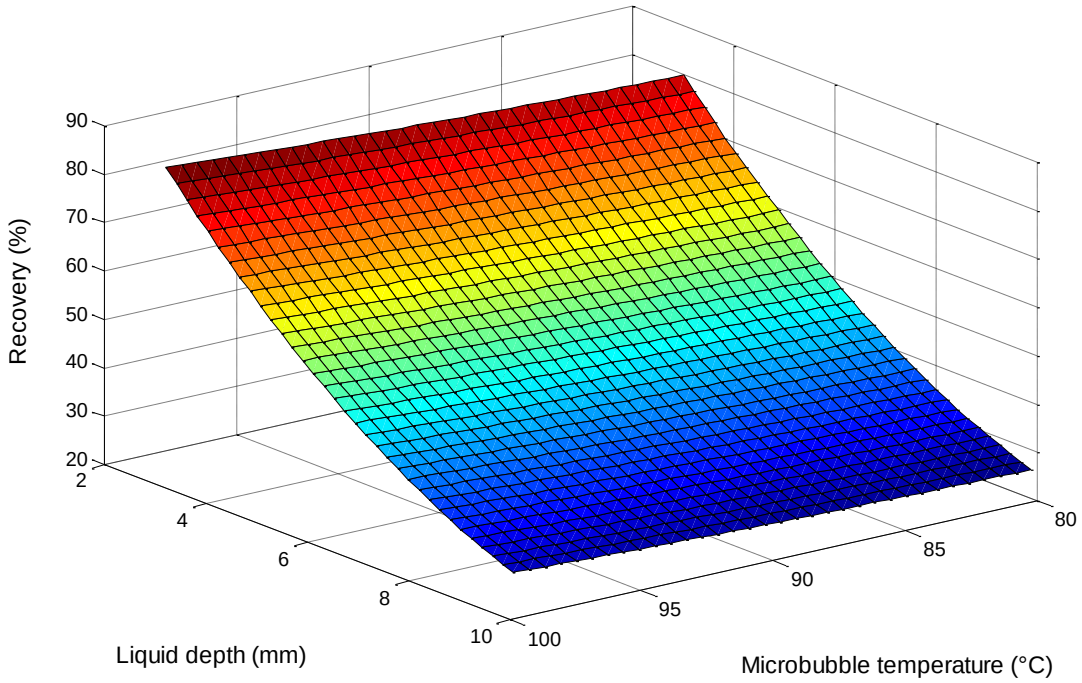

Figure 4.21: Response surface predicting removal efficiency of ethanol from the model equation: effect of liquid level and microbubble air temperature.

As can be seen, ethanol recovery depends more on the liquid depth than on the microbubble air temperature. In the regression model, x_2 has greater coefficient than x_1, in addition there is weak interaction between them ($\beta_{12} = -0.2036$). The negative sign of the interaction coefficient implies that higher recovery performance for ethanol can be achieved by maintaining shallow liquid depths and high microbubble air temperatures. The explanations of the individual effects of each of these factors have already been discussed earlier in this chapter.

According to the quadratic model, reducing the depth of the liquid mixture from 10 mm to 3 mm while maintaining the microbubble air temperature at its lowest value (i.e. 80°C), leads to an increase of about 213% in the removal efficiency of ethanol. However, only 6.5% improvement can be obtained in the recovery efficiency by increasing the microbubble air temperature from 80 to 100°C at the liquid level of 3 mm.

Since the current approach involves manipulating thermo-chemically unstable liquids (i.e. bio-oils) and taking into the consideration the huge difference in the stripping efficiency of ethanol between these two factors, applying high temperatures is not favourable. Higher bubble temperatures cause a higher increase in the liquid temperature (see figure 4.12). Furthermore,

it is important to consider the economic aspects of the process. If high temperatures have to be employed, more energy and more safety precautions would be required. Therefore, it is highly favourable and recommended to improve the removal efficiency of ethanol by reducing the liquid mixture level rather than by increasing the inlet microbubble temperature.

4.6.2 Effect of microbubble air temperature and evaporation time on the removal efficiency of ethanol

The combined effect of both the microbubble air temperature and the evaporation time on the separation efficiency of ethanol at the zero level of the liquid depth (i.e. 7 mm) is presented in figure 4.22 as a 3-D response surface. It is clear that the recovery efficiency of ethanol increases by increasing both the initial temperature of the microbubbles and the time of evaporation the effect that is also demonstrated by the positive sign of their interaction coefficient in the model.

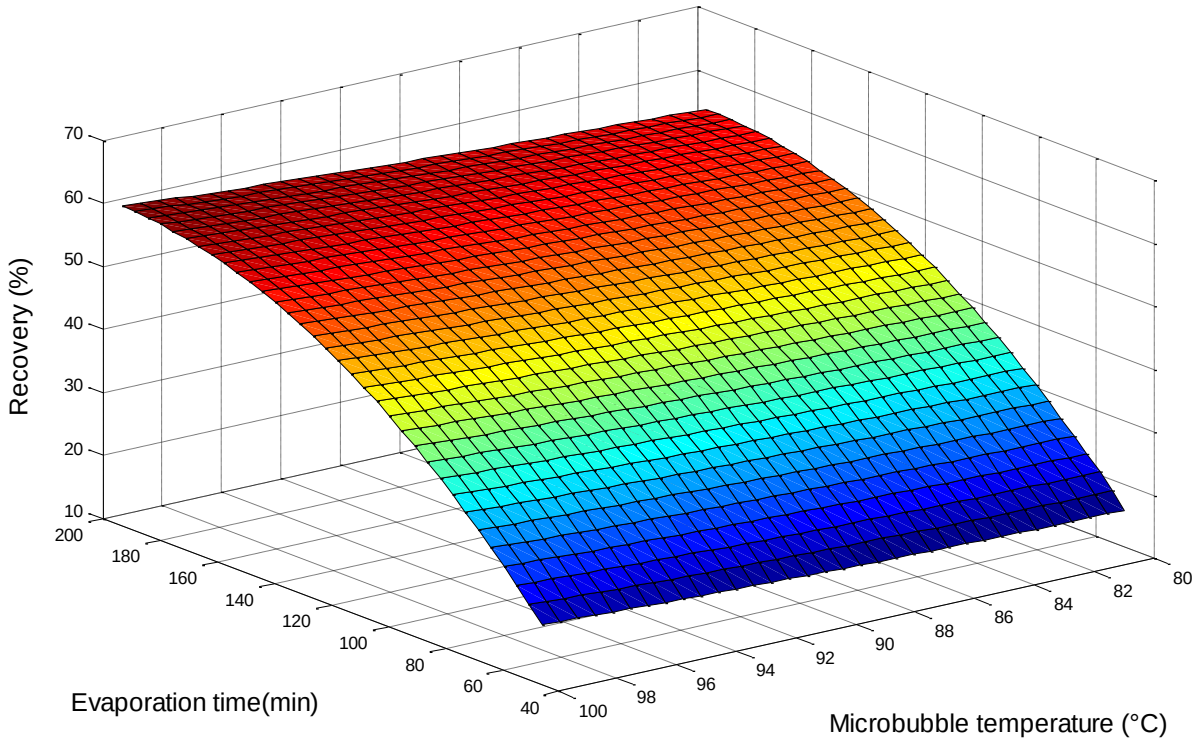

Figure 4.22: Response surface predicting removal efficiency of ethanol from the model equation: effect of evaporation time and microbubble air temperature.

According to the fitted multivariable model (equation 4.1), 59.8% of ethanol can be removed from the liquid mixture by maintaining the microbubble temperature and the evaporation time at their maximum values of 100°C and 200 min respectively. As stated before, both evaporation time and microbubble temperature, if increased, will cause a rise in the temperature of the liquid. Therefore, increasing the separation efficiency of ethanol by increasing either the evaporation time or the temperature of the microbubbles is not an attractive option, neither for the aim of the current approach nor for the process economics, when compared to the effect of reducing the liquid depth.

4.6.3 Effect of liquid depth and evaporation time on the removal efficiency of ethanol

Figure 4.23 shows the dependency of the removal efficiency of ethanol on both the depth of the liquid mixture and the time of evaporation when the microbubble temperature is at its mid value of 90°C.

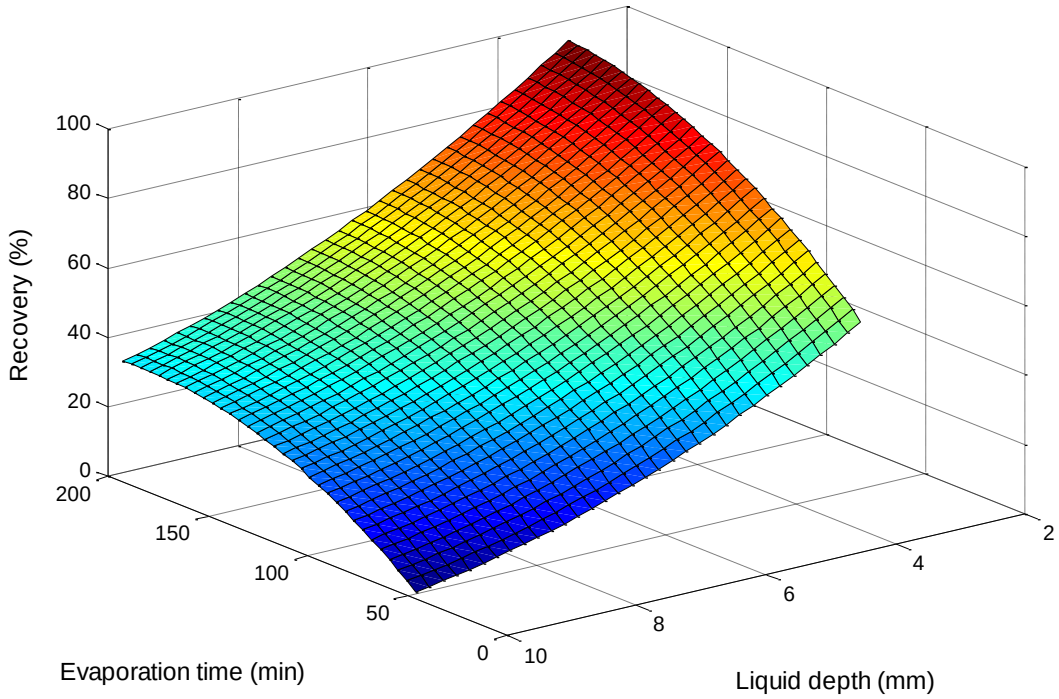

Figure 4.23: Response surface predicting the removal efficiency of ethanol from the model equation: effect of liquid level and evaporation time.

It is observed that a higher separation efficiency can be obtained at the minimum level of liquid depth and maximum level of evaporation time. Although the recovery efficiency increases as

the time of evaporation increases, its effect is less significant than that of the liquid layer height. According to the model developed, 200 min is required to recover 32.4% of ethanol from the liquid mixture when the liquid depth is 10 mm, and it is the same time that required to remove around 95.6% from the same mixture if its depth is decreased to 3 mm. Thus, if the same levels of separation are required to be achieved with higher liquid depths, then longer evaporation times should be applied, thereby increasing the energy consumed for operating the system as well as increasing the temperature rise of the liquid mixture.

4.7 Summary

In this chapter, the separation of the binary liquid mixture of ethanol-water by microbubble batch distillation technique has been investigated experimentally for the purpose of:

- Examining the feasibility of this technique in separating liquid mixtures.
- Studying the effect of different operating factors as well as the effect of the fluidic oscillator on the separation efficiency.
- Testing the hypothesis of dominating evaporation/mass transfer over sensible heat transfer within thin liquid levels.

Eexperiments have been conducted with different liquid depths, different air microbubbles temperatures and evaporation times. The central composite rotatable design method (CCRD) has been used as an experimental design tool to study the effect of these parameters on the removal efficiency of ethanol from the liquid mixture and on the temperature rise of the liquid mixture. An empirical model has also been developed using the experimental data to estimate the removal efficiency of ethanol for this system and the effectiveness of the model was verified through an R^2 value of 0.982.

Microbubble distillation system was successful in separating ethanol from a liquid mixture with a removal efficiency of around 81% for ethanol compared to about 30% for water at a liquid depth of 3 mm, microbubble air temperature of 90 °C and evaporation time of 125 min. The individual and combined effects of the process variables indicate that liquid depth has the most significant effect on the recovery of ethanol from the liquid mixture. The minimum level of liquid depth in the bubble tank is determined as optimum for achieving the maximum removal efficiency of ethanol and the minimum rise in liquid temperature, however as the liquid thickness increases, the recovery efficiency of ethanol decreases and the temperature rise

of the liquid mixture increases. This indicates that the selectivity of vaporization over sensible heat transfer is controllable and can be achieved by tuning liquid level. The results show that evaporation time has a less important influence than liquid depth on the recovery of ethanol, while microbubble temperature has the least significant effect on the process. It was also proven that microbubbles generated with aid of the fluidic oscillator using a Point Four ceramic diffuser were more effective in the recovery of ethanol than fine bubbles generated without fluidic oscillation however, no improvement has been recorded at higher liquid levels. The current data also indicate that the separation process of an ethanol-water liquid mixture using a microbubble mediated separation system can be accomplished with only a small increase in the liquid temperature (around 4 °C) at the minimum liquid level of 3 mm, indicating that this approach is suitable for treating thermally sensitive solutions such as bio-oil.

The University Of Sheffield.

Chapter Five

Separation of Azeotropic Mixtures: An Application for the Upgrading of Bioethanol

Chapter Five

Separation of Azeotropic Mixtures

5.1 Introduction

This chapter has been conducted on a hypothesis that reducing the height of liquid level through which bubble rises would lead to a non-equilibrium condition between the contacted gas and liquid phases. This means that liquid mixtures whose separation is restricted by the equilibrium barrier in the traditional distillation, can be separated according to this assumption. For this purpose, the feasibility of separating the azeotropic mixture of ethanol-water using microbubble-mediated batch distillation is investigated as a step also for bioethanol upgrading into a fuel grade quality. The effects of the depth of the liquid mixture in the bubble tank and of the inlet air microbubble temperature on the process efficiency were examined. The work presented in this chapter has been published in the American Institute of Chemical Engineers Journal (Abdulrazzaq, N., Al-Sabbagh, B., Rees, J.M. & Zimmerman, W.B., 2016. Separation of azeotropic mixtures using air microbubbles generated by fluidic oscillation. *AIChE Journal*, 62(4), pp.1192–1199).

This chapter is organized as follows. The next section presents a general review about azeotropic mixtures and common methods for their separation. Then, experimental results on the effect of the height of liquid level and temperature of the air microbubbles on the efficiency of breaking the azeotrope and on the temperature of the liquid mixture are discussed. A comparison study between the effectiveness of microbubble mediated distillation and that of traditional atmospheric distillation is also included. In the last section, the conclusions from this study are drawn.

5.2 Azeotropic mixture

An azeotropic mixture is a liquid mixture comprising two or more components whose proportion cannot be altered by conventional atmospheric distillation. The separation of liquid

mixtures into their pure components by traditional distillation exploits the difference between the concentrations of the vapor and liquid phases at equilibrium. However, this cannot be attained with azeotropic mixtures because the equilibrium vapor and liquid concentrations are identical (Julka et al. 2009).

This thermodynamic equilibrium barrier to distillation makes the purification and recovery of some components difficult. Azeotropes exist in many common and important industrial chemical processes, including the production of ethanol, isopropanol, methyl acetate, vinyl acetate and tetrahydrofuran (Pereiro et al. 2012). Furthermore, the application of bio-oils can also be problematic due to azeotropic properties. Bio-oils contain high amounts of water which cannot be completely removed due to the formation of azeotropes with the other organic components (Naik et al. 2010; Pan et al. 2012).

An azeotropic mixture can be either positive or negative depending on its boiling point. The positive mixture boils at a temperature lower than the boiling point of either of its constituents and also lower than that of any ratio of this mixture. A negative azeotrope on the other hand, boils at a temperature which is higher than that of any of its constituents as well as higher than that of any ratio of its components. An ethanol-water azeotrope consisting of about 88 %mol. ethanol and 12 %mol. water is an example of a positive azeotrope. This mixture boils at 78.2 °C, whilst its components ethanol and water boil at 78.4 °C and 100 °C respectively. Figure 5.1 shows the phase diagram for an ethanol-water mixture.

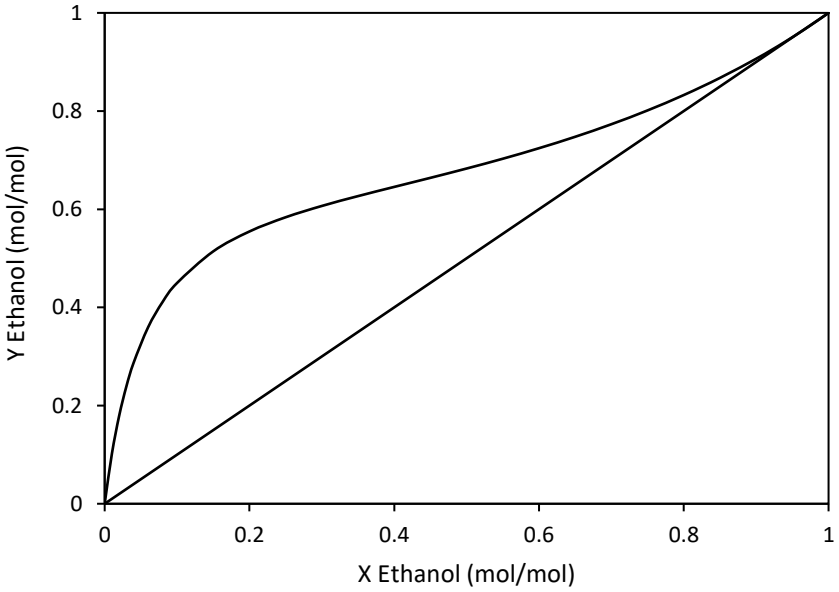

Figure 5.1: Liquid-vapor equilibrium diagram for an ethanol-water mixture (Flick 1998).

The separation of azeotropic mixtures is considered to be one of the most challenging tasks in chemical processes and bespoke methods are often needed to facilitate their separation (Luyben 2014). Different techniques have been explored in order to resolve azeotropic systems. These mainly include pressure swing, extractive and azeotropic distillation. The first method involves the use of two or more distillation columns at different pressures, whilst in the other two methods, an additional agent referred to as an entrainer (light entrainer in the case of azeotropic distillation and heavy solvent in the case of extractive distillation) is added to enable the separation process to occur (Luyben 2014). Entrainers can alter the relative volatility of the azeotropic constituents to facilitate their breaking (Julka et al. 2009). In azeotropic distillation, the additional agent needs to be carefully selected to ensure that it forms another azeotrope with one of the mixture constituents, then it could be removed by a further separation step such as distillation, or any other separation mode, which means that additional energy is required for its recovery (Matsuda et al. 2011; Ponce-De-León & Field 2000). The technique of azeotropic distillation is widely applied in the alcohol industry, particularly for the separation of water from ethanol (ethanol dehydration) (Bastidas et al. 2010). Cyclohexane is the entrainer that is commonly used for separating the water-ethanol azeotrope. When cyclohexane is added to the mixture, a second azeotrope that boils at 62.1°C is formed with water. After heating this ternary mixture, the binary azeotropic mixture of water-cyclohexane is evaporated first, leaving nearly pure ethanol. In extractive distillation, on the other hand, the entrainer should have a higher boiling point than any of the mixture components and should not form any azeotrope with either of them. Ethylene glycol is a feasible entrainer for the separation of the ethanol-water azeotrope by extractive distillation (Julka et al. 2009). These techniques can be effective for breaking azeotropic systems, however, they are associated with high energy requirements and can present with operational difficulties (Oliveira et al. 2013; Corderi et al. 2013).

Recently, new membrane technologies, including pervaporation (pv) and vapor permeation (vp), have been applied to the task of separating azeotropic mixtures. In order to achieve separation, a membrane which is more permeable for one of the azeotropic species than it is for the other is used (Aouinti & Belbachir 2008). These methods, however, have been challenged by several factors including those associated with scaling up of the separation units, high investment cost and rapid fouling of the membranes which restrict their application in the industrial field (Tang et al. 2013; Holtbruegge et al. 2013).

Due to the limitations of the existing methods for resolving the azeotropic mixtures, a simple, reliable and low cost technique is sought. In this work, the novel microbubble distillation technique has been explored to investigate its feasibility for breaking the azeotrope of the ethanol-water mixture. The purification of ethanol has been the focus of many recent studies as ethanol is one of the most widely used biofuels and any improvements in its production could potentially lead to significant reductions in environmental pollution (Pacheco-Basulto et al. 2012; Shirsat et al. 2013).

5.3 Results and discussion

Experiments were carried out by taking the azeotropic mixture of ethanol-water and distilling it under three different depths of liquid mixture (3, 5 and 10 mm) and two different air microbubble temperatures (80 and 90°C) for the purpose of exploring their effect on breaking the azeotrope. The methodologies employed in this study are described in Section 3.2.3 for the experimental procedure, section 3.4.1 for the liquid composition measurement and section 3.4.2.2 for the gas phase measurement. The variation of the final concentration of ethanol in the liquid and vapor phases as well as the evaporation rate of the liquid mixture with the depth of the liquid corresponding to each of the air microbubble temperatures investigated are shown respectively in figures 5.2, 5.3 and 5.4. Experiments were carried out in triplicate and in a random arrangement to calculate the error bar for each experiment.

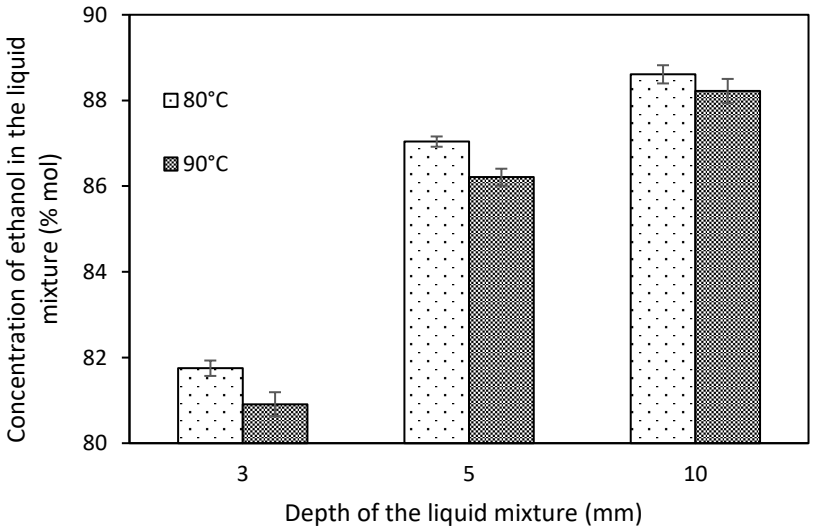

Figure 5.2: Variation of the final concentration of ethanol in the liquid mixture with the liquid mixture level. The error bars represent the standard error.

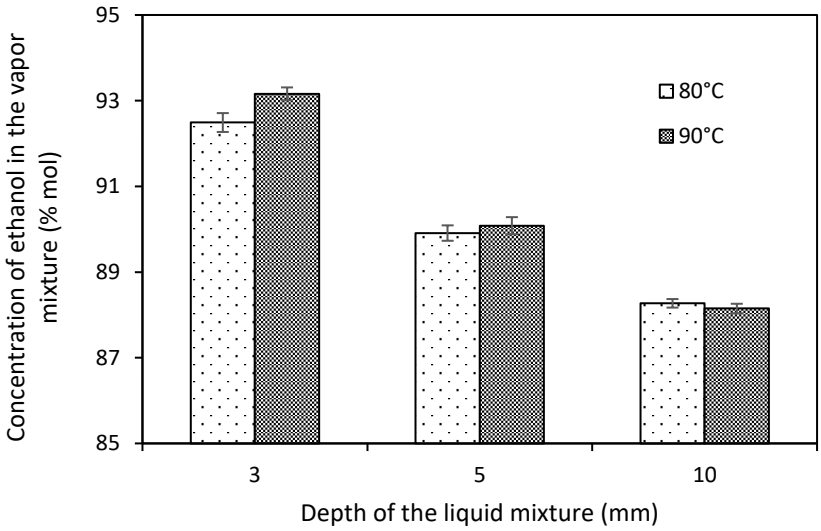

Figure 5.3: Variation of the final concentration of ethanol in the vapor phase with the liquid mixture level at a microbubble temperature of 90°C. The error bars represent the standard error.

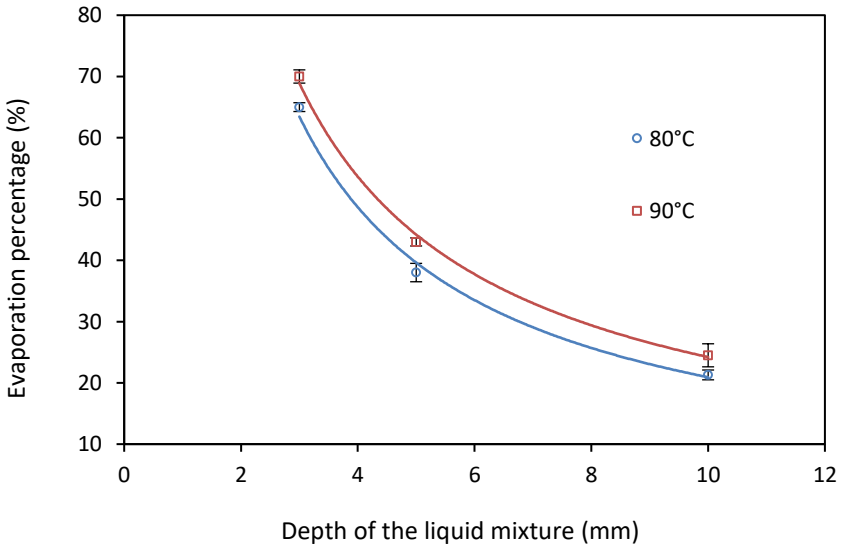

Figure 5.4: Variation of the percentage of evaporation of the liquid mixture versus liquid mixture height at a microbubble temperature of 90°C. The error bars represent the standard error.

The data in figures 5.2, 5.3 and 5.4 indicate that the depth of the liquid layer has a significant effect on the elimination of the azeotrope. For the two air microbubble temperatures considered, the final concentration of ethanol in the liquid mixture decreased and the vapor concentration increased with decreasing liquid depth, with almost no azeotropic separation occurring at the liquid depth of 10 mm, indicating that the efficiency of breaking the azeotrope is better at lower liquid levels.

The effect of the evaporation time on the efficiency of breaking the azeotrope was also investigated by performing an additional experiment using 3 mm liquid depth and 90°C microbubble temperature and measuring the concentration of both liquid and the corresponding vapors at different times. The results are presented in figure 5.5 which shows the change in the concentration of ethanol vapor produced by microbubble distillation and their corresponding concentrations at equilibrium state.

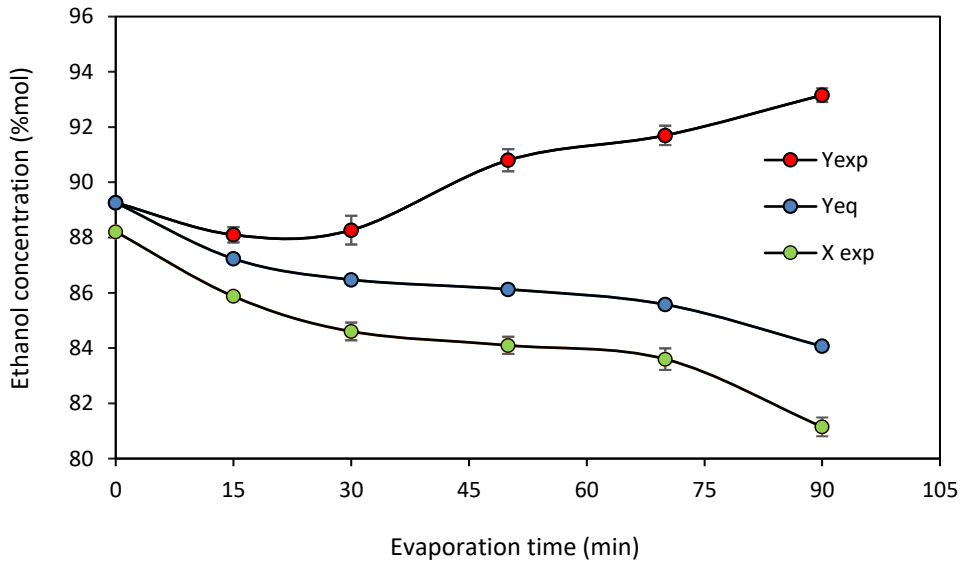

Figure 5.5: Concentration of ethanol in the vapor phase by microbubble distillation (Yexp) and their corresponding concentrations at the equilibrium state (Yeq) for given concentrations of the liquid (Xexp) at different evaporation times. Initial conditions are: 88 %mol. ethanol solution, 3 mm liquid level and 90°C air microbubble temperature. The error bars of each point represent the standard error of the experiment.

The results in figure 5.5 show that vapor concentrations from microbubble distillation are higher than those at equilibrium and the longer the time available for evaporation the wider is the gap between the experimental and the equilibrium conditions, indicating that better separation performance can be achieved at longer evaporation times. The reason behind this outcome is that as the time passes, the liquid depth becomes much thinner due to evaporation which in turn

increases the stripping efficiency of ethanol from the liquid mixture as demonstrated in the previous figures. Thus, if the same level of separation has to be attained with deeper liquid depths, longer evaporation times would be required to break the equilibrium barrier.

It is important to mention that extending the time of the experiment for more than 90 min causes a drop in the gas sensor signal for the outlet vapors. This can be attributed to the fact that as the time passes the concentration of ethanol in the liquid starts to deplete increasing the chance of water vaporization. Another reason that the liquid layer becomes too shallow and clear spots are created over the diffuser surface beyond this time, allowing air to escape to the header space of the bubble tank without contacting the liquid. Therefore, a duration of 90 min has been selected for running the experiments.

5.4 Comparison study between microbubble distillation and traditional distillation

Liquid-vapor data have been generated for other ethanol compositions for the purpose of making a comparison study between the performance of our novel microbubble mediated distillation approach and that of traditional distillation. Experimental conditions such as liquid level, evaporation time and inlet microbubble temperature, were kept constant for these experiments at the optimum values 3 mm, 90 min and 90°C respectively. The results are listed in table 5.1. The liquid composition was measured by GC analysis and the vapor concentration was measured by the ethanol gas sensor.

Table 5.1: Comparison between the vapor composition obtained by the microbubble distillation technique and those for isothermal equilibrium (Flick 1998).

Concentration of ethanol in liquid (%mole)	***Equilibrium vapor concentration (%mole)***	***Vapor concentration of ethanol obtained from microbbuble distillation (%mole)***
92.3	92.58	96.51
88.3	89.32	94.36
80.7	83.73	93.17
64.7	74.62	89.03
37.3	63.54	81.01
21.8	56.48	73.27
11.8	47.26	57.33

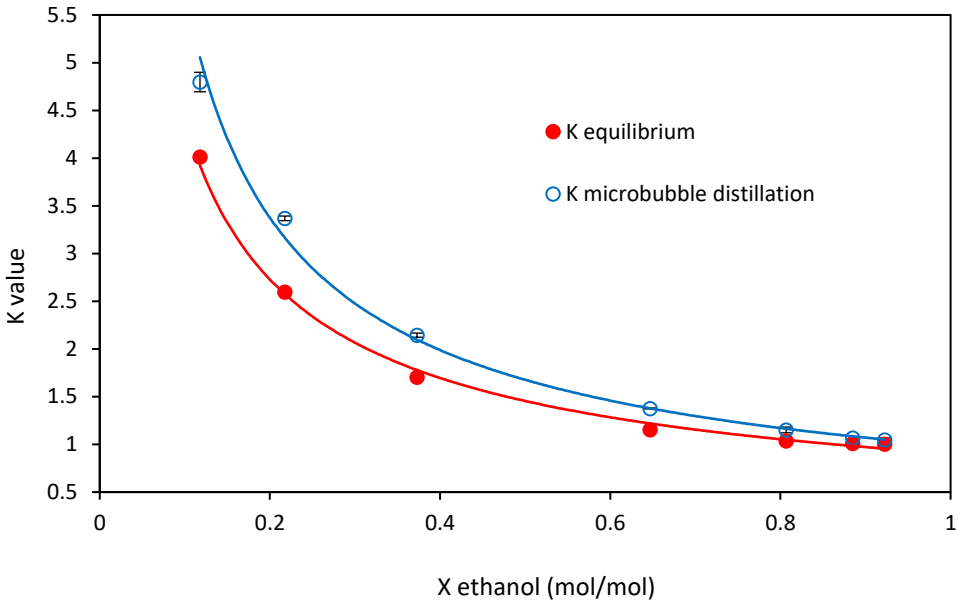

Figure 5.6: Comparison between the K-values of ethanol obtained by the microbubble distillation (K microbubble distillation) and the corresponding equilibrium values (K equilibrium) at different liquid ethanol compositions. The error bars represent the standard error of the experiments. The initial conditions are 3 mm liquid level and 90°C microbubble temperature.

Figure 5.6 presents a comparison between the values of the vapor –liquid distribution coefficient (Kequilibruim) of ethanol at equilibrium conditions and those obtained by the current work (Kmicrobubble distillation) at different ethanol liquid compositions, where K is the distribution coefficient which is the ratio of the mole fraction of ethanol in the vapor phase to its mole fraction in the liquid phase. The results presented in table 1 and figure 5.6 clearly demonstrate that the vapor concentrations, and consequently the K values, for the separation of the ethanol-water binary mixture using the microbubble mediated distillation technique are higher than those achieved at the isothermal equilibrium state for all liquid compositions considered here, including the azeotrope.

The possible explanation for these findings is that since hot, bone dry air microbubbles are injected into the cold liquid, non-equilibrium driving forces exist for both heat and mass transfers between the contact phases. Moreover, the microbubbles in the current method are injected slowly into the liquid so that there is laminar flow around the bubbles which, in turn, acts so as to prevent the liquid and gaseous phases from reaching equilibrium rapidly, thereby ensuring continuous heat and mass transfers. Unlike closed systems in which liquid molecules can

vaporize until equilibrium is established, the current system mimics open systems with continuous transfer of ethanol molecules from the liquid side to the bubble side under both diffusion and internal convection due to bubble motion. As a result of this, equilibrium is disrupted and according to Le Chatelier's principle, the equilibrium should be shifted toward more vaporization to compensate for the molecules of ethanol removed from the system:

$$C_2H_6O\ (l) \rightleftharpoons C_2H_6O\ (g).$$

In this scenario, the ethanol concentration in the bubble phase would be higher than the ratios predicted by the equilibrium theory for all liquid phase mole fractions and within the short contact time available during the ascent of the bubbles in shallow liquid depths as demonstrated in figure 5.6. The shallower the liquid depth, the easier it is to maintain non-equilibrium conditions between the contacted phases, both chemically and thermally, which is crucial for continuing and increasing the rate of transfer processes (see figure 5.5). Conversely, deeper liquid layers are associated with a lesser quantity of vaporization due to thermal equilibrium with the surrounding liquid. This effect can be further confirmed from the results presented in figure 5.7. This figure displays the time profiles of the outlet air temperature from the bubble tank during the experiment for different liquid levels which shows that upon decreasing the height of liquid level, the bubbles exiting the system are hotter.

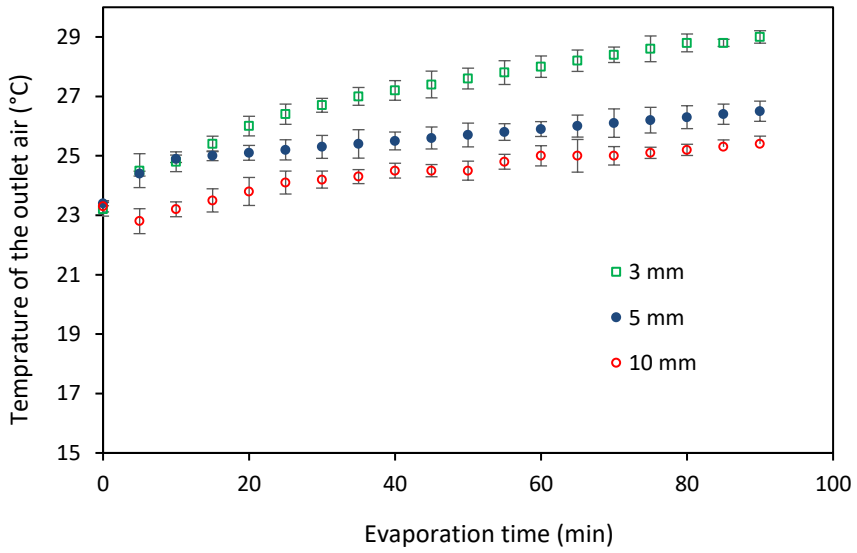

Figure 5.7: Temperature of the outlet air from the bubble tank plotted against evaporation time for the azeotropic mixture at different liquid levels for an air microbubble temperature of 90°C and evaporation time of 90 min. The error bars represent the standard error for each reading.

As stated before, the deeper the level of the liquid mixture, the longer the residence time available for the bubbles to transfer their heat to the surrounding liquid. Therefore, bubble exits from shallower depths are expected to be hotter as they leave the liquid after a shorter time interval.

Since the carrier gas in microbubbles automatically breaks the azeotrope through the introduction of a third component, and the microbubble temperature can be held at a different temperature from the liquid, vapor-liquid equilibrium is never established. Hence, microbubble distillation should be generally applicable to any other azeotropic mixture. The shifting of the azeotropic equilibrium condition $(x_i = y_i)$ & $(T^{liq} = T^{vap})$ into non-equilibrium conditions $(x_i \neq y_i)$ & $(T^{liq} \neq T^{vap})$ that has been achieved here, is one of the unique features of the new technique "microbubble distillation". x_i and y_i are mole fraction of i_{th} component in the liquid and gas phases respectively, T^{liq} and T^{vap} are the temperatures of liquid and gas phases respectively.

Interestingly, the breaking of the azeotrope barrier was achieved with just a small temperature rise in the liquid mixture. The experimental temperature profile of the liquid mixture against evaporation time is presented in figure 5.8. It is noticed that there is no substantial augmentation in the temperature of the liquid mixture from its initial value of 20°C. The minimum liquid temperature rise, of around 4°C, was obtained at the lowest liquid depth (i.e. 3 mm).

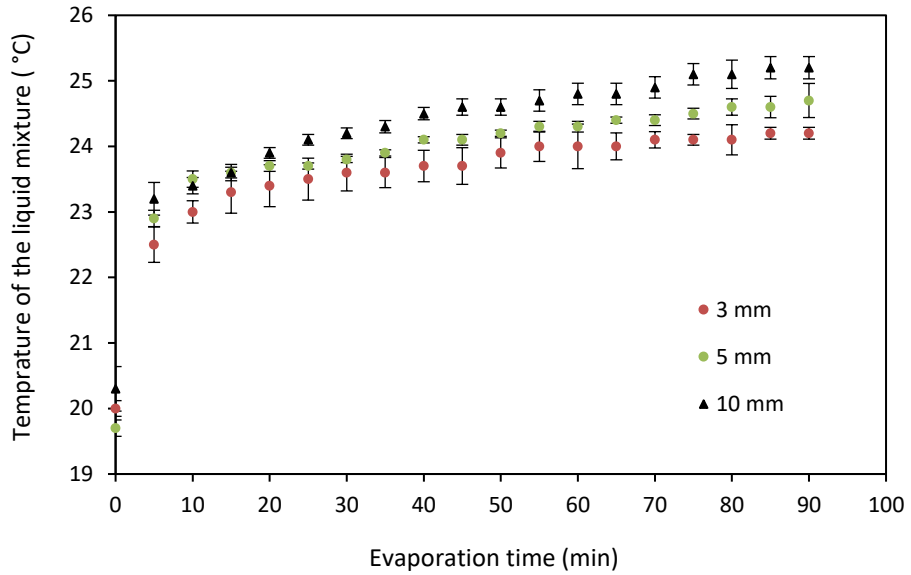

Figure 5.8: Temperature of the azeotropic liquid mixture against time for different liquid levels at a microbubble air temperature of 90°C and evaporation time of 90 min. The error bars represent the standard error.

The small rises in liquid temperature during distillation process could be related to the low values of the heat transfer coefficient for the fluidic oscillation actuated microbubbles which were introduced gently into the liquid. Zimmerman et al. (2013) estimate that for bubbles of sizes 200 microns injected slowly into the liquid, the heat transfer coefficient is around 0.1 W/m^2 K. As mentioned before, longer residence times in the liquid medium results in condensation of the bubble cargo. As a consequence, the liquid temperature will be raised by the exothermic effect of the condensation process. This is the reason behind increasing the temperature of the liquid as the depth of the liquid level increased. These results suggest that the optimal separation for azeotropic systems using microbubble mediated distillation technology can be attained with a minimal liquid temperature rise.

5.5 Summary

In this part of study, the hypothesis that the ability to achieve non-equilibrium operation between the contact phases by tuning the height of the liquid film to control the contact times for the rising bubbles, is tested with an azeotropic binary mixture of ethanol-water. Data obtained from this work showed that it is possible to break the ethanol-water azeotrope by using microbubble distillation technique. From the experimental work, it was found that decreasing the liquid mixture level in the bubble tank enhances the separation efficiency of ethanol from its azeotropic mixture with water. Ethanol, with a purity of about 94% mol., was obtained under conditions of liquid mixture depth of 3 mm and inlet microbubble air temperature of 90°C. At a higher liquid level of 10 mm, however, no separation for the azeotrope was achieved due to thermal equilibrium with the liquid. The separation process was accomplished with just a slight increase in the temperature of the liquid mixture, indicating, once again, that this regime is favorable for separating thermo-chemically unstable solutions.

The University Of Sheffield.

Chapter Six

Separation of a Multi-component Mixtures: An Application for the Upgrading of a Bio-oil mixture

Chapter six

Separation of Multi Components Mixture

6.1 Introduction

This work focuses mainly on studying the feasibility of upgrading bio-crude oils through simultaneously reducing the water content and the acidity using microbubble mediated distillation technology. A range of experiments was conducted with a model bio-oil mixture using the experimental rig that was shown in figure 3.5 and the experimental procedure that was described in section 3.2.3. The study explored the effect of varying the height of liquid mixture in the bubble tank, the temperature of the inlet air microbubbles and the time of evaporation on the upgrading process. The materials and operating conditions applied in this work can be found in sections 3.3.3.1 and 3.3.3.2 while the chemical analysis can be found in sections 3.4.2.3 and 3.4.3.

The chapter is organized as follows: section 2 presents details of the model bio-oil mixture applied in this work. Section 3 displays the results and discussions of the separation experiments, highlighting the effects of the above mentioned operating conditions on the stripping efficiency of each component in the model mixture as well as their impact on the temperature of the liquid mixture. The conclusions are drawn in section 4.

6.2 Model pyrolysis oil mixture

There are two major problems with bio-crude oils: high water content (15-30%) meaning low calorific value and high acidity (around 15%) due to the presence of low molecular weight carboxylic acids (Oasmaa et al. 2004; Oasmaa et al. 2005; Lohitharn & Shanks 2009; Oasmaa et al. 2011; Liu et al. 2012; Kim et al. 2012; Drese et al. 2011). These acids cannot only make the bio-oils corrosive but also accelerate the undesirable polymerization of other components in the bio-oil mixture (Resasco & Crossley 2015; Hu et al. 2012). Selective extraction of these unfavorable components, therefore, will have a positive influence on: bio-oil heating value, corrosiveness and stability upon storage.

In the case of a real bio-oil mixture which is composed of more than 300 components with a wide range of boiling points and different chemical functional groups, it is difficult to understand and explain the interactions between components and the changes that occur in the liquid properties after the upgrading process, especially when applying a new approach. Further, the complete analysis of real pyrolysis oil mixtures is very difficult. By studying simulated bio-oil mixtures, we can reduce the difficulty posed by the sophisticated nature of real bio-oil mixtures and simplify the system in terms of the number of chemical components and hence the analysis process (Tripathi et al. 2010). This allows a better understanding of the effect of microbubble mediated distillation technology in the upgrading process and helps to improve the process strategies and the system design to achieve an effective upgrading for the real bio-oil mixture.

The model bio-oil mixture that was applied in this study contained water 30%, acetic acid 15% and 1-hydroxy-2-propanone (acetol) 55% all by volume percent. Water was chosen as it is the major component in the bio-oil mixture (Czernik & Bridgwater 2004). Acetic acid was chosen to create the acidic condition of the bio-oil. Acetol was selected as a representative of the higher molecular weight components in bio-oil mixtures. Both acetic acid and acetol were used as they present in higher concentrations in their corresponding groups (Pan et al. 2012; Bertero et al. 2012; Wang et al. 2013). The composition of the target species (i.e. water and acetic acid) were chosen to simulate the total moisture and carboxylic acid contents in the typical bio-oil mixture (Balat et al. 2009; Zhang et al. 2013). It must be noted that the concentration of these components varies from one bio-oil to another depending on the type of biomass and on the pyrolysis process conditions. Studies on different model bio-oil mixtures can be found extensively in the literature (Elliott & Hart 2009; Mahfud et al. 2007; Wu et al. 2008; Hu et al. 2013; Drese et al. 2011; Zhou et al. 2014; Maggi & Delmon 1994; Fisk et al. 2009; Teella et al. 2011; Wang et al. 2013).

6.3 Results and discussion

6.3.1 Effect of depth of the liquid mixture

The concentrations of the model components were measured at different evaporation times while changing the height of liquid level in the bubble tank from 3 mm to 5 mm. Results are presented in figures 6.1, 6.2 and 6.3 for the concentrations of water, acetic acid and acetol

respectively. These liquid levels were chosen as they have shown higher separation efficiencies compared to deeper levels with both binary and azeotropic mixtures. The inlet air temperature was kept constant at 100 °C for all of these runs.

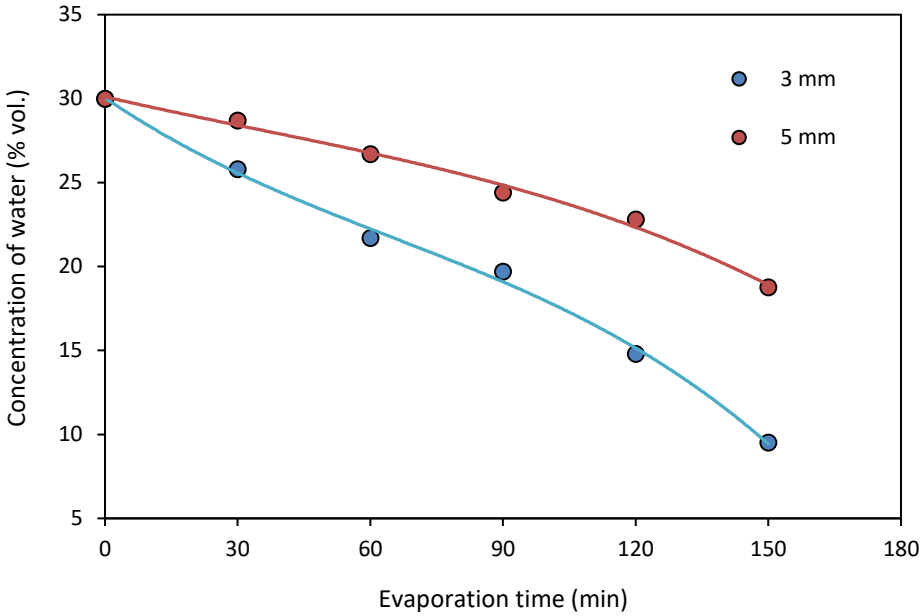

Figure 6.1: Variation of the concentration of water in the model mixture with time at liquid depths of 3 mm and 5 mm.

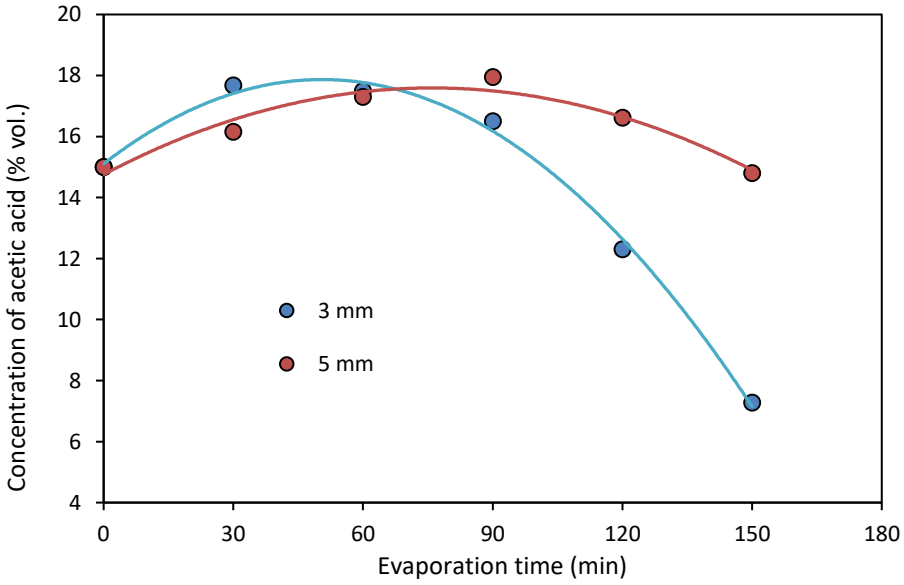

Figure 6.2: Variation of the concentration of acetic acid in the model mixture with time at liquid depths of 3 mm and 5 mm.

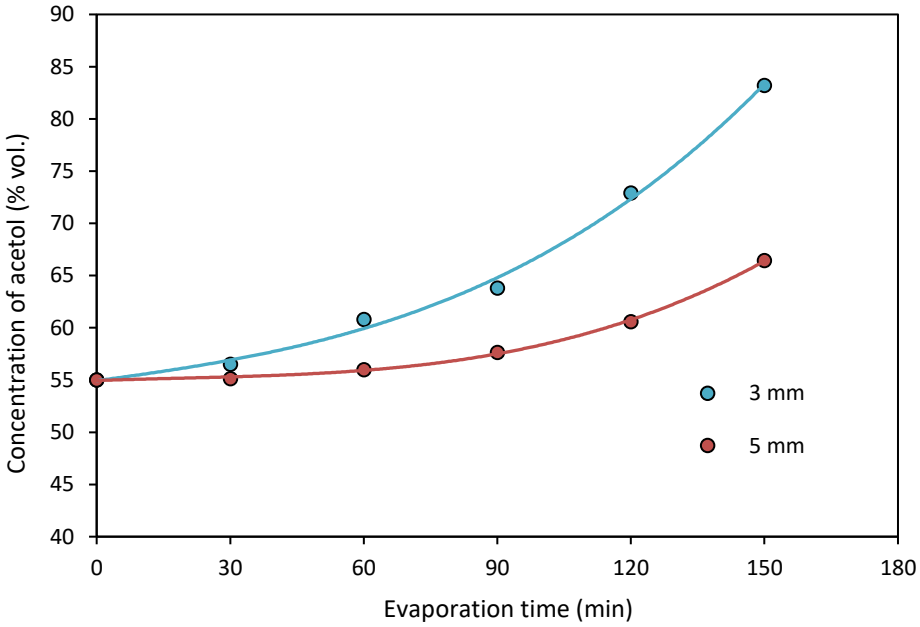

Figure 6.3: Variation of the concentration of acetol in the model mixture with time at liquid depths of 3 mm and 5 mm.

Overall, it can be seen from the results that the rate of separation for both water and acetic acid is higher at a liquid level of 3 mm compared to those occurring at a liquid level of 5 mm. The concentration of water has dropped with time for both depths from its initial value of 30% in the feed mixture to only 9.51% for the liquid level of 3 mm and to 18.76% for the liquid level of 5 mm after 150 min as depicted in figure 6.1.

Acetic acid content increased noticeably in the first 60 min of the experiment at liquid level 3 mm from 15% initially to 17.5% as shown in figure 6.2. Its augmentation, however, was continued for the first 90 min of the experiment at liquid level 5 mm. Acetic acid content then started to decrease gradually for both depths after these durations, before attaining lower values of 7.28% and 14.8% at 3 mm and 5 mm respectively after 150 min.

Acetol concentration, on the other hand, exhibited an increase all the time for both levels. The concentration of acetol rose from 55% in the feed mixture to about 66.44% at level 5 mm after 150 min. Reducing the liquid level to 3 mm resulted in this compound being more concentrated in the final solution, as evident in figure 6.3, with a final concentration of 83.21% after the same time of evaporation. Visual inspection of the samples after the end of the experiment is another confirmation that final mixtures are richer in acetol compared to their initial

concentration. The light yellow color of the final mixture means that acetol is the dominate component since both water and acetic acid are colorless solutions.

Evaporation of components from liquid mixtures depends on their tendency to escape to the vapor phase (i.e. on their vapor pressures). Water has the highest vapor pressure (or the highest volatility) compared to the other components (i.e. acetic acid and acetol), hence it is expected to transfer faster to the dispersed phase. The quick stripping of water caused the marked boost that was recorded in the acid concentration during the first period of the test at level 3mm. At the higher liquid depth (5 mm), a rise in the acid composition was also observed but this occurred at a slower rate because of the slower evaporation of water from the liquid mixture. As time proceeds, the concentration of water in the liquid phase starts to drop due to vaporization, resulting in an increase in the evaporation of the second volatile component (i.e. acetic acid) from the solution.

These data also indicate that the depth of liquid mixture is a key parameter influencing the efficiency of upgrading the model mixture by microbubble distillation as demonstrated before in the previous chapters with bioethanol purification. The concentration of the target components in the simulated mixture drop more sharply at the lower liquid depth. This is due to the shorter contact time of the microbubbles in the liquid bulk at shallow liquid depths which prevents them from cooling and dissipating their contents by condensation effect.

Figure 6.4 shows complementary information about the separation efficiency of each component in the model bio-oil mixture for the two liquid depths considered in this work: 3 mm and 5 mm. Separation efficiencies were calculated according to Eq. (3.1) depending on the initial and final volumes of each component in the liquid mixtures. The results in this figure reflect two important points: the first one is the ability to preferentially drive off the volatile species contained in the model mixture as well as the remarkable effect of mixture depth on their recovery efficiencies. About 84% of water was removed from the mixture at liquid level 3 mm followed by 75.7% for acetic acid and 24.3% for acetol which is the component with least volatility in the mixture. When liquid level was increased to 5 mm, the recorded values were reduced to 57.4%, 32.8% and 17.7% accordingly.

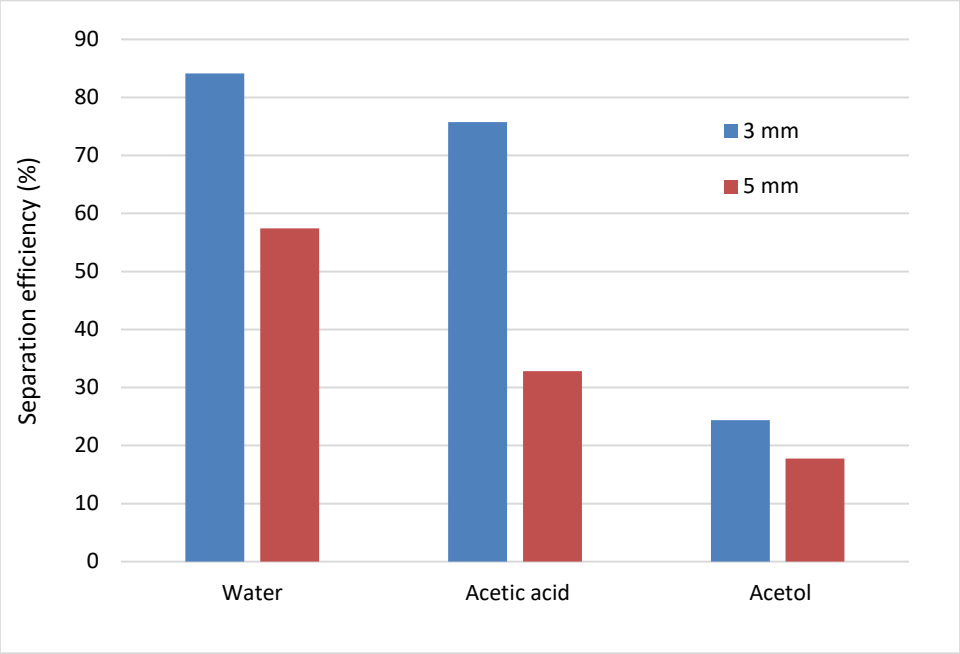

Figure 6.4: Graph of the separation efficiency of each component in the model bio-oil mixture at two liquid levels: 3 mm and 5 mm, after an evaporation time of 150 min.

Figure 6.5 shows the temperature of liquid mixture as a function of evaporation time. The temperature was recorded every 5 min during the experiment. The data show that the temperature of the liquid mixture increased by around only 5.5 and 7 °C during the experiment the at liquid levels of 3 and 5 mm respectively. These trends are similar to those obtained with the previous tested mixtures.

As mentioned earlier, the biggest hurdle in the upgrading of bio crude oils is their poor heat stability under high operating temperatures which would initiate undesirable polymerization reactions and coke formation. The key challenge, therefore, is to improve their characteristics without damaging their properties. As is evident from the current results, these concerns have been addressed successfully with application of a microbubble distillation technique through reducing water and acid contents drastically without transferring significant heat to the mixture.

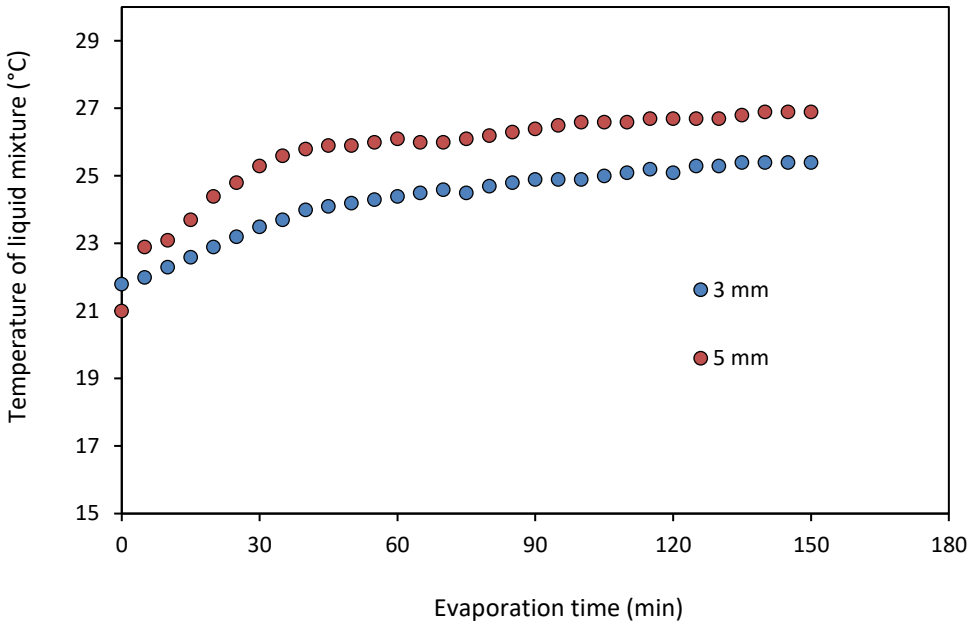

Figure 6.5: Time profile for the temperature of the liquid mixture during the experiment after 150 min at two different liquid levels.

The final samples of the liquid mixture after 150 min for both liquid levels were measured by GC-MS as well to check if other compounds are produced during the separation process or not. Figure 6.5 shows the GC-MS spectra for the samples after 150 min for liquid levels 3 mm and 5 mm. No peaks for new components have been recognized other than those for the components of the model mixture, confirming that no chemical reactions occur during the separation process.

(a)

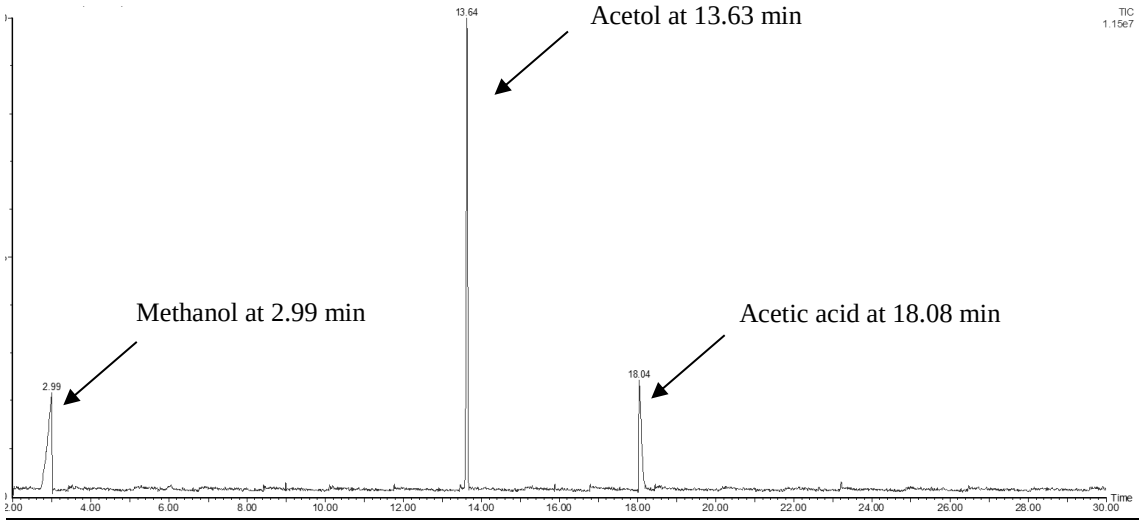

(b)

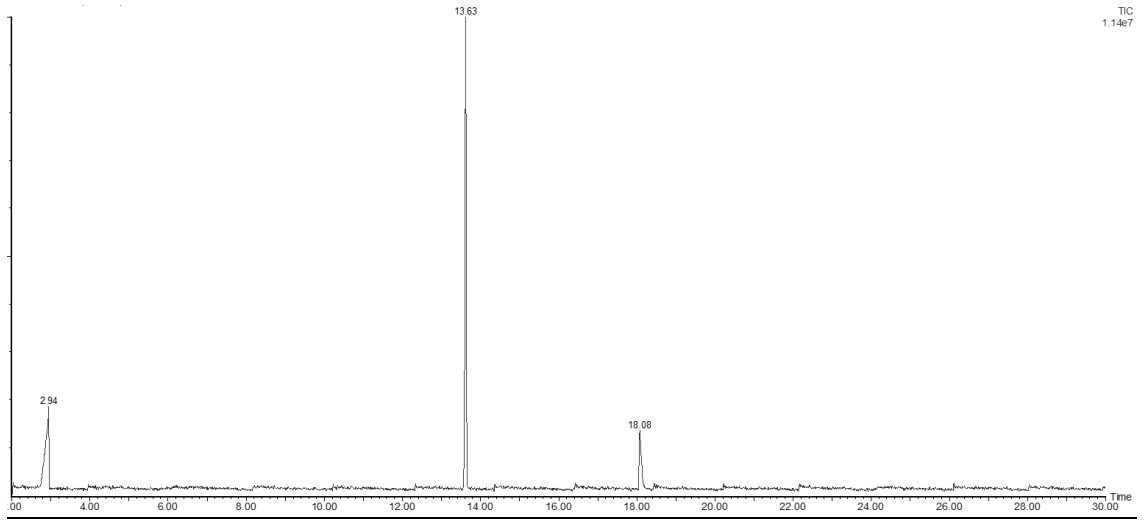

Figure 6.6: GC-MS spectrum for samples at 150 min (a) 5 mm and (b) 3 mm liquid levels. Three peaks can be recognized: the first one for the solvent methanol with a retention time of 2.99 min. The second one for acetol and the third one for acetic acid with retention times of 13.63 min and 18.08 min respectively.

6.3.2 Effect of microbubble air temperature

In order to understand the effect of the temperature of the inlet air microbubbles on the separation efficiency of water and acetic acid from the model mixture, a set of experiments were also conducted at a temperature of 80 °C. In these experiments the depth of liquid mixture was fixed at 3 mm. The results are shown in figures 6.7, 6.8 and 6.9 for water, acetic acid and acetol respectively.

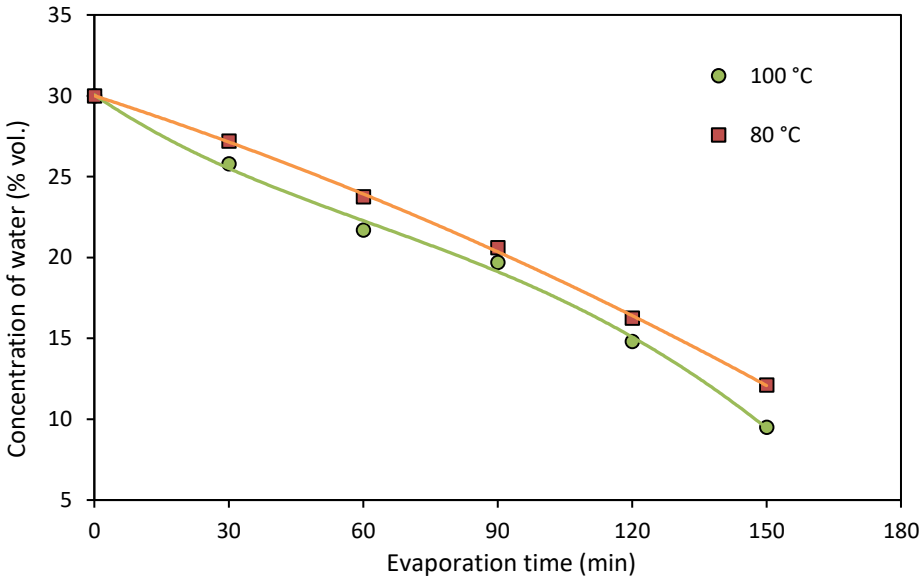

Figure 6.7: Variation of the concentration of water in the model mixture with time at two microbubble air temperatures.

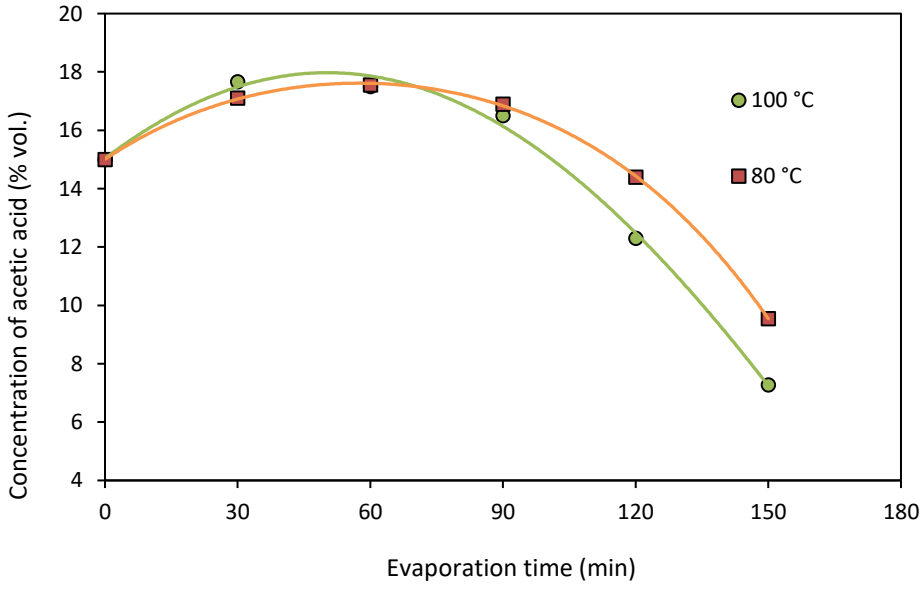

Figure 6.8: Variation of the concentration of acetic acid in the model mixture with time at two microbubble air temperatures.

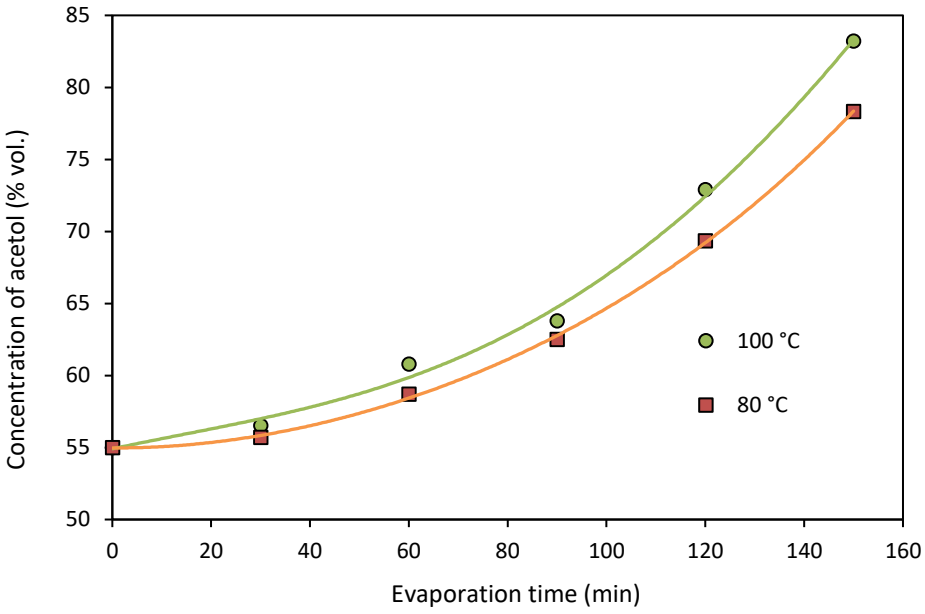

Figure 6.9: Variation of the concentration of acetol in the model mixture with time at two microbubble air temperatures.

The results prove that higher evaporation temperatures led to higher separation rates for both water and acetic acid from the liquid mixture. When the evaporation temperature was 80 °C, water content dropped to 12.12%. When the temperature rose to 100 °C, the water content reduced to 9.51% as shown in figure 6.7. Acetic acid content decreased more sharply at the higher temperature as shown in figure 6.8. The acid concentration was reduced to 9.55% at 80° C compared to 7.28% at 100° C.

The observed increase in the recovery efficiency of both water and acetic acid with bubble temperature can be explained by consideration of the level of available energy for the injected air microbubbles. Energy transported by the gaseous phase increases along with the temperature of the injected microbubbles. Therefore, the temperature of the liquid phase will rise as a consequence of the increase in sensible heat that is transferred to the liquid. The higher liquid temperatures result in an increase in the kinetic energy of its molecules, as well as in the vapor pressure of its components. Consequently, this will lead to an increase in the fraction of evaporated components to the bubble phase. This is in agreement with our previous results obtained from the separation of the ethanol-water system by microbubbles which demonstrated an improvement in the separation efficiency of ethanol with increasing bubble temperature (Abdulrazzaq et al. 2016).

The temperature of the solution increased by only 4°C during this test compared to 5.5 °C at an air temperature of 100 °C as shown in figure 6.10. The trend of increasing the temperature of the liquid mixture with increasing the temperature of air microbubbles is similar to what was obtained before with the ethanol-water binary system.

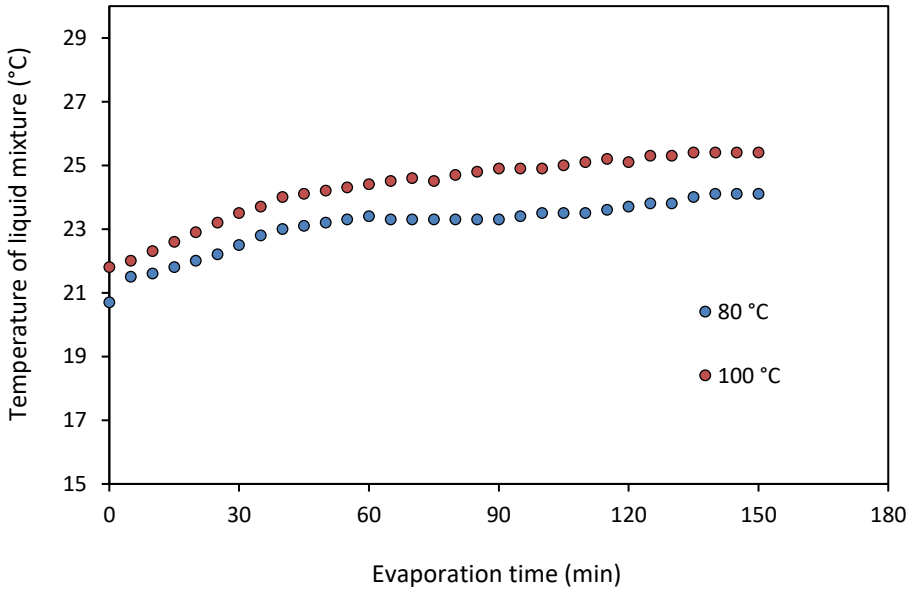

Figure 6.10: Time profile for the temperature of the liquid mixture during the experiment after 150 min at two different air microbubble temperatures.

6.4 Summary

The work reported here focused on the possibility of separating a model bio-oil mixture using a microbubble mediated distillation technique. The main hypothesis of this part is that thermally sensitive bio-oil mixtures can be upgraded through separating excess water and acids without destroying their quality by heating and polymerization. After the upgrading process, most of the water and acid contents were removed from the mixture, thereby increasing the heating value and reducing the corrosivity which were both desirable for the further application of bio-fuels or as a pretreatment for further upgrading steps. The lower the liquid level, the better the separation efficiencies for the target components. Water content of the model mixture fell from 30% to 9.51% and the acidity content fell from 15% to 7.28% after an evaporation time of 150 min under conditions of 3 mm liquid depth and 100°C microbubble air temperature. At 5 mm liquid depth, water and acetic acid were reduced to 18.76% and 14.8% respectively

under the same operating conditions. It was also found that the removal efficiencies for both water and acetic acid were decreased with the decrease of the injection temperature. The major advantage that has been noticed from applying the microbubble distillation technique is the ability to selectively separate the problematic volatile components while minimizing the temperature rise of the liquid mixture. The temperature of the liquid mixture was increased slightly during the experiment, demonstrating that this technique is guaranteed to be suitable for improving the quality of pyrolysis fuels without damaging their useful properties. The current technology was found to be superior as compared to the conventional upgrading methods in terms of successful upgrading and energy saving. To the best of our knowledge, upgrading of pyrolysis fuels by microbubbles has not been reported anywhere to date. Future work will continue to apply this technology to the upgrading of real bio-oil mixtures.

The University Of Sheffield.

Chapter Seven

Non-equilibrium chemical thermodynamics modelling and analysis of single microbubble evaporation dynamics

Chapter Seven

Non-equilibrium chemical thermodynamics modelling and analysis of single microbubble evaporation dynamics

7.1 Introduction

A computational model of a single gas microbubble immersed in a liquid of ethanol-water mixture is developed and solved numerically. This complements the earlier binary distillation experiments with ethanol-water mixture stripped by hot air microbubbles. The proposed model has been developed using Galerkin finite element methods (Zimmerman 2007) to predict the temperature and vapor content of the gas microbubble as a function of its residence time in the liquid phase. The key element of this model is that microbubble internal mixing occurs on a time scale of ~10^{-3}s (Zimmerman et al. 2013), so an evaporating mixture or condensing vapour must obey a rate law that evolves on this rapid time scale. No such rate law has been previously used, so it is introduced here originally. This modelling study also aims to explore the effect of important parameters such as bubble size, initial bubble temperature and liquid composition on the efficiency of the stripping process. These predictions are of primary importance not only for the robust design of the system but also for the optimization of the operating parameters of the process.

This chapter is organized as follows: section 2 presents the governing equations for the computational model with their initial and boundary conditions. Section 3 describes the numerical methods for solving the equations. A sensitivity study to investigate the effect of the main parameters governing the process is presented in section 4. Section 5 presents a comparison between experimental data and modelling predictions, while in section 6 conclusions of this study are drawn.

7.2 Model definition

The system investigated comprises a single fluidic oscillator air microbubble, as shown in figure 7.1, of a diameter 200µm (dispersed phase) which rises due to a buoyancy force in an infinite reservoir of ethanol-water mixture. The width of the liquid domain is taken to be 10 times that of the bubble radius. Modelling domains of 6-10 bubble radius widths have shown that the walls have little effect on the bubble shape and velocity field (Yu & Fan 2008). Due to axisymetry, half of the computational domain was considered to reduce the time required for calculations. The configuration of the model is shown in figure 7.1.

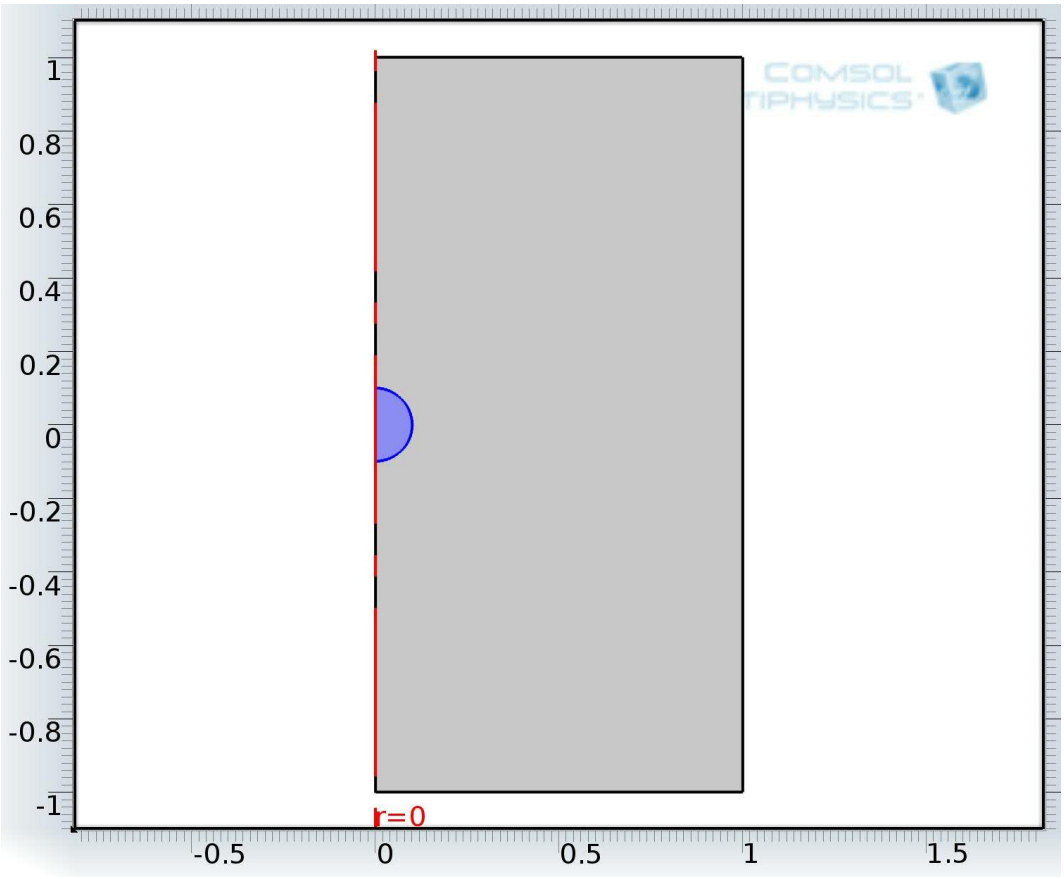

Figure 7.1: The 2-D axisymmetric model configuration.

The modelling study of this system incorporates a time dependent model for the temperature and concentration profiles inside the bubble. Circulation patterns due to bubble motion are also set up inside and around the bubble. To simplify the system, the model adopted here is based on the following assumptions:

- The bubble has spherical shape. This is because the bubble is sufficiently small that surface tension is dominant so there is no deformation from the spherical shape. This assumption is a good approximation for the micro-sized bubble used in this study.
- The bubble is always rising at its terminal velocity - this simplifies the calculations through focusing only on the mass and heat transfer dynamics.
- The pressure inside the bubble is constant which is reasonable for the rather small residence times (i.e. small liquid heights) applied in this study.
- The concentration profile in the liquid phase is constant. The continuous phase is completely mixed with a constant bulk concentration. This assumption is reasonable so attention can be restricted to solving the transfer equations only inside the bubble instead of solving them both inside and outside.
- No chemical reaction occurs in either phase.

7.2.1 Governing equations

In this system, heat and mass transfers occur simultaneously leading to heating and vaporization of the liquid. The time dependent temperature and concentration profiles of the microbubble can be obtained from the simultaneous solution of the energy and mass transfer equations inside the bubble. Considering the simplifications previously mentioned, the following equations for mass and heat transfers are the main governing equations for this model:

$$\frac{\partial c_i}{\partial t} + u \cdot \nabla c_i = D \nabla^2 c_i \tag{7.1}$$

$$\frac{\partial T}{\partial t} + u \cdot \nabla T = \alpha \nabla^2 T \tag{7.2}$$

where c_i is the molar concentration of ethanol (i=1) and water (i=2) in the bubble, T is the temperature of the bubble field, D is molecular diffusivity, u is the velocity inside the bubble and α is the thermal diffusivity. Eq. 7.1 was solved for the bubble only, while Eq. 7.2 was solved for both bubble and liquid bulks. Gas properties (thermal conductivity, heat capacity and thermal diffusivity) are considered to be temperature dependent and calculated according to polynomial empirical correlations (Assael et al. 1996; Himmelblau 1989). Gas density and gas molecular diffusivities are taken as constant. Liquid mixture properties (density, viscosity

and thermal conductivity) were calculated according to the concentration dependent correlations reported by Khattab et al. (2012) for the density and viscosity and by Reid et al. (1987) for the thermal conductivity. The physical properties for this computational model is listed in Appendix C.

The internal velocity field of the bubble is calculated by Hill's spherical vortex (Hill 1894) which is the solution of the Navier-Stokes equation adopted by Hadamard and Rybcynski for small spherical bubbles rising under a buoyancy force (Panton 1984). The stream function for this flow is given by:

$$\psi = \frac{1}{2} U_t \, R^2 \left(\frac{r}{R}\right)^2 \left[1 - \left(\frac{z}{R}\right)^2 - \left(\frac{r}{R}\right)^2\right] \tag{7.3}$$

from which the dimensionless radial (r) and axial (z) velocity components are derived:

$$u_r = -\frac{1}{r}\frac{\partial \psi}{\partial z} \tag{7.4}$$

$$u_z = \frac{1}{r}\frac{\partial \psi}{\partial r} \tag{7.5}$$

The velocities are computed to be:

$$u_z = U_t \left(1 - \left(\frac{z}{R}\right)^2 - 2\left(\frac{r}{R}\right)^2\right) \tag{7.6}$$

$$u_r = U_t \frac{r}{R}\frac{z}{R} \tag{7.7}$$

$$U_t = \frac{1}{3}\frac{gR^2}{\mu}\Delta\rho \tag{7.8}$$

where u_z and u_r are the velocity vectors in axial and radial coordinates respectively, R is the radius of the bubble, U_t is the Hadamard terminal velocity for a bubble rising under gravity force g, μ is the viscosity of the surrounding liquid and $\Delta\rho$ is the density difference between the bubble and the surrounding liquid.

The external velocity field outside the bubble (in the liquid domain) is calculated from the dimensionless Stokes stream function equation for a uniform far-field flow (Lamb 1879):

$$\psi = -\frac{1}{2}U_t\, r^2 \left[1 - \frac{3}{2}\frac{R}{\sqrt{r^2+z^2}} + \frac{1}{2}\left(\frac{R}{\sqrt{r^2+z^2}}\right)^3\right] \tag{7.9}$$

From which the axial and radial velocities are calculated using the formulas that given by equations (7.4) and (7.5).

7.2.2 Initial and Boundary conditions

Eq. (7.1) and (7.2) must be solved with suitable initial and boundary conditions. Microbubble containing bone dry air is injected initially at temperature T_0 (the initial concentrations for water and ethanol are zero). For the liquid domain, the initial temperature is 293K for all calculations.

Boundary conditions were introduced for both heat and mass transfers. The temperature at the side walls of the computational domain is fixed at 293K. For the gas-liquid interface, to our knowledge, all the previous studies on the systems consisting of gas and liquid phases in contact with each other are limited to the assumption of liquid-vapor equilibrium for calculating the composition of species at the gas-liquid interface (Campos & Lage 2000; Zimmerman et al. 2013; MacInnes et al. 2012; Rivier et al. 2002; Cui et al. 2012; Ribeiro et al. 2005). Fixing the surface concentration of the transport species to their saturation values, however, cannot be justified for the current system since it is working far from equilibrium conditions (Abdulrazzaq et al. 2016). In this case, a kinetic model for the evaporation rate can be adopted, for instance, Langmuir law for evaporation from thin films (Zemansky & Dittman 1997), to calculate the mass flux for each component at the interface:

$$\dot{n}_i = k_i\left(x_i \gamma_i P_i^* - P_i\right) \tag{7.10}$$

where $\dot{n}_i$ is the evaporative flux for each component at the interface, k_i is the evaporation constant which represents the amount of component evaporated per unit time per unit area per unit partial pressures difference, x_i is the mole fraction, γ_i is the activity coefficient, P_i^* is the saturation vapor pressure at the gas-liquid interface and P_i is the partial pressure of the vapor at the bubble bulk for each component.

For the case of heat transfer, the boundary condition is:

$$-\hat{n}\cdot K_g \nabla T_g - \hat{n}\cdot K_l \nabla T_l = \sum \dot{n}_i \, \Delta H_{vi} \tag{7.11}$$

The difference between the heat flux transported to the surface and the heat flux transported away was calculated using Fourier's law which is equated to the latent heat of vaporization ΔH_{vi} weighted by the evaporation rate $\dot{n}_i$ at the interface for each component. $\hat{n}$ is the normal vector and K_g and K_l are the thermal conductivities of air and liquid respectively. The heat flux in the liquid phase can be neglected because the outside thermal resistance is very small compared to the inside resistance in the gas phase (Alabovskii, 1972).

Eq. (7.10) is introduced originally in this work. No such rate equation has been used before in the modelling of gas-liquid interfaces. This equation simplifies to Raoult's Law at equilibrium conditions, (i.e. $k_i \to \infty$), thereby stating that evaporation (or condensation) is driven by the interfacial partial pressure from its predicted Raoult's Law value at equilibrium. Partial pressures of vapor components in the bubble P_i were calculated using the ideal gas law as shown in equation 7.12 because of the conditions of low pressures and high temperatures considered here. The activity coefficients were calculated using the Wilson model (equation 7.13), while vapor pressures P_i^* were calculated using the Antoine equation (equation 7.16).

Ideal gas law:

$$P_i = C_i R_g T \tag{7.12}$$

Wilson equation:

$$ln\gamma_i = -ln\left(x_i + \Lambda_{ij}\right) + x_j \left[\frac{\Lambda_{ij}}{x_i + \Lambda_{ij} x_j} - \frac{\Lambda_{ji}}{\Lambda_{ji} x_i + x_j}\right] \tag{7.13}$$

where:

$$\Lambda_{ij} = \frac{V_j}{V_i} exp\left[-\frac{\lambda_{ij}}{R_g T}\right] \tag{7.14}$$

$$\Lambda_{ji} = \frac{V_i}{V_j} exp\left[-\frac{\lambda_{ji}}{R_g T}\right] \tag{7.15}$$

where $\lambda_{ij}\ and\ \lambda_{ji}$ are Wilson parameters for ethanol water mixture (Assael et al. 1996), V_i and V_j are the molar volumes of ethanol and water respectively (Khattab et al. 2012), x_i and x_j are mole fractions of ethanol and water respectively and R_g is the gas constant.

Antoine equation:

$$\ln P^* = A - \frac{B}{C + T} \tag{7.16}$$

where *A*, *B* and *C* are Antoine constants (Assael et al. 1996).

The evaporation parameter k_i is difficult to predict. Himus & Hinchley (1924) measured this parameter experimentally for pure water evaporated by air and found it to be around 5×10^{-6} mol/m^2 Pa s. For our system, this unknown parameter was estimated using a least squares error method and our experimental data on the separation of ethanol-water mixtures (Abdulrazzaq et al. 2016) with the value found by Himus & Hinchley as an initial guess. Figure 7.2 shows a parametric study for the estimation of K value. The minimum error was associated with a value of 2.4×10^{-5} mol/m^2 Pa s for water as shown in figure 7.2. For ethanol, the best approximation was found to be 2.5 times greater than that of water, in accord with the ratio of their vapor pressures.

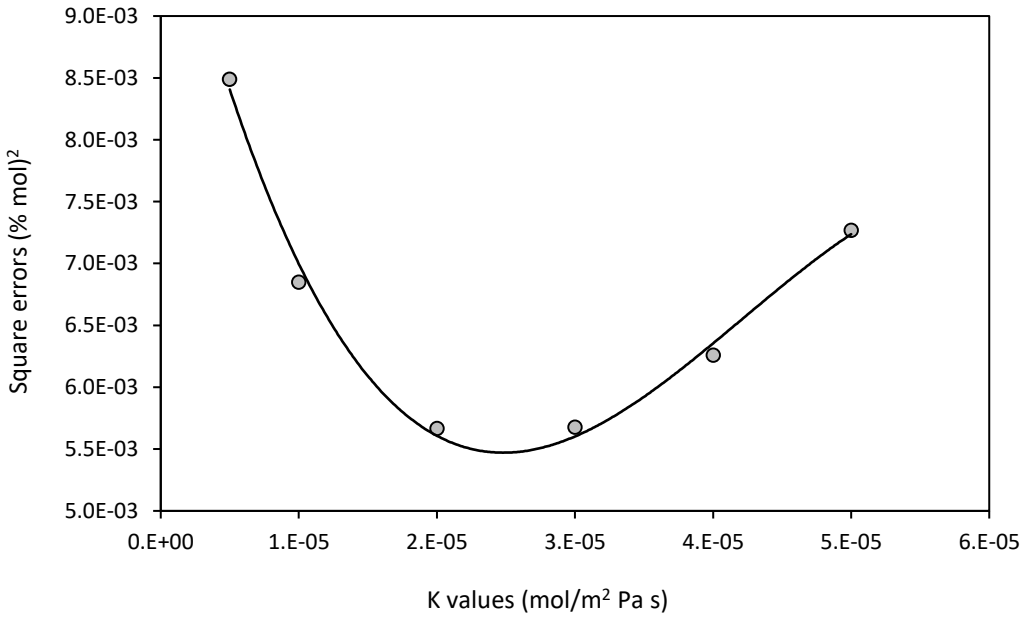

Figure 7.2: k values versus the square errors.

7.3 Numerical method

Numerical analyses were carried out using the Galerkin finite element method (FEM) with COMSOL Multiphysics V4.3a in order to solve the governing equations. Analyses were carried out on two computers. The first one contained an Intel Core i5-2430M CPU running at 2.4 GHz with 6 GB of installed memory and the second one had 12 processors and 96 GB of installed memory. 56620 triangular mesh elements were used to create the domain of the computational model. Due to the axisymmetry, calculations were carried out in a semi-circle in the *r-z* plane as shown in figure 7.3.

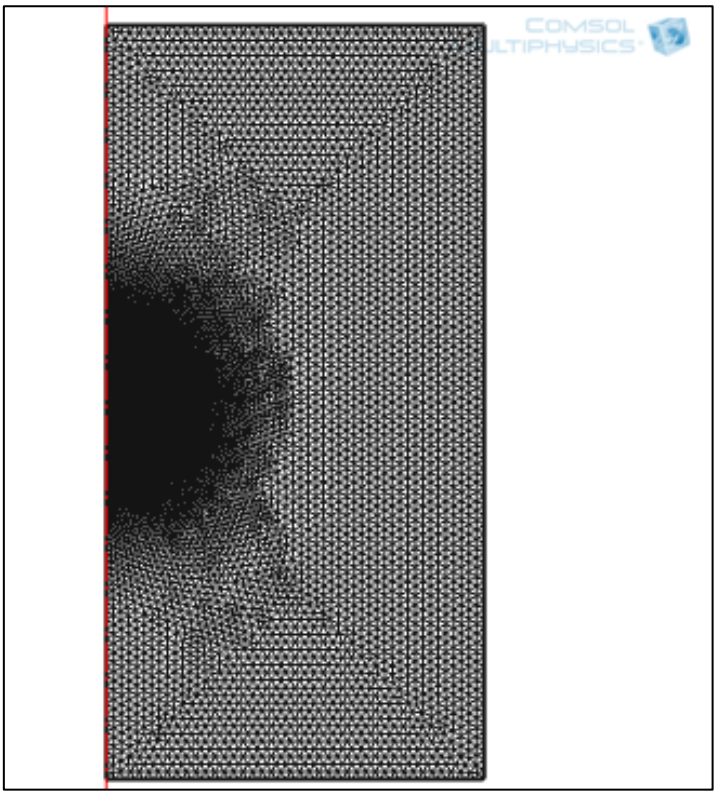

Figure 7.3: The 2-D axisymmetric, free triangular mesh used for modelling.

7.3.1 Grid convergence study

It is well known that the accuracy and stability of the numerical results are affected significantly by the quality of the mesh. The higher the number of mesh elements, the higher the accuracy that can be achieved. However, computational time and memory requirements are serious limitations. Mesh sensitivity analysis aim to find the optimum number of elements at which

the required accuracy can be achieved in a short running time. In the current work, the numerical stability of the results was checked by varying the mesh refinement whilst monitoring the change in the average mole fraction of ethanol and the non-dimensional bubble temperature ratio (T_b/T_0) after 0.002 s. Mesh comparisons are presented in table 7.1. The average mole fraction of ethanol and the temperature ratio differed by only 0.0057% and 0.0027% respectively between grid meshes containing 56620 and 100790 elements. For this reason, grid (1) was adopted for the further calculations as it has the least computational cost.

Table 7.1: Grid convergence results at t=0.002 s

Grid	***No. of elements***	***Concentration of ethanol [%mole]***	T_b/T_0
1	56620	0.70460	0.74728
2	68236	0.70461	0.74727
3	86422	0.70463	0.74726
4	100790	0.70464	0.74726

Numerical stability was also explored while changing the size of the computational domain of the liquid phase. The results are given in table 7.2 which demonstrate excellent stability for both bubble concentration and temperature, so case 1 was selected for the current study.

Table 7.2: Domain size convergence results at t=0.002 s

Case	***Width×height of the computational domain***	***No. of elements***	***Concentration of ethanol [%mole]***	T_b/T_0
1	10 R×10 R	56620	0.70460	0.74728
2	15 R×15 R	66880	0.70460	0.74728
3	20 R×20 R	81628	0.70459	0.74728

7.4 Results and Discussion

The results of the numerical study for the circulating microbubble are presented in this section. The initial focus will be on discussing the trends of the temperature and concentration profiles of the microbubble with time. A sensitivity study of the effect of varying bubble size, initial

bubble temperature and liquid composition on the modelling results will be presented in the subsequent section.

7.4.1 Modelling profiles

The microbubble profile of ethanol concentration distribution, temperature field and velocity vectors is shown in figure 7.4 after 0.0015 s.

Clearly, the temperature profile is nearly isothermal at 294 K and the concentration profile of ethanol is nearly constant throughout the bubble at around 1.64 mol/m^3. This outcome is mainly due to the intensive internal circulation of the microbubble, as shown clearly in figure 7.5, which helps to homogenize it both thermally and chemically at sufficiently early residence times in the liquid (Ubal et al. 2010; Ubal et al. 2011; Zimmerman et al. 2013).

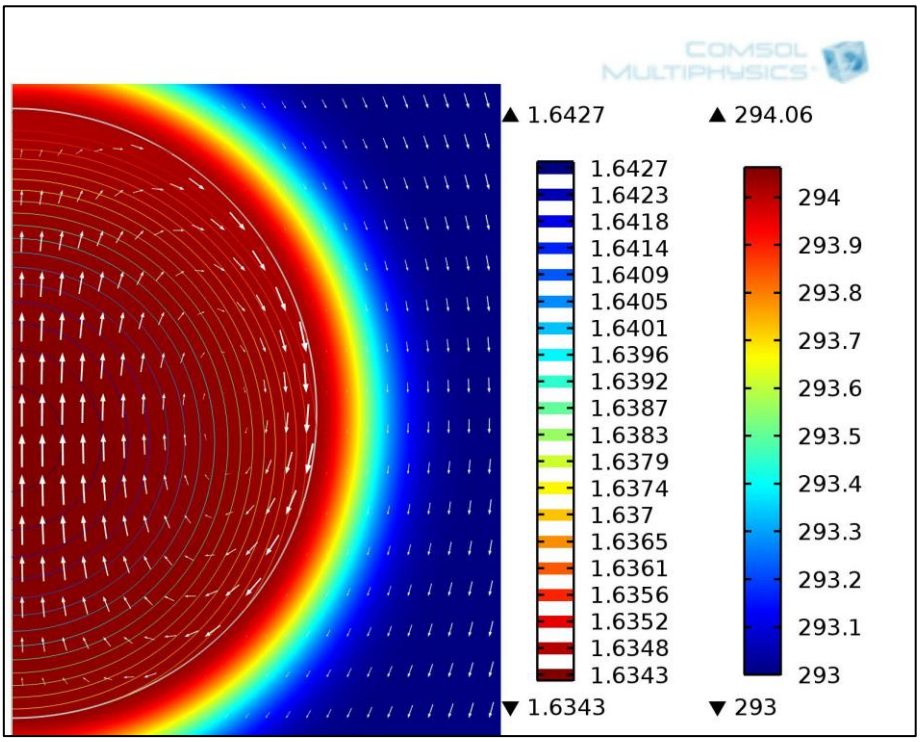

Figure 7.4: Microbubble profile with R=100 microns, T_0=423 K, ambient liquid temperature of 293 K and 50% mole initial ethanol liquid concentration after $t = 0.0015$ s. The arrows represent the steady state velocity field inside and outside the bubble. The contours indicate ethanol concentration (mol/m^3) inside the bubble and the shading represents the temperature (K).

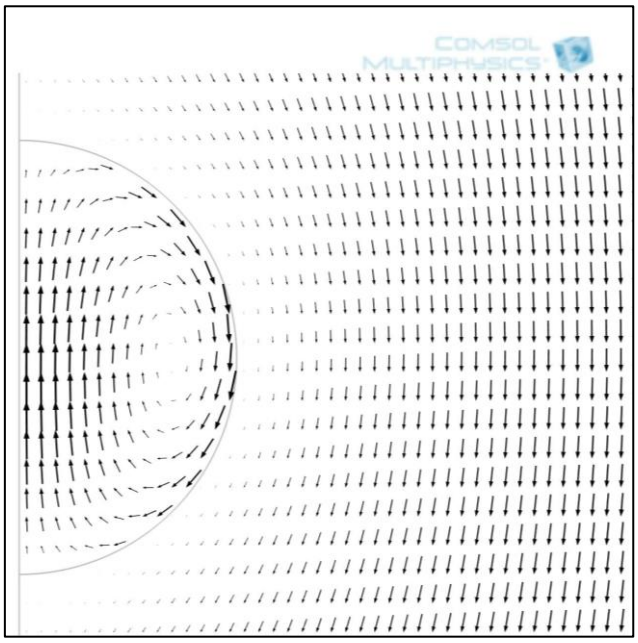

Figure 7.5: The steady state velocity field inside and around the bubble.

Figures 7.6, 7.7 and 7.8 show respectively the time profiles for the average bubble temperature, the average bubble concentration and the average mole fraction obtained from the numerical modelling.

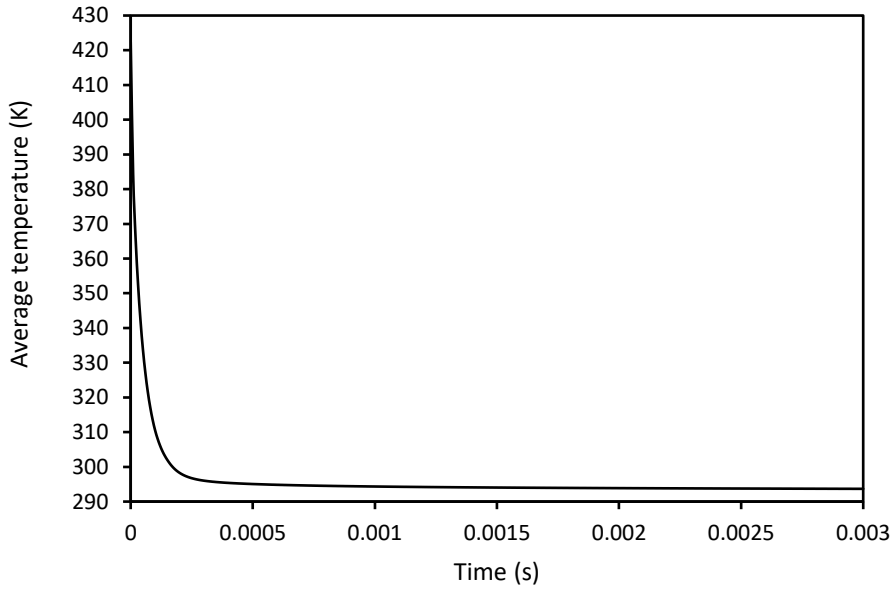

Figure 7.6: The variation of the average microbubble temperature with time. The initial conditions are 50% mole ethanol liquid concentration and bone dry air with T_0 =423 K injected in the microbubbles.

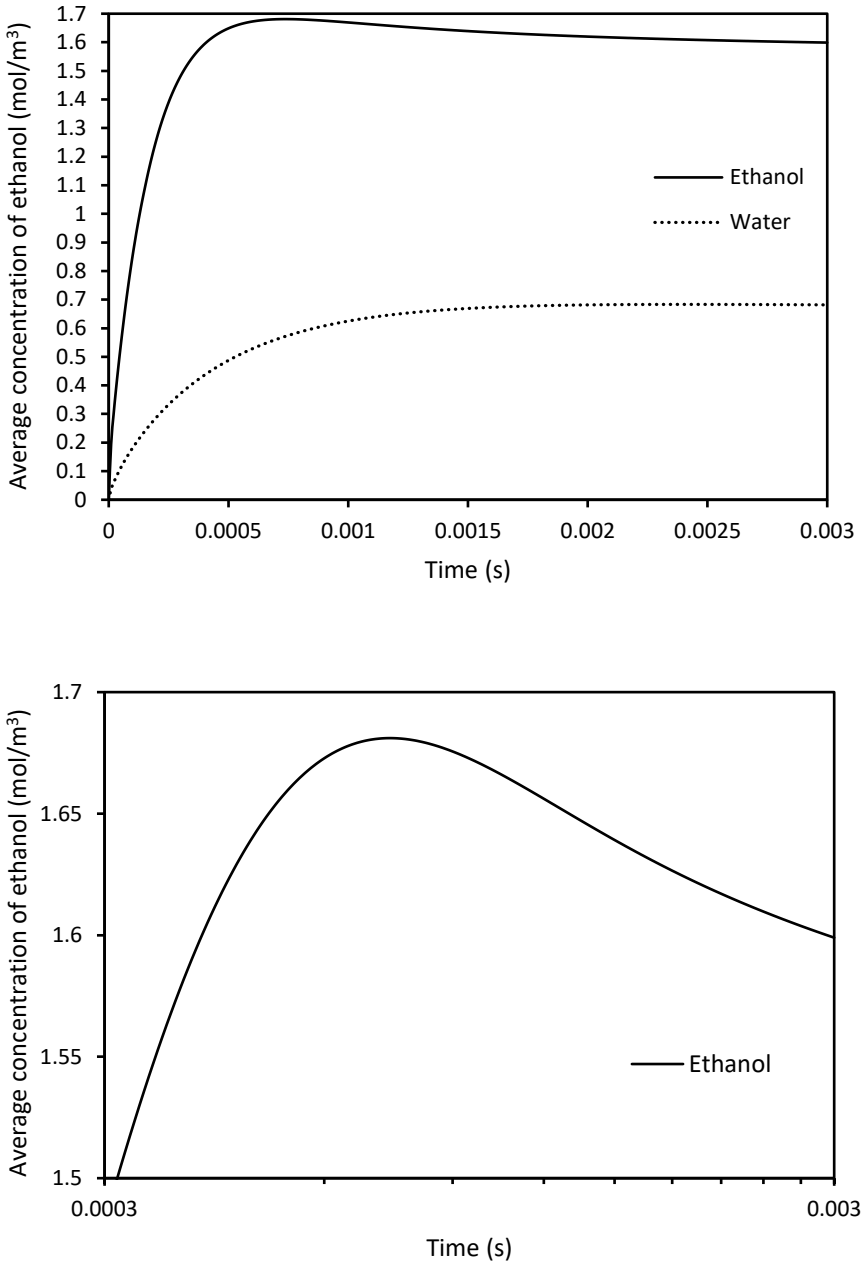

Figure 7.7: The variation of the average concentration of ethanol and water in the microbubble with time. The initial conditions are 50% mole ethanol liquid concentration and bone dry air with T_0=423 K injected in the microbubbles.

Modelling profiles indicate that the heat and mass transfer dynamics of the microbubble are strongly time-dependent. Figure 7.6 shows that the average temperature profile decreases rapidly with time from its initial value of 423 K until it almost reaches equilibrium with the

ambient temperature of 293 K after 0.003 s. This behavior can be attributed to the effect of liquid evaporation into the bubble. When vaporization occurs, latent heat of evaporation is lost which causes the bubble temperature to decrease sharply at short contact times.

Figure 7.7 shows the change of the average composition of ethanol inside the circulating microbubble with the residence time in the liquid phase. This figure clarifies how the maximum ethanol concentration is rapidly attained within a very short contact time (around 0.00072 s) in the liquid due to the high internal convection which leads to a fast evolution of the vapor concentration in the microbubble. Beyond this point (i.e. 0.00072 s), condensation of the previously evaporated vapors occurs as the bubble cools, causing a decrease in the bubble concentration and sensible heat transfer to the liquid. This means that there is competition between the latent and sensible heat transfers and the dominance of either of them depends on the residence time of the microbubble in the liquid phase. At shorter bubble residence times, a greater level of evaporation can be achieved, however, at longer contact times, sensible heat becomes more important.

It is possible to control the contact time of the rising microbubbles in the liquid so that the transfer processes (i.e. evaporation and heat transfer) can be preferentially selected for transfer to or from the microbubble. Contact times for the microbubbles can be set experimentally by altering the depth of the liquid through which bubbles can rise. If the application requires high heat transfer efficiency, higher liquid depths are used to maximize sensible heat transfer. However, for applications where temperature rise is not favorable, for instance those dealing with thermally sensitive materials, shallower liquid levels should be applied to reduce the residence times of the bubbles and to achieve more evaporation. These results are consistent with the previous findings of the evaporation of the ethanol-water binary system which demonstrated that the recovery efficiency of ethanol from the liquid phase increased as the height of liquid mixture layer decreased (Abdulrazzaq et al. 2016).

Figure 7.8 presents the time profiles of the mole fractions of ethanol and water at the bubble bulk which show that the maximum ratio for ethanol to water was achieved at $t=1.3\times10^{-4}$ s and decreased thereafter. The reason for this outcome is that the chance of ethanol evaporation is higher initially because of its higher vapor pressure than that of water. However, as time passes, the concentration difference of ethanol across the film at the gas-liquid interface drops, leading to an increase in the likelihood of water vaporization. It is important to mention that at this time

the bubble internal temperature is about 305 K which is still higher than the ambient liquid temperature.

Figure 7.9 presents information about the change of the evaporation rate ($\dot{n}$) at the bubble surface with time. As can be seen, the evaporation rates for both ethanol and water are higher initially and then drop to negative values which reflect the condensation effect.

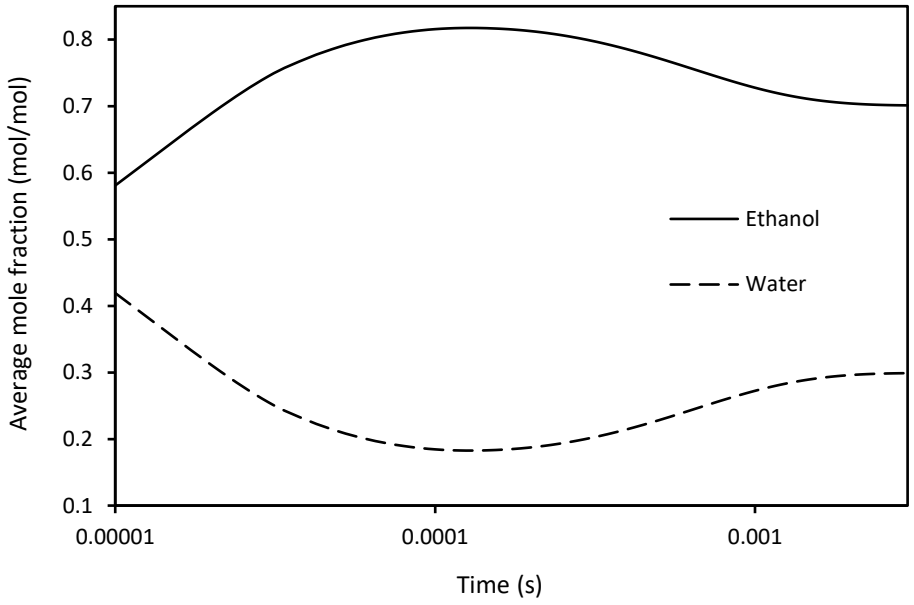

Figure 7.8: The variation of the average mole fractions of ethanol and water in the microbubble with time. The initial conditions are 50% mole ethanol liquid concentration and bone dry air with T_0=423 K injected in the microbubbles.

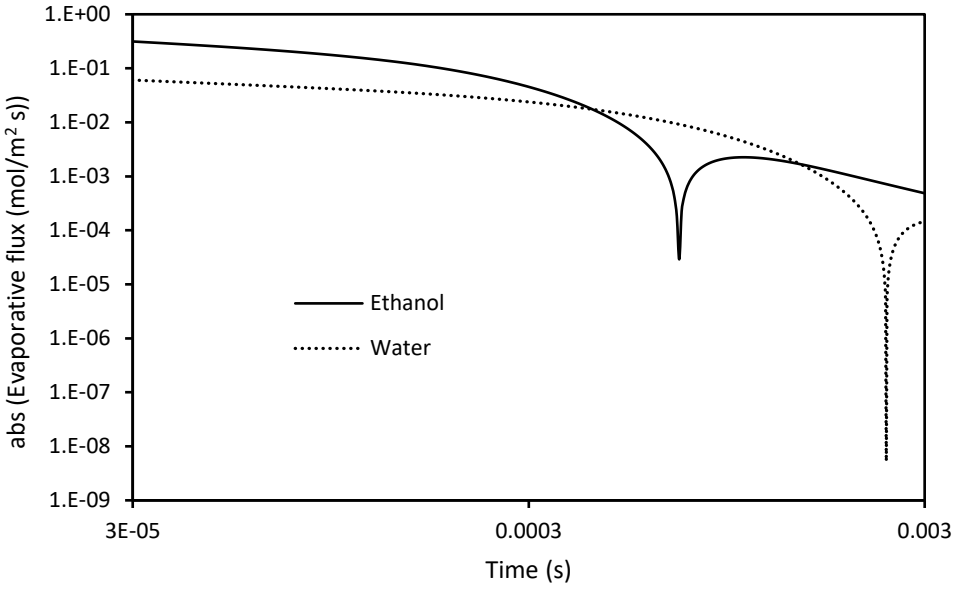

Figure 7.9: A log-log plot for the average mass fluxes for ethanol and water at the bubble skin versus time. The initial conditions are 50% mole ethanol liquid concentration and bone dry air with T_0=423 K injected into the microbubbles. The results show that the interfacial fluxes for ethanol and water switch from evaporation to condensation at 7.2×10^{-4}s and 2.4×10^{-3}s respectively.

7.4.2 Model sensitivity analysis

The next step is to study the influence of some of the key parameters that affect the separation efficiency of liquid mixtures by microbubbles such as bubble size, microbubble air temperature, the initial composition of the liquid mixture and evaporation constant (i.e. k_i parameter) on both the bubble concentration and bubble temperature profiles.

7.4.2.1 Variation of bubble size

The most critical parameter that affects the interfacial mass and heat transfers across the gas-liquid interface is bubble size. Figure 7.10 shows the effect of different bubble sizes (different terminal velocities) on the average concentration of ethanol obtained from seven model computations. Liquid concentration and initial temperature of the bubble were kept at 50% mole and 393 K for all calculations.

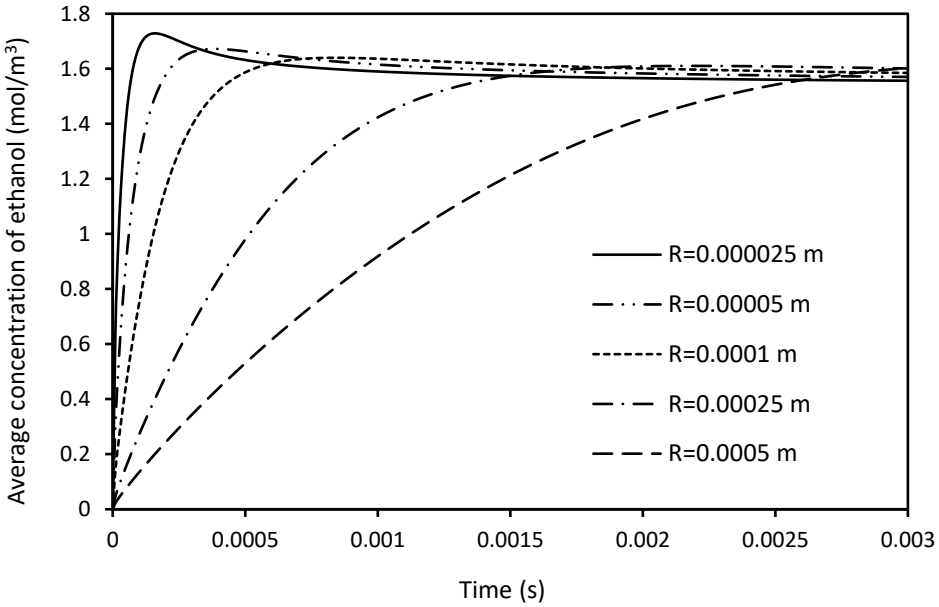

Figure 7.10: Variation of the average concentration of ethanol with bubble size. The initial bubble temperature is T_0 =393 K and the initial liquid concentration is 50% mole ethanol.

Numerically, these results demonstrate that small bubbles are more efficient in the stripping of ethanol than larger bubbles especially at very short residence times in the liquid. In comparison with fine bubbles, microbubbles have higher surface area to volume ratios and faster mass transport which leads to a faster evolution of the vapor concentration inside them and thereby make microbubbles more effective than fine bubbles in the separation process at shorter contact times. As time passes, the concentration of microbubbles approaches that of the larger bubbles. This occurs because microbubbles lose most of their contents when they cool due to the condensation effect. This explains why there is almost no difference in the separation of ethanol for the experiments with and without the existence of the fluidic oscillator at the liquid level 30 mm (see figure 4.3).

Figure 7.11 shows clearly how tiny bubbles can deliver most of their provided enthalpy at sufficiently shorter residence times in the liquid phase whilst larger bubbles are almost still at their initial injection temperature at short times because of their weak internal convection.

Figure 7.12 depicts the difference between the profiles of microbubble and fine bubbles at $t =$ 0.0003 s. Numerically, it was found that the solute concentration gradient in the fine bubble is confined to a relatively thin layer around the bubble skin. In addition, the temperature profile seems to be unchanged from its initial injected value (around 390 K) with only a thin layer in

the vicinity of the bubble surface which is nearly equal to the liquid temperature. The microbubble, by contrast, is well mixed at this time. The temperature profile is nearly isothermal as well as the concentration profile is almost constant.

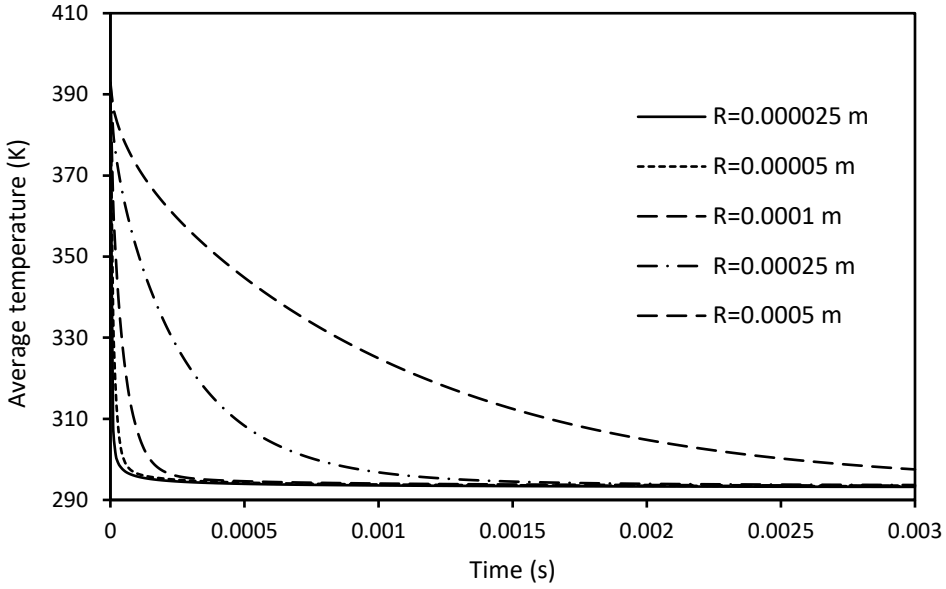

Figure 7.11: Variation of the average temperature of the bubble with bubble size R=0.0005 m (top), R =0.00025 m, R =0.0001 m, R =0.00005 m, R =0.000025 m (bottom). Initial bubble temperature is T_0 =393 K and initial liquid concentration is 50% mole ethanol.

These findings are in agreement with the results of an analogous study by Ubal et al. (2010) on a single buoyant rising liquid drop. In their model, a study of the effect of the drop internal circulation on the mass transfer dynamics confirmed that the evolution of mass transfer for a circulating drop is much faster than that of a rigid drop (i.e. without circulation) in which the mass profile is confined within a thin layer near the drop surface. Similar numerical results were obtained by Guy et al. (1992) on modelling the heat and mass transfer dynamics of hot gas bubbles rising in water which confirmed that the mass transfer is faster for the bubbles with internal circulation.

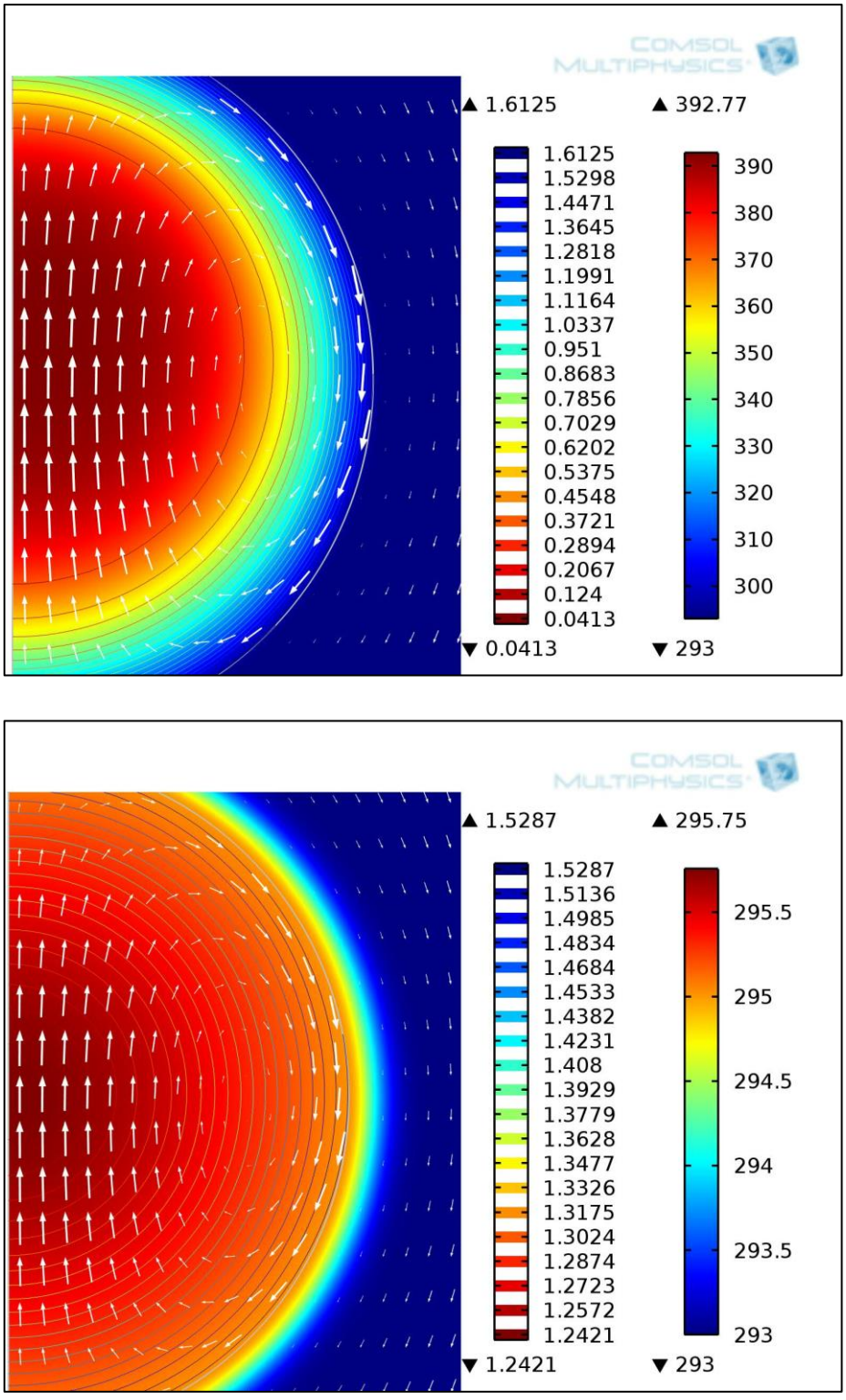

Figure 7.12: The temperature and concentration profiles at $t = 0.0003$ s. for (a) fine bubble with R=0.0005 m and (b) microbubble with R=0.0001 m. The initial conditions are 50% mole ethanol liquid concentration and bone dry air with T_0 =393 K injected in the microbubbles.

7.4.2.2 Variation of inlet gas temperature

Figure 7.13 presents the comparison of five average ethanol concentration profiles at various inlet microbubble temperatures. The liquid temperature and initial liquid mole fraction were kept at 293 K and 50% mole respectively for all modellings.

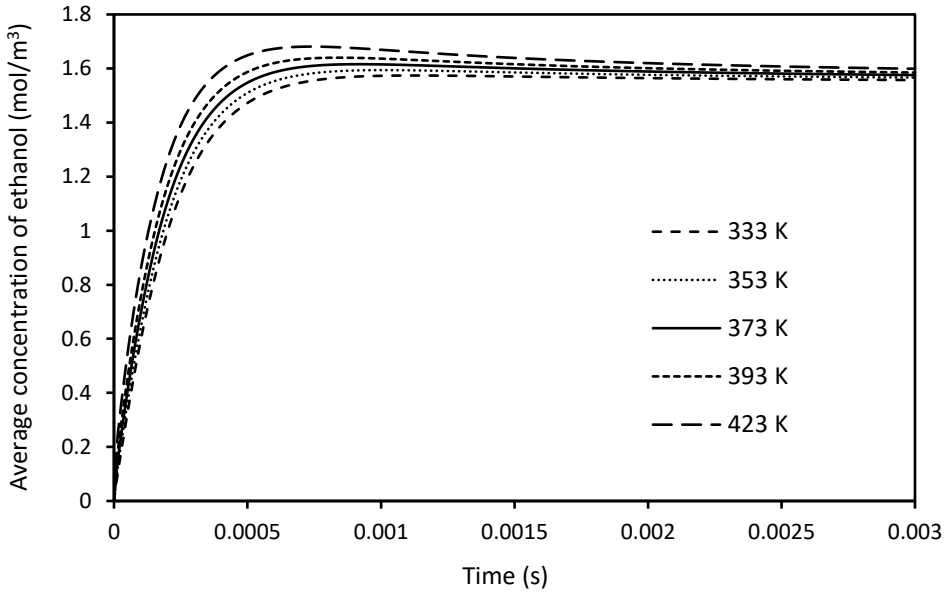

Figure 7.13: Variation of the average concentration of ethanol with bubble temperatures T_0 =423 K (top line), 393 K, 373 K, 353 K and 333 K (bottom line). The initial condition is bone dry air injected into the microbubbles.

The results show that the maximum concentration of ethanol rises with the inlet microbubble temperature and that the lower the initial bubble temperature, the slower the re-condensation progressed. These findings are consistent with the results of the experimental work for both binary and azeotropic mixtures which show that by increasing the injection temperature of the air microbubbles, the removal efficiency of ethanol increases.

At longer residence times, all bubbles reached thermal equilibrium with the surrounding liquid mixture as shown in figure 7.14. The expected additional evaporation at equilibrium achieved by injecting higher bubble temperatures can be neglected at this level of heating due to two effects. Firstly, the volumetric heat capacity of the liquid, which is the density of a substance multiplied by the heat capacity (ρcp) is three orders of magnitudes higher than that of the vapor

(Zimmerman et al. 2013). Secondly, the size of the computational domain is an order of magnitude larger than the bubble radius.

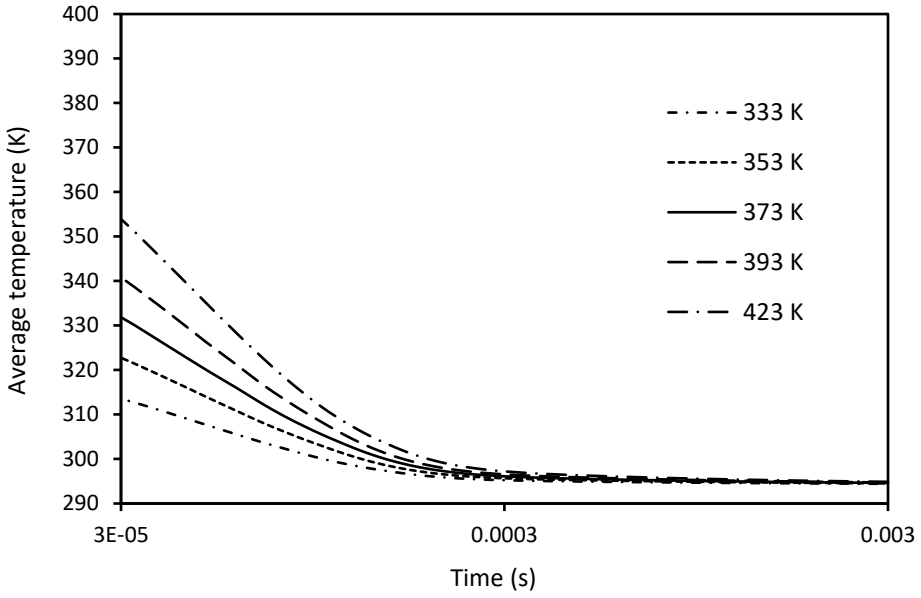

Figure 7.14: Semi-log plot of the variation of the average bubble temperature at different initial bubble temperatures T_0 =423 K (top line), 393 K, 373 K, 353 K and 333 K (bottom line). The initial condition is bone dry air injected into the microbubbles.

7.4.2.3 Variation of liquid mixture concentration

In order to check the influence of ethanol content in the liquid phase on the heat and mass transfer dynamics of the bubble, a sensitivity study was performed which involved changing the mole fraction of ethanol in the liquid phase. Generally, liquid properties such as density, viscosity and surface tension have great impact on the bubble behavior as they can affect both the bubble size and the residence time.

Figure 7.15 shows the concentration profiles of ethanol at five different liquid ethanol mole fractions. The initial condition is bone dry air at an injection temperature of 393 K. Table 7.3 lists the concentrations of ethanol in the microbubble regime achieved by numerical calculations with the isothermal equilibrium values (Flick 1998).

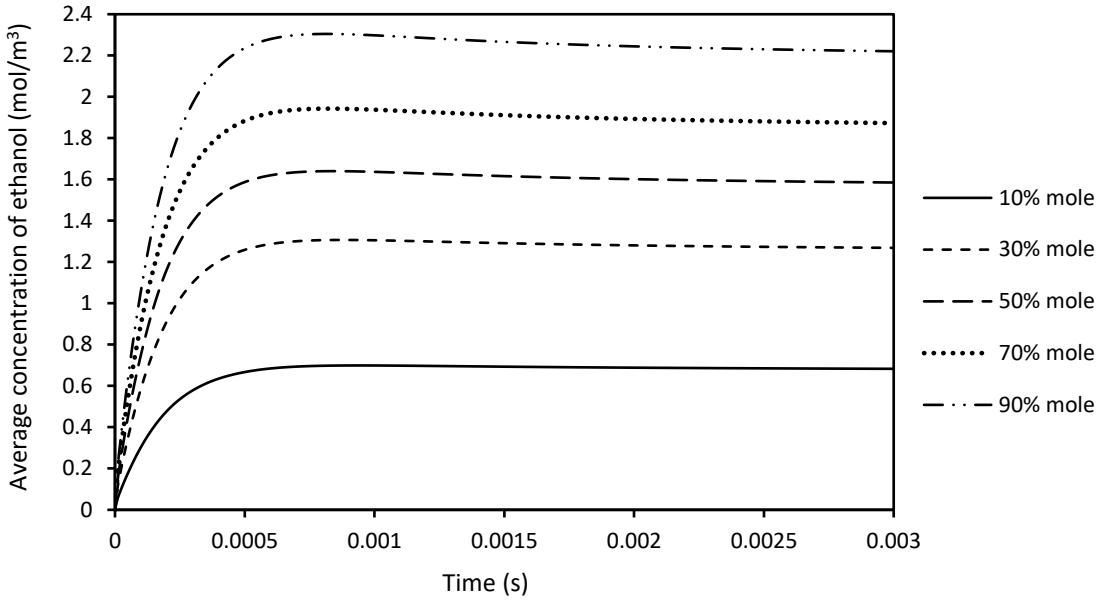

Figure 7.15: Average concentration profile data for ethanol at different liquid compositions: 90% mole ethanol (top line), 70% mole, 50% mole, 30% mole, 10% mole (bottom line). The initial condition corresponds to bone dry air at T_0 =393 K injected into the microbubbles.

Table 7.3: Ethanol vapor concentrations in the bubble regime as predicted by the numerical study and isothermal equilibrium data for different initial liquid ethanol mole fractions.

Liquid concentration (% mol)	***Vapor concentration at t=0.00014 s (% mol)***	***Vapor concentration at t=0.003 s (% mol)***	***Final T_b at t= 0.003 s (K)***	***Isothermal equilibrium data at Final T_b (%mole)***
10	59.9	43.6	293.4	44.9
30	75.8	62.0	293.5	60.9
50	81.9	70.1	293.5	68.6
70	87.3	78.1	293.6	77.6
90	94.6	90.2	293.5	90.8

Not surprisingly, the average concentration of ethanol in the bubble phase increases as the concentration of ethanol in the ambient liquid phase rises as a result of increasing its proportion, and consequently its saturation pressure at the gas-liquid interface. The most interesting

findings can be seen in the data presented in table 7.3, which clearly demonstrate that the concentrations of ethanol in the bubble phase are higher than those achieved at equilibrium state within short residence times for all liquid ethanol compositions considered in this study. With sufficiently long contact times (in excess of around 0.003 s) the bubble achieves equilibrium conditions both chemically and thermally.

7.4.2.4 Variation of *k* parameter

Although the value of *k* parameter was estimated here by least square analysis method using our experimental data from the separation of ethanol-water mixtures (Abdulrazzaq et al. 2016), it is important to understand how this parameter affects the behavior of the system. Figures 7.16 and 7.17 show the sensitivity of the time profiles of the average temperature and concentration respectively to different values of *k* . The initial liquid ethanol concatenation and the initial bubble temperature were fixed at 50% mole and 393 K for all cases.

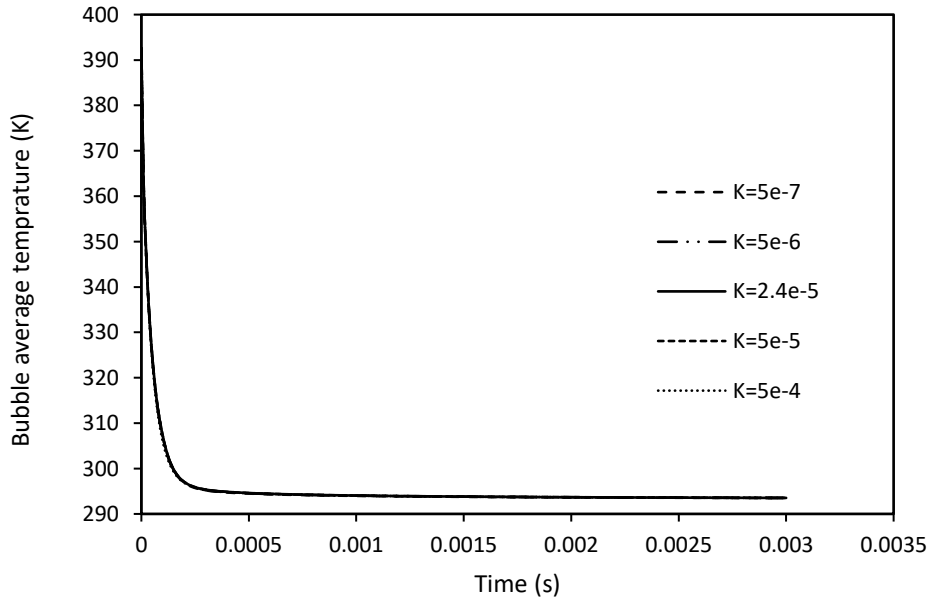

Figure 7.16: Variation of the average temperature of the bubble with *k* value (mol/m^2 Pa s). Initial bubble temperature is T_0 =393 K and initial liquid concentration is 50% mole ethanol.

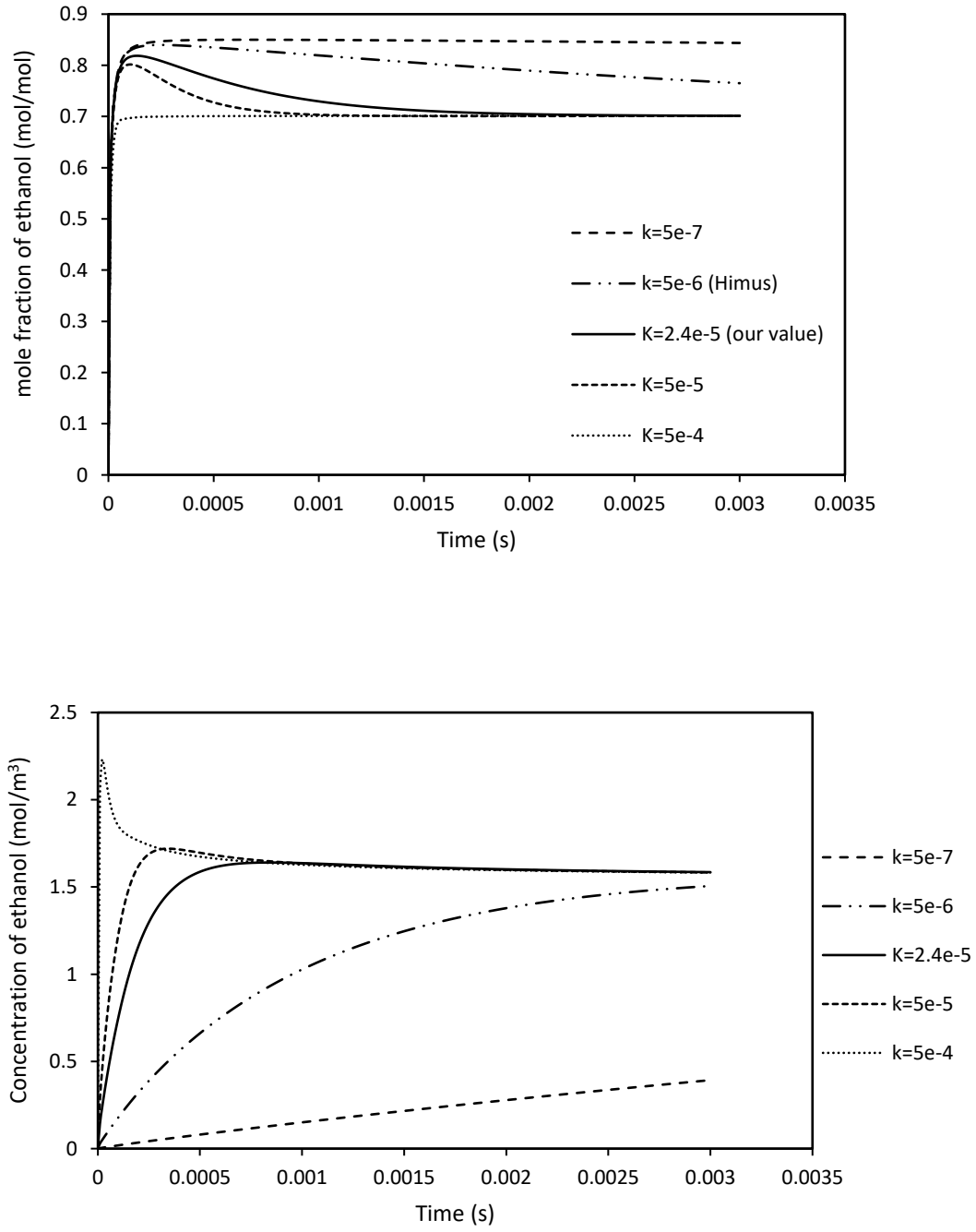

Figure 7.17: Variation of the average concentration of ethanol with k value (mol/m^2 Pa s), top is mole fraction (mol/mol) and bottom is concentration (mol/m^3). The initial bubble temperature is T_0 =393 K and the initial liquid concentration is 50% mole ethanol.

It is clear from the data that the smaller the value of k , the slower the mass transfer evolution and this associated with nearly isothermal systems. On the other hand, large values of k (i.e.

k_i=5e-4 mol/m^2 Pa s) correspond to equilibrium systems with flashing significant amount of vapor at very short contact time followed by re-condensation as the bubble cool down. It can also be noticed that the *k* value applied in the current work (i.e. k_i =2.4e-5 mol/m^2 Pa s) ensures non-equilibrium dynamics that are appropriately rapid so it is consistent with the observation of our system which is neither always at isothermal nor always at equilibrium.

Figure 7.18. presents the difference between the mass boundary condition adopted here at the gas-liquid interface (i.e. Eq. 7.10) and that for the equilibrium state. The equilibrium boundary condition at the interface was stated by fixing the partial pressure of each component to the saturation pressure at the interface temperature (Raoult's law):

$$P_i = x_i \gamma_i P_i^* \tag{7.17}$$

From which the molar concentration for each component was calculated at the interface temperature T_s using the ideal gas law:

$$c_i^*(T_s) = \frac{x_i \, \gamma_i \, p_i^*(T_s)}{R_g \, T} \tag{7.18}$$

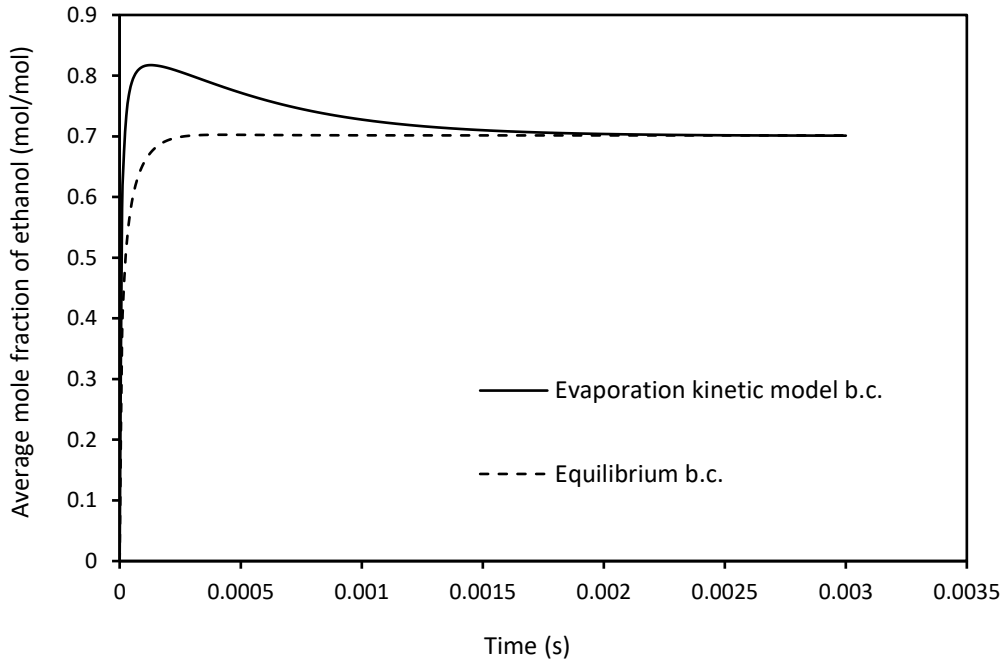

Figure 7.18: The average mole fraction profiles of ethanol at different boundary conditions at the gas-liquid interface.

7.5 Comparison between experimental and modelling data

In order to assess the validity of the model, the results of the modelling work have been compared with the results from our previous experimental work on ethanol-water system. The modeling approach adopted here used the concentration of this single bubble size to predict the concentration of ethanol that was measured experimentally at the top of the liquid mixture layer in the header space of the bubble tank (Abdulrazzaq et al. 2016). Typically, the assumption of a single bubble size distribution is reasonable for microbubbles generated by fluidic oscillation since interactions between bubbles are infrequent and bubble size distribution is very narrow (Zimmerman et al. 2008; Hanotu et al. 2013; Hanotu et al. 2012).

The most challenging part in the comparison is computing the residence time of the bubbles in the liquid for our experiments. This time is a combination of three elements: *i)* the formation time of the bubble from the pore of the diffuser, when it is in a contact with the liquid but has not released *ii)* the ascending time in the liquid and *iii)* the time for the bubble to burst at the top surface. For this reason, we have taken the temperature of the header space that measured by the experiments as an indication for the contact time at which the bubble exits. The average temperature in the header space for the range of liquid compositions that tested in the experiments was around 300 K and according to the numerical results this value coincides with a time of about 0.00014 s.

Figure 7.19 compares the model predictions at t= 0.00014 s with the experimental data that obtained from the separation of ethanol-water mixtures under conditions of 3 mm liquid height and 90 °C microbubble air temperature (table 5.1). The same initial conditions were used in both the experimental work and the modellings for microbubble temperature, liquid mixture temperature and liquid ethanol compositions.

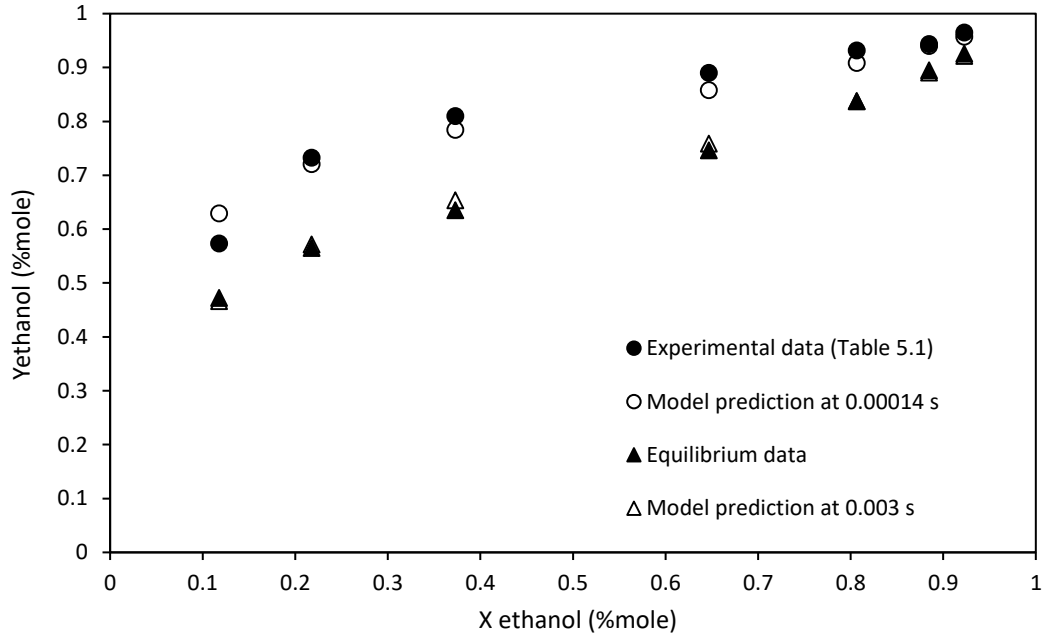

Figure 7.19: Comparison between experimental and modelling vapor mole fractions data (Y ethanol) for different liquid ethanol mole fractions (X ethanol) after 0.00014 s and 0.003 s. The initial conditions are bone dry air with T_0=363 K injected into the microbubble and 293 K liquid temperature.

It can be clearly seen that the experimental data for the separation of ethanol-water mixtures are consistent with the findings of the computational model at both the non-equilibrium stage (short residence times in the liquid or thin liquid levels) and then equilibrium stage (longer residence times or high liquid depths) for all liquid ethanol compositions considered in the experimental work. Our previous experiments also showed a decrease in the liquid temperature with decreasing liquid depth in the bubble tank, an increase in the outlet gas temperature with decreasing liquid depth, and an improvement in the stripping efficiency of ethanol upon decreasing the depth of the liquid mixture and increasing the temperature of the air microbubbles, all of which are compatible with the predictions of this computational model.

7.6 Summary

A numerical study of a single superheated air microbubble with internal circulation rising in a binary system of ethanol-water has been conducted. The hypothesis that has been tested in this modelling study, is that during a short residence time for the bubble in the liquid, vaporization is dominated and non-equilibrium thermal and chemical operation can be achieved while at

longer residence times sensible heat transfer to the surrounding liquid is favored causing a condensation of the bubble vapors.

It was found that the enrichment of ethanol in the vapor phase is higher than the expected ratios estimated by equilibrium theory at short contact times for a range of initial bubble temperatures and liquid ethanol compositions. It was also found that vaporization is faster than heat transfer to the liquid and that maximum evaporation occurs after a very short contact time in the liquid. This leads to the conclusion that selectivity between evaporation and heat transfer can be engineered by controlling the residence time of the bubbles in the liquid so that maximum evaporation can be achieved with no or minimal heat transfer.

The modelling results were validated by comparing them with data obtained by previous experimental work on the separation of an ethanol-water system by hot air microbubbles. The results from the single bubble model give an excellent prediction of the vapor concentrations obtained by the experimental work on thin liquid films at different liquid ethanol mole fractions.

It worth mentioning here that the kinetics analysis of the ternary mixture data is substantially more difficult, which is why only the binary system challenge is undertaken in this chapter.

The University Of Sheffield.

Chapter Eight

Conclusions and Recommendations for Future Work

Chapter Eight

Conclusions and Recommendations for future work

8.1 Introduction

This chapter summarizes the main conclusions of this study and presents recommendations for future work. Detailed conclusions for each section of this work can be found in their respective chapters.

8.2 Conclusions

This study was focused on setting the basics of a novel distillation technique involving the use hot air microbubbles and investigating its efficiency in the separation and purification of multicomponent liquid mixtures. The efficiency of this technique was also explored in the upgrading and the separation of biofuels, including bioethanol and thermally sensitive pyrolysis oils.

Microbubble distillation is a new technology and still under investigation, but, upon scale up, it promises to contribute effectively to the purification of numerous chemicals. The findings of this work demonstrate that this novel technique has major advantages over traditional separation methods and has great potential to be adapted and applied into any energy industry where distillation is involved. The results obtained from the present study have led to the following conclusions:

- **Reducing the energy requirements associated with traditional separation methods.** The current technique provides a non-wasteful system by heating the gas phase rather than the liquid phase to achieve vaporization and this contributes significantly to save the energy that dissipated in traditional vaporization techniques through heating the liquid only for the purpose of equilibrating with the vapor phase. Additionally, no high pressures or temperatures are required for the separation process nor additional chemicals and fouling membranes. Capital and maintenance costs are

low and the microbubbles used in the separation were generated by an energy efficient method using the novel technology of fluidic oscillation.

- **The ability to engineer the liquid level in the bubble tank so that the selectivity of vaporization over sensible heat transfer can be achieved.** The experimental data in chapter 4 showed that reducing the liquid layer height in the bubble tank from 30 mm to 3 mm, had the result of increasing the separation performance of ethanol considerably from 12% to 81%, as well as decreasing the temperature rise of the liquid mixture. This lead to conclusion that maximum separation with minimum sensible heat transfer can be obtained through minimizing the liquid height in the bubble tank. The results also reported an improvement in the separation efficiency of ethanol from the liquid mixture as the microbubble air temperature is increased. This study was also aimed to explore the effect of the fluidic oscillator on the separation efficiency and the results showed that bubbles with fluidic oscillation perform better in the evaporation than those generated without fluidic oscillation. The concentration of ethanol in the remaining solution under oscillatory flow was decreased from 50% to 21.82% vol. at liquid level of 3 mm, microbubble air temperature of 90°C and evaporation time of 125 min compared to 28.7% vol. ethanol in the final solution using steady flow under the same operating conditions.

- **Elimination of the azeotrope with purity that is dependent on the volume of the liquid mixture in the bubble tank.** The experimental results that presented in chapter 5 demonstrates that microbubble distillation can be successfully used to achieve non-equilibrium operation through decreasing the residence time of the microbubbles in the liquid. Compositions higher than those achieved by equilibrium condition for all liquid ethanol mole fractions were obtained. Experimental results indicated that the breaking of the azeotropic point of the ethanol-water mixture could be achieved using very small liquid mixture levels in the bubble tank. A maximum purity of ethanol (98.2% vol.) was obtained from the use of a thin liquid depth of 3 mm and a microbubble temperature 90°C. However, when the solution thickness was increased to 10 mm, thermal and chemical equilibrium conditions were maintained and no separation was achieved. The findings in chapter 4 and 5 were modelled by a computational study later in chapter 7 which confirmed that at shorter residence times, liquid-vapor ratios in this system do

not obey the equilibrium theory, whilst at longer contact times, equilibrium is established between the contact phases both chemically and thermally. The modelling data also confirmed that maximum vaporization occurred quickly due to the rapid internal circulation of the microbubble while heat transfer was slower. Therefore, by controlling the contact time of the microbubbles, it is possible to achieve separation with minimum or no heat transfer to the liquid.

- **Increasing the purity of products and concentrating solutes without having to boil the mixture, it can thus be used to treat thermally sensitive liquids.** The study conducted in chapter 6 demonstrated that the upgrading of thermally sensitive bio-oil mixtures using microbubble mediated distillation is feasible without destabilizing their properties by heating. Water and other low molecular weight problematic components can be separated simultaneously from bio-oil mixtures at temperatures far below their boiling points. The separation of a mixture of three model compounds of bio-oil: water, acetic acid and acetol was investigated in the current project. After the upgrading process, the water content of the model mixture was found to have been lowered from 30% to 9.51% and its acetic acid content from 15% to 7.28% after 150 min under conditions of a liquid depth of 3 mm and an air temperature of 100°C. It was also found that at higher microbubble temperatures, the recovery efficiency for water together with the acetic acid from the model mixture was enhanced. Improving the quality of these fuels will have a positive effect on reducing greenhouse gas emissions through reducing the dependence on fossil based fuels.

8.3 Recommendations for future work

Following the findings of the current work, several suggestions for the future studies are made:

1. Studying the feasibility of separating more complex and denser model mixtures that contain high molecular weight aldehydes, phenols and sugars and also the feasibility of upgrading real bio-oil mixtures.
2. Extension of the binary computational model into multicomponent systems and studying the effect of the same parameters that were explored in this work.
3. Exploring the use of other types of "off-the-shelf" diffusers with different hydrophilic and hydrophobic properties and different porosities and testing their performance in the

efficiency of separation.

4. Upgrading the system to work on a continuous fashion. Owing to the fact that the current work was limited to batch operation mode, it is recommended for future work to investigate the use of multiple stages with continuous flow of thin liquid layer as shown in figure 8.1 to allow the separation of multicomponent mixtures in single unit.

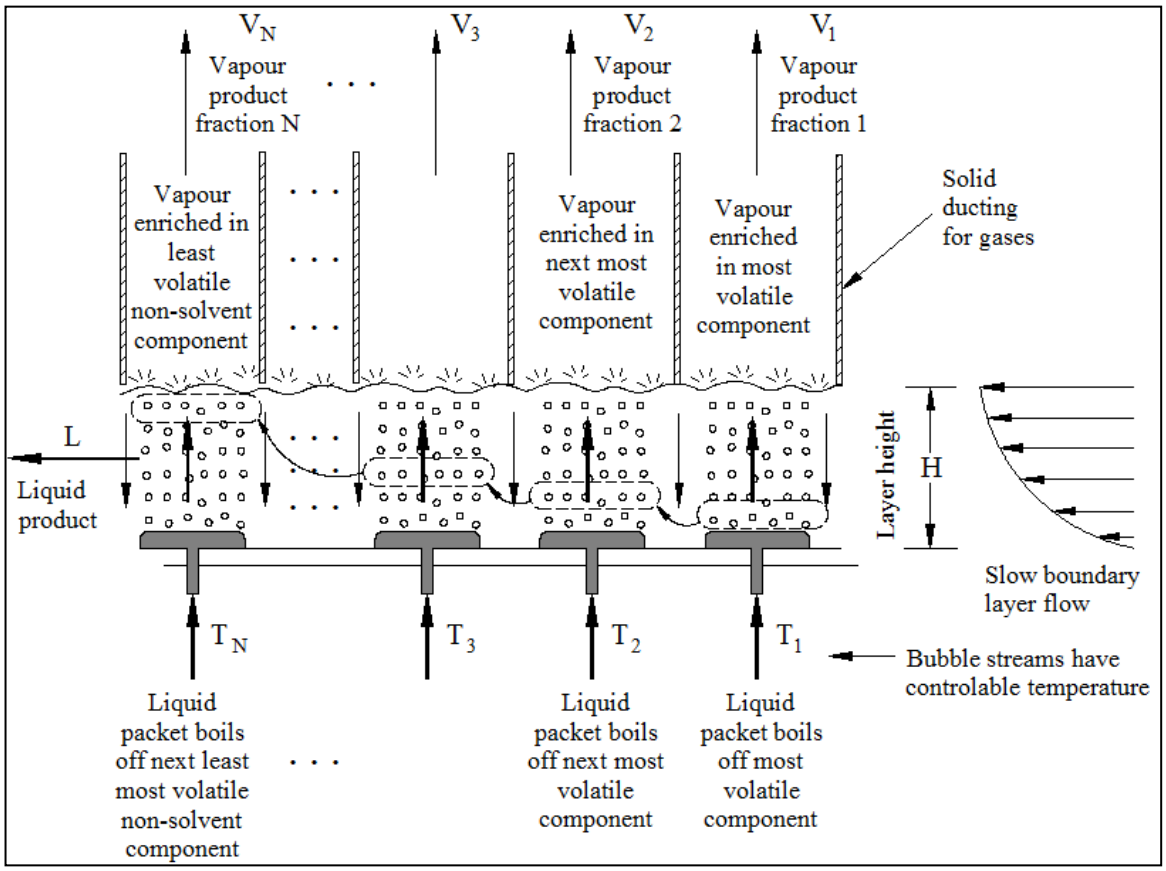

Figure 8.1: Continuous microbubble mediated distillation column concept.

In the continuous system, liquid enters as a thin film of height H at the bottom of the vessel with a superficial velocity U. The liquid solution L is fractionally distilled and the vapor products V_n are taken off at the top. The liquid mixture that traverse the vessel is vertically well mixed due to the bubble recirculation, but horizontally varies in composition and temperature. The bubbles in each segment of the vessel can be heated at different temperatures, appropriate to achieve the desired boiling point for the target component to be driven off preferentially in that segment. Ideally, the lowest temperature at the inlet is the slightly above the boiling point of the least volatile component, and the temperature of the carrier gas creating the microbubbles is increased in each segment, appropriate for the next highest boiling point component.

The University Of Sheffield.

References

References

Abdulrazzaq, N., Al-Sabbagh, B., Rees, J.M. & Zimmerman, W.B., 2016. Separation of azeotropic mixtures using air microbubbles generated by fluidic oscillation. *AIChE Journal*, 62(4), pp.1192–1199.

Agarwal, A., Ng, W.J. & Liu, Y., 2011. Principle and applications of microbubble and nanobubble technology for water treatment. *Chemosphere*, 84(9), pp.1175–1180.

Ahmad, R., Hamidin, N. & Ali, U.F., 2013. Bio-oil Product from Non-catalytic and Catalytic Pyrolysis of Rice Straw. *Australian Journal of Basic and Applied Science*, 7(5), pp.61–65.

Ahmed, M.M., Nordin, M.F. & Azizan, M.T., 2010. Upgrading of Bio-Oil into High-Value Hydrocarbons via Hydrodeoxygenation. *American Journal of Applied Science*, 7(6), pp.746–755.

Alabovskii, A.N., 1972. Thermal interaction at the gas-liquid interface in an apparatus with an immersed burner. *Journal of Engineering Physics and Thermodynamics*, 22(1), pp.83-87.

Al-mashhadani, M.K.H., Bandulasena, H.C.H. & Zimmerman, W.B., 2012. CO2 Mass Transfer Induced through an Airlift Loop by a Microbubble Cloud Generated by Fluidic Oscillation. *Industrial & Engineering Chemistry Research*, 51(4), pp.1864–1877.

Aouinti, L. & Belbachir, M., 2008. A maghnite-clay-H/ polymer membrane for separation of ethanol-water azeotrope. *Applied Clay Science*, 39(1–2), pp.78–85.

Asadullah, M., Rahman, M.A., Ali, M.M., Rahman, M.S., Motin, M.A., Sultan, M.B. & Alam, M.R., 2007. Production of bio-oil from fixed bed pyrolysis of bagasse. *Fuel*, 86(16), pp.2514–2520.

Aslan, N., 2008. Application of response surface methodology and central composite rotatable design for modeling and optimization of a multi-gravity separator for chromite concentration. *Powder Technology*, 185(1), pp.80–86.

Assael, M.J., Trusler, J.P.M. & Tsolakis, T.F., 1996. *Thermophysical properties of fluids*, London: Imperial College Press.

Baeyens, J., Kang, Q., Appels, L., Dewil, R., Lv, Y. & Tan, T., 2015. Challenges and opportunities in improving the production of bio-ethanol. *Progress in Energy and Combustion Science*, 47, pp.60–88.

Balat, M., Balat, M., Kırtay, E. & Balat, H., 2009. Main routes for the thermo-conversion of biomass into fuels and chemicals. Part 1: Pyrolysis systems. *Energy Conversion and Management*, 50(12), pp.3147–3157.

Bastidas, P.A., Gil, I.D. & Rodriguez, G., 2010. Comparison of the main ethanol dehydration technologies through process simulation. *20th European Symposium on Computer Aided Process Engineering* (2010), (ESCAPE20).

Bayerbach, R. & Meier, D., 2009. Characterization of the water-insoluble fraction from fast pyrolysis liquids (pyrolytic lignin). Part IV: Structure elucidation of oligomeric molecules. J*ournal of Analytical and Applied Pyrolysis*, 85(1–2), pp.98–107.

Bertero, M., De La Puente, G. & Sedran, U., 2012. Fuels from bio-oils: Bio-oil production from different residual sources, characterization and thermal conditioning. *Fuel*, 95, pp.263–271.

Bhattacharya, P., Hassan, E.B., Steele, P., Cooper, J. & Ingram, L., 2010. Effect of acid catalysts and accelerated aging on the reaction of methanol with hydroxy- acetaldehyde in bio-oil. *Bioresources*, 5(2), pp.908–919.

Boucher, M.E., Chaala, A., Pakdel, H. & Roy, C., 2000. Bio-oils obtained by vacuum pyrolysis of softwood bark as a liquid fuel for gas turbines. Part II: Stability and ageing of bio-oil and its blends with methanol and a pyrolytic aqueous phase. *Biomass and Bioenergy*, 19(5), pp.351–361.

Bredwell, M.D. & Worden, R.M., 1998. Mass-transfer properties of microbubbles. 1. Experimental studies. *Biotechnology progress*, 14(1), pp.31–8.

Bridgwater, A. V., Toft, A.J. & Brammer, J.G., 2002. A techno-economic comparison of power production by biomass fast pyrolysis with gasification and combustion. *Renewable and Sustainable Energy Reviews*, 6(3), pp.181–248.

Bridgwater, A.V., 1999. Principles and practice of biomass fast pyrolysis processes for liquids. *Journal of Analytical and Applied Pyrolysis*, 51(1–2), pp.3–22.

Bridgwater, A.V., 2003. Renewable fuels and chemicals by thermal processing of biomass. *Chemical Engineering Journal*, 91(2–3), pp.87–102.

Bridgwater, A.V., 2012. Review of fast pyrolysis of biomass and product upgrading. *Biomass and Bioenergy*, 38, pp.68–94.

Burns, S.E., Yiacoumi, S. & Tsouris, C., 1997. Microbubble generation for environmental separations and industrial. *Separation and Purification Technology*, 11(3), pp.221–232.

Campos, F.B. & Lage, P.L.C., 2000. Heat and mass transfer modeling during the formation and ascension of superheated bubbles. *International Journal of Heat and Mass Transfer*, 43(16), pp.2883–2894.

Centeno, A., Laurent, E. & Delmon, B., 1995. Influence of the Support of CoMo Sulfide Catalysts and of the Addition of Potassium and Platinum on the Catalytic Performances for the Hydrodeoxygenation of Carbonyl, Carboxyl, and Guaiacol-Type Molecules. *Journal of Catalysis*, 154(2), pp.288–298.

Chaala, A., Ba, T., Garcia-perez, M. & Roy, C., 2004. Colloidal Properties of Bio-oils Obtained by Vacuum Pyrolysis of Softwood Bark : Aging and Thermal Stability. *Energy & Fuels*, 192(6), pp.1535–1542.

Chaumat, H., Billet, a. M. & Delmas, H., 2007. Hydrodynamics and mass transfer in bubble column: Influence of liquid phase surface tension. *Chemical Engineering Science*, 62(24), pp.7378–7390.

Chen, W., Luo, Z., Yu, C., Li, G., Yang, Y., Zhang, J. & Lu, K., 2014. Catalytic transformations of acids, aldehydes, and phenols in bio-oil to alcohols and esters. *Fuel*, 135, pp.55–62.

Chiaramonti, D., Bonini, M., Fratini, E., Tondi, G., Gartner, K., Bridgwater, a. V., Grimm, H.P., Soldaini, I., Webster, a. & Baglioni, P., 2003. Development of emulsions from biomass pyrolysis liquid and diesel and their use in engines—Part 1 : emulsion production. *Biomass and Bioenergy*, 25(1), pp.85–99.

Chuntanalerg, P., Kulprathipanja, S., Chaisuwan, T., Aungkavattana, P., Hemra, K. & Wongkasemjit, S., 2015. Performance polybenzoxazine membrane and mixed matrix

membrane for ethanol purification via pervaporation applications. *Journal of Chemical Technology & Biotechnology*, 91(4), pp.1173–1182.

Cochran, W.G. & Cox, G.M., 1992. *Experimental Designs* 2nd ed., New York: Wiley.

Corderi, S., Gonzalez, B., Calvar, N. & Gomez, E., 2013. Ionic liquids as solvents to separate the azeotropic mixture hexane/ethanol. *Fluid Phase Equilibria*, 337, pp.11–17.

Cset.iastate.edu Available http://www.cset.iastate.edu/research/current-research/pyrolysis-process-development-unit/. [Accessed 2nd December 2012].

Cui, X., Li, X., Sui, H. & Li, H., 2012. Computational fluid dynamics simulations of direct contact heat and mass transfer of a multicomponent two-phase film flow in an inclined channel at sub-atmospheric pressure. *International Journal of Heat and Mass Transfer*, 55(21–22), pp.5808–5818.

Czernik, S. & Bridgwater, A. V, 2004. Overview of Applications of Biomass Fast Pyrolysis Oil. *Energy & Fuels*, 18(2), pp.590–598.

Czernik, S., Johnson, D., K. & Black, S.K., 1994. Stability of wood fast pyrolysis oil. *Biomass and Bioenergy*, 7(1–6), pp.187–192.

Demirbas, A., 2011. Competitive liquid biofuels from biomass. *Applied Energy*, 88(1), pp.17–28.

Díaz, M.E., Iranzo, A., Cuadra, D., Barbero, R., Montes, F.J. & Galán, M.A., 2008. Numerical simulation of the gas–liquid flow in a laboratory scale bubble column. *Chemical Engineering Journal*, 139(2), pp.363–379.

Di Carlo, S. & Falasconi, M., 2012. Drift correction methods for gas chemical sensors in artificial olfaction systems. In W. Wang, ed. Advances in chemical sensors. InTech.

Diebold, J.P., 2000. A Review of the Chemical and Physical Mechanisms of the Storage Stability of Fast Pyrolysis Bio-Oils. *NREL/SR-570-27613*.

Diebold, J.P. & Czernik, S., 1997. Additives To Lower and Stabilize the Viscosity of Pyrolysis Oils during Storage. *Energy & Fuels*, 11(5), pp.1081–1091.

Drese, J.H., Talley, A.D. & Jones, C.W., 2011. Aminosilica materials as adsorbents for the selective removal of aldehydes and ketones from simulated bio-oil. *ChemSusChem*, 4(3),

pp.379–85.

Edzwald, J., 1995. Principles and applications of dissolved air flotation. *Water Science and Technology*, 31(3–4), pp.1–23.

Elkasabi, Y., Mullen, C. a. & Boateng, A. a., 2014. Distillation and Isolation of Commodity Chemicals from Bio-Oil Made by Tail-Gas Reactive Pyrolysis. *ACS Sustainable Chemistry & Engineering*, 2(8), pp.2042–2052.

Elliott, D.C. & Hart, T.R., 2009. Catalytic hydroprocessing of chemical models for bio-oil. *Energy and Fuels*, 23(2), pp.631–637.

Fakheri, F., Moghaddas, J., Zadghaffari, R. & Moghaddas, Y., 2012. Application of central composite rotatable design for mixing time analysis in mechanically agitated vessels. *Chemical Engineering and Technology*, 35(2), pp.353–361.

Fernando, S., Adhikari, S., Chandrapal, C. & Murali, N., 2006. Biorefineries : Current Status , Challenges , and Future Direction. *Energy & Fuels*, 20(4), pp.1727–1737.

Fisk, C.A., Morgan, T., Ji, Y., Crocker, M., Crofcheck, C. & Lewis, S. a., 2009. Bio-oil upgrading over platinum catalysts using in situ generated hydrogen. *Applied Catalysis A: General*, 358(2), pp.150–156.

Fivga, A., 2011. *Comparison of the effect of pre-treatment and catalysts on liquid quality from fast pyrolysis of biomass*.

Flick, E.W., 1998. *Industrial Solvents Handbook* 5th ed., NY: William Andrew Noyes Publications.

Francis, M.J. & Pashley, R.M., 2009. Application of a bubble column for evaporative cooling and a simple procedure for determining the latent heat of vaporization of aqueous salt solutions. *Journal of Physical Chemistry B*, 113(27), pp.9311–9315.

Garcia-Perez, M., Chaala, A., Pakdel, H., Kretschmer, D. & Roy, C., 2007. Characterization of bio-oils in chemical families. *Biomass and Bioenergy*, 31(4), pp.222–242.

Gardener, J.W. & Bartlett, P.N., 1999. *Electronic noses: principles and applications*, New York: Oxford University Press, Inc.

Gayubo, A.G., Aguayo, A.T., Atutxa, A., Valle, B. & Bilbao, J., 2005. Undesired components

in the transformation of biomass pyrolysis oil into hydrocarbons on an HZSM-5 zeolite catalyst. *Journal of Chemical Technology & Biotechnology*, 80(11), pp.1244–1251.

Gayubo, A.G., Aguayo, T., Atutxa, A., Aguado, R., Olazar, M. & Bilbao, J., 2004. Transformation of Oxygenate Components of Biomass Pyrolysis Oil on a HZSM-5 Zeolite . II . Aldehydes , Ketones , and Acids. *Industrial & Engineering Chemistry Research*, 43, pp.2619–2626.

Guo, Z., Wang, S., Gu, Y., Xu, G., Li, X. & Luo, Z., 2010. Separation characteristics of biomass pyrolysis oil in molecular distillation. *Separation and Purification Technology*, 76(1), pp.52–57.

Guo, Z., Wang, S., Xu, G. & Cai, Q., 2011. Upgrading of bio-oil molecular distillation fraction with solid acid catalyst. *Bioresources*, 6(3), pp.2539–2550.

Gupta, A. & Verma, J.P., 2015. Sustainable bio-ethanol production from agro-residues: A review. *Renewable and Sustainable Energy Reviews*, 41, pp.550–567.

Guy, C., Carreau, P.J. & Paris, J., 1992. Heat and mass transfer between bubbles and a liquid. *The Canadian Journal of Chemical Engineering*, 70, pp.55–60.

Hanotu, J., Bandulasena, H.C.H., Chiu, T.Y. & Zimmerman, W.B., 2013. Oil emulsion separation with fluidic oscillator generated microbubbles. *International Journal of Multiphase Flow*, 56, pp.119–125.

Hanotu, J., Bandulasena, H.C.H. & Zimmerman, W.B., 2012. Microflotation performance for algal separation. *Biotechnology and bioengineering*, 109(7), pp.1663–73.

Hanotu, J., Karunakaran, E., Bandulasena, H., Biggs, C. & Zimmerman, W.B., 2014. Harvesting and dewatering yeast by microflotation. *Biochemical Engineering Journal*, 82, pp.174–182.

Hill, M.J.M., 1894. *On a Spherical Vortex*, The Proceedings Of The Royal Society Of London.

Himmelblau David M., 1989. *Basic principles and calculations in chemical engineering* 5th ed., Prentice-Hall, Inc., Englewood Cliffs.

Himus G.W. & Hinchley A.R.S.M., 1924. The effect of a current of air on the rate of evaporation of water below the boiling point. *chemistry and Industry*, pp.840–846.

Hiwale, R.S., Bhate, N.V., Mahajan, Y.S. & Mahajani, S.M., 2004. Industrial Applications of Reactive Distillation : Recent Trends. *International journal of chemical reactor engineering*, 2, pp.1–53.

Holtbruegge, J., Wierschem, M., Steinruecken, S., Voss, D., Parhomenko, L. & Lutze, P., 2013. Experimental investigation, modeling and scale-up of hydrophilic vapor permeation membranes: Separation of azeotropic dimethyl carbonate/methanol mixtures. *Separation and Purification Technology*, 118, pp.862–878.

Hosny, A.Y., 1996. Separating oil from oil-water emulsions by electroflotation technique. *Separations Technology*, 6(1), pp.9–17.

Hu, X., Gunawan, R., Mourant, D., Lievens, C., Li, X., Zhang, S., Chaiwat, W. & Li, C.-Z., 2012. Acid-catalysed reactions between methanol and the bio-oil from the fast pyrolysis of mallee bark. *Fuel*, 97, pp.512–522.

Hu, X., Wang, Y., Mourant, D., Gunawan, R., Lievens, C., Chaiwat, W., Gholizadeh, M., Wu, L., Li, X. & Li, C.Z., 2013. Polymerization on Heating up of Bio-Oil : A Model Compound Study. *AIChE Journal*, 59(3), pp.888–900.

Ikura, M., Stanciulescu, M. & Hogan, E., 2003. Emulsification of pyrolysis derived bio-oil in diesel fuel. *Biomass and Bioenergy*, 24(3), pp.221–232.

Inaba, H., Aoyama, S., Haruki, N., Horibe, A. & Nagayoshi, K., 2002. Heat and mass transfer characteristics of air bubbles and hot water by direct contact. *Heat and mass transfer*, 38(6), pp.449–457.

Islam, M.R., Parveen, M. & Haniu, H., 2010. Properties of sugarcane waste-derived bio-oils obtained by fixed-bed fire-tube heating pyrolysis. *Bioresource Technology*, 101(11), pp.4162–4168.

Iwayama, O., Tsutome, H. & Endo, Y., 2007. A liquid concentration method and apparatus. *Japanese patent*, P2007-5472.

Jacobs, H.R., 1988. Direct-Contact Heat Transfer for Process Technologies. *Journal of heat transfer*, 110, pp.1259–1270.

Jeffrey, C.M. & Kimberly, F.S., 2012. *Statistical Analysis of Chemical Sensor Data, Advances in Chemical Sensors*, InTech.

Jiang, X. & Ellis, N., 2010. Upgrading Bio-oil through Emulsification with Biodiesel: Thermal Stability. *Energy & Fuels*, 24(4), pp.2699–2706.

Jiang, X.-X., Zhong, Z.-P., Ellis, N. & Wang, Q., 2012. Characterisation of the mixture product of ether-soluble fraction of bio-oil (ES) and bio-diesel. *The Canadian Journal of Chemical Engineering*, 90(2), pp.472–482.

Julka, V., Chiplunkar, M. & Young, L.O., 2009. Selecting Entrainers for Azeotropic Distillation. *Reactions and Separation*, 105(3), pp.47–53.

Junming, X., Jianchun, J., Yunjuan, S. & Yanju, L., 2008. Bio-oil upgrading by means of ethyl ester production in reactive distillation to remove water and to improve storage and fuel characteristics. *Biomass and Bioenergy*, 32(11), pp.1056–1061.

Kanchanalai, P., Lively, R.P., Realff, M.J. & Kawajiri, Y., 2013. Cost and energy savings using an optimal design of reverse osmosis membrane pretreatment for dilute bioethanol purification. *Industrial and Engineering Chemistry Research*, 52(32), pp.11132–11141.

Kang, Y.H., Kim, N.J., Hur, B.K. & Kim, C.B., 2002. A numerical study on heat transfer characteristics in a spray column direct contact heat exchanger. *KSME International Journal*, 16(3), pp.344–353.

Karimi, E., Briens, C., Berruti, F., Moloodi, S., Tzanetakis, T., Thomson, M.J. & Schlaf, M., 2010. Red Mud as a Catalyst for the Upgrading of Hemp-Seed Pyrolysis Bio-oil. *Energy & Fuels*, 24(12), pp.6586–6600.

Khalaf, W., 2009. Sensor array systems for gases identification and quantification. In M. A. Strangio, ed. *Recent advences in technologies*. InTech.

Khalaf, W., Pace, C. & Gaudioso, M., 2008. Gas Detection via Machine Learning. *World academy of science, Engineering and technology*, 37, pp.139–143.

Khalaf, W., Pace, C. & Gaudioso, M., 2009. Least square regression method for estimating gas concentration in an electronic nose system. *Sensors*, 9(3), pp.1678–1691.

Khattab, I.S., Bandarkar, F., Fakhree, M.A.A. & Jouyban, A., 2012. Density, viscosity, and surface tension of water+ethanol mixtures from 293 to 323K. *Korean Journal of Chemical Engineering*, 29(6), pp.812–817.

Kim, T., Kim, J., Kim, K., Lee, S., Choi, D., Choi, I. & Weon, J., 2012. Journal of Analytical and Applied Pyrolysis The effect of storage duration on bio-oil properties. *Journal of Analytical and Applied Pyrolysis*, 95, pp.118–125.

Kim, T.S., Oh, S., Kim, J.Y., Choi, I.G. & Choi, J.W., 2014. Study on the hydrodeoxygenative upgrading of crude bio-oil produced from woody biomass by fast pyrolysis. *Energy*, 68, pp.437–443.

Klass, D.L., 2004. Biomass for Renewable Energy and Fuels. *Encyclopedia of Energy*, 1, pp.193–212.

Kumar, S., Kusakabe, K., Raghunathan, K. & Fan, L.S., 1992. Mechanism of heat transfer in bubbly liquid and liquid-solid systems: single bubble injection. *AIChE Journal*, 38(5), pp.733–741.

Lamb, H., 1879. *Hydrodynamics* 6th ed., (Printed 1994) Cambridge University Press.

Lappas, A.A., Samolada, M.C., Iatridis, D.K., Voutetakis, S.S. & Vasalos, I.A., 2002. Biomass pyrolysis in a circulating fluid bed reactor for the production of fuels and chemicals. *Fuel*, 81(16), pp.2087–2095.

Li, F., Yuan, Y., Huang, Z., Chen, B. & Wang, F., 2015. Sustainable production of aromatics from bio-oils through combined catalytic upgrading with in situ generated hydrogen. *Applied Catalysis B: Environmental*, 165, pp.547–554.

Li, X., Gunawan, R., Lievens, C., Wang, Y., Mourant, D., Wang, S., Wu, H., Garcia-Perez, M. & Li, C.Z., 2011. Simultaneous catalytic esterification of carboxylic acids and acetalisation of aldehydes in a fast pyrolysis bio-oil from mallee biomass. *Fuel*, 90(7), pp.2530–2537.

Liao, H.T., Ye, X.N., Lu, Q. & Dong, C.Q., 2013. Overview of Bio-Oil Upgrading via Catalytic Cracking. *Advanced Materials Research*, 827, pp.25–29.

Liu, W.J., Zhang, X.-S., Qv, Y.-C., Jiang, H. & Yu, H.-Q., 2012. Bio-oil upgrading at ambient pressure and temperature using zero valent metals. *Green Chemistry*, 14(8), pp.2226–2233.

Liu, X., Cheng, S., Liu, H., Hu, S., Zhang, D. & Ning, H., 2012. A survey on gas sensing technology. *Sensors*, 12(7), pp.9635–9665.

Lohitharn, N. & Shanks, B.H., 2009. Upgrading of bio-oil : Effect of light aldehydes on acetic acid removal via esterification. *Catalysis Communications*, 11(2), pp.96–99.

Lozano-parada, J.H. & Zimmerman, W.B., 2010. The role of kinetics in the design of plasma microreactors. *Chemical Engineering Science*, 65(17), pp.4925–4930.

Luque, L., Westerhof, R., Van Rossum, G., Oudenhoven, S., Kersten, S., Berruti, F. & Rehmann, L., 2014. Pyrolysis based bio-refinery for the production of bioethanol from demineralized ligno-cellulosic biomass. *Bioresource Technology*, 161, pp.20–28.

Luyben, W.L., 2014. Methanol/Trimethoxysilane Azeotrope Separation Using Pressure-Swing Distillation. *Industrial & Engineering Chemistry Research*, 53(13), pp.5590–5597.

MacInnes, J.M., Pitt, M.J., Priestman, G.H. & Allen, R.W.K., 2012. Analysis of two-phase contacting in a rotating spiral channel. *Chemical Engineering Science*, 69(1), pp.304–315.

Maggi, R. & Delmon, B., 1994. Characterization and upgrading of bio-oils produced by rapid thermal processing. *Biomass and Bioenergy*, 7(1–6), pp.245–249.

Mahfud, F.H., Ghijsen, F. & Heeres, H.J., 2007. Hydrogenation of fast pyrolyis oil and model compounds in a two-phase aqueous organic system using homogeneous ruthenium catalysts. *Journal of Molecular Catalysis A: Chemical*, 264(1–2), pp.227–236.

Matsuda, K.M., Huang, K.H. & Iwakabe, K.I., 2011. Separation of Binary Azeotrope Mixture via Pressure-Swing Distillation with. *Journal of Chemical Engineering of Japan*, 44(12), pp.969–975.

Mercader, F.D.M., Groeneveld, M.J., Kersten, S.R.A., Venderbosch, R.H. & Hogendoorn, J.A., 2010. Pyrolysis oil upgrading by high pressure thermal treatment. *Fuel*, 89(10), pp.2829–2837.

Moens, L., Black, S.K., Myers, M.D. & Czernik, S., 2009. Study of the Neutralization and Stabilization of a Mixed Hardwood Bio-Oil. *Energy & Fuels*, 23(13), pp.2695–2699.

Mohan, D., Pittman, C.U. & Steele, P.H., 2006. Pyrolysis of Wood/Biomass for Bio-oil: A Critical Review. *Energy & Fuels*, 20(3), pp.848–889.

Mullen, C.A. & Boateng, A.A., 2008. Chemical Composition of Bio-oils Produced by Fast Pyrolysis of Two Energy Crops. *Energy & Fuels*, 22(7), pp.2104–2109.

Muroyama, K., Oka, Y. & Fujiki, R., 2012. Transport Properties of Micro-Bubbles in a Bubble Column. *Journal of Chemical Engineering of Japan*, 45(9), pp.666–671.

Murtala, A.M., Shawal, N.N., Adilah, A.K., Usman, H.D., Energy, R. & Skudai, U.T.M., 2012. Characterization of Bio-oil into Functional Groups and Assessment of its Green Chemical Values. *UMT 11th International annual symposium on sustanibility science and management*, pp.1343–1350.

Naik, S., Goud, V. V., Rout, P.K. & Dalai, A.K., 2010. Supercritical CO2 fractionation of bio-oil produced from wheat-hemlock biomass. *Bioresource Technology*, 101(19), pp.7605–7613.

Naik, S.N., Rout, P.K., Naik, M.K., Goud, V., Fransham, P. & Dalai, A.K., 2010. Fractionation of Bio-oil By Supercritical CO 2. *Bioresource Technology*, 101(19), pp.7605–7613.

Naske, C.D., Polk, P., Wynne, P.Z., Speed, J., Holmes, W.E. & Walters, K.B., 2012. Postcondensation Filtration of Pine and Cottonwood Pyrolysis Oil and Impacts on Accelerated Aging Reactions. *Energy & Fuels*, 26(2), pp.1284–1297.

Nolte, M.W. & Liberatore, M.W., 2011. Real-Time Viscosity Measurements during the Accelerated Aging of Biomass Pyrolysis Oil. *Energy & Fuels*, 25, pp.3314–3317.

Oasmaa, A. & Czernik, S., 1999. Fuel Oil Quality of Biomass Pyrolysis Oils State of the Art for the End Users. *Energy & Fuels*, 13, pp.914–921.

Oasmaa, A., Elliott, D.C. & Korhonen, J., 2010. Acidity of Biomass Fast Pyrolysis Bio-oils. *Energy & Fuels*, 24(12), pp.6548–6554.

Oasmaa, A., Korhonen, J. & Kuoppala, E., 2011. An Approach for Stability Measurement of Wood-Based Fast Pyrolysis. *Energy & Fuels*, 25(7), pp.3307–3313.

Oasmaa, A. & Kuoppala, E., 2003. Fast Pyrolysis of Forestry Residue . 3 . Storage Stability of Liquid Fuel. *Energy & Fuels*, 17, pp.1075–1084.

Oasmaa, A., Kuoppala, E., Selin, J., Gust, S. & Solantausta, Y., 2004. Fast Pyrolysis of Forestry Residue and Pine . 4 . Improvement of the Product Quality by Solvent Addition. *Energy & Fuels*, 1(13), pp.1578–1583.

Oasmaa, A. & Meier, D., 2005. Norms and standards for fast pyrolysis liquids 1 . Round robin

test. *Journal of Analytical and Applied Pyrolysis*, 73(2), pp.323–334.

Oasmaa, A., Peacocke, C., Gust, S., Meier, D. & Mclellan, R., 2005. Norms and Standards for Pyrolysis Liquids . End-User Requirements and Specifications. *Energy & Fuels*, 19(5), pp.2155–2163.

Oasmaa, A., Sipila, K., Kuoppala, E. & Miljo, M., 2005. Quality Improvement of Pyrolysis Liquid : Effect of Light Volatiles on the Stability of Pyrolysis Liquids. *Energy & Fuels*, 19(6), pp.2556–2561.

Obeng, D.P., Morrell, S. & Napier-Munn, T.J., 2005. Application of central composite rotatable design to modelling the effect of some operating variables on the performance of the three-product cyclone. *International Journal of Mineral Processing*, 76(3), pp.181–192.

Oliveira, F.S., Pereiro, A.B., Rebelo, L.P.N. & Marrucho, I.M., 2013. Deep eutectic solvents as extraction media for azeotropic mixtures. *Green Chemistry*, 15(5), pp.1326–1330.

Ortiz-Toral, P.J., Satrio, J., Brown, R.C. & Shanks, B.H., 2011. Steam Reforming of Bio-oil Fractions: Effect of Composition and Stability. *Energy & Fuels*, 25(7), pp.3289–3297.

Pace, C., Fragomeni, L. & Khalaf, W., 2016. Developments and applications of electronic nose systems for gas mixtures classification and concentration estimation. In A. De Gloria, ed. *Applications in electronics pervading industry, environment and society*. Switzerland: Springer International Publishing.

Pace, C., Khalaf, W., Latino, M., Donato, N. & Neri, G., 2012. E-nose development for safety monitoring applications in refinery environment. *Procedia Engineering*, 47, pp.1267–1270.

Pacheco-Basulto, J.A., Hernandez-McConville, D., Barroso-Munoz, F.O., Hernandez, S., Segovia-Hernandez, J.G., Castro-Montoya, A.J. & Bonilla-Petriciolet, A., 2012. Purification of bioethanol using extractive batch distillation: Simulation and experimental studies. *Chemical Engineering and Processing*, 61, pp.30–35.

Pan, C., Chen, A., Liu, Z., Chen, P., Lou, H. & Zheng, X., 2012. Bioresource Technology Aqueous-phase reforming of the low-boiling fraction of rice husk pyrolyzed bio-oil in the presence of platinum catalyst for hydrogen production. *Bioresource Technology*, 125,

pp.335–339.

Panton, R.L., 1984. *Incompressible Flow*, NY: John Wiley & Sons.

Pattiya, A., Sukkasi, S. & Goodwin, V., 2012. Fast pyrolysis of sugarcane and cassava residues in a free-fall reactor. *Energy*, 44(1), pp.1067–1077.

Pattiya, A., Titiloye, J.O. & Bridgwater, A. V, 2006. Fast Pyrolysis of Agricultural Residues from Cassava Plantation for Bio-oil Production. *The 2nd joint international conference on sustainable energy and environment*, 7, pp.1–5.

Peng, Y. & Wu, S., 2011. Fast pyrolysis characteristics of sugarcane bagasse hemicellulose. *Cellulose chemistry and technology*, 45(9–10), pp.605–612.

Pereiro, A.B., Araujo, J.M.M., Esperanca, J.M.S.S., Marrucho, I.M. & Rebelo, L.P.N., 2012. Ionic liquids in separations of azeotropic systems - A review. *Journal of Chemical Thermodynamics*, 46, pp.2–28.

Ponce-De-León, C. & Field, R.W., 2000. Comparison of anionic membranes used to concentrate nitric acid to beyond the azeotropic mixture. *Journal of Membrane Science*, 171(1), pp.67–77.

Rehman, F., Medley, G.J.D., Bandulasena, H. & Zimmerman, W.B.J., 2015. Fluidic oscillator-mediated microbubble generation to provide cost effective mass transfer and mixing efficiency to the wastewater treatment plants. *Environmental Research*, 137, pp.32–39.

Reid, R.C., Prausnitz, J.M. & Poling, B.E., 1987. *The properties of gases and liquids*, McGraw-Hill, Inc. United States.

Resasco, D.E. & Crossley, S.P., 2015. Implementation of concepts derived from model compound studies in the separation and conversion of bio-oil to fuel. *Catalysis Today*, 257(P2), pp.185–199.

Ribeiro, C. p., Borges, C.P. & Lage, P.L.C., 2007. Sparger effects during the concentration of synthetic fruit juices by direct-contact evaporation. *Journal of Food Engineering*, 79, pp.979–988.

Ribeiro, C.p. & Lage, P.L.C., 2004. Direct-contact evaporation in the homogeneous and heterogeneous bubbling regimes. Part I: experimental analysis. *International Journal of*

Heat and Mass Transfer, 47(17–18), pp.3825–3840.

Ribeiro, C.P., Borges, C.P. & Lage, P.L.C., 2005. Modelling of direct-contact evaporation using a simultaneous heat and multicomponent mass-transfer model for superheated bubbles. *Chemical Engineering Science*, 60(6), pp.1761–1772.

Ribeiro, C.P. & Lage, P.L.C., 2004. Direct-contact evaporation in the homogeneous and heterogeneous bubbling regimes . Part II : dynamic simulation Cl. *International Journal of Heat and Mass Transfer*, 47, pp.3841–3854.

Ribeiro, C.P. & Lage, P.L.C., 2005. Gas-Liquid Direct-Contact Evaporation: A Review. *Chemical Engineering & Technology*, 28(10), pp.1081–1107.

Rivier, C.A., García-Payo, M.C., Marison, I.W. & Von Stockar, U., 2002. Separation of binary mixtures by thermostatic sweeping gas membrane distillation - I. Theory and simulations. *Journal of Membrane Science*, 201, pp.1–16.

Rout, P.K., Naik, M.K., Naik, S.N., Goud, V. V, Das, L.M. & Dalai, A.K., 2009. Supercritical CO2 Fractionation of Bio-oil Produced from Mixed Biomass of Wheat and Wood Sawdust. *Energy & Fuels*, 23(12), pp.6181–6188.

Ryabtsev, S. V, Shaposhnick, A. V, Lukin, A.N. & Domashevskaya, E.P., 1999. Application of semiconductor gas sensors for medical diagnostics. *Sensors and Actuators, B: Chemical*, 59, pp.26–29.

Şenol, O., Viljava, T.-R. & Krause, a. O.I., 2005. Hydrodeoxygenation of methyl esters on sulphided NiMo/γ-Al2O3 and CoMo/γ-Al2O3 catalysts. *Catalysis Today*, 100(3–4), pp.331–335.

Shawal, N.N., Murtala, A.M., Adilah, A.K. & Usman, H.D., 2012. Identification of functional groups of sustainable bio-oil substrate and its potential for specialty chemicals source. *Advanced Materials Research*, 557–559, pp.1179–1185.

Shirsat, S.P., Dawande, S.D. & Kakade, S.S., 2013. Simulation and optimization of extractive distillation sequence with pre-separator for the ethanol dehydration using n-butyl propionate. *Korean Journal of Chemical Engineering*, 30(12), pp.2163–2169.

Sipila, K., Kuoppala, E., Leena, F. & Oasmaa, A., 1998. Characterization of biomass-based flash pyrolysis oils. *Biomass and Bioenergy*, 14(2), pp.103–113.

Sirsi, S.R. & Borden, M.A., 2012. Advances in Ultrasound Mediated Gene Therapy Using Microbubble Contrast Agents. *Theranostics*, 2(12), pp.1208–1222.

Takahashi, M., 2005. Potential of Microbubbles in Aqueous Solutions : Electrical Properties of the Gas - Water Interface. *Journal of Physical Chemistry B*, 109(46), pp.21858–21864.

Tang, B., Bi, W. & Row, K.H., 2013. Dehydration of ethanol by facile synthesized glucose-based silica. *Applied biochemistry and biotechnology*, 169(3), pp.1056–68.

Teella, A., Huber, G.W. & Ford, D.M., 2011. Separation of acetic acid from the aqueous fraction of fast pyrolysis bio-oils using nanofiltration and reverse osmosis membranes. *Journal of Membrane Science*, 378(1–2), pp.495–502.

Tesař, V., 2012. Microbubble generation by Fluidics. Part II: Bubble formation mechanicsm. *Proc. of Colloquium Fluid Dynamics, Prague*, 1, pp.1–20.

Tesař, V., 2014. Microbubble generator excited by fluidic oscillator's third harmonic frequency. *Chemical Engineering Research and Design*, 92(9), pp.1603–1615.

Tesař, V., 2007. "Paradox" of flow reversal caused by protective wall-jet in a pipe. *Chemical Engineering Journal*, 128(2–3), pp.141–154.

Tesař, V. & Bandalusena, H.C.H., 2010. Bistable diverter valve in microfluidics. *Experiments in Fluids*, 50(5), pp.1225–1233.

Tesař, V. & Bandalusena, H.C.H., 2011. Bistable diverter valve in microfluidics. *Experiments in Fluids*, 50(5), pp.1225–1233.

Tesař, V., Hung, C.H. & Zimmerman, W.B., 2006. No-moving-part hybrid-synthetic jet actuator. *Sensors and Actuators A: Physical*, 125(2), pp.159–169.

Thegarid, N., Fogassy, G., Schuurman, Y., Mirodatos, C., Stefanidis, S., Iliopoulou, E.F., Kalogiannis, K. & Lappas, A.A., 2014. Second-generation biofuels by co-processing catalytic pyrolysis oil in FCC units. *Applied Catalysis B: Environmental*, 145, pp.161–166.

Tripathi, M.M., Hassan, E.B.M., Yueh, F., Singh, J.P. & Steele, P.H., 2010. Study of the Effect of Ultraviolet Exposure on Bio-oil by Laser-Induced Fluorescence Spectroscopy. *Energy & Fuels*, 24(14), pp.6187–6192.

Tsai, W.T., Lee, M.K. & Chang, Y.M., 2006. Fast pyrolysis of rice straw , sugarcane bagasse and coconut shell in an induction-heating reactor. *Journal of Analytical and Applied Pyrolysis*, 76(1–2), pp.230–237.

Tsuge, H., 2014. Characteristics of microbubbles. In H. Tsuge, ed. *Micro- and nanobubbles: fundamentals and applications*. Pan Stanford Publishing Pte. Ltd.

Ubal, S., Grassia, P., Harrison, C.H. & Korchinsky, W.J., 2011. Numerical simulation of multi-component mass transfer in rigid or circulating drops: Multi-component effects even in the presence of weak coupling. *Colloids and Surfaces A: Physicochemical and Engineering Aspects*, 380(1–3), pp.6–15.

Ubal, S., Harrison, C.H., Grassia, P. & Korchinsky, W.J., 2010. Numerical simulation of mass transfer in circulating drops. *Chemical Engineering Science*, 65(10), pp.2934–2956.

Vazquez, A., Sanchez, R.M., Salinas-Rodríguez, E., Soria, A. & Manasseh, R., 2005. A look at three measurement techniques for bubble size determination. *Experimental Thermal and Fluid Science*, 30(1), pp.49–57.

Vázquez-Ojeda, M., Segovia-Hernández, J.G., Hernández, S., Hernández-Aguirre, A. & Kiss, A.A., 2013. Design and optimization of an ethanol dehydration process using stochastic methods. *Separation and Purification Technology*, 105, pp.90–97.

Venderbosch, R.H., Ardiyanti, A.R., Wildschut, J., Oasmaa, A. & Heeres, H.J., 2010. Stabilization of biomass-derived pyrolysis oils. *Journal of Chemical Technology & Biotechnology*, 85(5), pp.674–686.

Venderbosch, R.H. & Prins, W., 2010. Fast pyrolysis technology. *Biofuels bioproducts and biorefining*, 4(2), pp.178–208.

Wang, J., Cui, H., Wei, S., Zhuo, S., Wang, L., Li, Z. & Yi, W., 2010. Separation of Biomass Pyrolysis Oil by Supercritical CO2 Extraction. *Smart Grid and Renewable Energy*, 1(2), pp.98–107.

Wang, S., Gu, Y., Liu, Q., Yao, Y., Guo, Z., Luo, Z. & Cen, K., 2009. Separation of bio-oil by molecular distillation. *Fuel Processing Technology*, 90(5), pp.738–745.

Wang, S., Li, X., Zhang, F., Cai, Q. & Wang, Y., 2013. Bio-oil catalytic reforming without steam addition : Application to hydrogen production and studies on its mechanism.

International Journal of Hydrogen Energy, 38(36), pp.16038–16047.

Wang, Y., Wang, S., Leng, F., Chen, J., Zhu, L. & Luo, Z., 2015. Separation and characterization of pyrolytic lignins from the heavy fraction of bio-oil by molecular distillation. *Separation and Purification Technology*, 152, pp.123–132.

Wang, Z., Lin, W. & Song, W., 2012. Liquid product from hydrothermal treatment of cellulose by direct GC/MS analysis. *Applied Energy*, 97, pp.56–60.

Wesley, D.J., Brittle, S.A., Toolan, D.T.W., Howse, J.R. & Zimmerman, W.B., 2016. Development of an optical microscopy system for automated bubble cloud analysis. *Applied Optics*, 55(22), pp.6102–6107.

Wheatley, M.A. & Cochran, M., 2013. Ultrasound contrast agents. *Journal of Drug Delivery Science and Technology*, 23(1), pp.57–72.

Winnan, C.D., 2013. *Adventures in 3D printing: limitless possibilities and profit*, CreatSpace Independent Publishing Platform.

Worden, R.M. & Bredwell, M.D., 1998. Mass-Transfer Properties of Microbubbles. 2. Analysis Using a Dynamic Model. *Biotechnology Progress*, 14(1), pp.39–46.

Wu, C., Sui, M. & Yan, Y.J., 2008. A Comparison of Steam Reforming of Two Model Bio-Oil Fractions. *Chemical Engineering & Technology*, 31(12), pp.1748–1753.

Xu, F., Xu, Y., Lu, R., Sheng, G. & Yu, H., 2011. Elucidation of the Thermal Deterioration Mechanism of Bio-oil Pyrolyzed from Rice Husk Using Fourier Transform Infrared Spectroscopy. *Agricultural and food chemistry*, 59, pp.9243–9249.

Xu, Y., Wang, T., Ma, L., Zhang, Q. & Liang, W., 2010. Upgrading of the liquid fuel from fast pyrolysis of biomass over MoNi/Al2O3 catalysts. *Applied Energy*, 87(9), pp.2886–2891.

Yang, Y., Yi, J., Jin, R. & Mason, A.J., 2013. Power-Error Analysis of Sensor Array Regression Algorithms for Gas Mixture Quantification in Low- Power Microsystems. *12th IEEE SENSORS 2013 Conference; Baltimore, MD; United States*, 6688580.

Yu, F., Deng, S., Chen, P., Liu, Y., Wan, Y., Olson, A., Kittelson, D. & Ruan, R., 2007. Physical and chemical properties of bio-oils from microwave pyrolysis of corn stover. *Applied biochemistry and biotechnology*, 137–140(1–12), pp.957–70.

Yu, Z. & Fan, L.S., 2008. Direct simulation of the buoyant rise of bubbles in infinite liquid using level set method. *The Canadian Journal of Chemical Engineering*, 86(3), pp.267–275.

Zemansky, M.W. & Dittman, R., 1997. *Heat and Thermodynamics* 7thEd ed., NewYork: McGraw-Hill.

Zhang, C., Zhang, R., Li, X., Li, Y., Shi, W. & Ren, X., 2011. Bench-Scale Fluidized-Bed Fast Pyrolysis of Peanut Shell for Bio-Oil Production. *AIChE Journal*, 30(1), pp.11–18.

Zhang, L. & Kong, S., 2012. Multicomponent vaporization modeling of bio-oil and its mixtures with other fuels. *Fuel*, 95, pp.471–480.

Zhang, L., Liu, R., Yin, R. & Mei, Y., 2013. Upgrading of bio-oil from biomass fast pyrolysis in China : A review. *Renewable and Sustainable Energy Reviews*, 24, pp.66–72.

Zhang, Q., Chang, J., Wang, T. & Xu, Y., 2007. Review of biomass pyrolysis oil properties and upgrading research. *Energy Conversion and Management*, 48(1), pp.87–92.

Zhang, S., Yan, Y., Li, T. & Ren, Z., 2005. Upgrading of liquid fuel from the pyrolysis of biomass. *Bioresource Technology*, 96, pp.545–550.

Zhou, M., Tian, L., Niu, L., Li, C., Xiao, G. & Xiao, R., 2014. Upgrading of liquid fuel from fast pyrolysis of biomass over modified Ni/CNT catalysts. *Fuel Processing Technology*, 126, pp.12–18.

Zimmerman, W.B., 2007. *Multiphysics Modelling with Finite Element Methods*. World Scientific Publishing Company, Singapore.

Zimmerman, W.B., Al-Mashhadani, M.K.H. & Bandulasena, H.C.H., 2013. Evaporation dynamics of microbubbles. *Chemical Engineering Science*, 101, pp.865–877.

Zimmerman, W.B., Hewakandamby, B.N., Tesař, V., Bandulasena, H.C.H. & Omotowa, O.A., 2009. On the design and simulation of an airlift loop bioreactor with microbubble generation by fluidic oscillation. *Food and Bioproducts Processing*, 87(3), pp.215–227.

Zimmerman, W.B., Tesař, V. & Bandulasena, H.C.H., 2011. Towards energy efficient nanobubble generation with fluidic oscillation. *Current Opinion in Colloid & Interface Science*, 16(4), pp.350–356.

Zimmerman, W.B., Tesar, V., Butler, S. & Bandulasena, H.C.H., 2008. Microbubble Generation. *Recent Patents on Engineering*, 2(1), pp.1–8.

Zimmerman, W.B., Zandi, M., Hemaka Bandulasena, H.C., Tesař, V., James Gilmour, D. & Ying, K., 2011. Design of an airlift loop bioreactor and pilot scales studies with fluidic oscillator induced microbubbles for growth of a microalgae Dunaliella salina. *Applied Energy*, 88(10), pp.3357–3369.

The University Of Sheffield.

Appendices

Appendix A.

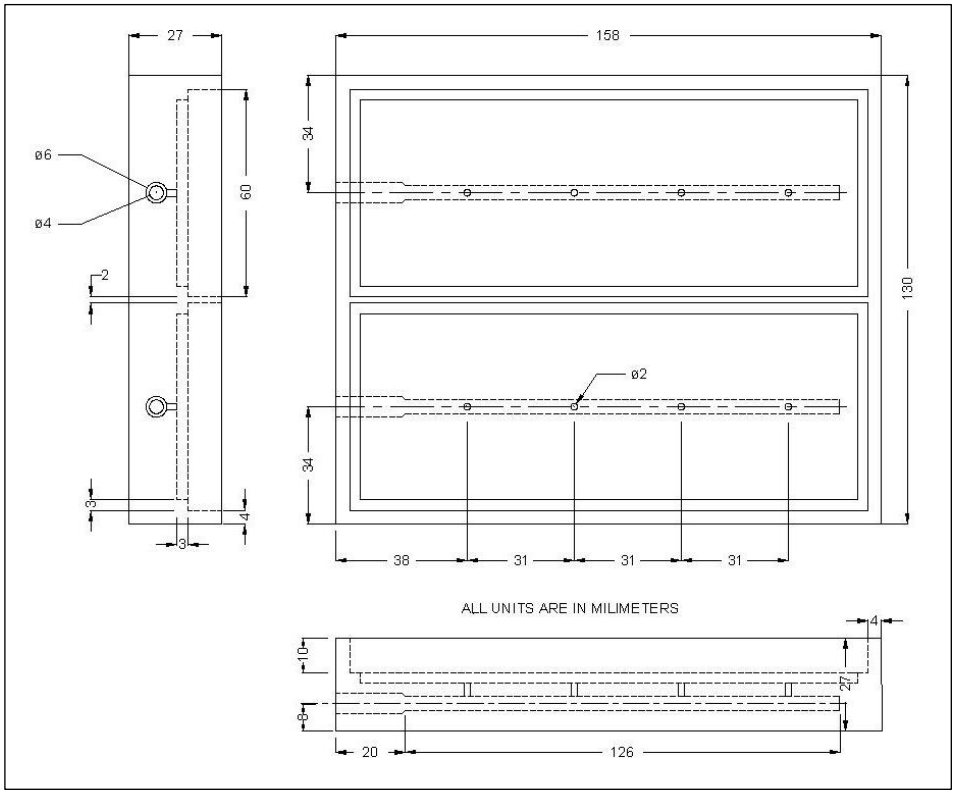

Figure A.1: CAD schematic diagram of the second built aluminum bespoke diffuser for the bubble tank.

Appendix B.

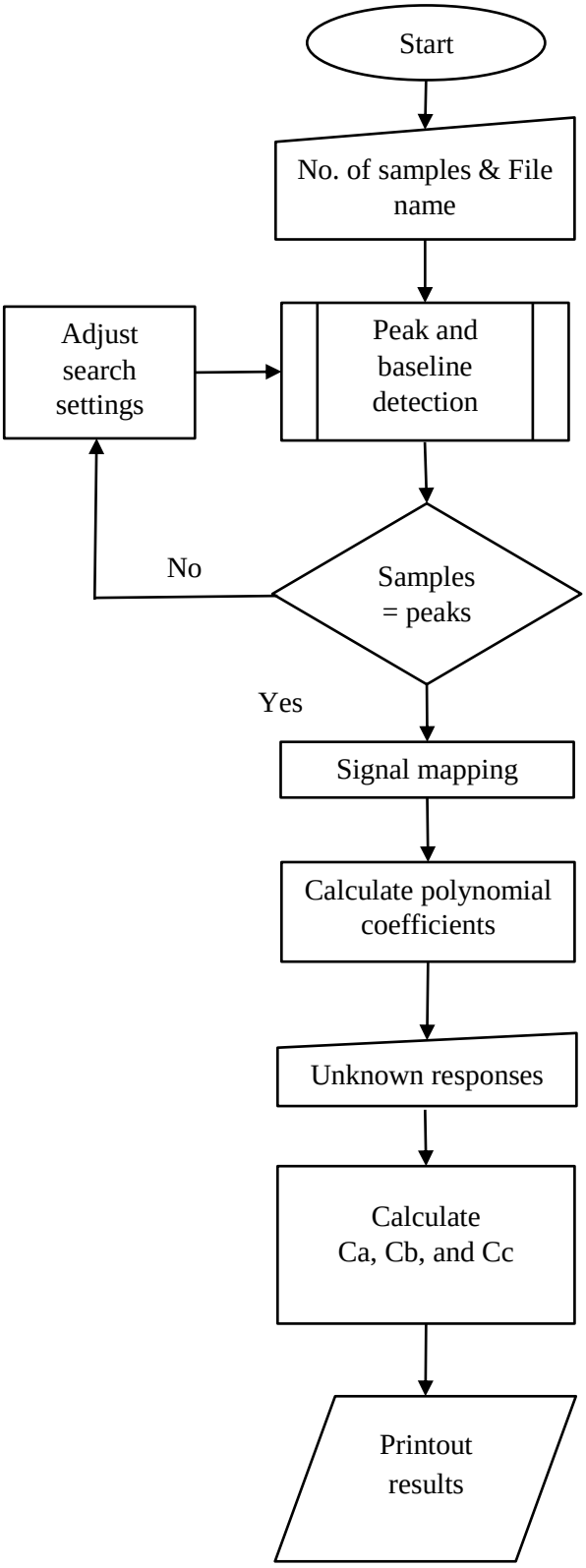

Figure B.1: Flow chart of the signal analysis procedure of the electronic nose.

Appendix C.

Physical properties for the evaporation dynamics of a hot bubble rising in an ethanol-water mixture (ethanol (1) and water (2))

Quantity	***Value***
Liquid mixture density	exp (x1 × ln ρ1+ x2 × ln ρ2- 30.808 [(x1 x2)/ T liquid]- 18.274 [(x1 x2(x2 - x1))/ T liquid] + 13.8 [(x1 x2)(x2 - x1)^2/T liquid]) kg/m^3
Ethanol density (ρ1)	0.791×10^3 kg/m^3
Water density (ρ2)	1×10^3 kg/m^3
Liquid mixture viscosity	exp (x1 × ln μ1 + x2 × ln μ2+ 724.652 [(x1 x2)/T liquid] + 729.357 [(x1 x2)(x2 - x1)/T liquid] + 976.05 [(x1 x2)(x2 - x1)2/T liquid]) Pa s
Ethanol viscosity (μ1)	1.1890×10 $^{-3}$ Pa s
Water viscosity (μ2)	1.003×10 $^{-3}$ Pa s
Cp water (liquid)	75.33 J/mol/K
Cp ethanol (liquid)	110.5 J/mol/K
Cp water (vapor)	33.46+0.688×10^{-2}(T-273) +0.7604×10^{-5}(T-273) ^{2}-3.593×10^{-9}(T-273)^3 J/mol/K
Cp ethanol (vapor)	61.34+15.72×10^{-2}(T-273)-8.749×10^{-5}(T-273)^2+19.83×10^{-9}(T-273)^3 J/mol/K
Cp air	28.09 + 0.1965×10^{-2} T+ 0.4799×10^{-5} T^2- 1.965×10^{-9} T^3 J/mol/K
P*water	133.322368 exp(18.3036 - (3816.44/(-46.13 + T))) Pa
P*ethanol	133.322368 exp(18.5242 - (3578.91/(-50.50 + T))) Pa
K air	(0.007058+ 0.0000578 T+ 1.9751×10-8 T^2) W/m/K
ΔHv water	56462.6 - 43.1784 T+ 0.000962433 T^2 + 3.5155e-6 T^3- 8.9825e-10 T^4 J/mole
ΔHv ethanol	1048.6 - 1.0921 (T - 273) + 0.010651 (T - 273)^2- 0.00020693 (T - 273)^3+ 1.1231 ×10-6 (T - 273)^4-2.4928×10^{-9} (T - 273)^5 J/kg

Publications

Abdulrazzaq, N., Al-Sabbagh, B., Rees, J.M. & Zimmerman, W.B., 2016. Separation of azeotropic mixtures using air microbubbles generated by fluidic oscillation. *AIChE Journal*, 62(4), pp.1192–1199.

Abdulrazzaq, N., Al-Sabbagh, B., Rees, J.M. & Zimmerman, W.B., 2016. Purification of bioethanol using microbubbles generated by fluidic oscillation: A dynamical evaporation model. *Industrial & Engineering Chemistry Research*, 55(50),pp. 12909-12918.